



UNIVERSITÀ
DEGLI STUDI
DI PADOVA

Sede Amministrativa: Università degli Studi di Padova

Centro Interdipartimentale di Studi e Attività Spaziali (CISAS)

SCUOLA DI DOTTORATO DI RICERCA IN: Scienze Tecnologie e Misure Spaziali (STMS)

INDIRIZZO: Astronautica e Scienze da Satellite

CICLO: XXIII

**THE IMPORTANCE OF BEING A CRATER:
A TOOL IN PLANETARY SURFACE ANALYSIS AND DATATION**

Direttore della Scuola: Ch.mo Prof. Giampiero Naletto

Supervisore: Dr. Francesco Marzari

Co-Supervisore: Dr. Gabriele Cremonese

Dottoranda: Elena Martellato

31 Gennaio 2011

for my Mum

Acknowledgements

My first thanks is to my Mum, whose endless encouragement and sacrifice made possible all my journey of studies up to the achievement of this thesis and the landing on my Moon.

During all these three years, I have been supported by many people whom I want express my deepest gratitude.

First and foremost, I would like to thank my PhD supervisors Gabriele Cremonese, who not only helped me through his constant presence, highlights scientific guidance, and the many facets of completing this PhD, but who also provided me with extraordinary experiences and opportunities for my researcher career, among them I want to mention the attendance to the 3rd MESSENGER flyby, and Francesco Marzari, who helped me through his invaluable support and unquestionable enlightening, always welcoming for academic inspiration and coding advices.

A special thanks to Matteo Massironi, for his praiseworthy geologic assistance, along with all the geologists, Lorenza Giacomini, Sabrina Ferrari and Giovanni Monegato. I would like to thank the astronomer Simone Marchi for providing me all the support regarding planetary dating. A last thank among the “Padova group” is for Patrizia Borin.

Special thanks goes also to all the “impact group”. To Betty Pierazzo, who first offered me a chance to enter the “impact community”, by introducing me to the iSALE developers, welcomed me in Tucson and gave me the fantastic and unique opportunity to meet Jay Melosh. To Natasha Artemieva, who gave me the first basis in hydrocodes theory and helped me with her stimulating discussions at PSI. To both Gareth Collins and Kay Wünnemann, who let me enter the iSALE community, and have always been available for enlightening advices and for all the coding assistance I have needed. In addition, I gratefully acknowledge all the developers of iSALE, including besides Gareth Collins and Kay Wünnemann, also Boris Ivanov, Jay Melosh and Dirk Elbeshausen. Finally, I would thank Veronica Bray.

The last but not the least thank is for all the wonderful guys at PSI during my stay, in particular Pasquale Tricarico for his precious assistance. The month I spent in Tucson is still now a bright memory that has accompanied me once I returned back to Italy, along with the warm sun of Arizona.

Contents

Acknowledgements	i
Contents.....	iii
Chapter 1: ABSTRACT	1
Chapter 2: INTRODUCTION.....	5
Chapter 3: IMPACT CRATERS	9
3.1 Craters: A tool in planetary studies.....	9
3.1.1 <i>Craters: A look into the Impactors Flux</i>	9
3.1.2 <i>Craters: A probe into the Original Target Topography</i>	11
3.1.3 <i>Craters: the search of the lost Water</i>	16
3.2 Crater Formation Process	20
3.2.1 <i>Contact and Compression Stage</i>	22
3.2.2 <i>Excavation and Transient Crater Growth Stage</i>	24
3.2.3 <i>Modification Stage</i>	27
3.3 Crater Morphologies.....	35
3.3.1 <i>Simple craters</i>	36
3.3.2 <i>Complex craters</i>	37
3.3.3 <i>Multiring Basins</i>	40
3.4 Impact signatures	43
3.5 Origins of Projectiles	49

Chapter 4: PLANETARY CHRONOLOGY	55
4.1 Introduction to age determination via crater counting.....	55
4.2 Neukum Production Function.....	59
4.3 Hartmann Production Function.....	70
4.4 Model Production Function.....	72
4.4.1 Modelling the Impactor Flux on the Earth-Moon system.....	73
4.4.2 Scaling Laws.....	75
4.4.3 MPF distribution.....	78
4.4.4 Moon's Chronology.....	79
4.4.5 Mercury's Chronology.....	83
4.5 Main weaknesses of the model	85
4.5.1 Secondary craters	85
4.5.2 A constant flux?	89
4.6 Counting S/W	90
Chapter 5: NUMERICAL MODELLING	95
5.1 Introduction to <i>Hydrocodes</i>	95
5.2 iSALE hydrocode	103
5.2.1 Discretization.....	104
5.2.2 Equations of State	105
5.2.3 Materials Models.....	107
5.2.4 Acoustic Fluidization	109
5.2.5 Porosity Model.....	116
5.3 Validation to laboratory experiments	119
Chapter 6: SPACE MISSIONS	123
6.1 Introduction.....	123
6.2 BepiColombo.....	124
6.3 MESSENGER.....	131
6.3.1 Mission Overview.....	132

6.3.2 <i>Spacecraft & Payload</i>	133
6.3.3 <i>MDIS</i>	135
6.4 Rosetta136	
6.4.1 <i>Mission Overview</i>	137
6.4.2 <i>Spacecraft & Payload</i>	139
6.4.3 <i>OSIRIS</i>	142
Chapter 7: RESULTS.....	143
7.1 Introduction to Applications	143
7.2 Crater Retention Age Determination: “ <i>R-duet</i> ”	147
7.2.1 <i>Raditladi</i>	147
7.2.2 <i>Rachmaninoff</i>	154
7.3 Numerical Modelling: Omeonga	161
7.3.1 <i>Background</i> 161	
7.3.1 <i>Omeonga description and geological setting</i>	162
7.3.2 <i>Remote sensing analysis</i>	165
7.3.3 <i>Impact or non-impact origin?</i>	168
7.3.4 <i>Numerical modelling of Omeonga</i>	169
7.4 Rosetta: A deciphering <i>Stone</i> for a so far away world.....	178
7.4.1 <i>Steins</i>	181
7.4.2 <i>Lutetia</i>	190
Chapter 8: CONCLUSIONS	203
Bibliography.....	209

Chapter 1

Abstract

This PhD thesis has been realized within the project of STC/SIMBIOSYS, the stereo channel composing the imaging system on board of the BepiColombo mission to Mercury and providing the global mapping in stereo mode of the Hermean surface. As the aim of this work is supporting the definition of the scientific requirements of STC, the impact craters have been recognized as the surface structure to be investigated, being the most important and common landform of any planetary body with a solid surface, but meanwhile far to be yet completely understood.

This thesis addresses to explore the *importance* of impact crater structure as a *tool* in investigating a variety of aspects of planetary bodies, whose remote sensing data is the only available information. Earth as well can take advantage from studying such a rarely occurring, complicated and highly dynamic process, as the combining effects of erosion, tectonics and volcanism can hide impact structures.

The first theme turns to impact craters not as an individual entity, but as a population of features on planetary surfaces, in particular Mercury. The cratering records, being the result of a long–repeated meteorite bombardment history, can be used to infer surface age after the application of a chronological model to statistical analysis. The data recently acquired by the MESSENGER mission during its three flybys with this planet were the starting point to study two new basins, i.e. Raditladi and Rachmaninoff. The MPF chronological model has been adopted to derive the crater retention age for these basins, whose impact events turned out to occur well after the LHB, posing some puzzles to the current impactor sources in the inner Solar System. In addition, Rachmaninoff interior plains could be emplaced in a very recent period (360 *Ma* ago), suggesting a long–lasting volcanism up to recent time, and hence a revision to our current knowledge on the thermal state of the planet is proposed

The second theme of my thesis addresses the investigation of the impact formation process. The current understanding of impact cratering as a whole has come from a suite of experimental, morphological, analytical and numerical studies. However, shocks codes represent one of the only feasible methods for studying impact craters, as they can simulate a large span of conditions beyond the reach of experiments, in addition to analyze the individual effect of any parameters acting during the impact event.

I have used iSALE shock code to simulate two craters, coming from a completely different environment, the Earth and one asteroid, recently observed by a space mission. In the first case, the knowledge of the surrounding area where the structure is located allowed to study in detail the impact crater collapse mechanism that origins a large crater. On the other hand, the good relatively knowledge of the formation of a simple crater allowed to investigate the composition and the structure of the asteroid. In both cases, the numerical modelling of the impact process has demonstrated to be a powerful *tool* to deepen our comprehension on the Solar System.

Riassunto

Questa tesi di dottorato è stata realizzata nell'ambito del progetto di STC/SIMBIOSYS, il canale stereo appartenente al sistema di imaging che a bordo della missione spaziale BepiColombo avrà l'obiettivo di fornire la mappatura globale della superficie di Mercurio in modalità stereo. Poiché lo scopo di questa tesi è di supportare la definizione dei requisiti scientifici della stereo camera, lo studio dei crateri da impatto è stato selezionato come argomento fondamentale. I crateri da impatto sono infatti la più importante e più diffusa morfologia su qualsiasi corpo planetario dotato di una superficie solida, ma allo stesso tempo non ancora completamente compresi.

Questa tesi vuole esplorare l'*importanza* dei crateri da impatto come *tool* nell'investigazione di una varietà di aspetti riguardanti i corpi planetari, dei quali si hanno a disposizione solo un numero esiguo di informazioni. Tuttavia, anche nel caso della Terra, per la quale si possiede una grande quantità di dati, lo studio di questo processo altamente dinamico può portare ad una migliore conoscenza del nostro pianeta e delle forze che tutt'ora lo modellano.

Il primo tema di questa tesi riguarda lo studio dei crateri da impatto non come un'entità singola, ma una popolazione di oggetti presenti sulle superfici planetarie, in particolare quella di Mercurio. La craterizzazione su di una superficie è il risultato di una lunga storia di bombardamento meteoritico, e può essere quindi usato per derivare l'età di quella superficie, se si applica un modello cronologico basato sull'analisi statistica dei crateri. I dati recentemente acquisiti dalla missione MESSENGER durante i suoi tre flyby con questo pianeta sono stati l'incipit per lo studio di due nuovi bacini, Raditladi e Rachmaninoff. Si è quindi adottato il modello cronologico MPF per derivare l'età in cui si sono formati questi due bacini. Il risultato di questa analisi è che entrambe le strutture si sono originate in un periodo successivo all'LHB, ponendo interrogativi sulle attuali sorgenti di impattori, considerando la notevole dimensione di queste due strutture d'impatto. Inoltre, le pianure interne di Rachmaninoff potrebbero essere molto giovani (360 *Ma* fa), suggerendo un prolungato vulcanismo, e, a sua volta, una revisione delle nostre attuali conoscenze sullo stato termico di questo pianeta.

Il secondo tema di questa tesi riguarda lo studio del processo di formazione di un impatto. La nostra attuale comprensione di un evento di impatto viene principalmente da studi sperimentali, morfologici, analitici e numerici. Tuttavia, gli shock code rappresentano l'unico procedimento che permette sia di esplorare condizioni non raggiungibili in laboratorio, sia di capire l'influenza di ciascuna variabile durante il processo di impatto.

In questa testi, si è usato iSALE per simulare due crateri, provenienti da due ambienti molto diversi, il nostro pianeta e un asteroide recentemente osservato da una missione spaziale. Nel primo caso, la buona conoscenza della regione dove è collocato il cratere ha permesso di approfondire il meccanismo che sta alla base del collasso di un cratere di grandi dimensioni. Invece, nel secondo caso, era il processo di formazione ad essere meglio conosciuto, dal momento che si trattava di una struttura semplice, e quindi la simulazione numerica è stata finalizzata a investigare la possibile composizione e struttura superficiale di questo asteroide. In entrambi i casi, la modellizzazione numerica del processo di impatto si è dimostrato un capace *tool* per migliorare la nostra conoscenza del Sistema Solare.

Chapter 2

Introduction

Craters everywhere ...

... Impacts have been recognized to be the leading actor in the Solar System since its dawning. The recent theories about planets formation state the dust nebula to coalesce into planetesimals, that in turn collide each others under gravitational forces to origin the planets. The Moon itself likely formed during a mega-impact of a Mars-sized planetesimal with Earth. Similar impacts may have stripped off the silicate mantle on Mercury, leaving the present iron-rich object (Benz et al., 1988) and may have removed the early primordial atmospheres of the planets (Melosh & Vickery, 1989).

The initial trend of intense flux during the accretionary epochs was followed by a decline up to an impact rate much lower and fairly constant. This scenario has led Earth, the Moon, and more in general the terrestrial planets and outer giant satellites, to share a common history of impact by asteroids and comets, as the ubiquitous craters recording on the airless bodies is testifying.

Earth was drawn in as well by impacts, but the presence of a dense atmosphere, that prevents the entrance of bodies smaller than a few tens of meters, and other dominant influence of processes like exploding volcanoes or ice instabilities, has not allow us up till about half a century ago to realize how much impacts have predominantly shaped our planet and the evolution of life.

Notwithstanding, asteroid and comet impacts have played a major role in the geological and biological history of the Earth, both in a positive and drawback view of evolution. On one side, a significant fraction of the Earth's prebiotic volatile inventory of organic molecules may have been delivered by infalling comets and asteroids during the heavy bombardment (e.g., Pierazzo & Chyba,

1999). On the other hand, impacts large enough to affect dramatically the fragile climate and ecosystems of the whole planet can cause prominent changes in the geologic record of fossilizable species of life, and can be identified as a reliable explanation for mass extinction events. For instance, Alvarez et al. (1980) first proposed that an 10–*km* impact event, successively associated to the Chicxulub crater (Messico), led to catastrophic environmental effects such as extended darkness, global cooling and acid rain that caused the dinosaur–killing Cretaceous–Paleogene (K/Pg, formerly K/T) extinction mass, ~65.5 *Myr* ago (Pope, 1997; Schulte et al., 2010; Toon et al., 1997).

These are only few themes of investigation cues that point out how the impact cratering has met the outstanding interest of the researchers community. Despite great effort has been spent in studying many aspects on impact craters, the current understanding of this feature remains incomplete, bearing in mind that is a “young” science. In fact, before the 1960s, collisions of extraterrestrial objects with Earth were not considered significant. The recognition of the importance of meteorite impacts on Earth has come largely from the study of other planets. Exploration of the Moon and the Solar System by astronauts and robotic spacecraft demonstrates that impact cratering has been, and still is, a major process in the origin and evolution of all the solid bodies of the Solar System, from Mercury to the moons of Neptune (French, 1998), whereas the uniqueness conditions characterizing this process —large amount of nearly instantaneous release of energy, in a relatively small area interested by outstanding pressure conditions— make impact craters a peculiar *tool* in planetary sciences.

Impact craters have been therefore identified as the argument of my research, being without shadow of doubt the most common and interesting landform that will be observed on planetary bodies.

Two topics have been argued during my PhD, each one concerning different aspect of impact cratering. The first one deals in addressing craters as a *population* of objects, that records a long history of meteoroids bombardment. The analysis of such records in conjunction with some assumptions about the rate of crater formation has been successfully applied in different topics, but first of all it represents an unquestionable tool to understand the geologic history of atmosphereless planets and small bodies surfaces. The impact craters size–frequency distribution was recognized as soon as the middle of the 1900s to be a means to infer crater retention age of a given surface, based on the fact that the frequency of impact craters superimposed on a given geologic unit is directly correlated with geologic time.

Since the first images of the Moon were available, many models have been advanced to derive ages from the statistical analysis of impact craters. In my thesis, I adopted a recent chronology model proposed by Marchi et al. (2009), who used the dynamical models of both the Main Belt Asteroids and Near Earth Objects (e.g., Bottke et al., 2002a, 2005a) to derive the impactor flux, which is then converted via scaling law into the MPF, in turn calibrated using the lunar rocks radiometric ages.

One of the strength point of this model, that is the implementation of a layered structure for the analyzed surfaces characteristic of planetary–like crust, has been at the basis of the crater retention age investigation performed in this thesis.

Crater counting with age determination purpose was focused on two newly discovered impact basins on Mercury, one of the most enigmatic among the terrestrial planets. The data acquired by NASA MESSENGER mission during its flybys with this planet revealed two similar double-ring basins, both ~300 km in diameter, Raditladi and Rachmaninoff, that soon appeared to be remarkably young, likely formed well after the end of the LHB, as the small number of craters within their rims testifies (e.g., Prockter et al., 2010).

The aim of this investigation was to explore the time span of the impact events that formed these basins, because both their remarkable large dimensions and supposed young origin was an intriguing puzzle in the understanding of the current population of impactors in the inner Solar System. In addition, the crater retention age investigation may give the possibility to evaluate if subsequent endogenic processes have interested those basins. Our current Mariner 10-based knowledge point out that the smooth plains emplacement lasted up the Caloris Basin formation (~3.6 Ga). Hence, if this analysis will suggest a more recent volcanic activity, it may lead to important implications in the global thermal evolution of Mercury since the young age of both the basins.

The second topic of my thesis deals in investigating the crater formation process via numerical modelling as a *tool* to explore the dynamic of the process itself, with particular care of the variables that might influence the mechanism of craters formation. In the former cratering studies, the impact process was learnt mainly through small-scale laboratory impact experiments and high energy explosions, that however could provide only a limited window into the impact dynamics, as not reachable conditions of mass and velocity peculiar of a “real” impact. The only feasible approach for studying impact craters is numerical modelling through hydrocodes, as they can simulate a large span of conditions beyond the reach of experiments, in addition to analyze the individual effect of any parameters acting during the impact event.

I have the opportunity to use iSALE shock code (Amsden et al., 1980; Collins et al., 2004; Ivanov et al., 1997; Wünnemann et al., 2003, 2006) to model two craters belonged to a completely different environment, i.e. Omeonga on the Earth, and a 21-km crater on Lutetia asteroid, which was recently flew by the Rosetta spacecraft.

Numerical modelling of Omeonga was aimed to integrate the geological observations in favour of an impact origin for the structure, as this feature is so hardly accessible by on-field investigations that only a suspicion on its origin could be inferred up to now. However, as Congo Craton, where the crater is located, is quite well constrained the numerical modelling was addressed to study in detail the impact crater collapse of a so large crater. In fact, only a specially provided mechanism could account for a crater morphology with terraced rim-walls and central uplift (Melosh, 1979).

My numerical simulations was focused in exploring a wide range of the peculiar parameters accounting for the formation of the peak-ring inside Omeonga. The results from this modelling was then coupled with the DTM profiles obtained from ASTER DEM, to discuss the reliability of the iSALE-

derived crater with the real features, accounting for all the subsequent environmental processes that had acted to modify it.

The second impact structure considered was imagined on (21) Lutetia, which was recently flew by the Rosetta spacecraft on its way towards the comet 67P/Churyumov–Gerasimenko. The large amount of data collected turned Lutetia to be a puzzling and complex asteroid, but could not provide a definitive finding regards the nature of this body. In fact, spectral properties suggest a composition similar to carbonaceous or enstatite chondrite, whereas the albedo was found higher than the one expected for these type of meteorites.

A crater of a 21-*km* crater was selected, as preliminary age dating showed it is the most recent large structure on Lutetia. Numerical modelling of this structure was focused in investigating how the final morphology of this crater may depends on different component materials and upper layering structure. The results from this modelling was then coupled with the DTM profiles. This discussion was aimed to provide some constraints on the nature of this asteroid and some clue in the post-impact modification. The overall analysis allowed to emphasize the increasingly importance of numerical modelling to a better understand of the evolution of our Solar System.

This thesis is subdivided into eight chapters. In the following one, I will introduce an overview of impact process and the resulting crater morphologies, in addition to all the aspects related to the study of impact craters. In Chapter 4 and 5, I will report the theory underlying the themes investigated, while in Chapter 6, I will briefly present some clue points of STC/SIMBIOSYS and an overview of two space missions, whose data I have used. Finally in Chapter 7, I will discuss the results on my thesis, whereas in Chapter 8 I will provide the conclusion of this thesis.

Chapter 3

Impact Craters

3.1 Craters: A tool in planetary studies

The Moon, the terrestrial planets and the icy satellites exhibit a surface with impact craters as the most common landforms, that are the results of asteroids and comets bombardment since the Solar System formation about 4.6 Gyr ago. They are then recognized as the favourite feature to related-cratering studies, that regards the inference of the ages of planetary surfaces and geologic events, the way they can reflect impact process and target material properties and a probe to discover, if it exists, water.

3.1.1 Craters: A look into the Impactors Flux

Since the early 1600's when Galileo Galilei pointed his 1½-in. telescope at the Moon and observed circular spots, there has been the controversy over the nature of craters. The early works were inclined to favor the volcanic origin, while the impact hypothesis was a merely speculation, firstly because an impactors source could not be explained in a space thought empty, and then because the nearly circularity of craters was not accounting for an oblique incidence of the eventual impactor. The successive works of Öpik and Gifford at the beginning of 1900's gave strength to the impact origin, thanks to the comparison with explosions.

The evidence that most large craters are sites of impacts of meteoritic bodies raises the question of the source and history of these bodies and their relation to the planetesimals from which planets are believed to accrete (Hartmann, 1972). This issue has been becoming more intriguing if the basin-forming population took place in more recent ages, long after the late heavy bombardment ($\sim 3.8 Ga$), at a time when the primary source of impactors was a NEO-like population.

In the present population, NEOs are quickly replenished, in time scales of tens of Myr, mainly from the Main Belt via slow orbital migration into major resonances. Such migration, due mainly to Yarkowsky effect, is size-dependent and it is negligible for objects larger than $\sim 10 km$. Therefore, larger bodies are mainly produced by dynamical chaos loss (Minton & Malhotra, 2010). Another source of large impactors is the sporadic direct injection into strong resonances due to collisions.

The recent discovery by MESSENGER of two young basins, Raditladi and Rachmaninoff on Mercury surface, gives rise to more questions regarding the source of impactors. Raditladi ($D = 250 km$), a 1st flyby discovered peak-ring crater, stands out for its peculiar low crater density of its interior plains, from which $\sim 1-Gyr$ age is inferred. Rachmaninoff ($D = 290 km$), a 3rd flyby discovered peak-ring crater, was found to originate about $3.4 Ga$ ago (Marchi et al., 2010 and cf. § 7.2). The NEO population has only a couple of members having sizes $> 20 km$, capable of forming a craters with such dimensions. This translates into a very low impact probability into Mercury, i.e. $6.1 \times 10^{-11} yr^{-1}$, implying that on average such a collision can happen every $16 Ga$. Hence, the present NEO population does not sustain the existence of such large and young basins. Given the uncertainties in the basin-forming crater scaling law, this paradox can be partially reduced assuming that the impactors could have smaller dimensions, say $D > 10 km$. In this case, the impact probability increases by about a factor of 5. Another possible source of impactors for Mercury in the long-sought Vulcanoids population supposed to reside within the orbit of Mercury (e.g., Strom & Sprague, 2003). Due to challenging observations, the search for Vulcanoids is still ongoing and the presence of these objects cannot be ruled out yet. However, recent surveys exclude the presence of bodies larger than $10 km$ (Steff et al., 2009). Although one can invoke a stochastic origin, if further investigations do not support it, this finding may have important implications for the impactor source regions.

3.1.2 Craters: A probe into the Original Target Topography

The formation of an impact crater is a fundamental and tangled process, but far to be still understood in its whole, since it depends upon a variety of parameters that work closely to result the final cavity. These parameters include size, speed, impact angle, and composition as regards the projectile, and surface gravity, material and structure of the surface where the crater forms (e.g., Melosh, 1989).

In particular, the shape and size of the final cavity are almost exclusively determined by the details of the excavation flow and its interaction with the target planet's strength and gravity. In this context, variations in target structure, such as layering, or irregular distribution of rocks with different mechanical properties, or presence of joints, cracks and other planes of weakness, may substantially draw the final outcome of an impact.

In the following, the outline of the most important factors affecting the morphology of a crater.

Layering in the target

A first case regards the effect of layering when a weak layer overlies a strong half space, such as for example craters formed in loose fragmental regolith that overlies the consolidated mare basalts. Quaide & Oberbeck (1968) found that the final crater shape depends on the ratio between the crater's rim-to-rim diameter D and the upper layer thickness L , as shown in Fig. 3.1.1. The options available for different values of the upper layer thickness was well adopted to estimate the regolith thickness on the Moon before the Apollo landings, and then on Mars and Phobos.

On the other hand, a crater may form on a strong layer overlying a weak one (Fig. 3.1.2). The presence of weak ice or water beneath a stronger rock or ice surface has been invoked as possible cause for the formation of central pit craters on the icy Galilean satellites and on Mars (Bray, 2009). In addition, a water-saturated substrate beneath the surface can be suggested as responsible of the peculiar form of Martian ejecta blankets. The existence of the water-saturated substrate may help the fluidization process, that greatly enhances the mobility of ejecta debris, converting the dry fragmental ejecta flows normally seen into fluid debris flows similar to terrestrial mud flows. These are emplaced as thin ground-hugging flows, which when impeded by topographic obstacles, are deflected, spread-out around or ponded against them. As a consequence, "rampart craters" display a single ejecta sheet that extends about one crater radius from the rim and ends in a low concentric ridge or outward-facing escarpment (e.g., Melosh, 1989).

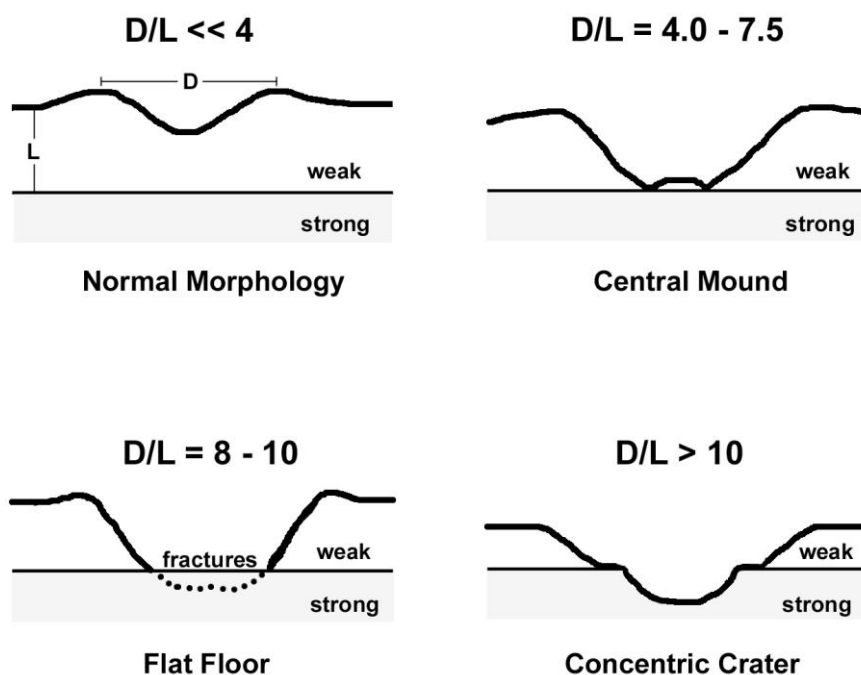
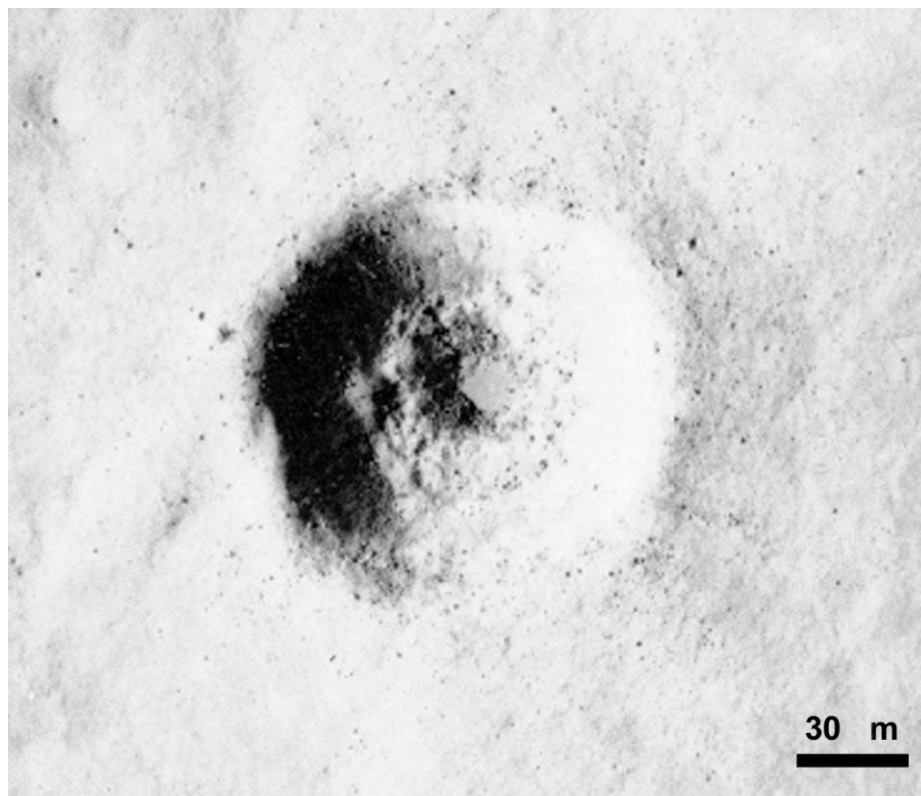


Fig. 3.1.1. (a) A 1.2-km-diameter simple crater on the Moon, which displays a bench low down on its wall, suggesting a weak layer overlying a more resistant rock unit. *Photograph AS15-9287*. (b) The morphology of craters formed in a weak layer overlying a stronger one. As the ratio between the crater diameter D and the weak layer thickness L increases, the crater may be described by a bowl shape, a low central mound, flat floor or interior benches on its walls. From Melosh (1989) and Quaide & Oberbeck (1968).

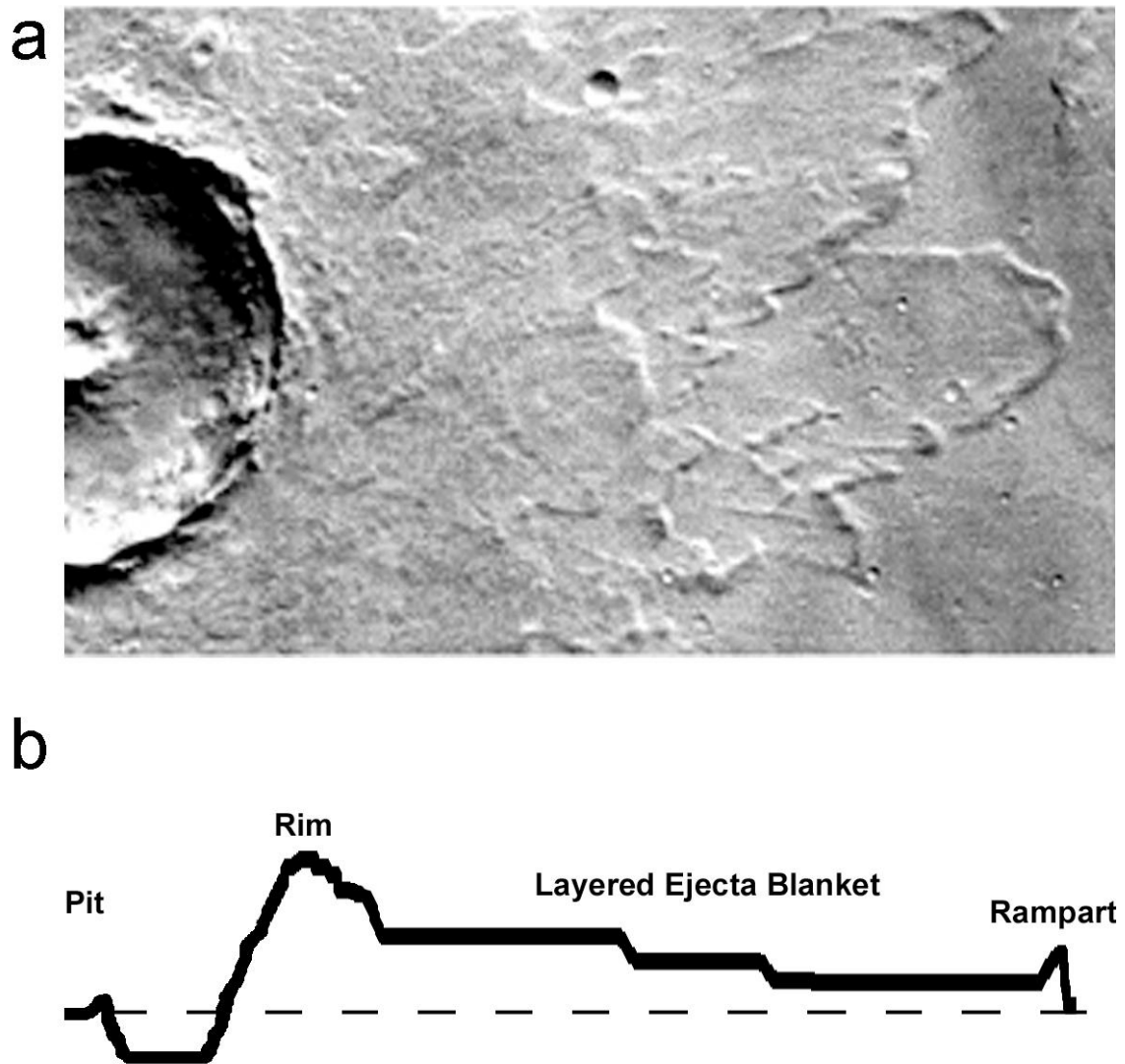


Fig. 3.1.2. (a) A 25-km-diameter Martian crater (THEMIS image I03218002), displaying both a pit morphology and a multiple layer ejecta sheet. (b) Sketched topographic profile. *From Bray (2009).*

Lines of weakness in the target

Joints, faults or planes of weakness in the target also play an important role in affecting the final crater shape and ejecta patterns (Gault et al., 1968). One of the most representative examples of structural control is Meteor Crater (Arizona), which displays a square–shape, rather than a circular one (Fig. 3.1.3). Its peculiar shape is caused by two orthogonal sets of vertical joints traversing the sedimentary basement rocks (Shoemaker, 1963). The excavation flow exploited these pre–existing planes of weakness, traveling more easily in directions parallel to the joints and hence supporting the cavity to expand in these directions (e.g., Bray, 2009; Melosh, 1989).

Complex craters behave in a different way to joint placement. During crater collapse, the rim slides away from the footwall parallel to lines of weakness. This preferential material slump creates concentrated terrace segments and polygonal crater rims.

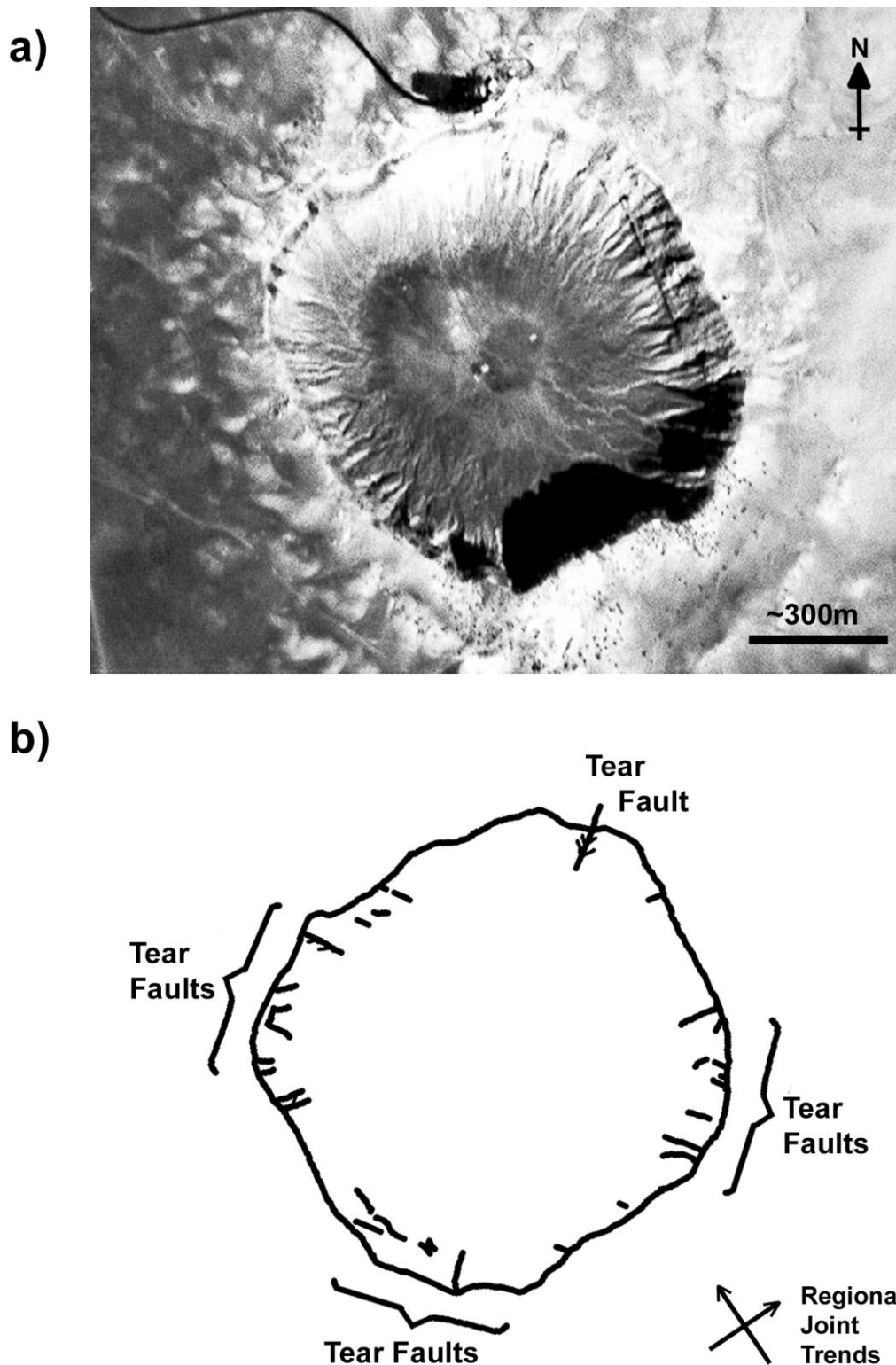


Fig. 3.1.3. (a) Meteor Crater (Arizona) in an image taken by the High Resolution Camera onboard the ESA Proba satellite. (b) The outline of Meteor Crater's rim-crest showing a square shape, as a consequence of an irregular structure of the target. Two prominent orthogonal joint sets occur in this area with trends cutting approximately diagonally across the crater's square shape. *Diagram from Melosh (1989), using data from Shoemaker (1963).*

3.1.3 Craters: the search of the lost Water

One of the most intriguing question in planetary sciences is the presence or not of water in other worlds than the Earth. A particular attention is devoted towards the Moon, in anticipation of future human activities (Colaprete et al., 2009). In fact, a source of water could enable long duration human activities, serve as a source of oxygen and provide hydrogen to be used as a rocket fuel.

But, does water really exist on the Moon? The first analyses in the returned samples of Apollo and Luna programs found only some traces of water and hydrates, that were consequently ascribed to terrestrial contamination. The Moon was therefore considered quite dry for the successive decades, while the possible accumulation of water in lunar poles has remained an unfulfilled question for several decades (e.g., Pieters et al., 2009).

A change in this perspective came firstly from the data collected by the neutron spectrometer onboard the Lunar Prospector that provided evidence of hydrogen near the lunar poles (Feldman et al., 1998, 2000, 2001). The large areas in the lunar polar regions could work as a cold trap, having a temperature low enough (< 100 K) to catch hold of water ice as well as volatile species (Paige et al., 2010). This volatile material proved to be stable and largely protected from processes of removal once deposited in these cold traps and covered by a few cm-layer of regolith (Spudis et al., 2010). As the Moon has been bombarded with water-bearing objects such as comets and meteorites and implanted with solar wind hydrogen, some of this material might migrate in the lunar exosphere through ballistic trajectories and then collect in the permanently shadowed cold, where it would be stable over geological time (e.g., Arnold, 1979; Clark, 2009; Colaprete et al., 2009, 2010; Gladstone et al., 2010; Spudis et al., 2010; Watson et al., 1961). Since these cold traps receive no direct solar illumination and emit little radiation, most are difficult to be observed from the Earth. Nevertheless, radar could identify deposits of frozen volatiles because, under certain conditions, they produce a unique backscatter signature. A high (> 1.0) ratio of same sense-to-opposite sense polarization and high reflectivity has been detected by radar on the Galilean satellites (Hapke, 1990; Ostro & Shoemaker, 1990), the residual south polar ice cap of Mars (Muhleman et al., 1991) and the inside of permanently shadowed polar craters in Mercury (Harmon & Slade, 1992; Butler et al., 1993). These characteristics are attributed to multiple internal reflection and/or coherent back-scatter produced by low-loss material, such as water ice (Ostro & Shoemaker, 1990).

The recent Lunar Crater and Sensing Satellite (LCROSS) mission was exactly devoted to investigate the permanently shadowed crater of the South Polar region on the Moon, in order to provide direct proofs to the several remote observations indicating the existence of water ice (e.g., Colaprete et al., 2010). On the other hand, other lunar missions, such as for example Chandrayaan-1, have on board some instruments designed to search for water.

LCROSS was scheduled to launch in 2009 along with the same carrier rocket of LRO, which separated shortly after launch from the LCROSS–Centaur stack. LCROSS Shepherding Spacecraft (SSc) was designed to perform the instrument calibration and target the Centaur at the planned impact site, i.e. Cabeus crater (Pieters et al., 2008). The material ejected just after the impact was tracked by the nine instruments, including cameras, spectrometers and a radiometer, onboard the SSc. The spectra showed evidence of an initial ejecta plume composed by water vapor, OH, small amounts of ice-rich ejecta and other volatiles that quickly passed out of the instrument FOV, followed by the emergence of water ice grains that continued to sublime for the entire 4–min period of observations and possibly continued sublimation from the heated surface near the impact site (Colaprete et al., 2010).

This water can be defined “Buried Water”, as it has been found excavating the permanently shadowed craters in the polar regions. However, considering this as the unique reservoir of water is reductive, as recent studies backing on new data from the last space missions to the Moon give strength to other different ways in which water can take place, each one being produced by own mechanisms.

The second type of water is the “Internal Water”. The Apollo and Luna returned samples pointed out a lack of highly volatile elements, especially the hydrogen, thought to be completely lost during the giant collision event that generated the Moon. Nevertheless, Saal et al. (2008) made spectrometry analyses on lunar samples to give some constraints of indigenous volatile (CO_2 , H_2O , F, S and Cl) contents of the most primitive basalts in the Moon, giving the assumption that diffusive volatile loss was caused only by partial degassing during eruption. They tried to estimate the pre–eruptive water content in the lunar volcanic glasses through numerical modelling of diffusive degassing of the very-low-Ti glasses. They found a more than 700 p.p.m. water content, probably originated in an undifferentiated volatile-rich lunar mantle below of the lunar magma ocean, or in an ilmenite–rich dense layer formed during the late-stage cooling and crystallization of the lunar magma ocean.

The last type is “Surficial Water”. Sunshine et al. (2009) used data acquired by the Deep Impact spectrometer to confirm the presence of OH and H_2O on the lunar surface, in addition to a hydration process driven by solar radiation, involving the entire lunar surface. Pieters et al. (2009) confirmed these findings as they detected a 3 μm –absorption feature in the Chandrayaan-1 Moon Mineralogy Mapper (M^3) spectrometer data. For silicate bodies, such feature is attributed to water-bearing materials, implying that the Moon contains primary hydrated mineral phases, uncommon in the limited Apollo, Luna and lunar meteorite collections. These unsampled phases might be endogenic to the Moon and freshly exposed by craters in ancient highland terrain, or they may form during an impact event by a water–bearing comet or asteroid. On the other hand, H_2O and OH species might also be continuously created when solar–wind protons interact with the O–rich surfaces during the formation of lunar soil particles. In addition, fresh broken surfaces and soil grains may readily react with protons from the solar-wind, forming strong surficial OH bonds. Either of these may be highly dependent on the temperature and solar–illumination environment. The process for producing OH/ H_2O on the Moon may provide an

ongoing mechanism for delivery of these volatile elements to cold traps in the polar permanently shadowed regions. Perhaps most importantly, harvesting the lunar regolith for volatiles now becomes a serious option for long-term human activity.

Mars is a planet that appears as well to be a dry place, whose present conditions yield to have liquid water only in a so highly unstable state that it is not expected to be present on the surface in any significant quantity. However, the presence of craters with fluidized ejecta morphologies could be interpreted as the signature of ground ice (§ 3.1.2), while crater morphometric characteristics have been used to map out variations in depth to ground ice and to constrain ice abundance over time (e.g., Barlow, 2004; McEwen et al., 2010).

Landforms on Mars seem to be very intimately connected to the cycle of water, which might have caused the formation of deep integrated valley systems, catastrophic flood channels and recent valleys (e.g., McEwen et al., 2007, 2010). In particular, valley networks and likely associated fluvial sediments indicate that precipitation and surface runoff must have occurred for sustained periods in the Hesperian around Valles Marineris, suggesting an active hydrological cycle beyond the Noachian in this region (Weitz et al., 2010). The major issues involving the formation of fluvial landforms on Mars relate to the water source, the erosional mechanism and the ultimate fate of water. Although the spatial distribution, overall morphology, and source regions of these landforms differ from their terrestrial counterparts (e.g., Gulick, 2001), water was available periodically throughout Mars' geological history in sufficient quantities over the required duration to provide a full suite of fluvial landforms.

One particular feature, the gully channels, first discovered by the Mars Orbiter Camera (MOC) onboard the Mars Global Surveyor (MGS), and then observed by CRISM onboard the Mars Reconnaissance Orbiter (MRO), exhibits morphologies similar to the terrestrial ones, raising the hypothesis that liquid water was present on the surface in geologically recent times, within the past 1 Myr (e.g., Malin & Edgett, 2000). Lanza et al. (2010) showed that, on the basis of their area-slope relationship, Martian gullies formed after saturation of near-surface regolith by a liquid. The contributing area acts to generate and focus through flow in the shallow subsurface, and the slope gradient controls how efficiently this process occurs, as well as the stability of the regolith mantle on the slope. This model favors a source of liquid that is broadly distributed within the source area and shallow. Lanza et al. suggested that such liquid could be generated by melting of broadly distributed icy materials such as snow or permafrost. This interpretation is strengthened by observations of polygonal and mantled terrain in the study areas, which are both suggestive of near-surface ice. On the other hand, the bright gullies formation mechanism is investigated as well by Kolb et al. (2010), by modelling water-rich and wet sediment-rich flows using HiRISE images. They proposed on the contrary that bright gullies are not definitive evidence of recent liquid water on the surface of Mars.

Mineralogic signatures, as the formation of phyllosilicate, sulphate and carbonate minerals, first recorded by the OMEGA experiment on Mars Express, may have significant implications for a past

presence of water (e.g., Bibring et al., 2006; Ehlmann et al., 2008; Murchie et al., 2009; Mustard et al., 2008; Poulet et al., 2005; Wray et al., 2008). In fact, these minerals, mainly associated with Noachian outcrops, are consistent with an early active hydrological system sustaining the long-term contact of igneous minerals with liquid water, even if they probably do not occur together (Poulet et al., 2005). The two major families of alteration products detected by OMEGA, phyllosilicates and sulphates, could thus trace two different processes separated in time, referring to two major climatic episodes in the history of Mars: an early Noachian Mars, resulting in the formation of hydrates silicates, followed by a more acidic environment in which sulphates formed, rather than clays.

In this context, Martian craters can be used as well as a powerful tool to testify the presence or the absence of water below the surface. The detection of fresh impact craters with bright floors and ejecta in the northern lowlands of Mars (Byrne et al., 2009b), along with data acquired by the Phoenix probe landed in the northern hemisphere of Mars (Smith et al., 2008), suggests that there are substantial water ice deposits just below the surface over large area.

Reufer et al. (2010) performed numerical modelling of hypervelocity impacts on Mars, accounting for the possibility of a thin layer of sub-surface water ice, to confirm the fact that impacts themselves may have risen the temperature and the pressure of the water ice deposits locally to values which allow phase change. In fact, impact induced water ice to undergo phase changes that involved also the behavior of the material during the cratering process. One idea would be the production of liquid water in large amounts, which later refreezes and directly produces a flat and clean water ice crater floor. The formation of such a pool of liquid water is not assured because the liquid can drain relatively quickly through a heavily fractured crater floor. However, a relatively thick solid ice layer which is not penetrated by the impact may prevent this. Another more important effect of liquid water during the cratering process is the change of the water ice material parameters. The coefficient of friction for damaged water ice changes dramatically if it is partially melted (Senft & Stewart, 2008). Such a mixture of solid and liquid water flows much more easily compared to purely solid ice and will exhibit different behavior at the later stages of crater formation. It is reasonable to assume that we have a desiccated loose layer above an ice layer below. The ice layer may be relatively thin such that the impact can penetrate it completely and continue into a harder substrate below. Evidence that the ice layer is thin has been presented by Byrne et al. (2009a, b) and it may be a natural consequence of the sublimation and desiccation process. If the surface layer is relatively porous, the sublimed water vapor need not only to escape to the atmosphere, but will also migrate to lower, cooler levels to build-up a denser layer of ice. Such behaviour has been observed in the KOSI experiments (Benkhoff et al., 1995).

This Martian model was first proposed when the Mars Odissey spacecraft neutron and gamma-ray spectrometers have shown that the uppermost decimeters of the Martian northern lowlands contain an amounts exceeding 50% by mass, of a hydrogen-bearing molecule poleward of $\pm 60^\circ$ latitude (e.g., Feldman et al., 2002, 2004). The H_2O is assumed to be covered by a thin desiccated layer of fines and

lightly consolidated material, which prevents direct, unambiguous spectroscopic identification. The existence of polygonal structures and “scallop” (Lefort et al., 2009) strongly supports the idea that desiccation produced by sublimation of ice in the uppermost layer of the Martian soil might be a global phenomenon.

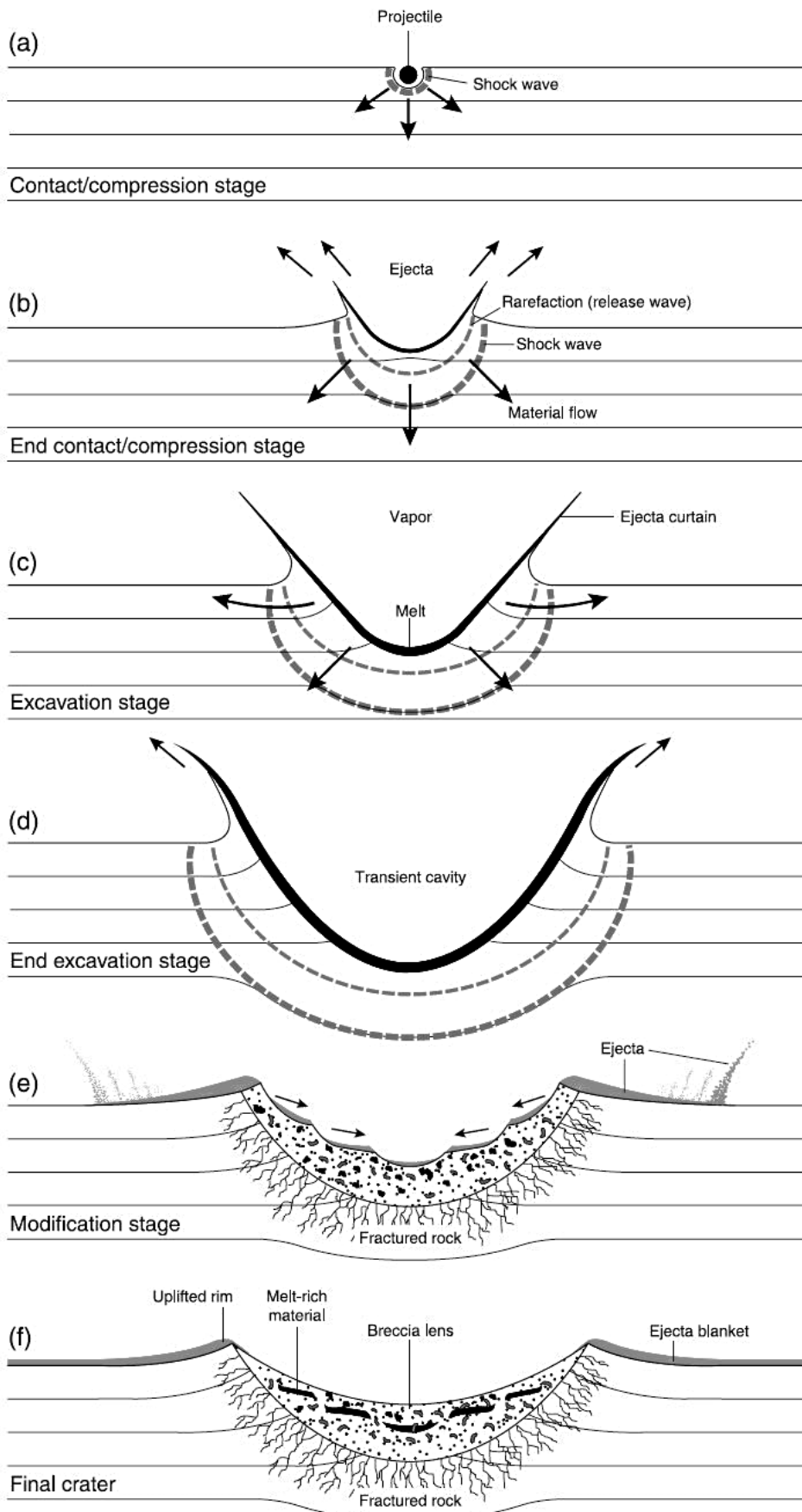
3.2 Crater Formation Process

A “hypervelocity impact crater” is a structure resulting from the collision of a cosmic projectile with another planetary bodies, beginning with the first contact of the two bodies and ending with the final motions of debris around the crater (e.g., Melosh, 1989; Melosh & Ivanov, 1999; French, 1998).

The impact formation process works through the propagation at supersonic velocity of a shock wave, i.e. a step-like discontinuity in pressure, density, particle velocity and internal energy (Melosh, 1989). Shock compression is a non-isentropic process (thermodynamically irreversible) and results in the production of post-shock heat and in the melting or vaporization of the shocked material (Asay & Shahinpoor, 1993; Duvall & Fowles, 1963; Graham, 1993). The energy transferred from the projectile to the target results in the motion of the material that begins to flow away from the impact site, against strength or friction forces and gravity.

Although the impact process is continuous, for sake of simplicity, it is divided into three discrete stages, represented on Fig. 3.2.1, each one dominated by a different set of physical phenomena, in order to deeply understand forces and mechanisms occurring at a specific instant.

Fig. 3.2.1. *Following page.* Sequence of the stages characterizing the impact formation process. *From French (1998).*



3.2.1 Contact and Compression Stage

The first stage of formation of a crater begins when the leading edge of the approaching projectile contacts the target surface. In Fig. 3.2.2, the process is shown in a simplified geometry, i.e. a spherical projectile impacting vertically on a homogeneous target bounded by a plane free surface.

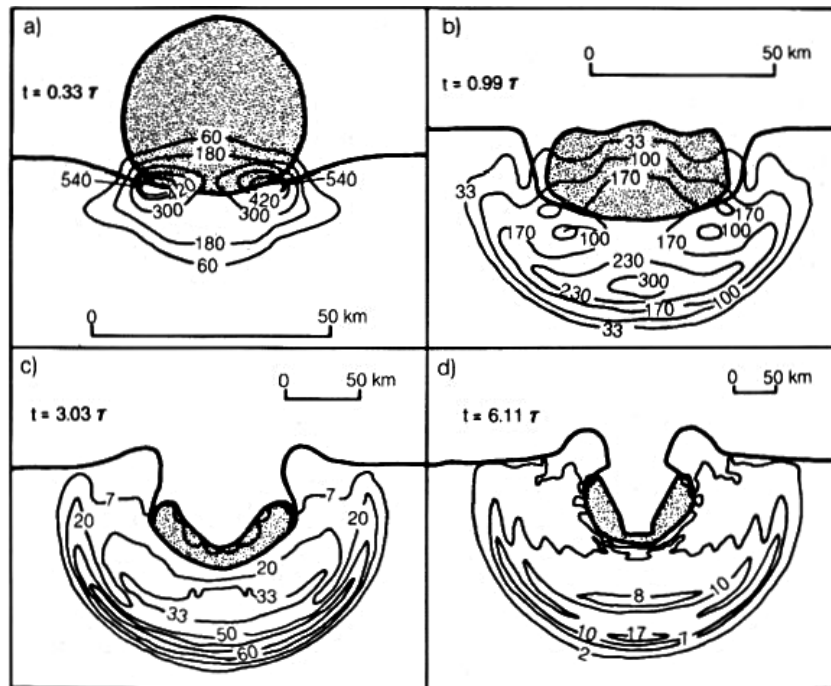


Fig. 3.2.2. Snapshots of the simulation of a vertical impact of a 46.4-km iron projectile on a gabbroic anorthosite target at 15 km/s. *From Melosh (1989).*

The outcome of this striking is the redistribution of the projectile kinetic energy into both kinetic and internal energy of all colliding materials by means of shock waves that radiate outward from the interface. The residual kinetic energy is spent for ejecting material and opening the transient cavity, while the internal energy heats both projectile and target. For sufficiently strong shock waves, this may result in melting or vaporization of the material near the impact site.

At the first contact (Fig. 3.2.2a), the edge of the projectile is almost instantly decelerated, while its rear continues the plunge into the target at the same velocity. Both target and projectile involved in the shocked zone are compressed and begin to distort in shape, while material outside of this zone is undisturbed until the actual arrival of the shock front. Fig. 3.2.2a shows two small regions of high pressure, that are associated with the process of jetting, i.e. a hot, heavily shocked mixture of projectile and target that jet from these high pressures zones at speeds several times faster than the projectile itself.

The transfer and conversion of the energy peculiar of the contact and compression stage takes place in a region as roughly large as the projectile and over a time interval lasting the time required for the projectile to travel a distance equal to its own diameter L , i.e.

$$\tau = \frac{L}{v_i \sin\theta}$$

where $v_i \sin\theta$ is the vertical component of the initial velocity of the projectile. Even for large projectiles, this time is short: 2 s for a 50–km–diameter projectile travelling at 25 km/s, and less than 0.01 s for a 100–m–diameter object traveling at the same speed.

When the shock wave propagating into the projectile get the rear surface (Fig. 3.2.2b), the projectile–target interface has been pushed roughly one-half the projectile diameter into the target. Shock pressures greatly exceed material strength that cause the projectile to flow hydrodynamically. At this time, both projectile and target are engulfed by the shock wave: the projectile is decelerated to a fraction of the initial impact velocity, while the target is accelerated to high speed. The highest pressures are attained locally, at the point where the projectile and the target's surface converge obliquely and the process of jetting dominates, and may range between 100 and 1000 GPa. The corresponding temperatures reach tens of thousands of degrees and vaporized material may be significantly ionized. However, the mean pressures are somewhat lower, although still high by conventional standards. Fig. 3.2.2b illustrates that, after the local pressure highs of the early contact stage have dissipated, the projectile and a comparably sized volume of the target are immersed in a broad zone of nearly uniform pressure. The subsequent cratering flow depends more on the pressure and size of this zone than on the extreme pressure high of jetting.

At the rear of the projectile, the shock wave is reflected forward as a rarefaction wave (Fig 3.2.2c), unloading the projectile to undergo phase transformation, either melting or vaporizing if its initial shock pressure is sufficiently high. The shock wave in the target continues to propagate outward, beginning to approximate a hemisphere centered roughly one projectile diameter below the surface, and loses rapidly as it travels away from the impact point because of two factors:

1. the expanding shock front covers an increasingly larger hemispherical area of increasing radial distance, thus reducing the overall energy density;
2. additional energy is lost by the target rocks through heating, deformation and acceleration.

After the rarefaction wave has reached the front end of the projectile and unloaded it completely, the projectile will play no further role in the formation of the impact crater, and the actual excavation of the crater is carried out by the expanding shock waves through the target rocks. The vaporized portion of the projectile may expand out of the crater as part of a vapor plume (Melosh, 1989; French, 1998), and the remainder may be mixed into the melted and brecciated target rocks.

Fig. 3.2.2d shows the starting excavation stage. The projectile and part of the target have unloaded to near–zero pressure, and the unloaded material is moving rapidly away from the impact site.

3.2.2 Excavation and Transient Crater Growth Stage

The excavation stage (Fig. 3.2.3) can be splitted as well into two different sub-stages, each one responsible for different physical phenomena: 1) the expansion of the shock wave, and 2) the excavation flow. The expansion and decay of the shock wave is the main regulator of thermodynamic processes during cratering, because the dynamic of the shock wave controls masses and temperatures of both the melt and vapor, whereas the excavation flow controls instead the shape and size of the final crater. Only a few aspects of cratering, such as vapor plume expansion and near-surface spallation, involve aspects of both stress wave expansion and excavation flow.

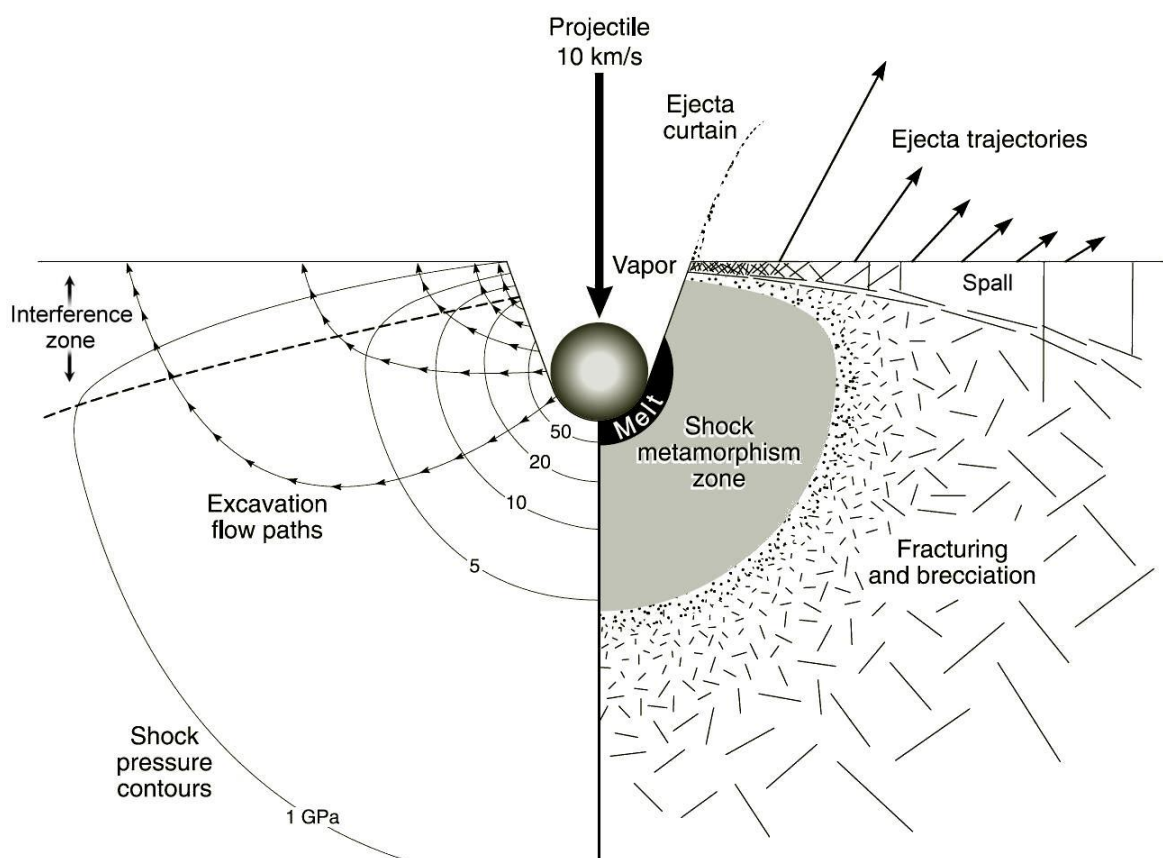


Fig. 3.2.3. Illustration of the impact site during the excavation stage, with the falloff of pressure and its implication for the final state of the target. Modified after Melosh (1989).

During the excavation stage, the shock wave, which acts as a detached entity on an hemispherical shell, expands rapidly away from the impact site with decreasing shock pressure, compressing and accelerating the material it encounters (Fig. 3.2.3) (Melosh, 1989; Kieffer & Simonds, 1980). Both the pressure and particle velocity are high in the shock, where they are given by the Hugoniot equation:

$$P - P_0 = \rho_0 u_p U$$

where P_0 and P are the pressures in front of and behind the shock front, respectively, ρ_0 is the uncompressed density, u_p the particle velocity (the velocity of a small area of the medium, that is alternately accelerated and decelerated as the wave passes), and U the shock velocity.

As the shock wave expands throughout the excavation stage, it weakens with time and might degrade into an elastic wave, carrying only about 10^{-4} of the original impact energy away from the site. The decline rate of the shock wave's strength determines the mass of melted or vaporized target material. The total mass of material melted or vaporized is computed by integrating the volume of material enclosed within the appropriate maximum pressure contours. At low impact velocities, the amount of melt or vapor is sensitive to geometric factors because the shape of the melted or vaporized region is complex, but at higher impact velocities the affected regions are nearly hemispherical and the mass of either melt or vapor is proportional to the square of the impact velocity. O'Keefe & Ahrens (1982) presented computations of melt and vapor masses for the impact of iron, gabbroic anorthosite and water projectiles on a lunar crust-like target (gabbroic anorthosite). They pointed out that the mass of melt produced in an impact is always larger than the vapor mass by nearly a factor of 10.

The geometry of the expanding shock wave generated by an impact is that of a sphere centered on a point some distance below the surface. Hence, the shock waves travelling upward intersect the free surface. As stress cannot be maintained at free surfaces, such as the original ground surface and the edge of the impactor, a family of rarefaction waves develops and follows the outward moving shock wave, thereby decompressing the target to ambient pressure. In the near-surface region, called interference zone, where stresses in the tensional release wave exceed the mechanical strength of the target rocks, the release wave is accompanied by fracturing and shattering of the target rock.

Material engulfed by the shock wave is accelerated by the sharp pressure gradient at the shock front. Then, the same material is accelerated down the more gradual pressure gradient of the rarefaction wave. The net velocity is the vector sum of these accelerations integrated over time. The thermodynamic irreversibility of these shock wave compared to the reversibility of the rarefaction wave means that this net velocity is non-zero; the target maintains some particle velocity, about 1/5 of the peak velocity in the shock wave (Melosh, 1985). This residual velocity is responsible for opening the crater cavity and marks the beginning of the *excavation flow*.

The mutual action of the pressure gradient behind the release waves and the inertia of the initial pulse motion causes the excavation flow to ultimately exhibit an upward-and-outward pattern. Material near the rim of the crater rises above the pre-impact surface and will be ejected. As the material involved in the excavation flow is located at an increasingly depth, it dips down more and more before turning upward and being ejected. Material located directly beneath the impact site continues moving downward and never reaches the surface, indicating the paths of target material that is displaced downward.

The *ejecta* deposit is a distinguishing feature that surrounds nearly all impact craters. It is made up by debris ejected on ballistic trajectories from the crater interior and then fallen back onto the surface of the planet on which the crater forms. As ejecta deposition is controlled by the velocity, angle and time of ejection of its component particles, the final morphology of this deposit depends upon the distance from the impact site. The innermost ejecta, being launched first, travel fastest and for a greater distances from the crater rim, and have velocity large enough to interact with the target causing mix and erosion. On the other hand, ejecta originating farther from the center are launched later and move more slowly, falling sooner nearer the crater rim, so the size of ejecta fragments near the base of the ejecta is expected to be larger than the fragments higher in the curtain. Moreover, crater size, target substrate characteristics as well as the presence or not of an atmosphere or volatiles, particularly liquid water, can definitively influence the outcome of the ejecta emplacement.

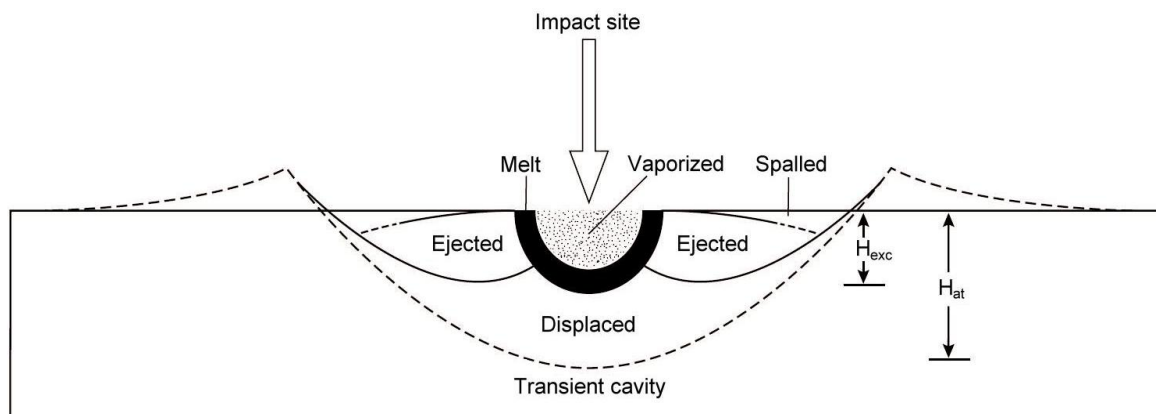


Fig. 3.2.4. Cross section through a theoretical transient crater, showing discrete zones from which various shock-metamorphosed materials are derived. Vaporized material, containing a mixture of vaporized target rock and projectile, expands upward and outward in the vapor plume. Melted material consists of melt that moves downward and then outward along the floor of the final transient cavity. Ejecta material, including a range of shock-metamorphic effects, is excavated from a maximum depth H_{exc} ($\sim 1/3 H_i$) and then ejected outward to and beyond the transient crater rim. Finally, the displaced material is driven downward up to a maximum depth H_{at} ($\sim 3/10 D_i$), never reaching the surface. From Melosh (1989).

As the cavity grows, roughly equal volumes of material are either ejected from the crater or displaced by plastic flow downward into the target (Fig. 3.2.4).

The excavation flow is retarded by any cohesive strength that the target material may retain plus dry friction (resistance to shear of granular materials) and gravity. Excavation stops when insufficient energy remains to lift the overlying material against the force of its own weight (Nolan et al., 1996). The culmination of the excavation stage is defined as the moment when the excavation flow ceases everywhere. If the transient crater growth is halted by the gravity alone, as would be the case for impacts

into liquid water, the timescale is of order $\sqrt{H_{at}/g}$, where H_{at} is the final crater depth and g is the acceleration of gravity. If the crater growth is halted by the elastic–plastic material strength Y , the timescale is given by $H_f\sqrt{Y/\rho}$ (Melosh & Ivanov, 1999).

The form of the transient cavity at the end of the excavation stage is called the *transient crater*. Evidence from numerical calculations and laboratory experiments suggests that the transient crater is approximately a paraboloid of revolution with a depth–to–diameter ratio of between 1:3 and 1:4 (Melosh, 1989; Collins, 2002).

3.2.3 Modification Stage

The transient crater is followed by a collapse principally led by gravity, that produces a shallower and thus more stable crater. The effects of this modification depend on the dimensions of the cavity: in small craters, debris are forced to slide and drain back, while in larger ones, alteration contemplates also uplift of the floor with the creation of central peaks or rings and failure of the rim into wide zones of stepped terraces. The inward and upward material motion during the modification stage results in a complex intermixture of breccia and impact melt inside the crater. The mechanical style of modification depends on the gravity field of the planet and the strength of near–surface rocks.

The timescale of collapse is of order of $\sqrt{D/g}$, corresponding to the period of a gravity wave of wavelength equal to the crater diameter D on a planet with surface gravity g . This interval may range from few tens of seconds for 10–km–diameter craters on the Earth to nearly 10 minutes for 300–km–diameter craters on the Moon. Crater collapse and modification thus take place on timescales very much shorter than most geologic processes.

Finally, an ultimate gravitational long–term modification takes place leading to the leveling of the crater, approached by viscous flow of the substrate in which the crater forms, by volcanic flooding and burial of the crater, or by erosional degradation of the rim and infilling of the crater cavity.

SIMPLE CRATERS

For simple craters, the main modification process is wall slumping, whose result is a breccia lens mixed with shocked debris and impact melt that overlies the true floor. The maximum thickness of the breccia lens is roughly half of the rim–to–floor depth H of the crater itself. The inner rims of simple craters stand near the angle of repose, after some have slipped into the cavity. The slope of the crater interior gradually decreases as the center is approached. The center itself is often occupied by a small flat floor.

The final simple crater geometry may be different, depending on the target material's typology. In media such as ductile metals or wet clay, plastic flow occurs after the deviatoric stresses exceeded some threshold Y , but without largely modifying the final shape of the transient cavity, since it remains close to a hemisphere. Thus, the crater depth-to-diameter ratio is close to $1/2$. On the other side, in media such as sand or fragmented rocks, the final geometry, close to a parabola with a depth-to-diameter ratio of the order of $1/5$, is reached by means of two mechanisms. The first one is dry friction, that leads to the continued growth of the transient cavity diameter after the moment when the cavity depth reaches its final value. The second one is the slumping of the steep transient cavity walls under the action of gravity. Both mechanisms act together, but dry friction is more important in laboratory-scale impact, while wall slumping dominates for natural craters more than 100 m in diameter.

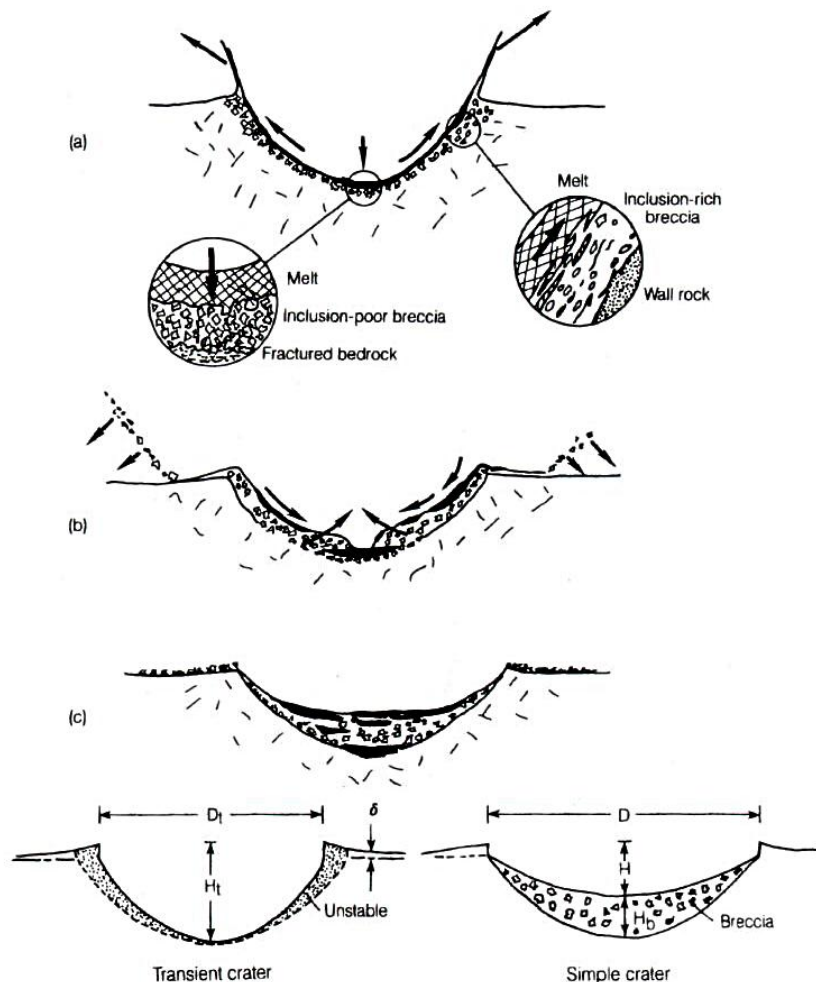


Fig. 3.2.5. (a, b, c) Formation of the breccia lens in a simple crater; (d) geometric model of simple crater formation. *From Melosh (1989).*

The most highly shocked rocks originally form near the crater's center in immediate proximity to the impact site. In fact, during the excavation stage, shocked and melted rocks are driven nearly straight downward and mix only slightly with the underlying less-shocked breccia. The melt near the crater walls has instead a large velocity component tangential to the walls. The melt and breccia in this zone is subjected to strong shear. Considerable mixing may take place, contaminating the melt flowing along the walls with clasts from the less-shocked breccia. In spite of this mixing, at the end of the excavation stage, the debris in the transient crater still retains its original shock stratigraphy with melt overlying breccia, which in turn overlies fractured bedrock (Fig. 3.2.5a). The debris lining the interior of the transient crater ceases its upward flow at the end of the excavation stage and begins to collapse inward as modification begins. The oversteepened rim of the transient crater slides downward, leaving behind a slope standing nearly at the angle of repose. Meanwhile, a slip surface develops near the toe of the slumping debris, allowing weakly shocked breccia to override and bury the central zone of nearly homogeneous melt (Fig. 3.2.5b). Debris slumping centripetally from the walls meets in the center and rapidly covers the transient crater floor. The last material to slide onto the floor is the clast-rich melt rock that originally lined the transient crater rim. This material forms the extensive sheets of mixed breccia on the top of the breccia lens (Fig. 3.2.5c).

The effects of collapse on the transient crater are estimated by assuming both the transient and the final crater as a paraboloid (Fig. 3.2.5d), so the difference in altitude z between a point on the crater wall and the lowest point in the crater center is given by $z = 4H \left(\frac{r}{D}\right)^2$. The height of the rim above the preimpact surface is given by $\delta = \frac{H_t}{40} \left(\frac{D_t}{r}\right)^3$. As the transient crater collapses, material from both the rim and the crater wall slides onto the floor of the crater, so, imposing that all the debris will form the breccia lens, one obtains:

$$D_t = \left(1 - \frac{5}{4} \frac{H_b}{H + H_b}\right)^{1/3}$$

where H_b is the maximum thickness of the breccia lens, while the depth of the transient crater H_t is assumed to be $H + H_b$. Substitution of the observed breccia lens thickness, $H_b \approx H/2$, gives for the transient crater diameter a value of $D_t \approx 0.84 D$. The final simple crater is thus about 19% larger than the initial transient one, but significantly shallower.

COMPLEX CRATERS

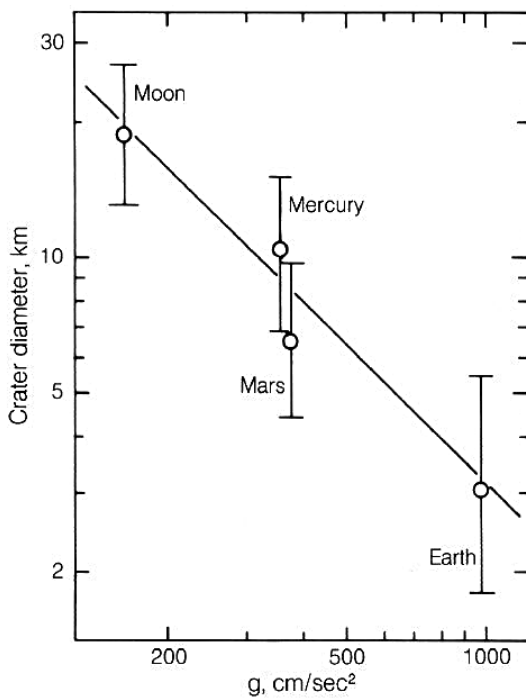


Fig. 3.2.6. Crater diameter at the simple-to-complex transition vs. gravity. From Melosh (1989).

As told before, a complex crater develops from a bowl-shaped transient crater by a process of gravity-driven collapse, that causes the deep target layer to uplift above the pre-impact surface (Fig. 3.2.7a). The process invoked for this uplift is the Acoustic Fluidization that accounts for a temporary fluid-like behaviour of materials plunged in a strong acoustic vibrations field (cf. § 5.2.4 for more details).

The central uplift begins as soon as the crater has stopped growing in depth, thus before the end of the excavation stage and the rim completion, and rises in a very short, of the order $(D/g)^{1/2}$, so breccia lenses have no chance to form by means of sliding of debris in the central region of these craters. The breccia in complex craters fills an annular moat between the central uplift and the crater rim. Some breccia and melt may also be draped over the central peaks themselves. The floors of these craters are veneered with breccia and melt rock lying in the same stratigraphic sequence with which they lined the transient crater cavity.

The wreath of terraces surrounding the crater floor also develops very quickly after the impact, before impact melt could solidify. This assertion is proved by the fact that the toes of these terraces fade smoothly into the solidified impact melt covering the crater floor without any sign of disruption by movement after the melt solidified. The terraces themselves are frequently veneered with impact melt that ponds in closed depressions formed by the backward-rotated terrace headscarps.

Complex craters represent one of the most common large-scale surface structures found on all the bodies throughout the Solar System. For complex craters, collapse leads to a substantial alteration of the appearance of the transient crater, producing final crater with central peaks or peak rings for still larger diameters, terraced walls and flat floor. Both the simple-to-complex and the peak-to-ring transitions are almost a consequence of collapse under gravity when some strength threshold is exceeded. The tangible role of gravity in these modifications is seen in Fig. 3.2.6, where the first one is plotted against gravity acceleration. A $1/g$ dependence is obtained.

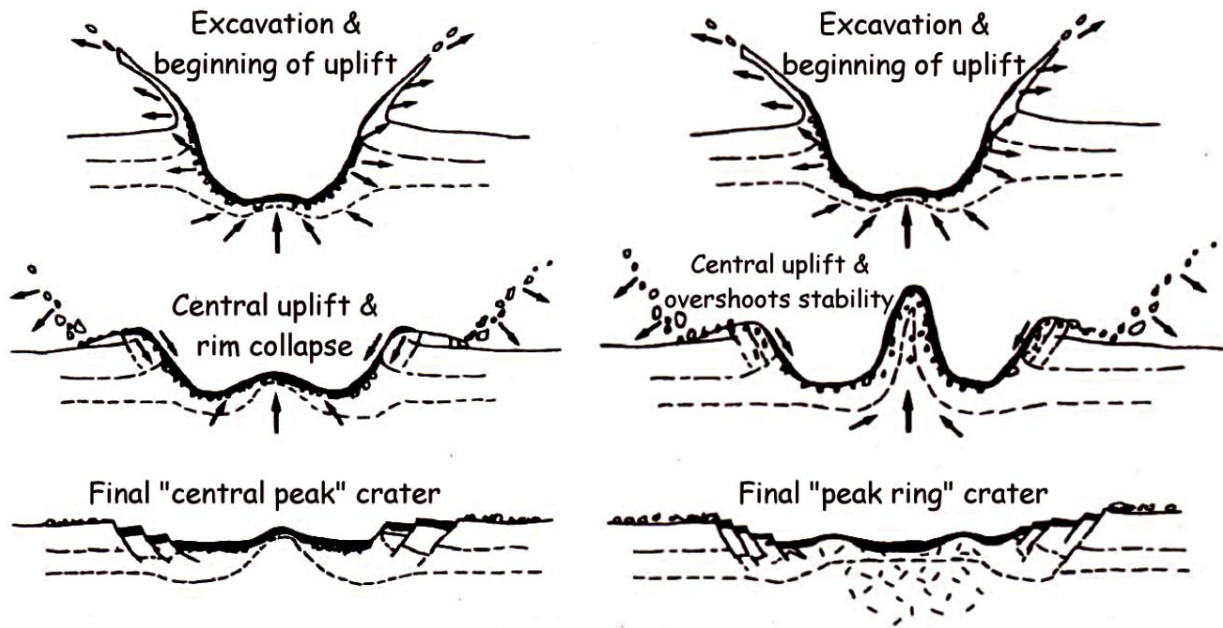


Fig. 3.2.7. Schematic illustration of the formation of a (a) complex crater with central peak and a (b) crater with peak rings. From Melosh (1989).

Peak–ring craters are thought to form when the central uplift collapses itself by gravity instability, as a diameter threshold is reached (Fig. 3.2.7b). The result is the rise of a ring of mountains surrounding its former site.

Principal features of a complex crater are the rim–to–rim diameter D , the rim–to–floor depth H and the floor diameter D_f . The width of the terrace zone is thus $D - D_f$ and its average slope is $(D - D_f)/H$. The parabolic rimmed transient crater of initial diameter D_t and depth H_t is assumed to collapse in such a way that the volume of the solid material surrounding it is conserved. As for the simple case, if the rim height is assumed to be $\delta = \frac{H_t}{40} \left(\frac{D_t}{r}\right)^3$, i.e. the rim volume equals the crater volume, the following relation may be written:

$$D_t^3 H_t = \frac{5D^3 H}{1 + 6 \left\{ 1 + (D_f/D) + (D_f/D)^2 \right\}^{-1}}$$

If the depth–diameter ratio of the transient craters forming large complex craters is assumed to be about 1/1.27, the same as for simple craters, the previous equation may be solved to obtain the transient crater and thus find 60% as the expansion of the crater during the course of its collapse.

MULTIRING BASINS

Multiring basins are the largest planetary impact structures. One of the theory describes the formation of multiring basins as an effect of crater collapse when the strength of layered media decreases with increasing depth.

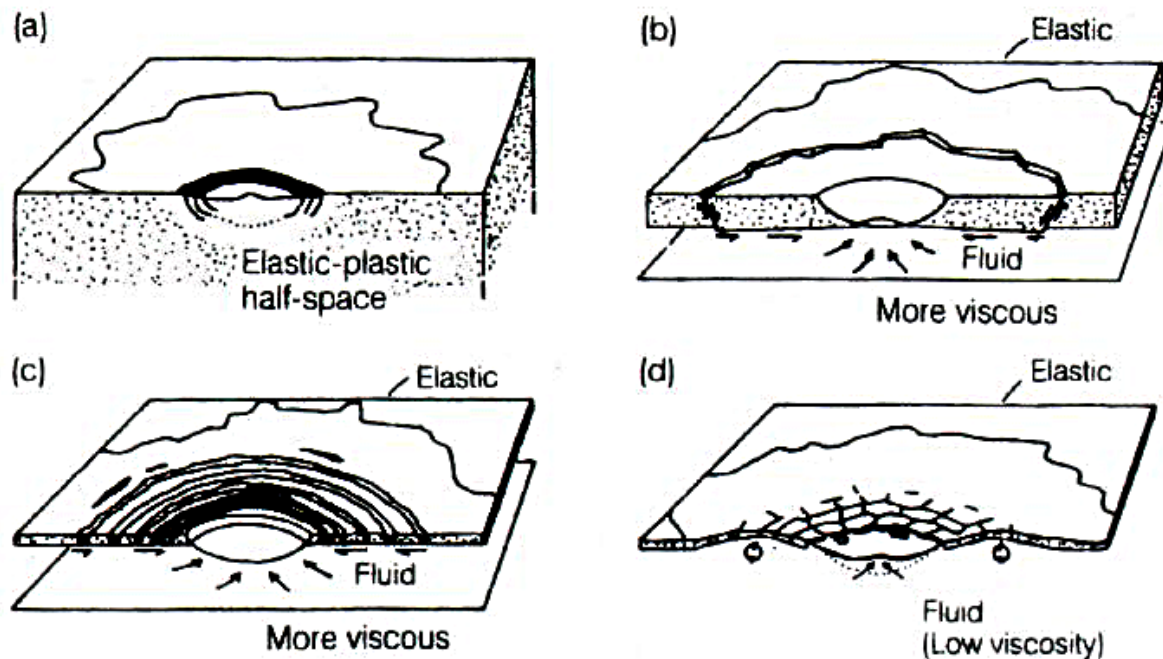


Fig. 3.2.8. The ring theory of multiring basins formation. *From Melosh (1989).*

When a crater forms in an elastic lithosphere overlying a fluid asthenosphere several processes may occur as described in Fig. 3.2.8. If the lithosphere is much thicker than the crater's depth, nothing special happens (Fig. 3.2.8a), and the result is a "normal" crater that is either simple or complex, depending upon its size. Acoustic fluidization may facilitate the crater's collapse and produce central peaks or internal rings with symmetrical profiles, but the acoustic field's range is too short to extend into the region where multiple rings form. If the transient crater's depth is larger than the lithosphere's thickness, at least one ring fracture may form outside the crater (Fig. 3.2.8b). This fracture develops because the asthenosphere flows inward beneath the lithosphere as it intrudes and partially fills the crater. This flow exerts an inward drag on the lithosphere, which, if it is strong enough, creates an extension fracture in the lithosphere. Although this fracture may be irregular in detail, following preexisting lines of weakness in the lithosphere, it is broadly circular and resembles the asymmetric scarps around lunar craters.

Recent modelling of the asthenospheric flow beneath a crater shows that an additional condition must be satisfied before multiple rings can develop: the presence of a higher-viscosity half space underlying the low-viscosity asthenosphere, allowing the formation of a low-viscosity channel. Of interest is that many rheologic models of Ganymede and Callisto call for an especially fluid layer of ice just below the surface. This fluid layer is underlain by stiffer phases of ice, giving rise to the type of low-viscosity channel needed for multiple-ring formation. In the case of the Moon, residual heat from the early magma ocean may have created the necessary low-viscosity channel at the time that the large lunar basins formed. The rather special rheologic conditions required for multiple-ring formation may explain their apparent rarity, and certainly argue against the idea that multiring basins are an inevitable stage in the crater size-morphology progression.

According to ring tectonics, the scarp forms at a distance from the crater's rim that is proportional to the rim diameter, not to the lithosphere's thickness. The scarp cannot form very close to the crater rim because shear stresses at the base of the lithosphere need to act over a broad area to build up large extensional forces within it. On the other hand, the scarp cannot be very far from the crater rim because a large-diameter ring fracture has so much area that it can resist the inward-directed forces. A balance is therefore struck, and the fracture, if it forms at all, occurs between about 1.3 and 1.6 crater radii from the center, depending upon details of the model. This ratio is sufficiently close to the $\sqrt{2}$ ratio found between diameters of adjacent rings on different planetary basins. After the formation of one ring scarp, which relieves the stresses acting on the annulus of lithosphere between the crater rim and the scarp, this process may repeat itself more times to form a second or even third ring scarps surrounding the crater. Each new ring scarp becomes a surface of stress relief and so the diameter of the next succeeding ring is a constant factor times the diameter of the last one. The scarps near the crater face inward because of the direction of the shear stress on their bases: the inward-directed asthenosphere flow produces a couple on the lithospheric blocks broken off at the ring fracture. This couple tends to tilt the lithospheric blocks outward, resulting in an inward-facing scarp with a gentle outward-dipping backslope.

Valhalla-type multiring basins (Fig. 3.2.8c) form when the transient crater's depth greatly exceeds the lithosphere's thickness that the lithosphere is disrupted to great distances from the initial crater. In this case, the shear stress S is so large that the lithosphere quickly fragments into multiple rings, which may occur as graben with width comparable to the lithosphere's thickness. Rather than treating the failure on a fracture-by-fracture basis, it must be regarded as a thin plastic sheet that is characterized by zones of failure.

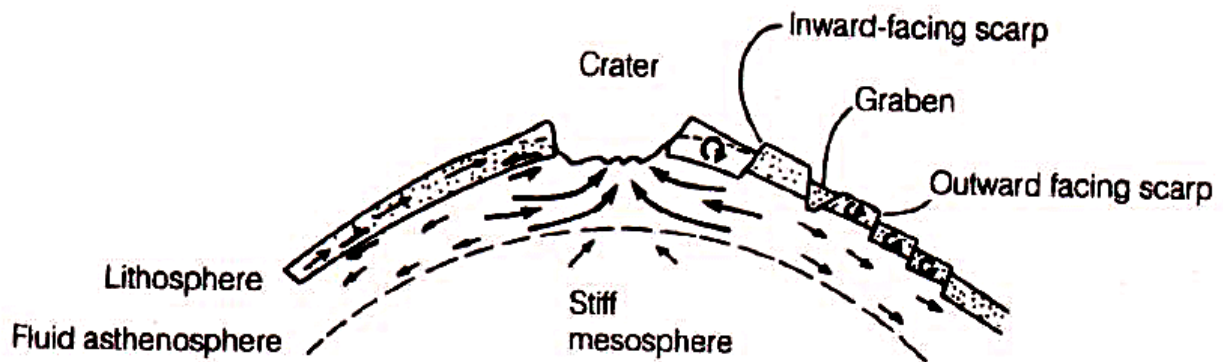


Fig. 3.2.9. Flow within the interior of a planet subsequent to an impact that penetrates its lithosphere. *From Melosh (1989).*

The fact that the more distant scarps surrounding Valhalla face outward is also explained by ring tectonic theory (Fig. 3.2.9). Near the rim of the transient crater, the asthenosphere flows rapidly inward toward the crater cavity. This rapid flow moves inward relative to the more slowly moving lithosphere and exerts a torque on the lithosphere that tilts the crustal blocks outward, raising inward-facing scarps. More than a few crater diameters farther away, however, the inward flow is weak or even changes sign to become outward as a result of surface loading by the ejecta blanket. At such distances from the crater's center, stresses are mainly transmitted horizontally through the lithosphere. Because the lithosphere's inner edge is pulled inward, so are its more distant portions, although to a lesser degree. Far from the crater's rim, the lithosphere thus moves inward relative to the asthenosphere, and the resulting torque tends to tilt crustal blocks inward, raising outward-facing scarps. At intermediate distances, simple graben is expected to form.

The final crater type predicted by ring tectonic theory (Fig. 3.2.8d) has not been observed on any planet or satellite to date. This crater type might originate when asthenosphere is so fluid that waves form within it as the crater is excavated. These waves, while travelling outward the crater, should fracture the lithosphere, firstly radially and subsequently concentrically.

3.3 Crater Morphologies

Impact craters can be generally described as "*circular rimmed depressions*" (Melosh, 1989), but this definition is far from reality, since Gilbert (1893) firstly recognized that craters morphology depends on crater's size. Hence, this parameter is used as term of classification to distinguish craters, as the major features of craters change with increasing size. In the following sections, I will describe the principal crater typology encountered in planetary surfaces.

However, it is to note that there are other factors affecting the morphology of a crater, either during the formation of the crater, either well after its completion. The target properties (§ 3.1.2), as the planet in question, work during the formation of the crater itself, whereas the action of erosional processes modifies the crater shape in time-scales very long after crater is formed. For example, Fig. 3.3.1 reports an example of craters of different age, and consequently different degradation degree.

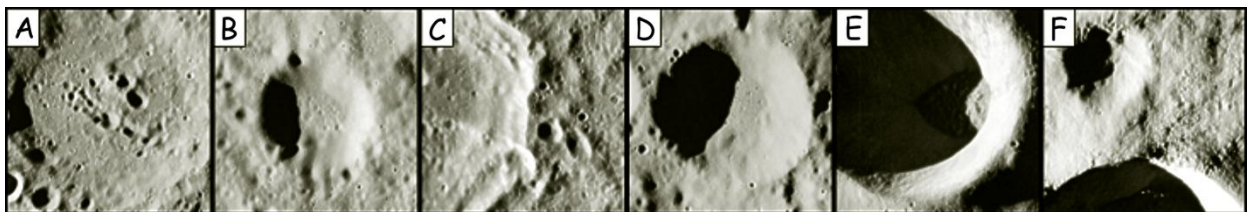


Fig. 3.3.1. Apollo 16 Metric Camera frame AS16-M-0040 showing various degradation degrees occurring in this region, from most degraded to least, indicating oldest to youngest. (A) 84-km-diameter crater with many superposed smaller craters. (B) 12-km-diameter crater with superposed craters yet on top of any ancient ejecta from crater in (A). (C) 61-km-diameter crater, known as Mandel'shtam crater, has a more distinct rim, yet still many smaller superposed craters. (D) 15-km-diameter crater with more intact rim and less superposed craters. (E) 12-km-diameter crater with some ejecta blocks around the rim and very few superposed craters. (F) 14-km-diameter crater with many ejecta blocks, obvious ejecta ray radially oriented from the crater, and very few superposed impacts. *Courtesy of NASA/JSC/Arizona State University.*

3.3.1 Simple craters

Simple craters (Fig. 3.3.2) are ranging in size from centimeter scales up to a critical value, of the order of tens kilometers, which marks the beginning of a new class of craters.

They are circular depressions, bowl-shaped and displaying a rim about 4% of the diameter. The slope of the crater wall is steepest close to the rim, decreasing smoothly towards the crater center forming an almost parabolic profile to the crater (Dence, 1973). As collapse of small cavities is governed by the internal friction of the target rocks, simple craters display an average rim slope roughly equal to the angle of repose of the target material (25–30°) independent of gravity (Melosh, 1989).

The rim-to-floor depth is generally about 1/5 of their rim-to-rim diameter (Pike, 1977), and is shallower than the value of the respective transient crater from which the crater has formed, because landslides occurred (§ 3.2.3). In fact, the floor of simples craters is characterized by a basal breccia lens, composed from a mix of rocks from all the layers intersected by the crater (Shoemaker, 1963), indicating that collapse from the crater walls contributes to the breccia lens formation.

Simple craters are created by the impact of a projectile moving at speeds exceeding a few kilometers per second. Craters produced by slower-moving projectile ($v_i < 1 \text{ km s}^{-1}$) tend to be irregular in plan with broad, less-defined rims, and are usually created by ejecta thrown out of large primaries.



Fig. 3.3.2. Crater Linné ($D = 2.5 \text{ km}$) on the Moon is one representative of simple craters. *Courtesy of NASA, Apollo database (AS15-9353).*

3.3.2 Complex craters

Craters greater in size than a threshold diameter depending on planet gravity show a completely different morphology. Beyond a transition range, where both features survive (e.g., Fig. 3.3.3), craters are characterized by slump terraced rims, single or multiple central peaks and a relatively flat inner floor (Fig. 3.3.4). The depth of complex craters increases very moderately with increasing diameter: Pike (1977) found that lunar complex craters depth increase as the 0.3 power of their diameter, result that is as well consistent with the depths of complex craters on Mercury and Venus.



Fig. 3.3.3. Bessel ($D = 16$ km) is an example of crater belonged to the “transition” range from simple-to-complex morphologies. The bowl-shape characteristic of simple craters has been erased by slumping of material from the inner part of the crater rim, causing a flatter, shallower floor. However, wall terraces and central peaks have not yet developed. *Courtesy of NASA, Apollo database (AS15-9328).*

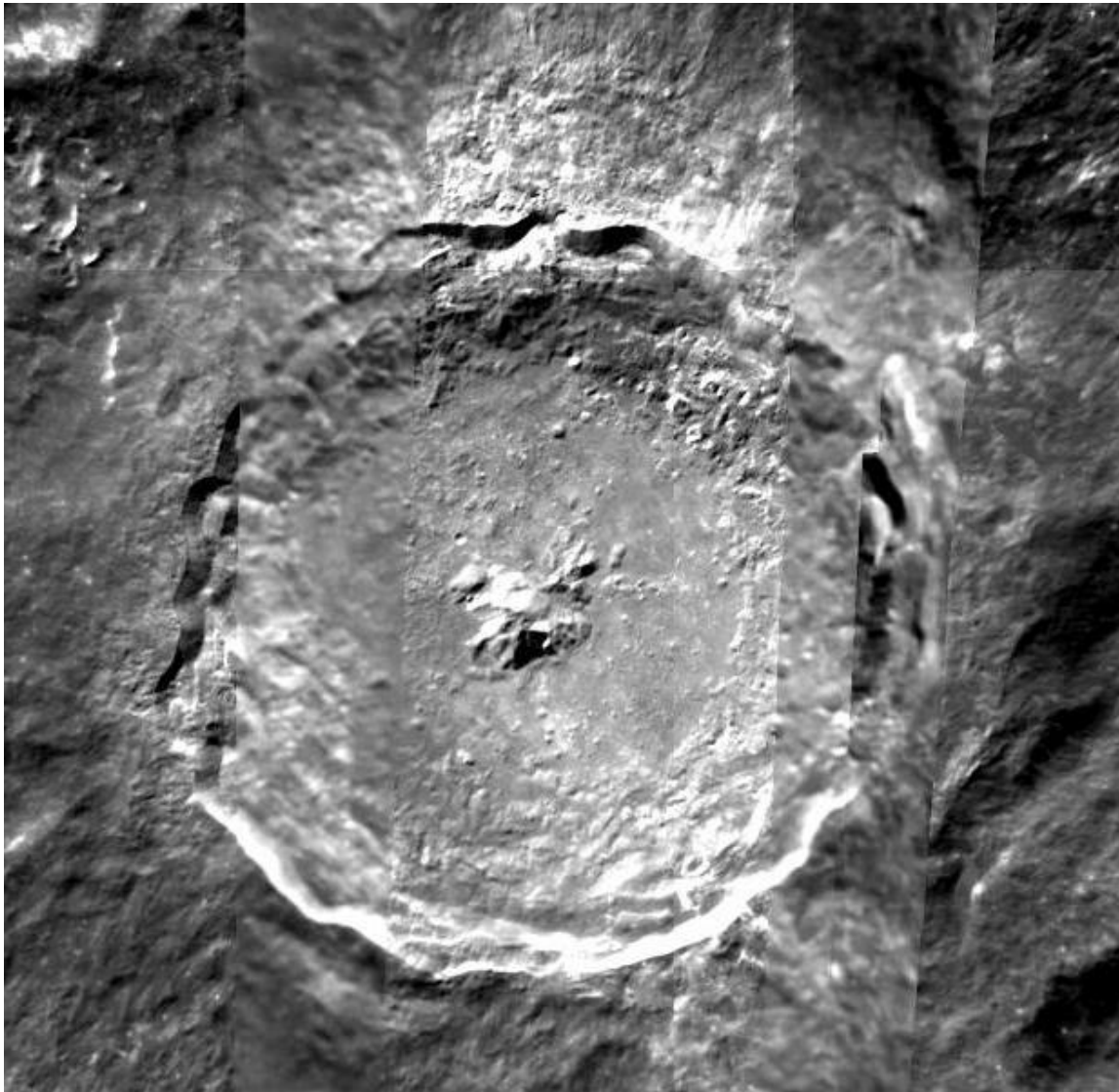


Fig. 3.3.4. Tycho Crater ($D = 85$ km) on the Moon is one representative of complex craters with central peak. It is characterized by flattened floor, a central peak and material that has slumped off the inner crater rim. *Courtesy of NASA, self-developed mosaic from Clementine database.*

Central peaks are composed of rocks that have originated in the layers under the floor and have risen during the final stage of the crater formation for about 8% of the final crater diameter. They get about 22% of the rim-to-rim diameter, and have in general lower high than the pre-impact surface.

The morphology of the central peaks depends as well on crater dimension. At lower range, only one peak develops. As crater size increases further, the central peaks complex begins to break up and an inner concentric ring (Fig. 3.3.5) of irregular mountain peaks, which is roughly half the rim-to-rim diameter (e.g., Melosh & Ivanov, 1999).

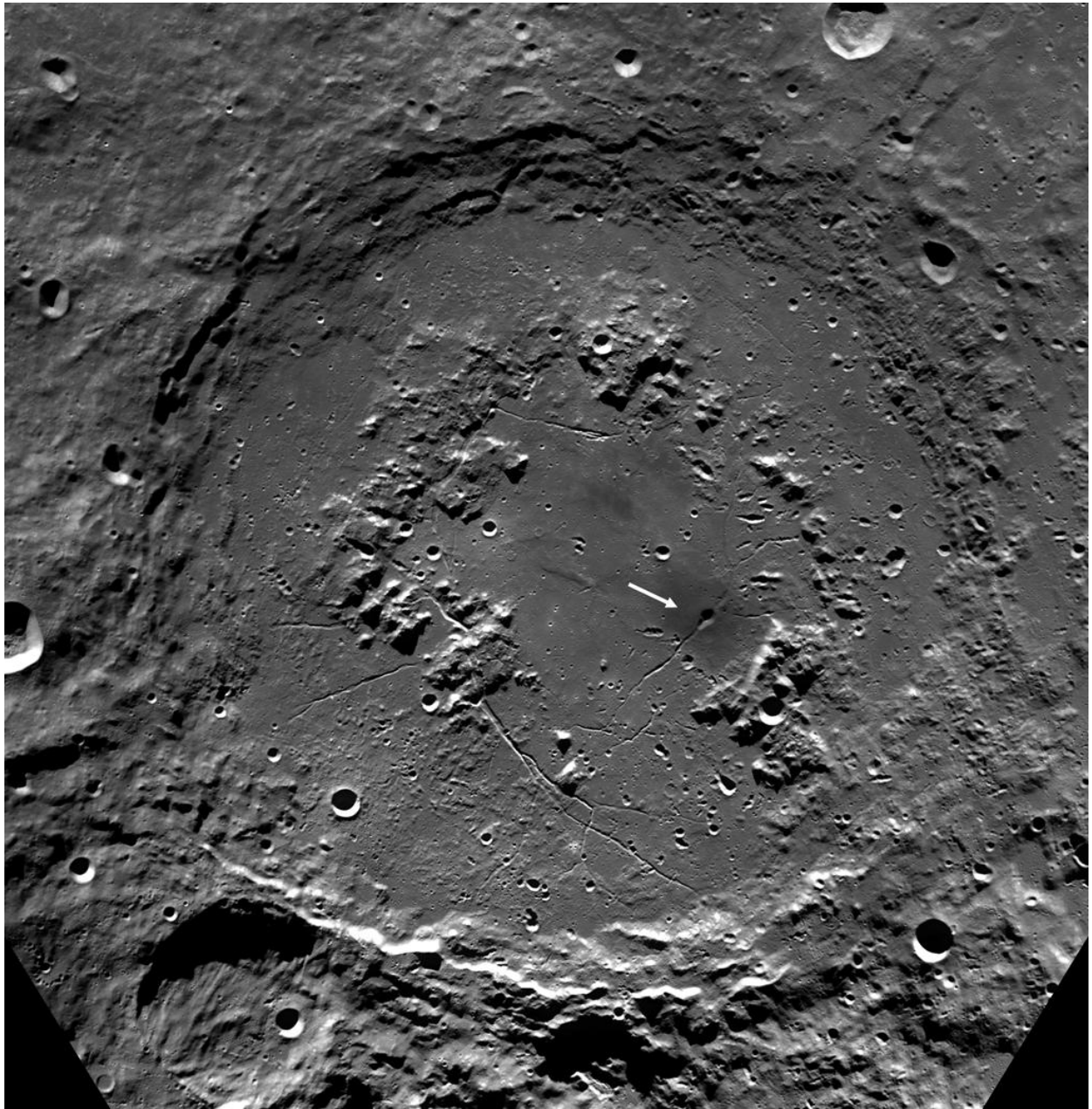


Fig. 3.3.5. Schrödinger ($D = 312$ km), located on the lunar farside near the Moon's South Pole, is one representative of complex craters with peak rings. The central uplift appears as an interior peak ring about 150 km in diameter, partially encircling the basin floor. The white arrow indicates a prominent, dark cone-shaped feature, that is a likely volcanic vent, surrounded by dark, explosively emplaced or pyroclastic material. *Courtesy of NASA, Clementine UVVIS database (mosaic).*

3.3.3 Multiring Basins

The largest impact features (Fig. 3.3.6) are called “basin” (Hartmann & Kuiper, 1962; Hartmann, 1981), being characterized by a large circular structure, whose rim is surrounded by additional concentric raised rings and a system of radial furrows. This impact morphology does not seem to be originated by the same collapsing process of peak ring craters, since it does not exhibit a symmetric profile and the transition diameter does not follow the $1/g$ dependence (Melosh, 1989).

Multi-ring basins appear to form as a tectonic response of the target’s lithosphere to the cavity created by the impact (Melosh & McKinnon, 1978; McKinnon & Melosh; 1980). In fact, the formation of multiple rings indicates the presence of a low-viscosity or low-strength layer below the surface. The extent of the ring system provides an indication of the strength and thickness of the lithosphere, with extensive rings forming in thin, weak lithosphere (Melosh, 1982).

Hartmann & Kuiper (1962) discovered that the spacing of adjacent rings occurs frequently in the ratio of about $\sqrt{2}:1$ and emphasized that the degree of mare lava flooding was quite independent from the size of the ring system. Usually, the inner basin is partially flooded with mare basalt, but otherwise has a fissured, hummocky floor, which is interpreted as solidified impact melt mixed with rock debris.

Extremely large impact structures on the planets and satellites seem to have affected the entire tectonic framework of those bodies. For example, Caloris basin (Fig. 3.3.7) on Mercury is believed to have affected large areas surrounding the basin and also to have caused a great amount of fracturing and surface disruption at its antipode (Fig. 3.3.8). A possible explanation is that these hilly and lineated terrains are originated by seismic waves focusing at the antipodal regions with respect to the impact (Fig. 3.3.9) (Strom & Sprague, 2003).

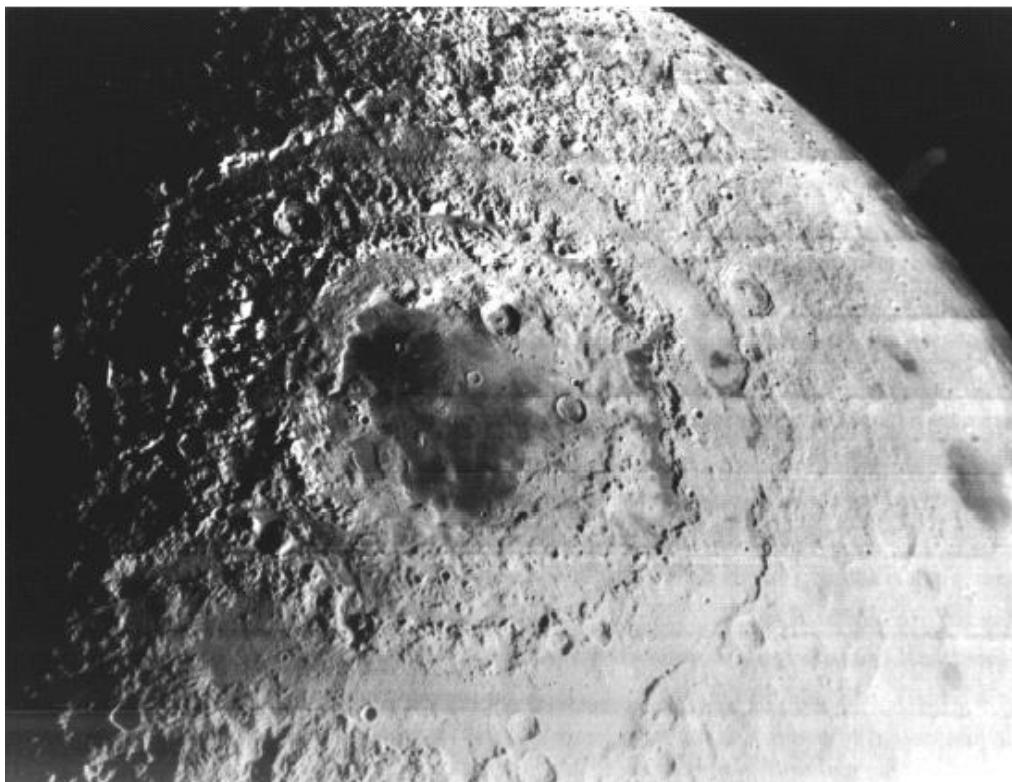


Fig. 3.3.6. Mare Orientale ($D = 900$ km) on the Moon is one representative of multiring basins. *Courtesy of NASA, Lunar Orbiter database.*

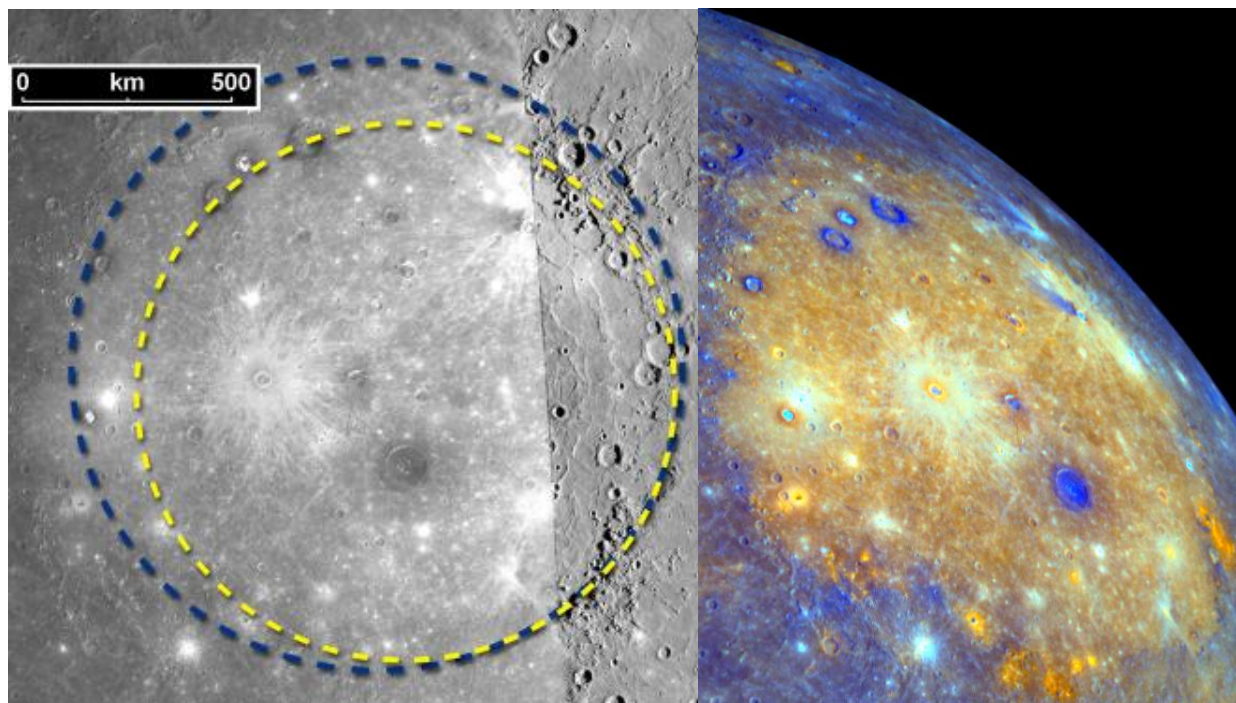


Fig. 3.3.7. Caloris basin ($D = 1550$ km) on Mercury, a second example of multiring basins. In the left panel, MESSENGER NAC captured all the extension of the basin, resolving its real dimension (blue line); in the right panel, an oblique color-component of the basin interior obtained from MESSENGER multispectral WAC. *Courtesy of NASA, MESSENGER database.*

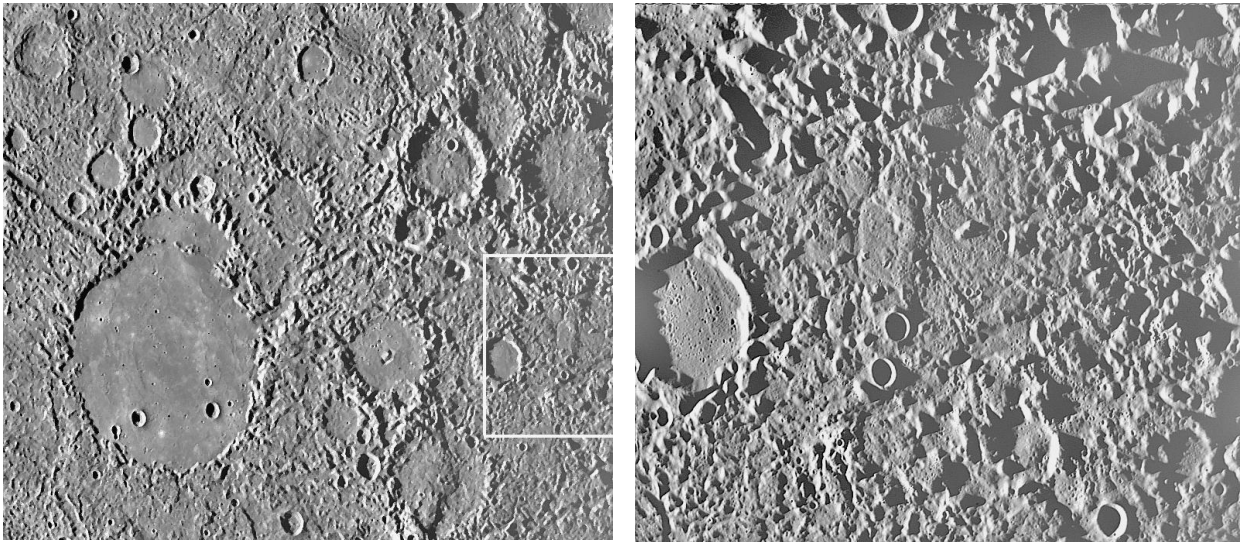


Fig. 3.3.8. (left) Example of hilly and lineated terrains located at the antipodal regions of Caloris basin on Mercury. (right) Outlined area in the left images, seen at higher resolution, shows a broken-up surface of hilly valleys. The hills range from 0.1 to 1.8 km high. From Strom & Sprague (2003).

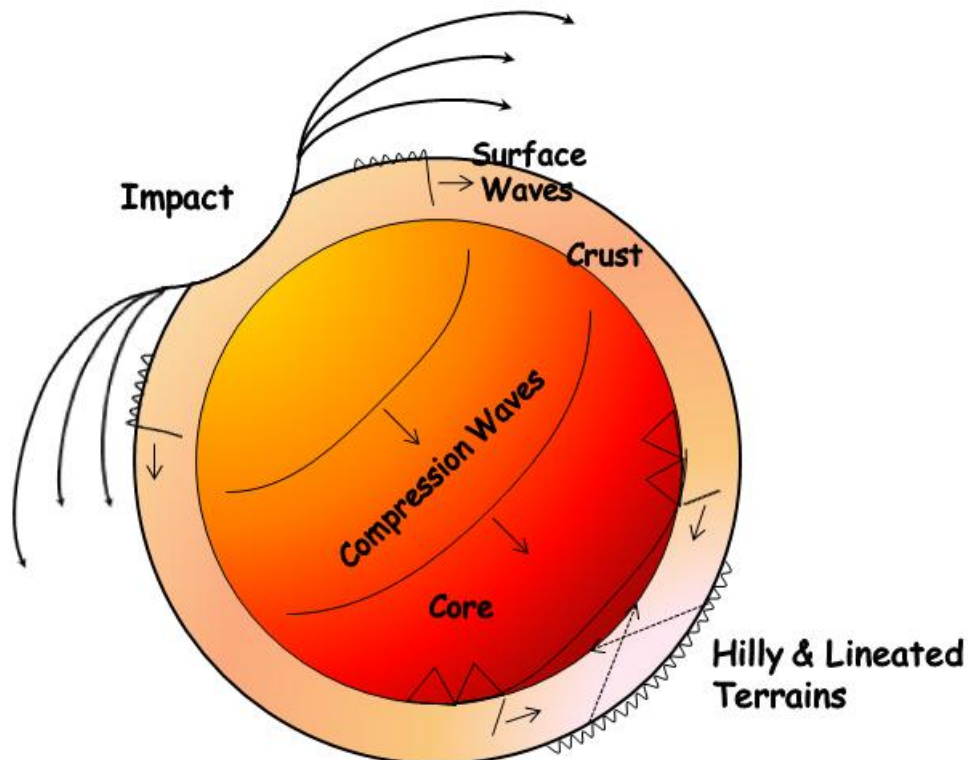


Fig. 3.3.9. The diagram shows the probable cause of the hilly and lineated terrain. Seismic waves generated by the Caloris impact were focused at the antipodal point, causing large ground movements resulting in the hilly and lineated terrains. Modified after Strom & Sprague (2003).

3.4 Impact signatures

Impact craters are the dominant landforms of the Moon and the other atmosphereless bodies of the Solar System, where they are easily recognized from their morphological characteristics. Impact craters occur also on Earth, although they are not as well recognizable, since mechanisms such as tectonics, volcanism, erosion, water and weather, cause the impact structures to be obliterated, deformed or buried within a geologically short time scales (Koeberl, 2004). Hence, it is necessary some common diagnostic criteria for the identification and confirmation of impact structures on Earth.

A first feature to identify impact structures is the circular physiographic surface pattern that can be detected by remote sensing. This circular region can display anomalous bedrock geology with respect to the surroundings, along with intense and localized deformation (fracturing, faulting and brecciation) or it may contain unusual volcanic or intrusive igneous rocks. The formation of impact structures involves shattering and brecciation of the rocks that already exist beneath the crater floor, followed by filling of the resulting crater by a variety of impact-produced breccias and frequently by post-impact sediments. All these impact-related processes produce distinctive changes in the physical properties of the rocks in and around the impact structures. Such changes might be expressed as variations in both the gravity and magnetic fields (e.g. French, 1998; Grieve & Pilkington, 1996).

Gravity anomalies. Impact structures are relatively shallow, but fracturing and brecciation of the target rocks extend to significant depths beneath the crater floor. Since the fractured rock is less dense than the unaltered target rock around the structure, impact craters often exhibit a negative crater anomaly, generally circular in shape and closely coincident with the crater boundaries (French, 1998).

Magnetic anomalies. Impact structures can show either no significant magnetic signature because of fragmentation (Scott et al., 1997), either strong local magnetic anomaly coming from the remnant magnetization of impact melt (Hart et al., 1995).

However, circularity alone is not enough to have an unquestioned identification of an impact feature. Remote-sensing observations and geophysical studies as well can provide only a possible clue for promising impact structures. The positive identification of an impact crater is achieved if on-ground studies turn out meteorites or rocks with evidence of shock waves modification (e.g., French & Koeberl, 2010; Grieve, 1991, 1998; Koeberl, 2004). The unique conditions of shock-wave environments, consisting on the sudden and brief onset and release of pressures, produce unique effects in the affected rocks (French, 1998; French & Koeberl, 2010).

Shock metamorphism is defined as “all changes in rocks and minerals resulting from the passage of transient, high-pressure shock waves” (French, 1968). The nature and intensity of the changes in the target rocks depend on the shock pressures and temperatures values (cf. Fig. 3.4.1 and Tab. 3.4.1). Lower shock pressures (~2–5 GPa) produce distinctive shatter cones (Roddy & Davis, 1977), while within 10 GPa rock fracturing and basal Brazil twinning in quartz are formed. Higher pressures (≥ 10 –45 GPa)

produce distinctive high-pressure mineral polymorphs as well as unusual microscopic deformation features in such minerals (Stöffler, 1972): (1) kink bands in micas (which however can be produced also by tectonic deformations), (2) planar deformation features (PDFs) in quartz and feldspar (10–25 GPa), (3) isotropic mineral glasses (diaplectic glasses) produced selectively (30–45 GPa), (4) selective mineral melting (40–60 GPa). Even higher pressures (≥ 60 GPa) cause partial to complete melting, whereas, near the impact point, shock pressures, which can exceed 100 GPa, cause the total melting and vaporization of a large volume of both projectile and target rocks.

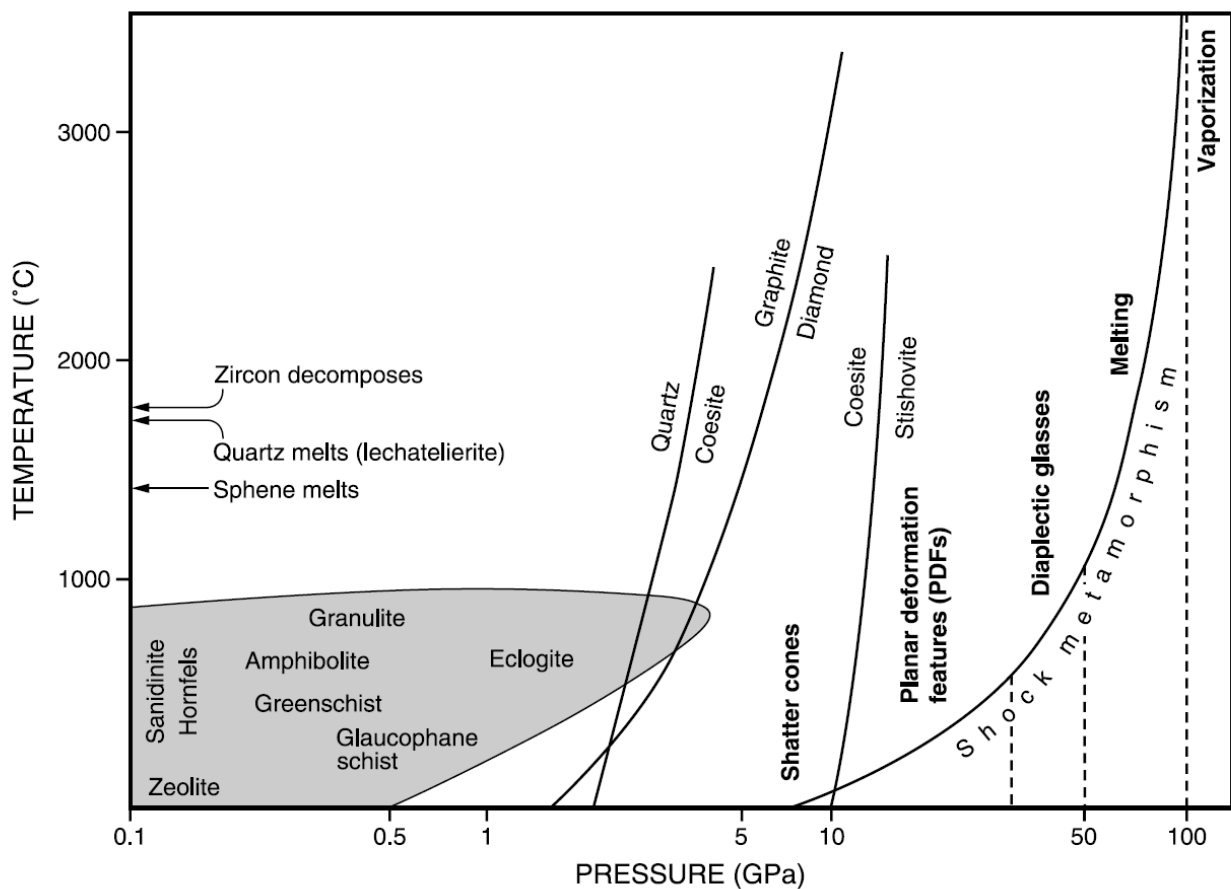
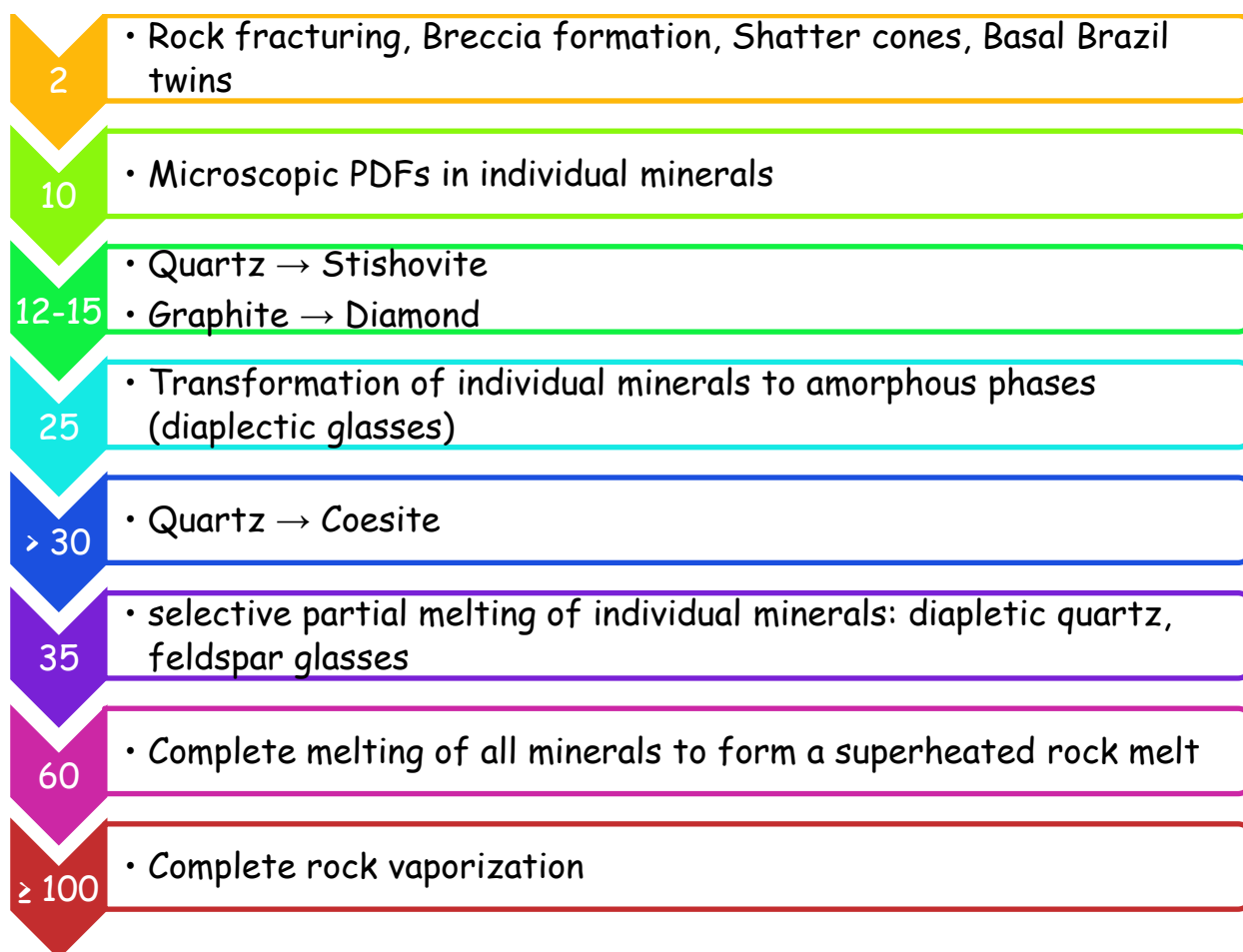


Fig. 3.4.1. Pressure–temperature plot showing comparative conditions for normal crustal metamorphism (shaded region at lower left: $P < 5$ GPa, $T < 1000^{\circ}\text{C}$) and shock metamorphism, which extends from ~ 7 to > 100 GPa. Stability curves for high–pressure minerals (coesite, diamond, stishovite) are shown for static equilibrium conditions. *From French (1998).*



Tab. 3.4.1. Shock metamorphism stages and effects. Arrows display the rising pressures (expressed in GPa) and the respective onset of metamorphic features. *Modified after French (1998).*

All these rocks affected by shock waves and other processes generated by hypervelocity meteorite impact events are overall called *impactites* (Dence, 1965, 1968; Dence et al., 1977; French, 1998).

One possible distinction among impactites is between the *parautochthonous* and the *allogenic* (or *allochthonous*) rocks (e.g., French, 1998). The *parautochthonous* rocks are found beneath the crater and correspond to the lower displaced zone of the transient crater. Therefore, as they are subjected to relatively lower shock pressures, observed shock–deformation effects are generally limited to fracturing, brecciation and the formation of shatter cones, although higher-pressure mineral–deformation features may develop in a relatively small volume beneath the crater floor. The *allogenic* rocks are chiefly breccias and melts derived from single or multiple sources elsewhere from their final location. They principally fill the crater and form the ejecta outside it.

The wide occurrence of typologies of impactites, i.e. breccias, melts, ejecta deposits, and distinctively shocked bedrock, reflects the fact that they form at different instants during the impact process, and hence at different peak–pressure value of the shock wave, that implies also different locations in the area involved in the impact (Fig. 3.4.2).

The diagnostic impactites are restricted to relatively small areas within the impact structures, and precisely (e.g., French & Koeberl, 2010): (1) in the crater–fill breccias, as discrete inclusions of shocked rock and melt; and (2) in restricted near–surface zone beneath the center of the crater floor, as shattered parautochthonous breccias.

In the following, a brief roundup of the principal impact–related features, while in Fig. 3.4.2, a schematic overview of the distribution of the impactites on the basis of their location with respect to the impact structure.

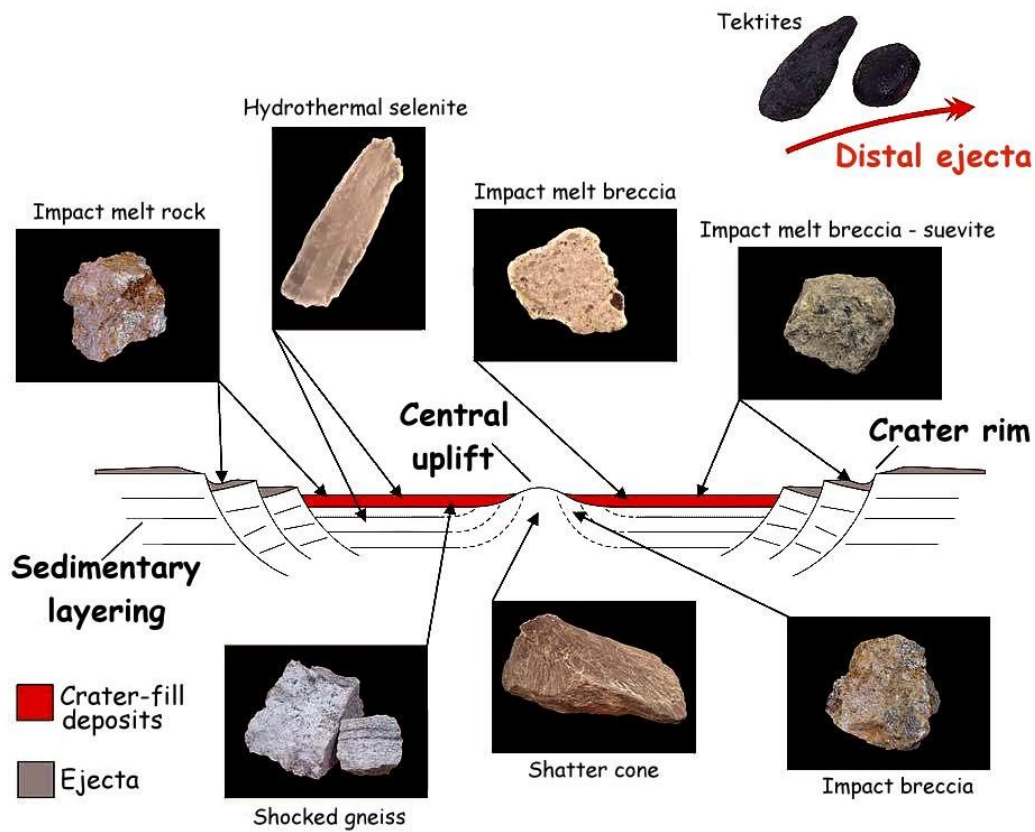


Fig. 3.4.2. Schematic diagram showing the location of the principal rocks samples typologies in a complex crater. Credits to PSI, Tucson, Arizona (<http://www.psi.edu/explorecraters/front.htm>).

SHATTER CONES



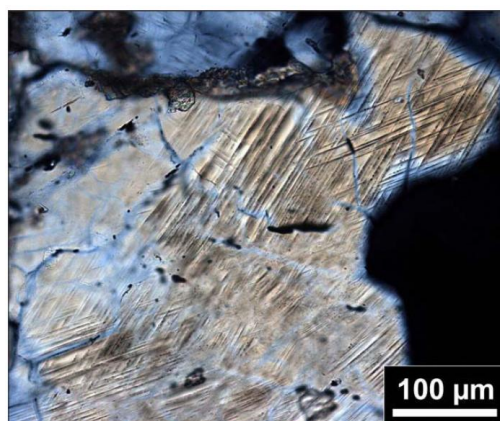
Fig. 3.4.3. Shatter cone (Haughton, Canada). The specimen shows in detail the typical features of shatter cones: nesting of multiple cones, generally parallel orientation of cone axes, radial divergence of striations downward and outward from the cone apices, and the distinctive subsidiary (“horsetailing”) along the cone surface. *From French (1998).*

Shatter cones (Fig. 3.4.3) are multiple sets of striated conical fractures that develop at relatively low shock pressures in impact craters (French, 1998; French & Koeberl, 2010). They represent an important diagnostic impact recognition feature, because: (1) they are found to be the unique shock–deformation effect that is visible at megascopic scales, (2) they can form in large volumes of any types of rocks, such as carbonates, shales, clastic sediments, granites, gabbros and other crystalline rocks; (3) they consist of penetrating fracture surfaces, along which the rock can be broken to reveal new cones or partial cones; (4) the striations on cone surfaces are distinctive and directional, as they consist of alternating positive and negative grooves that radiate downward and outward from the apex of the cone.

PLANAR DEFORMATION FEATURES (PDFs)

PDFs (Fig. 3.4.4) are distinctive shock–produced microstructures, that form at relatively low shock pressure (> 7–35 GPa). They occur as multiple, parallel, both narrow (< 2–3 μm) and closely–spaced (2–10 μm) planes of deformation in quartz grains (French, 1998; French & Koeberl, 2010). An interesting characteristic of PDFs it that they are oriented parallel to specific crystallographic planes within the quartz lattice, allowing to distinguish the shock–produced PDFs from the non–impact ones.

Fig. 3.4.4. Quartz grain (Bosumtwi, Ghana) displaying two intersecting sets of relatively fresh, continuous PDFs. *From French & Koeberl (2010).*



BRECCIA



Breccia is a rock formed by angular fragments of other rocks surrounded by a fine-grained “matrix”, but not containing melt. Some characteristic types of breccia can be found at the Ries crater (Fig. 3.4.5) (Germany).

Bunte Breccia is an allogenic polymict breccia, occurring beneath the overlying melt-bearing suevite breccias both inside and outside the crater (Hörz, 1982; Hörz et al., 1983), with sharp contact between the two units.

Suevite is a melt-fragment impact breccia composed of angular fragments of rocks and minerals, as well as glass inclusions, in a clastic matrix of similar but finer-grained materials (French, 1998).

Fig. 3.4.5. Photo of the Aumühle quarry near the north rim of the Ries (Germany). The reddish rock is Bunte Breccia, whereas the greenish rock is suevite.

PSEUDOTACHYLITE

Pseudotachylite is an unusual type of impactite breccia that occurs in the parautochthonous rocks of large impact structures, and appears not uniform over long distances and may change size and shape radically within meters or tens of meters.

DIAPLECTIC GLASSES

Shock-produced *diaplectic glasses* mainly develop from quartz and feldspar, preserving the original textures of the crystal and the original fabric of the mineral in the rock (French, 1998; French & Koeberl, 2010). The unique textures of the diaplectic glasses indicate formation without melting to the liquid state, being completely different from conventional glasses produced by melting a mineral to a liquid at temperatures above its melting point.

TEKTITES

Tektites (Fig. 3.4.6) are small, glassy pebble-like objects. They represent droplets of molten target rock that are ejected up into the Earth’s atmosphere, which then fall back to the surface up to several hundred kilometers from parent crater. Hence, they can be found in the distal ejecta deposit of a crater.



3.5 Origins of Projectiles

Impact cratering studies draw a wealth of information regarding a span of fields, among whose the nature of the bodies giving origin to craters holds an important issue to analyze, since it is closely related to chronology.

But, what we call projectile? *Meteoroid* is a small fragment of asteroidal or cometary origin, limited in sizes ($< 10^7$ kg). *Meteorite* is a meteoroid ranging from ~ 1 cm up to meters in size, which succeeds in touching the ground after the crossing of the atmosphere, because it has a sufficient mass to not completely vaporize. *Meteor* is a meteoroid, typically ranging from a few hundred micrometers up to centimeters in size, which hence completely vaporizes (e.g., Chapman, 2004; Flynn, 2004).

Meteorites can be classified on the basis of their mineralogical composition (Fig. 3.5.1), and precisely in aerolites, siderites and siderolites (e.g., McSween Jr, 1999).

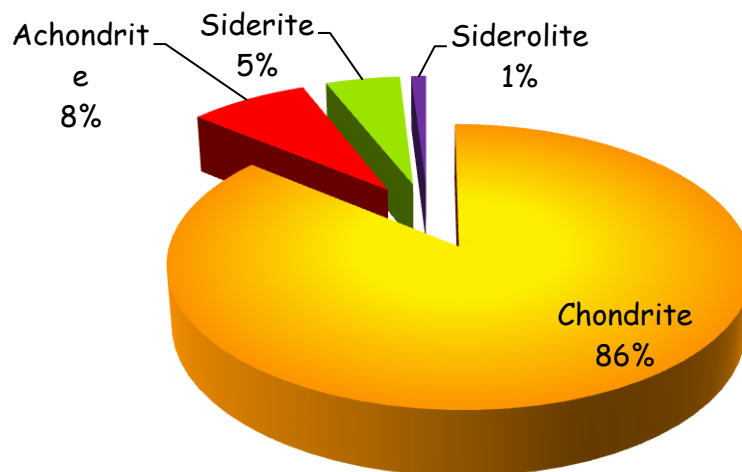


Fig. 3.5.1. Diagram with the relative abundances of the different types of meteorites. The percentage represents the fraction of meteorites that are seen falling. *Modified after McSween Jr (1999).*

Aerolites, or stony meteorites, are made up mostly of silicates, with a small quantity of Fe–Ni alloy, in turn subdivided into chondrites, which are among the most primitive rocks of the Solar System, and achondrites, which experienced chemical differentiation after incorporation into their parent bodies. Chondrites are mixtures of different types of materials formed in different parts of the Solar nebula under very different thermal conditions. They are made up by chondrules, i.e. rounded millimeter-sized particles that formed from molten silicate droplets (Rubin, 2000). Achondrites, characterized by the absence of chondrules, formed during a magmatic process in Vesta– or Moon– and Mars–like sized bodies. In particular, the meteorites that form during a crystallization of a magma are said “achondrites”, while the ones that form from residues of partial melting are said “primitive achondrites”.

Siderites, or iron meteorites, are made up mostly of Fe–Ni alloy and have origin from the inner core of differentiate bodies after a strong impact event. The different composition of siderites depends on the different composition of the parent body and the different degree of the partial melting.

Finally, siderolites, or stony–iron meteorite, are those that are made up both of stone and Fe–Ni alloys.

The meteorites reaching Earth’s surface can have both asteroidal or cometary origin (Fig. 3.5.2), but whatever their nature, before landing on Earth, they had to become Earth–crossing.

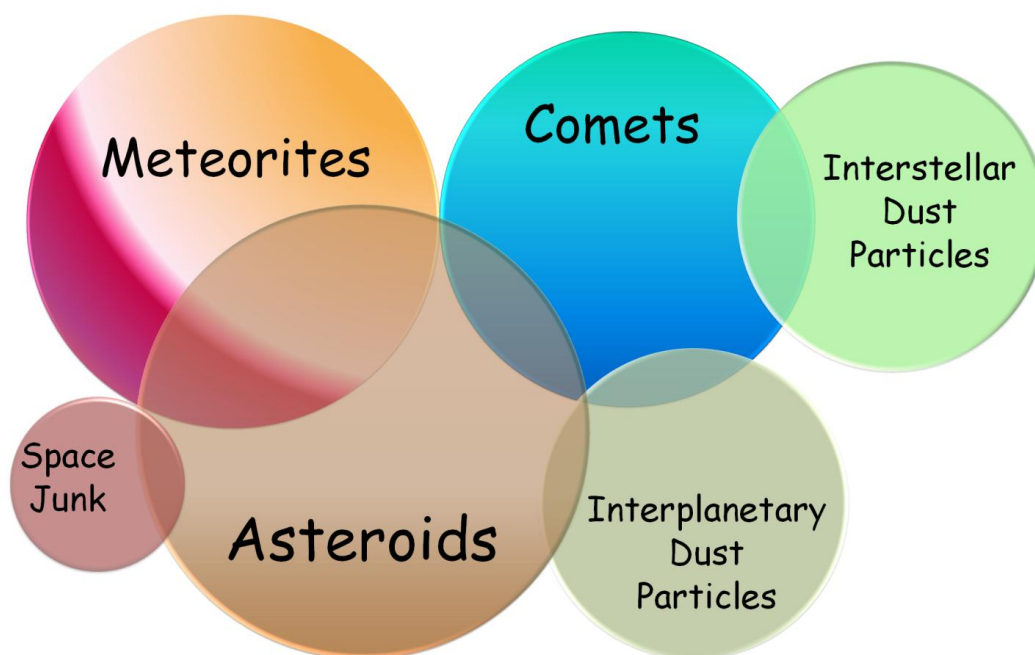


Fig. 3.5.2. Cartoon illustration of the many different groups of objects found within near–Earth space. One of the principal objectives for studying NEOs is to understand how these groups may be related. Thus, the regions of intersection denote key research areas. As surveys increase their capabilities, human–made space flight hardware (“space junk”) is also being increasingly found. *Modified after Binzel et al. (2002).*

Near–Earth Object (NEO) population consists of those astronomical bodies on orbits that bring them “near” the Earth (Gladman et al., 2000). They can be divided into three groups, depending on their osculating orbital elements (Fig. 3.5.3): Apollos ($a \geq 1.0$ AU; $q \leq 1.0167$ AU), Atens ($a < 1.0$ AU; $Q \geq 0.983$ AU) and Amors (1.0167 AU $< q \leq 1.3$ AU). Their dynamical lifetime is shorter than the age of the Solar System, and thus they must be resupplied by some more stable source (Öpik, 1963; Wetherill, 1979), that is likely to be the Main Belt Asteroids (MBAs), although some undetermined fraction of the NEOs could be of cometary origin (Wetherill, 1988).

Asteroids and comets represent different parts of a continuous spectrum of planetesimals formed in the primordial Solar nebula, and their distinction relies on the presence or not of a substantial fraction of ices within the objects, that provide the volatiles necessary for the object to develop a coma. In the standard scenario of Solar System formation, as the nebula was progressively cooling, materials condensate following a temperature– and Sun distance–dependent sequence: refractory materials, metal compounds, silicates and ices. In this description, the boundary to have ices as either vapor either condensed matter was called “frost line”, placed at about 4 AU. Hence, the region between Mars and Jupiter, the so-called Main Belt Asteroids (MBAs), was the natural location of asteroids, while in the region since 4 AU, in particular in the Kuiper belt beyond Neptune, comets had been forming. However, this initial glimpse was successively modified as comets near the giant planets zone have been scattered out of that region by gravitational interactions with those planets. As a result, the critical transition zone between rocky and icy objects has likely lost from the “stratigraphic” record (Weissman et al., 2002).

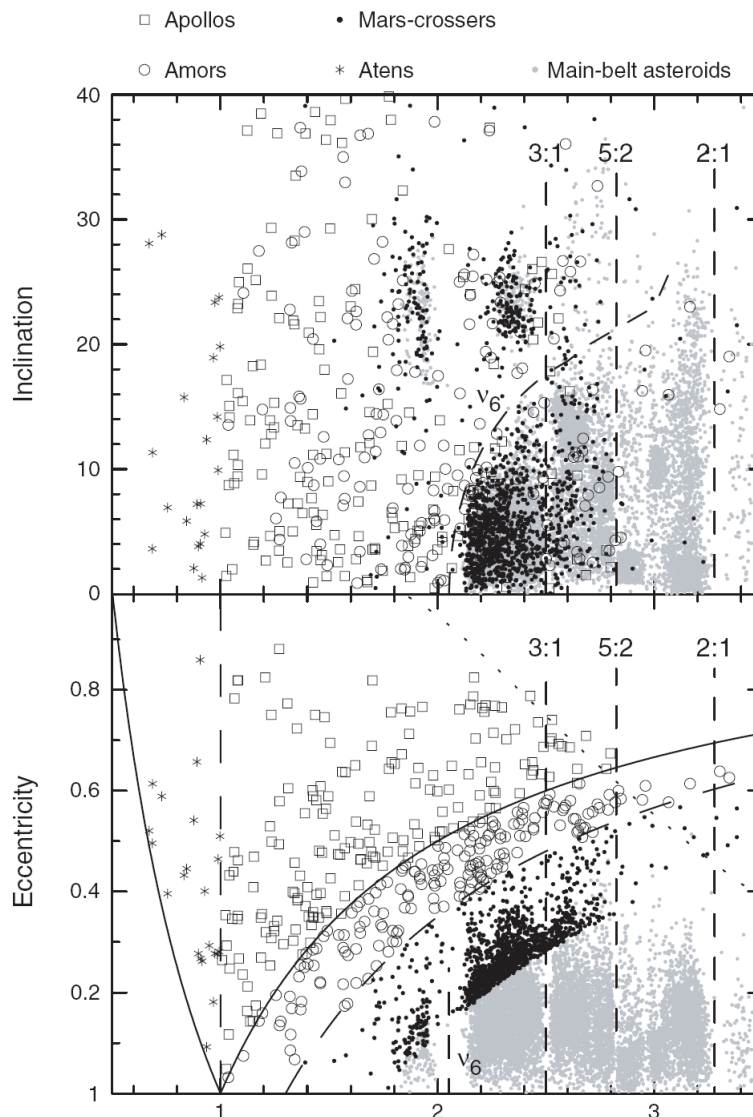


Fig. 3.5.3. The distribution of NEOs, Mars-crossers and Main-Belt asteroids with respect to semimajor axis, eccentricity and inclination. *From Morbidelli et al. (2002).*

A key component in tracing NEOs, and hence meteorites, origins includes the sketching out of the fraction of comets vs. asteroids (Binzel et al., 2002; Michel et al., 2005), issue which has been debated throughout the last 40 years. The initial proposed predominance of comets contribution relied on the fact that the Mars-crossing asteroid population was not large enough to keep the known Apollo population in a steady state (e.g., Öpik, 1961, 1963). On the other hand, the contrary attitude suggested that the Apollos themselves had an asteroidal origin as a result of multiple close encounters with Mars, and only those with high either eccentricities or inclinations might be extinct cometary nuclei (e.g., Anders, 1964; Anders & Arnold, 1965). A turning point in this issue took place when resonances are started to be used as the tool capable to force Main Belt bodies to cross the orbits of terrestrial planets (e.g., Williams, 1969; Wetherill, 1979; Wisdom, 1983, 1985a, 1985b).

Asteroids and comets slowly leak from their initial reservoirs, as a result of chaotic dynamics near planetary resonances, facilitated by collisions and other minor orbital perturbations, like the Yarkovsky Effect. Some dislodged bodies arrive in the terrestrial planet zone, becoming NEOs. Comets rapidly disintegrate as their volatiles are exposed to the Sun. Near–Earth Asteroids (NEAs) continue to suffer occasional collisional fragmentation. Then, they may encounter the Sun, a terrestrial planet or they may be ejected from the Solar System on hyperbolic orbits, on time–scales of a few million years (Chapman, 2004).

A variety of resonant phenomena have been taken into account to explain the increase in eccentricity of asteroids to become planet crossers. Resonances are divided into “powerful resonances” and “diffusive resonances” (e.g., Morbidelli et al., 2002). Powerful resonances, which show gaps in the MBA distribution, are the v_6 secular resonance at inner edge of the asteroid belt and the mean motion resonances with Jupiter 3:1, 5:2 and 2:1 at 2.5, 2.8 and 3.2 AU, respectively. In the following a brief mention to the v_6 and 3:1 resonances, that have been used to develop the planetary chronology (c.f. 4.4).

The v_6 secular resonance occurs when the precession frequency of the asteroid’s longitude of perihelion is equal to the sixth secular frequency of the planetary system. The latter can be identified with the mean precession frequency of Saturn’s longitude of perihelion, but it is also relevant in the secular oscillation of the eccentricity of Jupiter (e.g., Morbidelli et al., 2002). As shown in the top panel of Fig. 3.5.3, the v_6 resonance marks the inner edge of the Main Belt. The effect of the resonance rapidly decays with the distance from the shown curve, so the space can be divided into two regions. The “powerful” region sees the resonance to cause a regular but large increase of the eccentricity of the asteroids: hence, the asteroids reach Earth–crossing orbits, and in several cases they collide with the Sun. The median time required to become an Earth–crosser is about 0.5 Myr. Accounting also for the subsequent evolution in the NEO region, the median lifetime of bodies initially in the v_6 resonance is 2 Myr, the typical end states being collision with the Sun (80% of the cases) or ejection on hyperbolic orbit (12%) (Gladman et al., 1997). The mean time spent in the NEO region is 6.5 Myr (Bottke et al., 2002a), and the mean collision probability with Earth, integrated over the lifetime in the Earth–crossing region, is $\sim 10^{-2}$ (Morbidelli & Gladman, 1998). In the border region, the effect of the v_6 resonance is less powerful, but is still capable of forcing the asteroids to cross the orbit of Mars at the top of the secular oscillation cycle of their eccentricity. To enter the NEO region, these asteroids must evolve under the effect of Martian encounters, and the required time increases sharply with the distance from the resonance (Morbidelli & Gladman, 1998). The dynamics in this region are complicated by the dense presence of mean motion resonances with Mars.

The 3:1 mean–motion resonance with Jupiter occurs at ~ 2.5 AU. Inside the resonance, one can distinguish two regions: a narrow central region where the asteroid eccentricity has regular oscillations that cause them to periodically cross the orbit of Mars, and a larger border region where the evolution of the eccentricity is chaotic and unbounded, so that the bodies can rapidly reach Earth–crossing and even

Sun-grazing orbits. Under the effect of Martian encounters, bodies in the central region can easily travel to the border region and be rapidly boosted into NEO space (e.g., Morbidelli et al., 2002). For a population initially uniformly distributed inside the resonance, the median time required to cross the orbit of the Earth is ~ 1 Myr, the median lifetime is ~ 2 Myr, and the typical end states are the collision with the Sun (70%) or the ejection on hyperbolic orbit (28%) (Gladman et al., 1997). The mean time spent in the NEO region is 2.2 Myr (Bottke et al., 2002a), and the mean collision probability with Earth, integrated over the lifetime in the Earth-crossing region, is 2×10^{-3} (Morbidelli & Gladman, 1998).

As regards the diffusive resonances, these include high-order mean-motion resonances with Jupiter, three-body resonances with Jupiter and Saturn and mean motions resonances with Mars (e.g., Morbidelli et al., 2002). These resonances cause most of Main Belt asteroids to have chaotic orbits (e.g., Nesvorný et al., 2002), although the total effect is weak. The time required to reach a planet-crossing orbit (Mars-crossing in the inner belt, Jupiter-crossing in the outer belt) ranges from several tens of Myr to Gyr, depending on the type of resonances and starting eccentricity (Murray & Holman, 1997).

A last topic regarding the origin of projectile is the issue of the importance of comets in contributing to the overall NEO population. Comets can be subdivided into two groups, according to the region of provenance: Kuiper Belt or Oort Cloud (e.g., Michel et al., 2005; Morbidelli et al., 2002). The population of Kuiper Belt includes the Jupiter-family comets (JFCs), while the Oort Cloud one includes the long periodic and Halley-type groups.

Recently studies have all pointed out to large uncertainties in the knowledge of the fraction of comets responsible of both current and past cratering on the Earth.

Weissman et al. (2002) suggested as best estimate a contribution of 10–30% to the NEO population, while Bottke et al. (2002a) pointed out to a contribution fewer than 10% and 1% from Jupiter-family and Oort cloud comets, respectively.

More recently, Strom et al. (2005) showed that when mapped through the impact cratering scaling-laws to form a production population, the modern-day asteroid population yields a very good match to the cratering record on the lunar surface, thus pointing to the asteroid belt as the primary source of impactors in the inner Solar System.

Chapter 4

Planetary Chronology

4.1 Introduction to age determination via crater counting

The surfaces of most planets, satellites and asteroids are scarred by vast numbers of impact craters, that exhibit degrees of preservation ranging from fresh craters with crisp rims and bright rays to heavily battered or buried craters (Melosh, 1989). The picture as described represents the outcome of a long history of impact cratering due to meteoroids that strike planetary surfaces, along with other events, such as secondary craters around large primaries, mutual overlap, burial by lava flows and erosion (e.g., Neukum et al., 1975a).

Analysis of these planetary records in conjunction with some assumptions about the rate of crater formation has been successfully applied in different topics, but first of all it represents an unquestionable tool to understand the geologic history of atmosphereless planets and small bodies surfaces (e.g., Arvidson et al., 1979; Hartmann, 2005). Actually, statistical analysis of the existing crater population in individual regions does yield *relative surface age*, if assuming that craters accumulate randomly on surfaces at a rate that is on average constant (e.g., Hartmann, 1977; Melosh, 1989; Neukum et al., 1975a; Neukum & Ivanov, 1994). This method relies on the fact that the frequency of impact craters superimposed on a given geologic unit is directly correlated with geologic time: the higher the frequency, the higher the age because of the longer exposure (cf. Fig. 4.1.1) (e.g., Hartmann et al., 1981; Neukum et al., 1975a; Wagner et al., 2010). *Absolute ages* can be obtained if the time-dependent impactor flux for a target body is known. However, available models are far from reproducing with accurate degree of reliability the early stages of the Solar System formation.

Some workers have developed alternative methods to infer absolute ages, based on relating the crater size–frequency distribution (SFD, hereafter) of the Apollo Landing sites to the radiometric ages of the respective lunar rocks. This crater SFD is used as well to obtain the corresponding lunar projectile SFD, once scaling laws have been applied. Age estimate for the other terrestrial planets and Jupiter satellites is inferred by converting still via scaling laws the same projectile SFD of the reference body (the Moon) to the crater SFD for the body at issue (e.g., Hartmann et al., 1981; Neukum, 1983; Neukum & Ivanov, 1994). The central issue of these methods thus relies on the accurate measurement of the crater production SFD, or "production function" (PFSFD, hereafter), a distribution that is assumed to have retained its original form and therefore reflects the SFD of projectiles which were responsible for the crater production. To meet this requirement, the crater population must not have yet reached a state of equilibrium between preexisting craters on the surface and newly ones, because it would not reflect the projectile SFD (Neukum & Ivanov, 1994).

During my PhD, I have contributed in defining a new technique, based on both dynamical models of the asteroids evolution in the inner Solar System and cross–calibration with the lunar chronology (Marchi et al., 2009; Massironi et al., 2009). This procedure will be preferred to previous methods since it avoids a multiple use of scaling laws, may simulate a non–constant impactor flux through time and allows to model variable thickness of the planetary upper layering.

Before describing in more details these crater chronology techniques, let report some useful definitions.

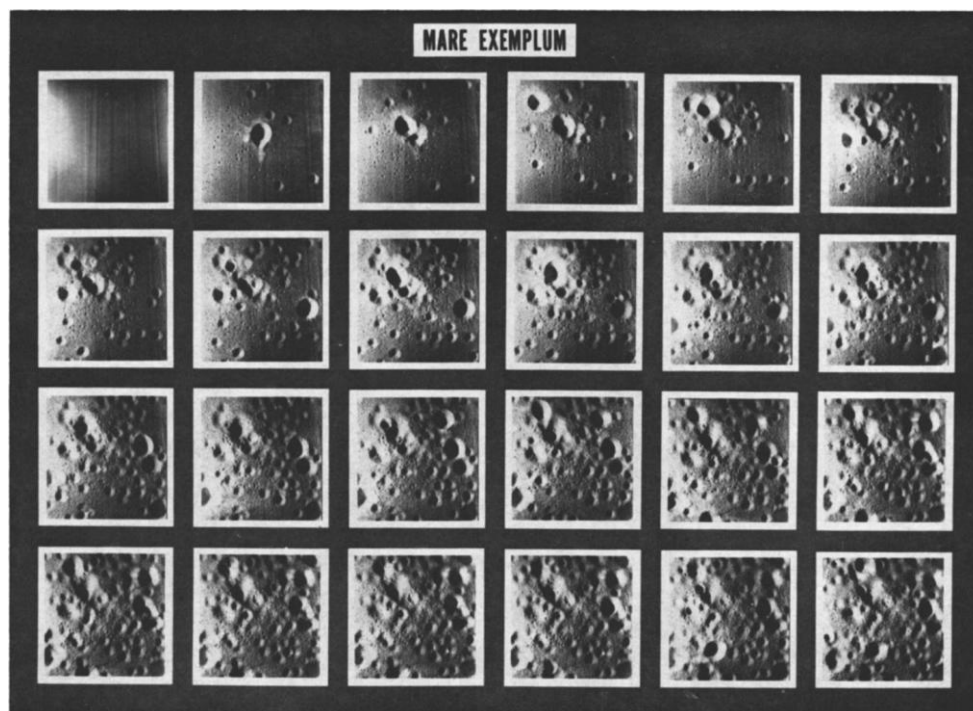


Fig. 4.1.1. Time-lapse sequence from a laboratory simulation illustrating the transition from a smooth plane surface to a surface that has been blanketed with impact craters. *From Gault (1970).*

Crater retention age is the value of ages determined from crater counts and date the length of time that topographic features of a specific scale (D) can be retained on a surface in the face of whatever erosion occurs (e.g., Hartmann, 1966, 1977; Hartmann & Neukum, 2001). The age of a surface based on the cratering record requires that (1) the crater population does not get the equilibrium, (2) only superposed craters are counted, and (3) all secondary and volcanic craters are eliminated from the counts (e.g., Strom & Sprague, 2003).

Radiometric ages date specific events of rock formation or metamorphism (Hartmann, 1977). The methods of radiogenic isotope dating are based on the spontaneous transformation of unstable radioactive atoms into stable atoms by one or several successive reactions (e.g. Faure, 1986; Stöffler & Ryder, 2001).

Impact chronology is the functional dependence of the accumulated crater frequency on age or exposure time (Neukum & Ivanov, 1994).

Production population is the SFD of all the primary craters that have ever formed since craters began to accumulate on a given surface (Melosh, 1989).

Cratering rate is defined as the rate of formation of craters of a specific D , or as the rate of impacts of given energy, but not as the number of impacts by particles of a given mass. The difference arises because the impact velocity on different planets differs because of orbital and gravitational effects. For instance, the modal impact velocities for the Moon, Mars and the Earth are 14, 10 and 18 km/s, respectively (e.g., Hartmann, 1966). According to energy scaling laws, crater diameter is approximately proportional to $(MV^2)^{1/3.3}$, where M is the meteorite mass and V the velocity. Hence, a crater of a given size on the Moon is produced by a meteorite 0.6 times or 2 times as massive on Earth and Mars, respectively (Hartmann, 1973).

Slope is the slope of the curve representing the crater frequency vs. crater diameter on a log–log plot (Neukum & Ivanov, 1994)

Equilibrium of a crater population indicates the point after which crater density becomes constant and only a lower limit on the age can be obtained (Melosh, 1989). Once equilibrium is achieved, the craters SFD no longer changes as more craters form, due to obliteration caused by both crater overlap and processes like ejecta emplacement, lava flows and eolian erosion (Hartmann, 1984; Woronow, 1977, 1978)

Geometric saturation represents the absolute upper limit to the crater density on a planetary surface (Melosh, 1989). Once saturation is achieved, the craters SFD no longer changes as more craters form, due to obliteration caused exclusively by direct crater overlap (Hartmann, 1984; Woronow, 1978).

The *Differential SFD* is the number of craters per unit area per diameter at time T . The *Differential cratering rate* is the number of craters per unit area per diameter per time at time T (Neukum & Ivanov, 1994).

The *Incremental SFD* tabulates the number N_{incr} of craters per unit area in the interval of D and $\sqrt{2}D$. The resulting distribution $N_{incr}(D)$ suffers, however, from the arbitrary choice of a starting diameter D (Melosh, 1989).

The *Cumulative SFD* tabulates the number N_{cum} of craters per unit area with diameters greater than or equal to a given diameter D , as a function of the diameter D . The resulting distribution $N_{cum}(D)$ has the important benefit that is not dependent from the bin size (e.g., Arvidson et al., 1979). The *Cumulative plot* displays in a log-log graphs the $N_{cum}(D)$ along with the confidence interval $\pm\sigma$:

$$\log N_{cum}(D) = \log \left(\frac{1}{A} \sum_{K=1}^i \left(n_k \pm n_k^{1/2} \right) \right)$$

The *Relative Plot*, or *R-plot*, is the ratio between the incremental crater distribution and a distribution with slope -3: the higher the vertical position, the higher the crater density and the older the surface. The reason of -3 as reference distribution is because most impact crater SFD distributions are within ± 1 of a -3 distribution, which is assumed to be the slope of heavily cratered regions near the saturation point. The R-plot was devised to better show the SFD of craters and the crater number densities for determining relative ages, since the cumulative plots may obscure slight but significant differences in crater population as they have the tendency to look all the same, apparently differing only in the absolute number density of craters (Arvidson et al., 1979; Hartmann, 1984; Melosh, 1989; Neukum & Ivanov, 1994; Strom & Sprague, 2003). Mathematically, the R value is expressed as follows:

$$R = \frac{D^3 N}{A \text{ bin}}$$

where D is the geometric mean diameter of the bin size, N is the number of craters in the size bin, A is the area counted and bin is the width of the interval of diameters where craters are counted.

4.2 Neukum Production Function

The method to achieve absolute age determination from crater statistics was well developed for the Moon since the middle of the 1900's century and accomplished by various groups concentrating on different aspects (e.g., Shoemaker, 1962; Hartmann, 1965, 1966; Neukum, 1983). The model elaborated by Neukum turns out to be an empirical chronology that relies in correlating the radiometric ages of rock samples coming from the Apollo landing sites with the crater frequencies derived from the investigation of images of those regions (e.g., Neukum, 1983; Neukum & Ivanov, 1994; Neukum et al., 1975a, 2001a). The central issue of this model is the determination of a calibration SFD over a large range of crater sizes, the *Neukum Production Function* (NPF, hereafter), that is trying to reproduce the production population on the Moon (Neukum & Ivanov, 1994; Neukum et al., 1975a, 1975b). In the followings, I am going to describe the *NPF-derived chronology*.

The crater population on a planet represents, at a first approximation, the mass-velocity distribution of the impactors responsible for the cratering record. Under the assumption of a mean impact velocity, a meteorite population of mass distribution $n(m, t)$ in the mass interval $(m, m+dm)$ causes a crater SFD $n(D, t)$ in the crater diameter interval $(D, D+dD)$ for a specific exposure time t . The relationship between the differential crater distribution $n(D, t)$ and the differential cratering rate $\varphi(D, t)$ is given by:

$$n(D, t) = \int_0^t \varphi(D, t') dt'$$

The function $\varphi(D, t)$ can be splitted in one function, $g(D, t)$, that reflects the underlying crater SFD, and another one, $f(t)$, that reflects the general functional dependence of cratering rate on time. In addition, if the crater diameter distribution shows a similar trend over the whole exposure time, then the function g depends only on D , i.e. $g(D, t) \equiv g(D)$, and the previous integral is solvable by separation of variables, i.e.:

$$\varphi(D, t) = g(D) \cdot f(t) \Rightarrow n(D, t) = g(D) \int_0^t f(t') dt' \equiv g(D) \cdot F(t)$$

These relationships can be rewritten in terms of cumulative crater frequency $N(D, t)$, instead of the differential ones, i.e.:

$$N(D, t) = \int_D^{\infty} n(D', t) dD' = \int_D^{\infty} \int_0^t \varphi(D', t') dD' dt' = \int_D^{\infty} \int_0^t g(D', t') f(t') dD' dt'$$

and assuming again a non-dependence on time of the size distribution, the cumulative crater frequency then becomes:

$$N(D, t) = \int_D^{\infty} g(D') dD' \int_0^t f(t') dt' \equiv G(D) \cdot F(t)$$

which is a production distribution. The production crater frequencies $N(D, t)$ show the same value for areas exposed for an equal length of time on one planet for diameter interval regardless of location on the planet, provided the impactor flux is isotropic and target material composition have no influence. In this case, for two crater populations N_1 and N_2 with ages t_1 and t_2 respectively, the relation

$$\frac{N_1(D, t_1)}{N_2(D, t_2)} = \frac{F(t_1)}{F(t_2)} = c$$

means that the ratio of the crater production population frequency on two areas is directly proportional to their functional dependence on the respective ages, but not to crater size. Hence, frequencies can be normalized each other's by shifting the cumulative distribution in $\log N$ -direction. This relation stands at the basis of the NPF definition.

The first step to define the SFD of an impact crater population, unmodified by endogenic processes, over a wide range in diameters, is to select some lunar regions of various ages, which are believed to have had a homogeneous geologic history. The areas of measurement and their crater populations have been selected in such a way that the crater frequencies measured in the different areas do overlap for the smallest and largest diameters, respectively (e.g., Neukum & König, 1976; Neukum & Ivanov, 1994; Neukum et al., 1975a). Craters detected had to meet the requirements to be "primary craters", while both secondary craters and volcanic features are avoided. In particular, secondary craters (cf. § 4.5.1) are recognizable because they are tracked down as herringbone pattern, elongated shape or clusters (e.g., Neukum & König, 1976; Oberbeck & Morrison, 1973), but sometimes their recognition may not have been quite complete, especially in the cases of isolated circular secondaries with no herringbone pattern. Such secondaries, however, are considered rare by Neukum (1977b). In addition, secondary craters do not uniformly contribute to the primary crater population at all sizes but in a rather limited size range, and their occurrence should be visible in form of a "bump" in the distributions. Neukum (1977b) suggested an uncertainty of $\pm 30\%$ in crater frequency due to the presence of secondaries.

The crater populations were measured in Lunar Orbiter and Apollo images, for a broad number of regions of the Moon, in the size range from 800 *m* up to more than 5 *km* (Neukum, 1977a), covering an age period of ≈ 4 *Gyr*, from the lunar highlands older than 3.8 *Ga*, to the maria with ages between approximately 3 and 3.8 *Ga*, up to very young craters, such as Copernicus and Tycho (< 1 *Ga*) (Neukum & Ivanov, 1994).

Cumulative crater frequencies and the respective statistical errors were calculated, as summarized in Fig. 4.2.1a. The investigated crater populations are then normalized to the Mare Serenitas one, because it was covering the widest size range with the best statistics (cf. Fig. 4.2.1b). The normalizing factor *c* is determined by taking the average ratio of the crater frequencies in the range where they overlap and are statistically best defined (Neukum et al., 1975a). Crater counts of a previous work of Greeley & Gault (1970) have been included as well for the completion of the size range distribution at small sizes (Neukum et al., 1975a).

After the normalization on $F(t) \propto t$, all the frequencies fall on a smooth curve which is the lunar calibration distribution (Neukum & Ivanov, 1994). Following the idea of Chapman & Haefner (1967) about the variation of the local SFD slope depending of the crater diameter range, Neukum (Neukum, 1983) proposed an analytical function to describe the cumulative number of impact craters on the Moon. The main assumption of this model is that the PF had been more or less stable from Nectarian to Copernican times, i.e. practically from more than 4 *Gyr* ago until now, in the diameters range accessible for counting craters and for all epochs of lunar history manifested in different geologic units on the Moon (e.g., Ivanov, 2008; Ivanov et al., 2002; Neukum & Ivanov, 1994; Neukum et al., 2001a), supporting as a consequence that the underlying asteroidal projectile SFD was stable with time (e.g. Neukum et al., 2001a; Wagner et al., 2002).

Hence, the lunar crater population can be described with a single size distribution function over the range in which measurements can be made, that is represented with a polynomial of order ≥ 7 in $\log D$ (Neukum & Ivanov, 1994). Within about two decades of refinement (Neukum, 1977a, 1983; Neukum et al., 1975a, 1975b), the NPF has been found to be described by an 11th degree polynomial in $\log D$, in the diameter range $10 \text{ m} \leq D \leq 300 \text{ km}$ (Neukum & Ivanov, 1994).

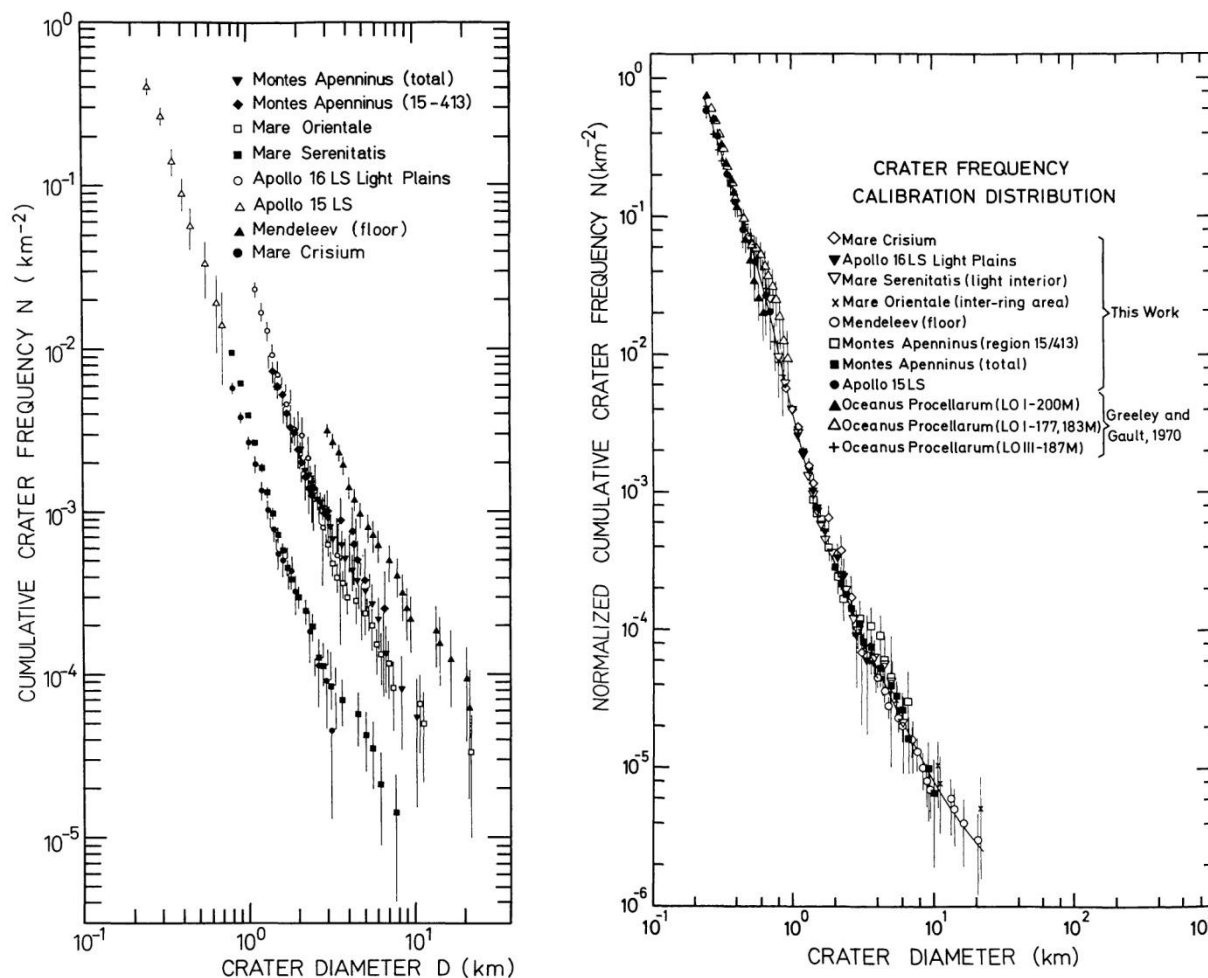


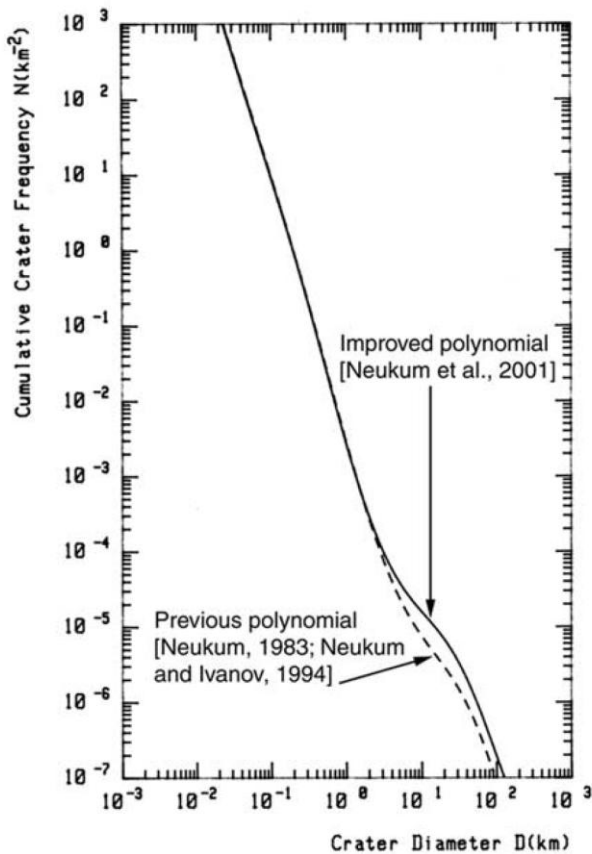
Fig. 4.2.1. (a) Absolute cumulative SFD of all populations measured. (b) Cumulative SFDs of all investigated populations normalized to the frequency of Mare Serenitas Light Interior. The solid line represents the polynomial approximation of the calibration SFD. From Neukum et al. (1975a).

More recently, the NPF was again updated (Ivanov et al., 1999, 2002; Neukum et al., 2001a), since the measured frequencies were deviating by a factor of ~ 2 from the previous theoretical production function polynomial (Neukum, 1983; Neukum & Ivanov, 1994). This deviation was due to the fact that it is difficult to find a large area on the Moon affected by a single resurfacing event, where one can measure a crater distribution at both small and large crater sizes. In order to improve the polynomial fit, new counts on the Orientale ejecta blanket were carried out. Lunar Orbiter and Clementine images were used at different spatial resolutions to cover all the crater size range (Wagner et al., 2002).

The polynomial representing the lunar NPF (Fig. 4.2.2), obtained in a least squares fit of all the data acquired in the crater diameter range from 0.01 km to 300 km, has finally the following form:

$$\log N_{cum} = a_0 + \sum_{j=1}^{11} a_j (\log D)^j$$

Standard Cumulative Crater Size Frequency Distribution
MOON Polynomial of 11th Degree



where D is the crater diameter in km, N_{cum} is the cumulative number of craters per km^2 per Gyr, and a_j are the fit coefficients, in particular the terms a_0 represents the time during which a geologic unit was exposed to the meteorite flux (e.g. Neukum et al., 2001a).

Any lunar primary production function crater population has to show a distribution in accordance with the derived calibration curve (Neukum, 1977a). Any departure from the NPF is ascribed to either endogenic processes, such as lava flows emplacement, or exogenic processes, such as superposition by other impact craters, erosion and ejecta blanketing emplacement (e.g., Hartmann et al., 2008; Ivanov et al., 2002; Neukum et al., 1975a). It is noteworthy that depositional and erosional processes result in a preferential loss of small craters relative to large ones, that is translated as an increase of the curve slope in the cumulative plot (Neukum & Ivanov, 1994).

Fig. 4.2.2. Cumulative plot of both previous and improved lunar NPF. Dashed: previous polynomial (Neukum, 1983; Neukum & Ivanov, 1994); Contiguous line: improved polynomial (Neukum et al., 2001a). From Wagner et al. (2002).

The measurement of crater frequencies in individual regions gives a means for determining relative surface age differences. To obtain absolute ages from crater SFD, the impact rate and its variation through geologic time has to be known.

Alternatively, the cratering chronology during the history of the Moon relies on correlating radiometric ages of lunar rock samples to the crater counts of the Apollo landing sites where those rocks were collected (e.g., Neukum, 1983; Neukum & König, 1976; Neukum & Ivanov, 1994; Neukum et al., 1975b). This is the reason why crater counts for the Apollo 11, 12, 14, 15, 16, 17 and the Luna 16 and 24

landing sites were performed. In addition, Montes Apenninus and Southern Terrae crater counts were as well taken into account. All these data provide age information for the time span up to 3 Gyr ago. On the other hand, the craters Tycho and Copernicus were studied for the determination of the impact history in the more recent past, since they have been suggested to be formed within the last Gyr (Neukum & König, 1976). Some enlightens for the cratering history of the last 600 Myr were obtained from the Canadian Shield impact crater frequencies. However, to employ the terrestrial cratons data, they were reduced to lunar conditions, by considering the smaller cross section of the Moon for meteoroids capture (Bschorr, 1970) and the different impact velocities of impactors of equal sizes, which will origin different-sized craters on either the Earth and the Moon (Neukum et al., 1975b). Each measurement was organized in a cumulative distribution, through which the NPF was laid as an envelope to the upper and lower values given by the statistical errors of the measure SFD points. The average frequency value given by the two envelopes was determined and then the value at $D = 1 \text{ km}$ was derived (e.g., Neukum et al., 1975b).

The 1 km -frequency values as extrapolated were hence linked to the individual radiometric age values of the lunar samples (Kirsten & Horn, 1974; Papanastassiou & Wasserburg, 1973; Turner, 1971). However, lunar samples of each landing site may display a certain bandwidth of radiometric ages (e.g., Neukum & Ivanov, 1994). This uncertainty is reflected on the assignment of rocks radiometric age to the crater SFD of the corresponding region. Two methods can be adopted to correlate a given crater SFD with a specific radiometric age, i.e. using either the youngest or the most frequently measured radiometric age among the samples collected in that region (e.g., Hiesinger et al., 2000). Neukum's model relied in this second option as it likely represents the time when a major event reset the region, time from which craters started to accumulate again on the surface.

The Neukum chronological model for the Moon is given by an empirical relation, represented in Fig. 4.2.3 and mathematically expressed as:

$$N(1) = 5.44 \cdot 10^{-14} (e^{6.93 T} - 1) + 8.38 \cdot 10^{-4} T$$

which related the cumulative number crater frequency per km^2 at $D = 1 \text{ km}$ with the crater retention age T in Gyr. This equation accounts for both the exponential drop-off in impact rate with a half-time of about 100 Ma at a time prior to about 3–3.3 Ga, when most of the multiring basins formed, and the more recent more or less constant cratering rate. Assuming a time-constant SFD for projectiles, the equation $N(I)$ implies that in an approximately 4 Gyr old area, 95% of the craters on the Moon were formed between 3 and 4 Gyr ago, while only 5% of the craters are younger than 3 Gyr (Neukum et al., 2001b)

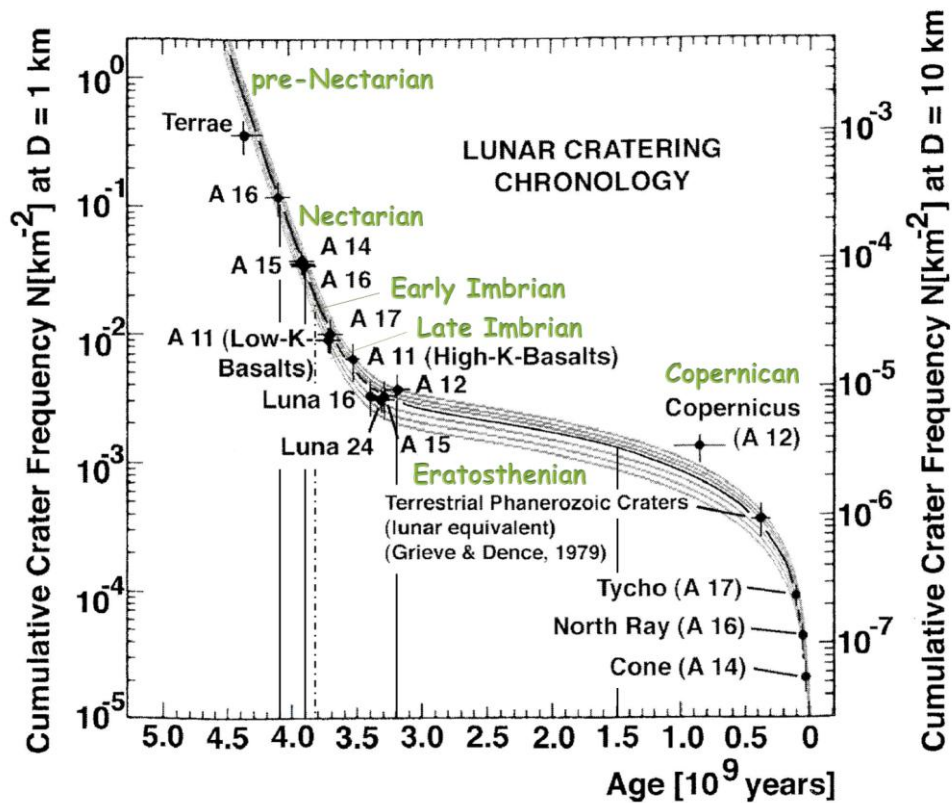


Fig. 4.2.3. Lunar cratering chronology which shows the empirical dependency of cumulative crater frequency N on surface formation age. For any given area, absolute model ages are derived from the crater retention age (y value of the SFD plot) at $D = 1 \text{ km}$ (x value). Gray curves give 10, 20 and 30% error in $\log N(D = 1 \text{ km})$. Chronostratigraphy system is as well shown. Modified after Hiesinger et al. (2000).

This equation allows to infer absolute ages for any region of the Moon, whose crater frequency is available (e.g. Neukum, 1983; Neukum & Ivanov, 1994; Neukum et al., 2001a). Possible uncertainties are inherent to (e.g. Hiesinger et al., 2000; Wagner et al., 2010):

1. crater SFD measurement procedure: influence of factors such as flooding, blanketing, secondary cratering, superposition, infilling, abrasion, mass wasting and volcanic craters (Neukum et al., 1975a);
2. images quality, i.e. spatial resolution and illumination conditions of the images where crater counts are performed: contrast, brightness and resolution of the images used are important issues because all can have influence on the detection of craters;
3. radiometric dating of rock samples, as previous observed;
4. derivation of the lunar cratering chronology model.

These points lead to uncertainties in crater model ages of the order of 20 to 30 Ma in the time prior to about 3.3 Ga , where the cratering rate decayed exponentially, while for the following time period they can rise up to 100 to even 500 Ma , since there is only a minor change of crater frequency with time (e.g. Wagner et al., 2002, 2010).

The crater chronological model as established for the Moon might be turned as a useful tool for age determination of other terrestrial planets too, if a new series of parameters regarding projectile sources, mechanical properties of rocks and impact scaling laws are provided. More in detail, to transfer the lunar impact crater SFD to other planets implies to take into account differences in projectile flux and impact velocity distribution, as well as gravity, atmosphere, crustal strength density and structure of the planetary targets (e.g. Hartmann, 1977; Neukum & Ivanov, 1994; Ivanov, 2008; Ivanov et al., 2001, 2002). The procedure (Fig. 4.2.4) relies on the following steps (e.g., Hartmann, 1977; Neukum & Ivanov, 1994; Ivanov et al., 2001, 2002; Neukum et al., 2001a, 2001b):

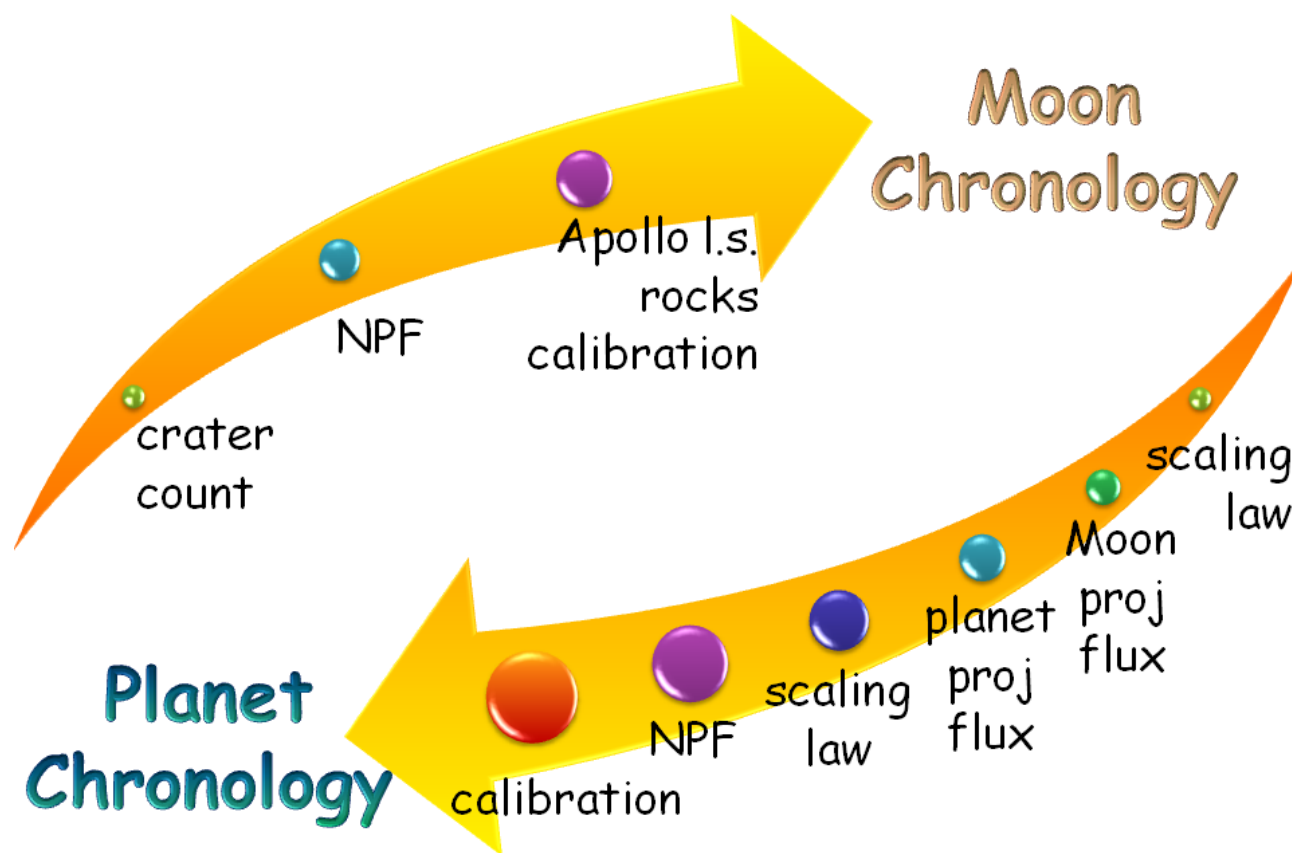


Fig. 4.2.4. Flowchart of the different steps needed with the Neukum chronological model to compare crater SFD and cratering rates on different planets.

1. The lunar measured crater SFD is used to estimate the lunar projectile SFD, by means of scaling laws.
2. Orbits and sizes of observed asteroids were used to both calibrate the projectile SFD and compute their associated impact velocity and probability. The projectile SFD is approximated with a polynomial of 14th degree valid for projectile diameters between ~0.25 *m* and ~27 *km*.

3. Main assumption of the model is that the cratering records on different bodies were originated by the same projectile population, hence the projectile SFD is unique for all the terrestrial planets.
4. The lunar-based projectile SFD is used to derive crater SFD of the planet at issue, through a further application of scaling laws, by assuming new impact velocity values and taking into account all the target parameters that control the relationship between projectile mass and velocity and the final crater dimensions.
5. The crater PF is normalized to the average impact rate ratio, since a specific planetesimal from any specified starting family will make different-sized craters on each planet.

Let analyze in more details all the different issues at the base of the conversion of the chronology from the Moon to another planet.

Projectile populations. The projectile capable of forming craters on the terrestrial planets today are NEOs, in turn coming primarily from three populations (e.g., Ivanov et al., 2002): (1) asteroids of the Main Belt (MB, hereafter), (2) Jupiter-family comets (JFCs), and (3) long period comets (LPCs) Cloud (Morbidelli et al., 2002). Other less important contributors include the Trojan asteroids and the Halley-type comets.

Each impactor population has undergone a specific accretion, collisional and evolutionary history, such that their SFDs are different one from another. Moreover, these populations produce planet-crossing projectiles with characteristic orbits and physical properties, such that sorting out the importance of various impactor populations can be complicated (Ivanov et al., 2002). Current dynamical models (e.g., Bottke et al., 2002a) and observational database yield to asteroids as the dominant impactors source on the terrestrial planets.

Average Impact Velocity. The distribution of impact velocity (Fig. 4.2.5) depends on the orbital parameters of Planet-Crossing Asteroids (PCAs, hereafter) striking the planet (e.g., Bottke et al., 2002a; Rabinowitz, 1993; Stuart & Binzel, 2004). Reliable sources for establishing the PCAs distribution are (e.g. Ivanov, 2008; Ivanov et al., 2001, 2002; Neukum et al., 2001a): (1) observational data listed in the “astorb.dat” file, with more than 30,000 small bodies, continuously updated at Lowell Observatory; (2) the debiased model population of Earth-crossing objects estimated by Rabinowitz (1993), in the case of our planet. The Öpik formulas, refined by Wetherill (1967), are applied to all the bodies. A random orientation of the nodes latitude is assumed, so that all mutual positions of inclined elliptical orbits have the same probability. For each target and projectile (PCA), the impact probability and velocity are calculated. The total impact probability and the average impact velocity are needed to compute the cratering rate (e.g., Ivanov et al., 2001, 2002; Neukum et al., 2001a).

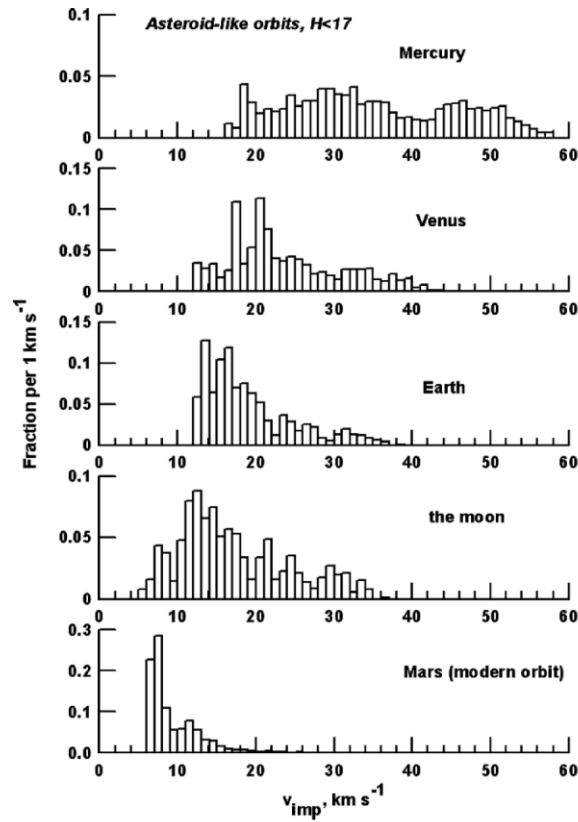


Fig. 4.2.5. Frequency of the impact velocity for terrestrial planets and the Moon, presented as the fraction of all impacts f , in velocity bins with the width of 1 km s^{-1} . From Ivanov (2008).

Scaling Law. Schmidt & Housen (1987) scaling law relates craters and projectiles, assumed to be only of asteroidal origin and hence having as mean density the value typical for S-type asteroids (2.7 g cm^{-3} ; Britt et al., 2002). This relation can be written as:

$$D_{at} = 1.16 \left(\frac{\rho_t}{\rho_p} \right)^{1/3} D_p^{0.78} (v \sin \alpha)^{0.43} g^{-0.22}$$

where D_{at} is the transient cavity diameter, D_p the projectile diameter, ρ_t and ρ_p the densities of target and projectile materials, respectively, v the impact velocity, α the impact angle and g the gravity acceleration (e.g. Pierazzo et al., 1997). The estimate of D_{at} from the rim crest diameter D depends on the cratering regime considered. Small craters are formed in the strength regime, in which the final crater dimensions are governed by projectile parameters and the target material strength. Larger craters, that experience more or less structural modifications, are formed in gravity regime, in which the energy needed to uplift target material in a planetary gravity field is larger than the energy due to plastic work (Neukum & Ivanov, 1994). In this case, for simple craters one can assume (Ivanov, 2008):

$$D_{at} \approx \frac{D}{1.25}$$

while, for complex craters, the Croft’s (1985) law is adopted to relate the transient cavity diameter D_{at} with the rim crest diameter D , by introducing the critical diameter value D_{sc} of transition between the two morphologies:

$$D_{at} \approx D_{sc}^{0.15} D^{0.85}$$

Cratering records. The estimated lunar cratering rate has been calibrated using returned samples that have been dated. But the case of the Moon is exclusive, since for the other planets only crater densities can be obtained. To translate the lunar crater chronology to other planets, we need to take into account the differences in planetary gravity, number of planet–crossing bodies, and orbital parameters of the potential projectiles, which in turn control their impact velocities and collisional probabilities (e.g., Ivanov et al., 2002).

In particular, deriving planet surface ages implies the estimate of the ratio “ R_{crater} ” of planets/Moon cratering, which in turns depends on the “ R_{bolide} ” (e.g. Hartman, 1977, Hartmann & Neukum, 2001, Ivanov et al., 2001, 2002), i.e. the planets/Moon impact rate ratio. These two quantities are different, since gravity and target material depends from the planet considered. Moreover, for a non–power-law projectile SFD, the R_{crater} is a function of crater diameter, because of factors involving the slope of the size distribution and also the transition from simple to complex craters.

As example of conversion of the lunar chronology to any other planetary body, I report in Fig 4.2.6 the Neukum–derived chronology for Mercury (Neukum et al., 2001b).

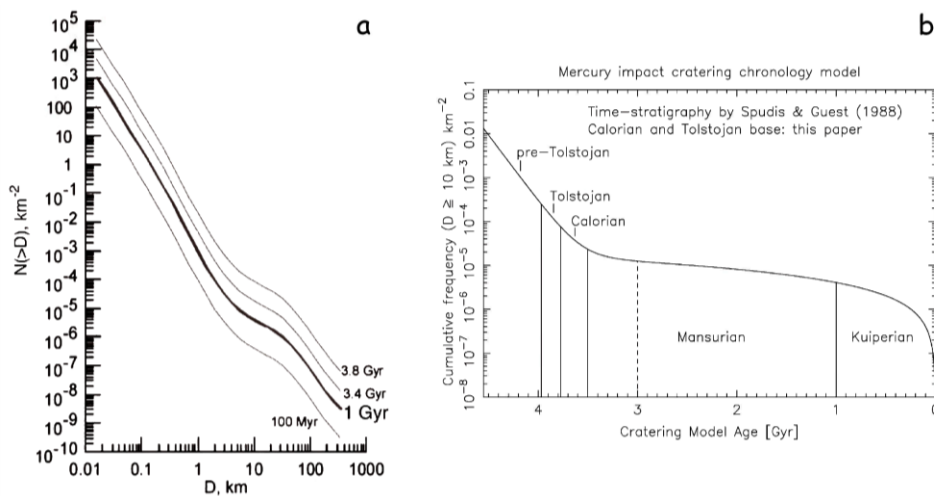


Fig. 4.2.6. (a) Mercury NPF isochrones. (b) Hermean impact cratering chronology model applied to the time-stratigraphic system for Mercury (Spudis & Guest, 1988). From Neukum et al. (2001b).

4.3 Hartmann Production Function

An independent study of production SFD was accomplished by Hartmann (e.g. Hartmann, 1995; Ivanov et al., 2002; Neukum et al., 2001a). Since his first works in analyzing the SD shape by means of the catalog of the measured lunar crater diameters (Hartmann, 1964, 1965), he found convenient the use of the log–incremental SFD with a $\sqrt{2}$ bin size. The *Hartmann Production Function* (HPF) was obtained by least–squares fitting of power–law segments to lunar mare crater data (Hartmann et al., 1981):

$$\log N_H = -3.82 \log D_L - 2.616, \quad D_L < 1.41 \text{ km} \rightarrow \text{steep secondary branch}$$

$$\log N_H = -1.80 \log D_L - 2.920, \quad 1.41 \text{ km} < D_L < 64 \text{ km} \rightarrow \text{primary branch}$$

$$\log N_H = -2.20 \log D_L - 2.198, \quad D_L > 64 \text{ km} \rightarrow \text{turndown branch}$$

After the Ranger probe high–resolution photography of the Moon in the 1960s, researchers soon recognized that these “primary” and “secondary” power–law segments matched those produced during rock fragmentation at lower and higher energies, respectively. In more details, the primary branch was assumed to reflect the size distribution observed in asteroids, which are believed to be mostly fragments of collisional events (e.g. Hartmann, 1964, 1969). On the other hand, the steep slope was interpreted as a mixture of primary impactors from space and secondary craters created by fallback ejecta (e.g. Shoemaker, 1965). By the 1980s, Neukum however concluded that part of the steep secondary branch was originated by debris falling from space, because he found that NPF does exist in space as he observed it on asteroid 951 Gaspra (e.g., Neukum & Ivanov, 1994). This issue (described in more details at § 4.5.1) was a starting point for the comparison between the two production functions, finding a satisfactory agreement of the general shape of both HPF and NPF (e.g., Hartmann, 1999).

Once the shape of the crater SFD being produced on the Moon is known, the deriving crater–based ages are then estimated by means of “isochrons”. A isochron is defined as the total number of craters in function of their sizes that formed on a given surface layer of specific age, and represents the observed crater diameter distribution on that surface if no subsequent process, like erosion or deposition, has modified it (Hartmann, 1999). It was adopted to derive Martian crater retention age (Hartmann, 2005):

1. Starting hypothesis was that the SFD and time dependence of impact flux were the same on Mars as on the Moon: the template curve was the crater SFD measured in the lunar maria, adopting the average age of 3.5 Ga.
2. R_{bolide} ratio at top of Mars atmosphere relative to the Moon was estimated for any specified meteoroid size; the average impact rate ratio R_{bolide} was assumed to remain the same through time, however, individual asteroid breakup events could produce variations in the ratio over short time periods.

3. Corrections for Mars/Moon crater diameter differences were included to take into account impact velocity and gravity scaling, that only at first-order may be considered D -independent.
4. The previous values are used to derive the SFD expected on a hypothetical Martian surface of the same age as the average of the lunar maria.
5. Further corrections are carried out to contemplate the loss of the smallest meteoroids during meteoroid fragmentation in the Martian atmosphere.
6. Using the average value of ~ 3.5 Ga and the measured relation of cratering vs. age from the Moon, the Martian crater density for a span of ages is derived.

As last remark on the Hartmann model, it is noteworthy to mention a recent work regarding a possible variability in the projectile rate (Hartmann et al., 2007). The lunar chronology highlights an intense decreasing cratering rate before 3.5 Gyr, corresponding to the late heavy bombardment, and a constant cratering rate over the last 3 Gyr. However, the impact history can be well constrained only in the time range from ~ 4.0 to 3.2 Gyr, for which Apollo and Luna samples are available (e.g., Neukum et al., 2001a). Synthesis of dates of impact melts in low-thorium non-KREEP lunar meteorites (Cohen et al., 2000, 2005) and of impact-produced glass spherules (Culler et al., 2000) infer a long-term decline in the rate of impacts on the Moon since ~ 3 Gyr ago. This suggestion was supported as well by Quantin et al. (2007) from geological considerations on the surface of Mars regarding landslide activity and more in general resurfacing processes. Fig. 4.3.1 displays the new proposed empirical curve derived for the lunar cratering rate, where a factor of about 3 was proposed to account for the total decline in impact cratering from 2.3 Gyr until today (Hartmann et al., 2007).

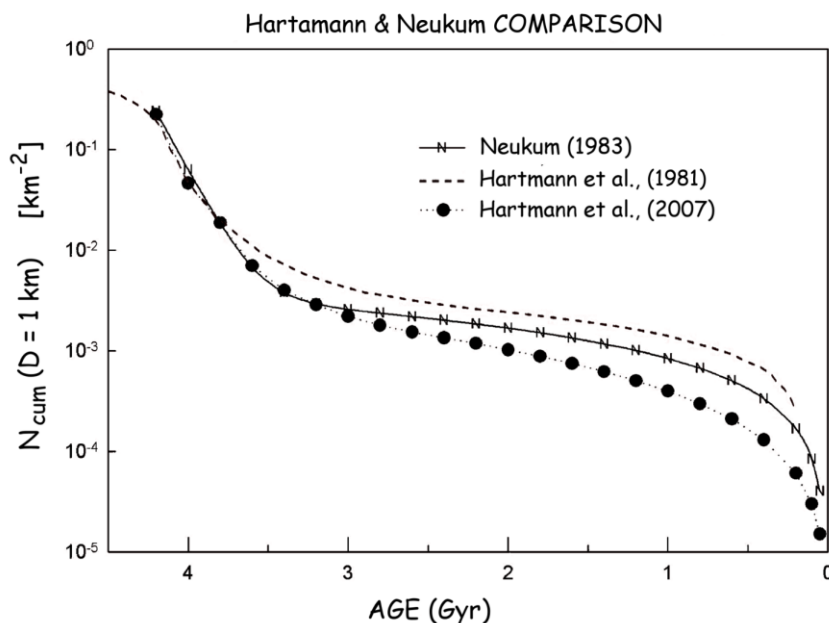


Fig. 4.3.1. Lunar cratering chronology represented as the cumulative crater frequency N at crater diameter $D = 1$ km as a function of the age. The graph shows all the three time dependence equations described in this chapter until now. Modified after Hartmann et al. (2007).

4.4 Model Production Function

Although the Neukum's chronology is not model-dependent because it is based on measured data, this apparent point of strength turns as a weakness, since all the procedure relies on the accuracy of the measurements in multiple overlapping regions, which can be inclined to severe error propagation, especially at large diameters. In addition, in some regions, the cumulative distributions of craters can be altered by surface processes like sporadic magma effusions, ejecta from other craters, etc. (Neukum & Horn, 1976).

In my thesis, the approach of Marchi et al. (2009) was adopted and will be presented in this chapter. *Model Production Function* (MPF) chronology uses dynamical models of both the Main Belt Asteroids (MBAs) and Near Earth Objects (NEOs) (Bottke et al., 2000, 2002a, 2005a, 2005b) to derive the impactor flux, which is then converted via scaling law into the MPF, in turn calibrated using the lunar rocks radiometric ages. Strength points of this model are the implementation of dynamical models, when they are available, to describe the impactors flux on a given planet, the possibility to simulate a non-constant impact flux through time and the geological interpretation of the upper crustal layering of the studied region (e.g., Massironi et al., 2009).

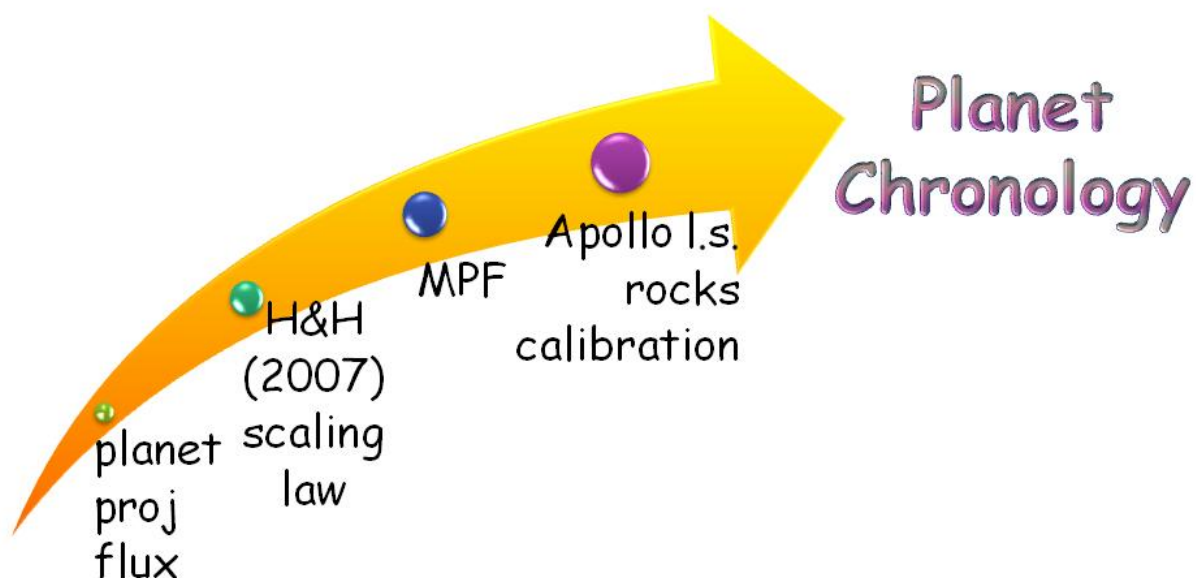


Fig. 4.4.1. Flowchart of the different steps needed to derive the MPF-based chronological model to any given planetary body.

4.4.1 Modelling the Impactor Flux on the Earth-Moon system

The present inner Solar System is continuously reached by a flux of small bodies having sizes smaller than a few tens of kilometers. A fraction of these bodies, i.e. those having perihelion $< 1.3 AU$, are called NEOs. Contributors to this flux are MBAs and Jupiter family comets (JFCs), but numerous studies on the dynamical evolution of these two populations have pointed to MBAs as the main source for the flux presently observed in the inner Solar System (e.g., Morbidelli et al., 2002), therefore the cometary contribution will be neglected in the further analysis. This flux is sustained by a few fast escape tracks, which are continuously replenished with new bodies as a result of collisional processes and semi-major axis mobility. The main gateways to the inner Solar System are the ν_6 secular resonance with Saturn and the 3:1 mean motion resonance with Jupiter (Morbidelli & Gladman 1998; Morbidelli et al., 2002). One of the most recent and accurate model concerning NEOs formation has been developed by Bottke et al. (2000, 2002a), while Bottke et al. (2005a, 2005b) modeled the main belt dynamical evolution. These models have been adopted in order to estimate the properties of the impactor flux at the Moon.

The flux of meteoroids may be described as a differential distribution, $\phi(d, v)$, which represents the number of incoming bodies per unit of impactor size (d) and impact velocity (v). An important quantity is the size distribution of the incoming bodies that is defined as $h(d) \equiv \int \phi(d, v) dv$, so, the meteoroid flux may be described by the following equation:

$$\phi(d, v) = h(d) f(d, v) \quad (4.4.1)$$

where $f(d, v)$ is the distribution of the impact velocities (i.e., the impact probability per unit impact velocity) for any dimension d , and is subjected to the normalization constraint, i.e. $\int f(d, v) dv \equiv 1$.

NEO orbital distribution model of Bottke et al. (2000, 2002a) is used. It was generated by integrating two sets of test particles placed into the ν_6 and 3:1 resonances (with 2×10^6 and 7×10^5 particles, respectively). Each particle is characterized by a calculated impact probability and impact velocity relative to the target body. Following the work of Marchi et al. (2005), Marchi et al. (2009) computed the impact velocity distribution, corrected for the gravitational cross-section of the targets (Fig. 4.4.2). They assumed the Moon to revolve around the Sun with an orbit identical to the Earth's one. Moreover, they corrected the impact probability provided by the Bottke et al. model in order to account for the different collisional lifetime of the particles. This is necessary because the orbital evolution of the particles is coupled with their size through the relationship $\tau \propto \sqrt{d}$ (Farinella et al., 1998; Bottke et al., 2005b), with τ being the particles' collisional lifetime. The meteoroid size distribution for the Earth (h_e) can be written as follows:

$$h_e(d) = P_e h_n(d) \tag{4.4.2}$$

where P_e is the intrinsic collision probability and h_n is the NEO differential size distribution. P_e was assumed to be $2.8 \times 10^{-9} \text{ yr}^{-1}$, after Bottke et al. (2005b), while h_n has been derived from Bottke et al. (2002a), which in turn will be scaled to the Moon and other bodies. If $\Sigma(d)$ is the Earth–Planet ratio of the impact probability as a function of meteoroid size (Marchi et al., 2005), the size distribution for the planet considered becomes:

$$h_p(d) = P_e h_n(d) \Sigma(d) \tag{4.4.3}$$

In Fig. 4.4.3, the previous equation was displayed as a cumulative size–distributions plot, for the Earth, the Moon and Mercury.

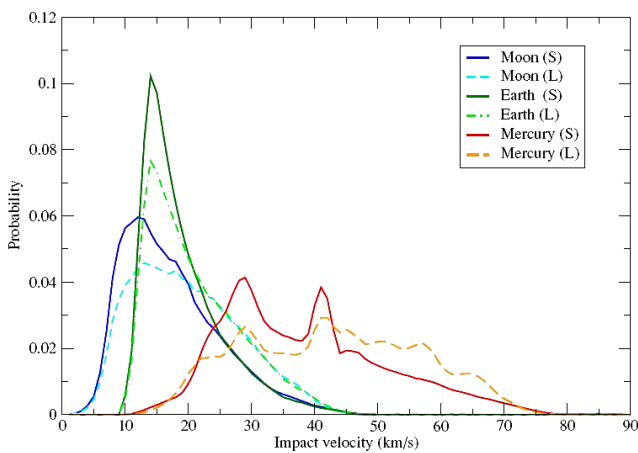


Fig. 4.4.2. Impactor velocity distribution on Earth, Moon and Mercury for different impactor sizes. The smallest (S) and the largest (L) used are 0.1 m and 72 km, respectively. From Marchi et al. (2005).

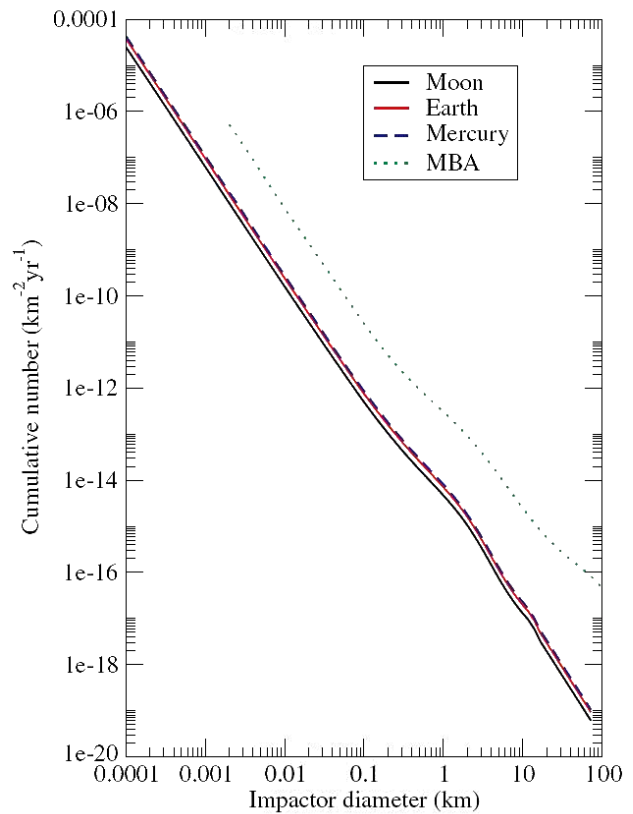


Fig. 4.4.3. Plot of the model cumulative distribution of NEO impactors for Earth, Moon and Mercury. The MBA size distribution is also shown. From Marchi et al. (2009).

4.4.2 Scaling Laws

The next step of the model foresees the introduction of scaling laws. Scaling laws are equations of the kind $D = S(d, v, \vec{p})$, i.e. a function of projectile diameter, velocity and impact angle, and a number of parameters \vec{p} , such as e.g. density, strength, etc. They attempt to describe the outcome of a cratering event based on the impact energy and on the physical properties of both the target and the projectile. Since the physics of crater formation is far to be well understood, several scaling laws have been developed, each of them predicts different results, depending on the way it is extrapolated from laboratory-scale experiments or numerical modelling.

In Marchi et al. (2009), three scaling laws were taken into account. The first one is by Holsapple & Housen (2007) (H&H, hereafter):

$$D = kd \left[\frac{gd}{2v_{\perp}^2} \left(\frac{\rho}{\delta} \right)^{\frac{2v}{\mu}} + \left(\frac{Y}{\rho v_{\perp}^2} \right)^{\frac{2+\mu}{2}} \left(\frac{\rho}{\delta} \right)^{\frac{2(2+\mu)}{\mu}} \right]^{\frac{\mu}{2+\mu}}, \quad (4.4.4)$$

where g is the target gravitational acceleration, v_{\perp} is the perpendicular component of the impactor velocity, δ is the projectile density, and ρ and Y are the density and tensile strength of the target. The quantities k and μ depend on the target material and v on its porosity. H&H estimated these latter parameters by a best-fit over a range of experiments done with different materials. From this study, the values $k = 1.03$ and $\mu = 0.41$ for cohesive soils, and $k = 0.93$, $\mu = 0.55$ for rocks were adopted. Moreover, $v = 0.4$ in all cases (H&H) is used. Eq. (4.4.4) accounts for the transition between strength and gravity regime, allowing a smooth transition between those extreme conditions.

The second scaling law considered is reported by Ivanov et al. (2001) (adapted from Schmidt & Housen, 1987):

$$\frac{D}{d(\delta/\rho)^{0.26}v_{\perp}^{0.55}} = \frac{1.28}{[(D_{sg} + D)g]^{0.28}} \quad (4.4.5)$$

where D_{sg} represents the strength-gravity transition crater. D_{sg} has been set equal to 120 m and 30 m for the Moon and the Earth, respectively (Asphaug et al., 1996).

Finally, the last scaling law considered is by Stuart & Binzel (2004) (adapted from Shoemaker et al., 1990):

$$D = 0.0224 \left(W \frac{\delta}{\rho} \right)^{0.294} \left(\frac{g_e}{g} \right)^{1/6} (\sin \alpha)^{2/3} \quad (4.4.6)$$

where, W is the impactor kinetic energy, g_e is the Earth gravity, and α is the impactor angle with respect to the surface (vertical impacts correspond to $\alpha = \pi/2$). The numerical multiplicative factor takes into account the correction from transient to final crater dimension (Stuart & Binzel, 2004).

The crater size D reported in these formulae should be regarded as the size of the final crater. However, following Pike (1980), a correction for the transition between simple and complex craters was also applied to all the scaling laws in the form of:

$$D = D \quad \text{if } D < D_{sc} \quad (4.4.7)$$

$$D = \frac{D^{1.18}}{D_{sc}^{0.18}} \quad \text{if } D > D_{sc} \quad (4.4.8)$$

where D_{sc} is the diameter of the transition from simple to complex crater. All impacts are assumed to occur at the most probable impact angle, namely, $\pi/4$ with respect to the normal to the surface.

All these scaling laws assume that the density and the strength of the target are constant throughout the body. However, most target bodies are characterized by a layered structure, with a density increasing with depth. Therefore, in order to produce a more realistic picture of the target density, the average density over a depth of about 10 times the radius of the projectile was assumed. This is because the size of the crater is about a factor of 10 larger than the size of the impactor. In particular, Marchi et al. (2009) considered the following lithosphere structure (Anderson, 2007) for the Earth (Fig. 4.4.4): a 2-*km* thick layer of sedimentary rocks, over a granitic upper crust down to 20 *km*, laying above a denser lower crust down to 40 *km*, in turn rising above a peridotitic lithosphere mantle, which is characterized by an upper layer with an average density of 3.2 g cm^{-3} (down to 150 *km*), and a lower layer with a higher density (3.3 g cm^{-3}). On the other hand, for the Moon (Toksöz et al., 1972), a 10-*km* layer of fractured silicates (megaregolith and heavily fractured anorthosite), on top of a bulk anorthosite crust, in turn lying above a peridotitic mantle (Fig. 4.4.4) was assumed. Regarding the strength, the value reported by Asphaug et al. (1996) for bulk silicates, namely, $Y_0 = 2 \times 10^8 \text{ dyne cm}^{-2}$ was used both for the Moon and Earth crusts. However, the authors assumed a linear increase of the strength, from zero at the surface up to Y_0 at the bottom of the heavily fractured layer for the Moon. This assumption was to account for the cohesionless regolith layer on the surface and the underlying megaregolith and anorthosite, which are likely characterized by a progressive decrease in fracture density with depth. A similar assumption was adopted also for the layer of sedimentary rocks on the Earth. The strength at the Earth's surface was set to $0.3 \times 10^8 \text{ dyne cm}^{-2}$.

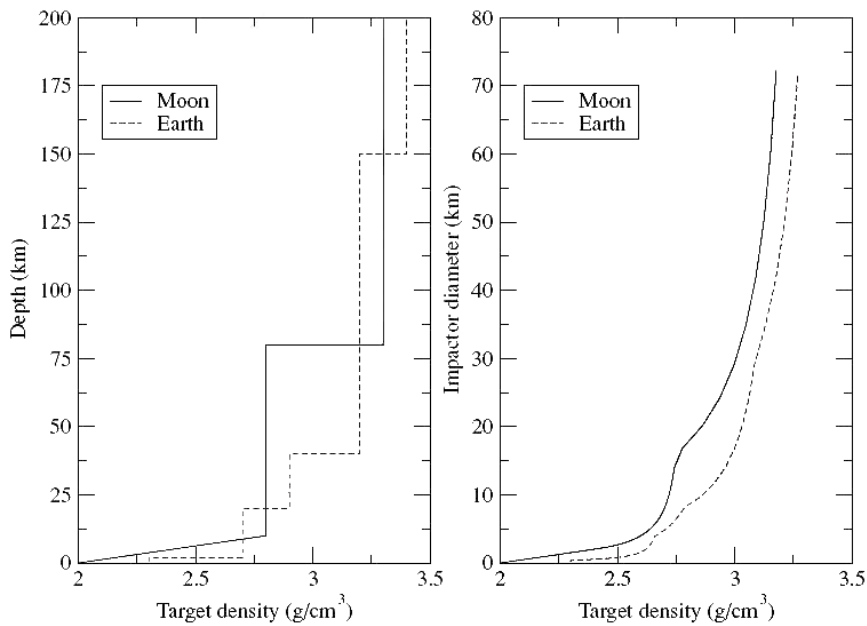


Fig. 4.4.4. Assumed density profiles for the Moon and the Earth. *Left panel:* lunar and terrestrial density profiles vs. depth. *Right panel:* average density vs. impactor size. From Marchi et al. (2009).

Following this description of the Moon crust, its upper layers should be mainly made of highly fractured materials, which behave like cohesive soils. Therefore, a sharp transition was set in the scaling law, from cohesive soil in the case of small impactor to hard rock for larger ones, at a projectile size of $1/20^{\text{th}}$ of the thickness of the heavily fractured silicate layer (i.e., 0.5 km). For the Earth, only the hard rock scaling law was used since only rocky layers had been assumed at the surface.

The impactor density was set to an average value of 2.7 g cm^{-3} (Britt et al., 2002).

4.4.3 MPF distribution

The crater SFD distribution was then derived for any target body, choosing the cumulative representation. If $\Phi(D)$ is the crater differential distribution, the MPF can be expressed as:

$$MPF(D) = \int_D^{\infty} \Phi(\tilde{D}) d\tilde{D}. \quad (4.4.9)$$

and it is represented for the Moon case in Fig. 4.4.5, by taking into account all the three different scaling laws for the conversion from the meteoroid flux to the crater distribution. The NPF curve for the Moon is shown as well for comparison.

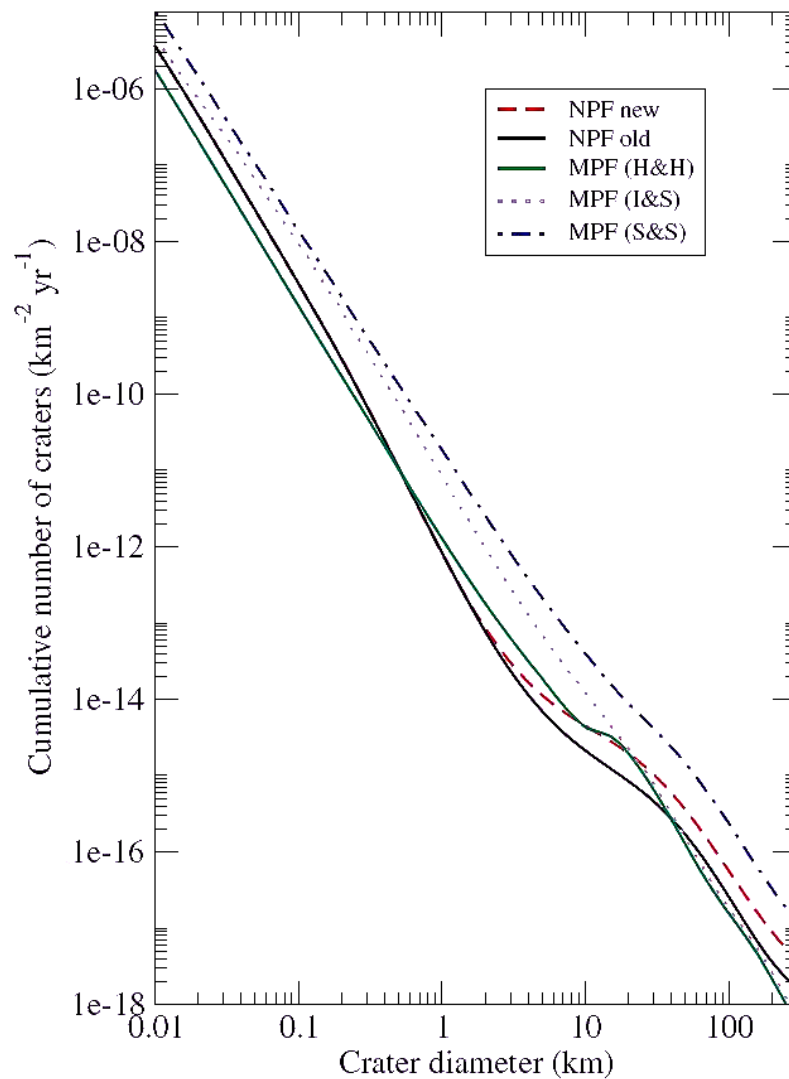


Fig. 4.4.5. Comparison of the MPFs obtained with different scaling laws. Two versions of the NPF are also shown. *From Marchi et al. (2009).*

Different scaling laws produce differences on the MPF as large as a factor of 10 for large craters. The MPF produced with the S&S scaling law is not in good agreement with the NPF throughout the whole size range. The main difference between the H&H and the I&S scaling laws occurs at crater sizes smaller than 10 km. This can be traced back to the choice of using the cohesive soil for small crater sizes in the H&H scaling law, which causes an inflection point in the MPF. This transition in the target's crustal properties produces an S-shaped feature in the MPF, that is present also in the NPF. This finding would suggest that the observed S-shaped feature in the NPF is caused by physical properties of the target, rather than reflecting the shape of the size distribution of the impactors, as proposed by Werner et al. (2002) and Ivanov et al. (2002). Actually, a weak wavy feature in the relevant size range is present in the $h_n(d)$ which, however, is smeared out when passing to the MPF.

From Fig. 4.4.5, one can see that MPF obtained with the H&H scaling law and the NPF are similar within a factor of 2 throughout the whole sizes range considered. The good agreement of the absolute density of craters per year derived from the observations (either the NPF or the HPF) and the MPF with the H&H scaling law suggests that this one is the more appropriate to derive the lunar cratering.

4.4.4 Moon's Chronology

The last step in this model is to employ the MPF as a reference for developing the lunar chronology. For this purpose, literature crater counts from the Apollo and Luna landing sites were calibrated with radiometric ages of rock samples collected in the respective regions. Terrestrial data were included as well in the calibration. A list of the regions used is reported in Tab. 4.4.1.

In order to obtain the lunar chronology, MPF shape was assumed to remain constant over time. For each calibration region, a proportionality factor was determined to obtain the best fit to the data by minimizing the χ^2 . Finally, the crater cumulative number N_l at $D = 1$ km was computed. The fitting procedure used was particularly important, as it directly affected the chronology.

One aspect going after this remark relied on choosing the weights given to the measured data points. In crater counting, the error assigned to each data point corresponds to the square root of the number of counts, under the assumption that the measurements follow a Poisson distribution (see also § 4.1 for the definition of cumulative distribution). However, in the case in which significant systematic effects are present, this procedure yields to underestimate the total error. This problem is more evident when dealing with small craters that are at the limit of the image resolution. Because of their large number, the statistical error for these craters is comparatively small. On the other hand, due to the difficult of

positively identifying craters at limit of the resolution, these measurements could be affected by a significant bias, leading to errors in the N_l values up to a factor of 3–4 in some regions, in turn causing a non-negligible effect on chronology. Marchi et al. (2009) adopted the following weights:

$$\sigma_t^2 = N + \kappa N^2 \quad (4.4.10)$$

where κ was set to 0.5. In this way, the total error (σ_t) for points with very low statistical σ were increased, while those with large statistical error were basically left unchanged.

Region	N_l (NEO) (km^{-2})	N_l (MBA) (km^{-2})	Age (Gyr)
Highlands	7.851×10^{-1}	2.018×10^{-1}	4.35
Nectaris Basin	1.327×10^{-1}	6.648×10^{-2}	3.92
Descartes Formation	2.490×10^{-2}	2.509×10^{-2}	3.92
Imbrium Apennines ^f	1.968×10^{-2}	1.931×10^{-2}	3.85
Fra Mauro Formation	2.595×10^{-2}	2.672×10^{-2}	3.85
Mare Tranquillitatis (old)	1.836×10^{-2}	1.832×10^{-2}	3.80
Taurus Littrow Mare ^e	1.579×10^{-2}	1.585×10^{-2}	3.70
Mare Tranquillitatis (young)	9.300×10^{-3}	9.357×10^{-3}	3.58
Mare Fecunditatis ^e	3.234×10^{-3}	3.257×10^{-3}	3.41
Mare Imbrium ^e	5.468×10^{-3}	5.526×10^{-3}	3.30
Mare Crisium	2.335×10^{-3}	2.377×10^{-3}	3.22
Oceanus Procellarum	3.683×10^{-3}	3.695×10^{-3}	3.15
Copernicus Crater (cont. ejecta)	1.321×10^{-3}	1.337×10^{-3}	0.80
Copernicus Crater (crater floor)	1.348×10^{-3}	1.343×10^{-3}	0.80
Terrestrial Phanerozoic craters	1.267×10^{-3}	7.655×10^{-4}	0.375
Terrestrial Phanerozoic craters (young)	3.835×10^{-4}	2.195×10^{-4}	0.120
Tycho crater (cont. ejecta)	3.391×10^{-4}	3.401×10^{-4}	0.109
Tycho crater (cont. ejecta)	1.644×10^{-4}	1.712×10^{-4}	0.109
North Ray crater	1.389×10^{-4}	1.421×10^{-4}	0.053
Cone Crater	6.970×10^{-5}	7.131×10^{-5}	0.025

Tab. 4.1.1. Description of the lunar and terrestrial calibration regions used in *Marchi et al. (2009)*.

MOON CRATERING

The fitting method was successful for most of the lunar regions considered, pointing out an overall agreement between the shape of the MPF and the data. Some discrepancies occurred for the highlands ($D > 100 \text{ km}$), Mare Crisium and Mare Tranquillitatis. Such discrepancies are imputable to a different shape of the impactor size–distribution in early times in the case of the highlands, whereas to magma flows covering the population of small craters (Boyce et al., 1977; Neukum & Horn, 1976), in the case of both Mare Crisium and Tranquillitatis. Indeed, the absolute radiometric ages derived from A11 samples (Mare Tranquillitatis) span from 3.5 to 3.85 Ga, whereas the ages of the Luna 24 basalts (Mare Crisium) are clustered into at least three different peaks at 2.5, 3.3, 3.6 Ga, respectively (Birck & Allègre, 1978; Stöffler & Ryder, 2001; Fernandes & Burgess, 2005). In the presence of such surface phenomena, the fit must be constrained on the basis of geological considerations, as the automatic fit may be misleading. In particular, as formerly suggested by Neukum & Horn (1976), the crater SFD derived for these regions leads to a composite curve in which smaller craters reflect the younger radiometric ages, while the larger ones correspond to older ages. Thus, for Mare Tranquillitatis, Marchi et al. forced the MPF to overlap the cumulative curve at 0.5 km for the age of 3.55 Gyr (referred to as *young*), and at 0.9 km for the age of 3.72 Gyr (referred to as *old*). Similar considerations hold also for Mare Crisium, where the MPF was fitted to craters with diameters in the range 1–2 km.

EARTH CRATERING

Earth craters hold an important function in cratering studies, since they can be analyzed in details and precisely dated, and so they can be used to further constrain the flux of meteoroids, in particular for young ages, that are scarcely represented in lunar data. In Marchi et al., two data sets of terrestrial craters have been taken into account:

1. all large craters ($D > 20 \text{ km}$) found on the North American and Euroasiatic cratons (Grieve & Dence, 1979), adopting for them an age of 0.375 Ga;
2. a subset of craters with radiometric ages less than 0.12 Ga, attempting to overcome biases due to erosion and burial of craters on the Earth's surface (Grieve, 1993).

Both cumulative distributions were fitted using Earth MPF, and the obtained N_1 was rescaled to the Moon, by implementing the lunar gravitational focusing and a different relationships between impactor and crater size on the two bodies. The resulting values for N_1 are shown in Tab. 4.4.1.

The lunar chronology was hence developed on the basis of the relationship between the derived N_1 values and the absolute ages. The radiometric ages proposed by Stöffler & Ryder (2001) were used. In order to describe the lunar chronology, Neukum (1983) suggested the following approximation:

$$N_1 = a(e^{bt} - 1) + ct \quad (4.4.11)$$

This function assumes a linear relationship between N_1 and the age t for $bt \ll 1$, while an exponential one for $bt \gg 1$. Although this is a rather simple description of the data, it accurately fits the data points in the Neukum chronology. Thus, Marchi et al. fitted this same equation to the MPF-based data points. The result is shown in Fig. 4.4.6. The derived coefficients are:

$$a = 1.23 \times 10^{-15}, b = 7.85, c = 1.30 \times 10^{-3}.$$

For comparison, Neukum & Ivanov (1994) obtained:

$$a = 5.44 \times 10^{-14}, b = 6.93, c = 8.38 \times 10^{-4}.$$

While the derived best fit is in overall agreement with the nominal MPF-based data points, there are some deviations, mainly concerning young data points, which lie systematically above the best-fit curve. It is remarkable that in this chronology, the proposed equation gives good fits for all the points older than Copernicus (which was an outlier in the chronology of Neukum & Ivanov (1994)), while it underestimates by a factor of 2 all the points younger than Copernicus.

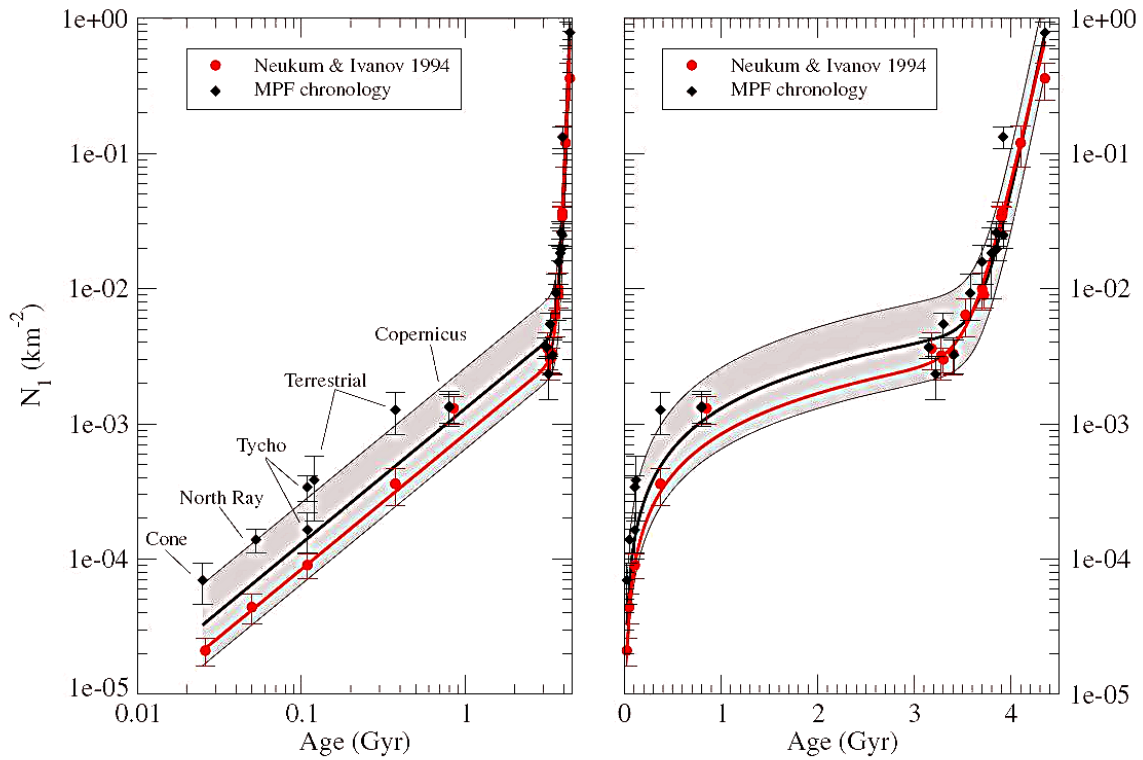


Fig. 4.4.6. Lunar Chronology (solid lines). N_1 values for the calibration regions obtained using MPF and those obtained by Neukum & Ivanov (1994) are also displayed. The shadowed regions encompass a factor of ± 2 around the MPF chronology curve. *From Marchi et al. (2009).*

4.4.5 Mercury's Chronology

The meteoroid size and velocity distributions have been specifically obtained for Mercury (Fig. 4.4.3 and Fig. 4.4.2) (Marchi et al., 2005). As regards the stratigraphy of Mercury, the upper shell is still poorly known (Nimmo, 2002; Nimmo & Watters, 2004). Hence, density and strength profiles are assumed similar to those adopted for the lunar ones (cf. Fig. 4.4.4), whereas the crust–mantle transition at the base of the Hermean elastic lithosphere was instead calculated on the basis of lobate scarp geometries (Watters et al., 2002). Therefore, a 10 km–thick layer of fractured silicates (regolith, megaregolith and heavily fractured silicates) on top of a bulk silicatic crust ($Y_0 = 2 \times 10^8 \text{ dyne cm}^{-2}$; $\rho = 2.8 \text{ g cm}^{-3}$), in turn overlaying a peridotitic mantle ($Y_0 = 3 \times 10^8 \text{ dyne cm}^{-2}$; $\rho = 3.3 \text{ g cm}^{-3}$) which begins at a depth of 40 km. Both strength and density increase linearly in the upper fractured layer, from 0 to $2 \times 10^8 \text{ dyne cm}^{-2}$ and from 2 to 2.8 g cm^{-3} , respectively (Massironi et al., 2009).

The resulting MPF is shown in Fig. 4.4.7, along with the overplot of the NPF for Mercury (Neukum et al., 2001b). The two production functions overlap at the extremes, i.e. $D < 0.3 \text{ km}$ and $D > 40 \text{ km}$. Inside this range, however, the two curves are quite different, with a maximum deviation of nearly a factor of 5 at $D \sim 3 \text{ km}$. The exact behaviour of the MPF in this range depends on the assumptions on the transition in the scaling law between cohesive soil and rock.

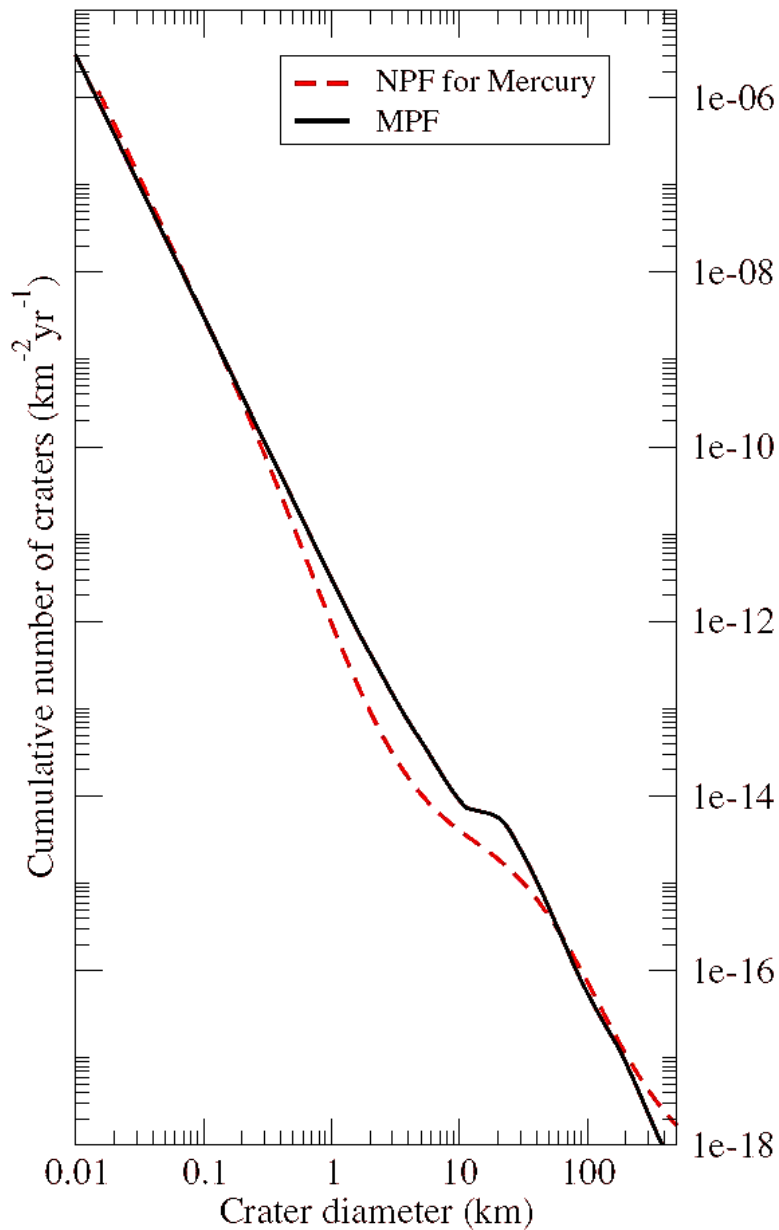


Fig. 4.4.7. MPF for Mercury, in comparison with the NPF. From Marchi et al. (2009).

4.5 Main weaknesses of the model

4.5.1 Secondary craters

An important issue in assessing crater chronology concerns secondary craters. Any production function assumes that the crater population considered is made up of randomly formed craters. However, not all the cratering records meet this condition, as secondary craters are not produced by impactors coming from space.

Secondary craters are produced instead during the early phases of the excavation stage by fallback of ejecta from primaries and hence they appear strongly clustered both in space and time (Melosh, 1989; Wilhelms, 1987). They are observed in any planetary body where impacts take place and gravitational acceleration is sufficient for ejecta blocks to fall back at velocity high enough to form in turn craters. There are environments less conducive to extensive secondary crater population, such as bodies with thick atmospheres that decelerate the ejecta (e.g., Venus, Earth and Titan), or objects with insufficient surface gravity to retain much ejecta (e.g., asteroids), or objects with high resurfacing rates that quickly erase small craters (e.g., Io). Thus, secondary craters result abundant on objects such as the Moon, Mercury and Mars (McEwen & Bierhaus, 2006).

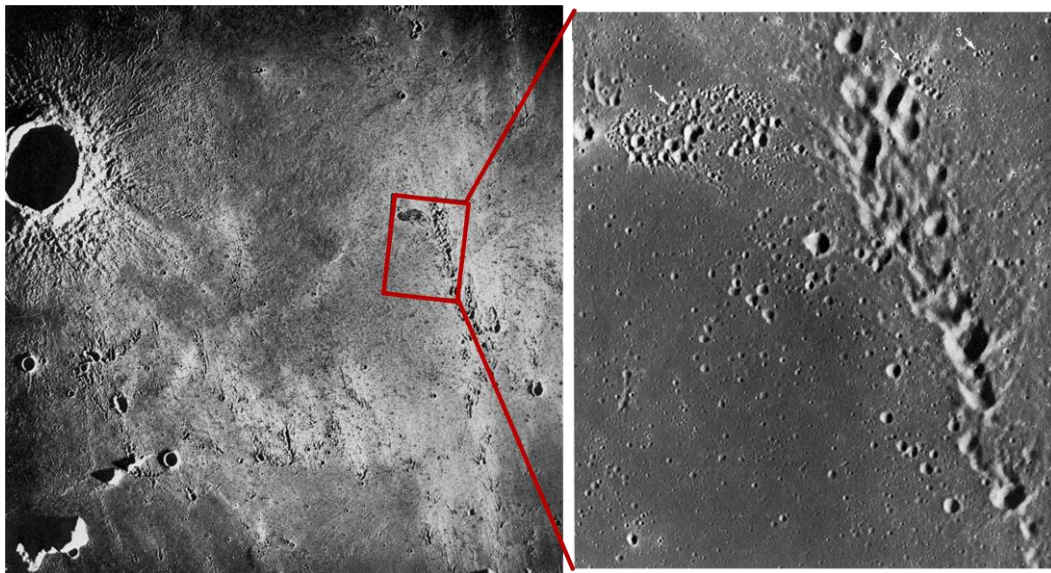


Fig. 4.5.1. (*left*) The photo (AS17-2291(M)) shows the southern area of Mare Imbrium. The large crater is Euler, which is surrounded by a profusion of bright rays and chains of secondary craters from Copernicus, located about 380 km southeast of the center of this picture. (*right*) The photo (AS17-3093(P)) magnified the area in the red box of the *left* one. *Courtesy of NASA.*

Since the earlier studies of lunar crater distributions in the 1960s, the predominance or not of secondaries vs. primaries has become an open question yet unresolved and increasingly debated with time, as the spatial mission to planetary bodies have been returning images at greater spatial resolution.

This issue stands mainly in the possibility to distinguish secondaries from primaries. Secondary craters are usually recognizable for their elliptical shape and shallow profile, and their occurrence in peculiar deposits, like V-shaped ridge pointing radially away from the originating crater, clusters, and chains (referred to as “*herringbone pattern*”) (Fig. 4.5.1) (Oberbeck & Morrison, 1974). However, the distal secondary field is produced by high-velocity ejecta that causes secondaries to be isolated, with a more regular shape and dimensions up to 5% of their parent crater sizes. In this case, they closely resemble smaller primaries, and a definitive distinction between the two population might not be reached.

In the following, I report a brief historical roundup and the state of art regarding the attitude of the different research groups about the origin of small craters. Shoemaker (1965) found that the *primary* crater SFD at small diameters, i.e. $D \leq 1\text{--}2\text{ km}$, displayed a steep slope, about -3 to -4 , that resembled the *secondary* crater SFD measured around large primaries. Shoemaker concluded that craters at that sizes were a mix population of both primaries and secondaries, but dominated by secondary craters especially at smaller sizes. The secondary origin at small scale was then soon widely accepted for craters that were formed close to a primary and that were organized into chains and clusters.

Subsequent studies of the Moon (e.g., Guinness & Arvidson, 1977; Wilhelms et al., 1978), Mars (e.g., Soderblom et al., 1974; Tanaka, 1986; Strom et al., 1992) and Mercury (e.g., Strom et al., 2008) reflected Shoemaker’s interpretation that secondaries dominate the cratering statistics below a crossover diameter (diameter below which secondaries are more abundant), while the influence of far secondaries was remaining controversial.

Recently, some authors have revived the idea proposed by Shoemaker (1965), by analyzing the statistics of small craters on Europa (Bierhaus, 2004; Bierhaus et al., 2001, 2005), Mars (McEwen & Bierhaus, 2006; McEwen et al., 2003, 2005), and the Moon (Dundas & McEwen, 2005). These recent studies showed that a single primary impact may generate $10^6\text{--}10^8$ secondary craters, which contribute to the spatially random population as they extend more than 1000 km from their parent crater. In addition, recent modelling of the excavation process (e.g., Artemieva et al., 2004; Head et al., 2002) supported that a single primary impact can generate tens millions of secondaries.

Bierhaus (2004) and Bierhaus et al. (2001, 2005) pointed out that Voyager and Galileo views show an abundance of small craters on the surface of Europa greater than that expected. Various spatial and clustering analyses, along with size-distribution similarities between clustered and random populations, demonstrated that most of Europa small craters ($> 95\%$) are secondaries (Bierhaus et al., 2005). Because there are so few large craters on Europa, the processes that generate ejecta forming secondary craters must be incredible efficient.

McEwen et al. (2005) reported rays of secondary craters extending as far as 1600 km from the ~10–km crater Zunil, which provides a well-preserved example of a primary crater with enormous numbers of distant secondary craters. A simulation of a Zunil-like impact provided $\sim 10^9$ rock fragments capable of forming distant secondary craters with diameter ≥ 10 m (McEwen et al., 2005; Artemieva, 2005). According to this simulation, ~70% of the craters larger than 10 m form at distances of 800 to 3500 km, whereas most craters larger than 50 m form within 800 km from the primary, in close agreement with results from Preblich et al. (2005). If the secondary crater production of Zunil is not highly unusual, then the total number of small craters on Mars is easily accounted for distant secondaries (e.g., McEwen & Bierhaus, 2006).

Dundas & McEwen (2007) analyzed crater densities in several clusters belonged to the bright ray system of Tycho ($D = 85$ km). The crater Tycho on the Moon produced, in its ray system, almost 10^6 secondary craters with diameter larger than 63 m. Erasure of small craters indicates that this is a strong lower limit, and the original number in these rays may have been much higher, as many as $\sim 10^7$ craters if rays were original saturated. The occurrence of this large number of secondaries suggested to the authors that similar results from Europa and Mars are not simply the product of rare ideal conditions. Instead, the production of many distant secondaries may be a common process for moderately oblique impacts on bodies which have significant mass and lack thick atmospheres. Although these results from Tycho considered only craters occurring in rays, which may be mapped and avoided in age estimates, they demonstrated that large numbers of distant secondaries can form from impact into heavily fragmented targets on which spallation is expected to be less important.

Wells et al. (2010) investigated the secondaries field of Tycho as well. By means of their technique based on radar circular polarization ratio, they found the presence of a ray close to the lunar south pole. This region is not in an obvious optical ray, but the orientation of asymmetric secondary ejecta blankets suggested that they represent an extension of the Tycho crater ray crossing Clavius crater. Because hidden rays may also occur beyond the edges of own optically bright crater rays, it is possible that these distal secondary craters typology is hardly discernible from the surrounding primary population. The authors argue that younger surfaces would be dominated by secondary craters below 1 km if superposed by a hidden ray.

Namiki & Honda (2003) reconsidered different options for the origin of the steep branch on the lunar maria, and concluded that secondaries are likely the major source, because of strong gradients in small-crater density with radial distance from Aristarchus ($D = 40$ km) and Diophantus ($D = 18$ km), extending as far as 15 crater diameters from the primary.

Finally, Bottke et al. (2005b, 2005c), studying the collisional and dynamical history of the MBA, explored whether the majority of small craters ($D < 0.1$ –1 km) on Mercury, the Moon and Mars was produced either by primary or by secondary impacts. Using their NEO model results (Bottke et al., 2005b, 2005c), and data from laboratory experiments and explosion craters (Schmidt & Housen, 1987;

Holsapple & Housen, 2007), they found that primary craters formed by $D \leq 0.1 \text{ km}$ projectiles should produce a differential power-law slope of -4.3 or shallower. This value is $0.5\text{--}0.8$ shallower than the differential slope values estimated from lunar and Martian craters (-4.8 to -5.1 : Ivanov et al. (2002)). Based on such results, they believed that the crater size-distributions on Mercury, Mars, and Moon are dominated by secondaries at small sizes.

The opposite attitude to the secondary craters issue is that small craters, aside from obvious secondaries (Neukum, 1983; Neukum & Wise, 1976), are dominated by primaries and hence the steep branch of the SFD arises from the debris falling from space (e.g., Neukum & Ivanov, 1994).

A support to this theory was inferred from the presence of small craters on asteroids of the MBA, whose surface gravity is so low that material ejected upon an impact will not fall back to the surface to create secondary craters. Crater counts on 951 Gaspra and 243 Ida showed a steep cumulative distribution, that was therefore caused by the preferential impacts of small primary projectiles (Neukum & Ivanov, 1994). On Ida, craters below a diameter of 1 km show a -2 equilibrium distribution, while craters above this size are still in production (Chapman et al., 1996a). The high crater frequency on this asteroid reflects a high surface age, most likely on the order of 2 Ga (Chapman et al., 1996a). On Gaspra, contrarily, the crater frequency is much lower and steep down to the smallest measurable crater sizes, implying a production function on this body and a crater retention age of about 200 Ma , which reflects the time when Gaspra was created by the disruption of a larger parent body (Neukum and Ivanov, 1994; Chapman et al., 1996b).

Furthermore, observations of bolides in the Earth's atmosphere (Ivanov, 2006) and of NEAs SFD responsible for the Earth and the Moon cratering (Werner et al., 2002) stem a primary origin for most small ($1\text{--}100 \text{ m}$) lunar craters. In particular, comparing bolides impact rate and lunar cratering history, Ivanov (2006) found that the currently observed meteoroid flux in the Earth-Moon system is approximately the same as in the last 100 Myr , provided that most of the small ($D < 200 \text{ m}$) craters counted on the young ($\leq 100 \text{ Myr}$) lunar surface are primary and not secondary. He argued that an overall realistic contamination from secondaries is below $25\text{--}50\%$ from the point of view of bolides and cratering rate comparison.

The non-predominance of secondary craters in Martian surface was as well supported. Werner (2006) demonstrated that the age error due to the erroneous count of secondary craters is less than a factor of 2. Hartmann (2005, 2007), Hartmann et al. (2008) and Quantin et al. (2006) inferred that, after excluding all obvious secondary craters, the measured crater distribution might be a homogeneous mixing between primaries and secondaries, and hence these lasts do not significantly affect the age derived from such a count.

A recent work of Head et al. (2010) tested the potentially contamination of secondary crater for Orientale ($D = 930 \text{ km}$), Imbrium ($D \sim 1160 \text{ km}$) and South Pole-Aitken ($D \sim 2500 \text{ km}$). The authors found that, in the case of the Orientale basin, the $N_{\text{cum}}(D \geq 20 \text{ km})$ values for the range between 500 and

1000 km from the rim crest are similar to the $N_{\text{cum}}(D \geq 20 \text{ km})$ values for typical, but not the most densely cratered, highlands. Similar relationships are seen for Imbrium and South Pole–Aitken basins. No annular zones of statistically significant increased crater density are observed, nor do secondaries traceable to these basins appear to contribute a significant number of craters $\geq 20 \text{ km}$ to the crater population of surrounding regions.

4.5.2 A constant flux?

One of the major and mostly debated open issues in planetary chronology is related to the cratering rate in the early times after the formation of the Moon. Arguments have been proposed in favor of a rapid and smooth decrease in the impact rate from the formation of the Moon about 3.5 Gyr ago (Hartmann et al., 1981; Neukum, 1983), followed by a constant impact rate (e.g., Neukum & Ivanov, 1994). On the other hand, studies of impact melts led some researchers (e.g., Ryder, 1990; Stöffler & Ryder, 2001; Cohen et al., 2000) to support the idea of an intense lunar bombardment about 3.9 Gyr ago which lasted some 100–200 Myr. From a dynamical point of view, such a short phase of intense bombardment has been recently explained in the more general context of the early stages of the evolution of the Solar System (Gomes et al., 2005). This scenario has also found some observational evidence in the work of Strom et al. (2005).

Despite these works, the LHB hypothesis has not found a unanimous consensus yet. For instance, Neukum & Ivanov (1994) argued against the LHB on the basis of the smooth behavior of their lunar chronology curve.

If this intense LHB did take place, it should have left some traces in the chronology curve, which therefore could be used to constrain the early stages of the cratering history. Unfortunately, there are only five measured regions having ages older than 3.85 Ga, and therefore it is not easy to draw firm conclusions. One of the most important regions is the Nectaris Basin. Neukum & Ivanov (1994) used a radiometric age of 4.1 Ga. The resulting NPF best fit for the lunar chronology curve is therefore very close to all the old regions and has a smooth behaviour in early times, reflecting a possible smooth decay in the impact rate (Fig. 4.4.6). Marchi et al. (2009) used instead the new estimate of 3.92 Ga for Nectaris Basin (Stöffler & Ryder, 2001), causing this point to move considerably far from the best fit. This finding, which is however based on a NEO distribution not present at the time of LHB, led to a change in the slope of the chronology curve, which in turn is in favor of the LHB.

4.6 Counting S/W

Crater retention age inference relies on the adoption of whatever chronological model to data collected from crater counts performed on geological units of common origin and age. Hence, the starting point in age determination is crater counting.

The standard procedure to collect crater statistical data was outlined in Woronow (1985). He stated that any crater whose center lies within the counting boundaries should be included, regardless of whether a portion of it lies beyond the boundaries or not. Conversely, any crater lying partially within the counting boundaries, but having its center outside the boundary, should be ignored.

Moreover, only primary craters have to be included in the dataset, while all the secondary features have to be avoided, since they are not related to the incoming flux of meteoroid, and hence with “time” (cf. § 4.5.1) (e.g., Neukum & König, 1976). Secondaries are identified as all the craters having one or more of the following characteristics: an elongated shape and being arranged either in a herringbone pattern or in clusters (Oberbeck & Morrison, 1973). Degraded “ghost” features that appear to predate the surface have to be avoided as well, since they had originated before the time span under investigation. Finally, depressions that appear to be volcanic, usually non-circular or in strings along fractures, have to not be included (e.g., Hartmann, 1999).

The first works regarding planetary chronology made use of manual crater detection. Manual counting done by experts can produce highly accurate crater surveys on a given image. Neukum et al. (1975a) and Greeley & Gault (1970) presented craters measurements by using two different facilities: (1) a device for monoscopic measuring on enlargement transparent photographs, and (2) a Zeiss “Stereokomparator” for stereoscopic measurements.

During this last period, many authors have focused their attention on the automation of both crater detection and count in any planetary surface, along with the capability of storing some other characteristics, e.g., crater center coordinates, diameter and depth (e.g., Bruzzone et al., 2004; Sawabe et al., 2006; Michael, 2003). These methods are mostly based in identifying craters as a circular feature on the reference surface. Although this may seem a simplification of the detection problem, the use of a simple model for crater detection allows the algorithms to be applied to data acquired from different sensor. Nevertheless, the procedure is not well-suited for all the conditions of illumination, surface properties and atmospheric state, the presence of false positives, the difficulty in recognition craters when degraded or arranged in overlapping clusters. To this regard, topographic data are taken as well into account to enforce the reliability of automation, by giving some constraints and avoid spurious elements (e.g., Bue and Stepinski, 2007; Michael, 2003), while 3D image data can give much effort to the success of automation in crater counting.

To fulfill the necessity of combining both the human precision obtained with manual counting and the new image formats and computer storage capabilities, I developed a semi-automatic program using

IDL. IDL (Interactive Data Language), under RSI (Research System Inc.), is a complete computing environment for the interactive analysis and visualization of data. IDL integrates a powerful, array-oriented language with numerous mathematical analysis and graphical display techniques. The IDL work environment consists on a Workbench application, that is a graphical front-end providing sophisticated code management, development, and debugging tools (cf. Fig. 4.6.1).

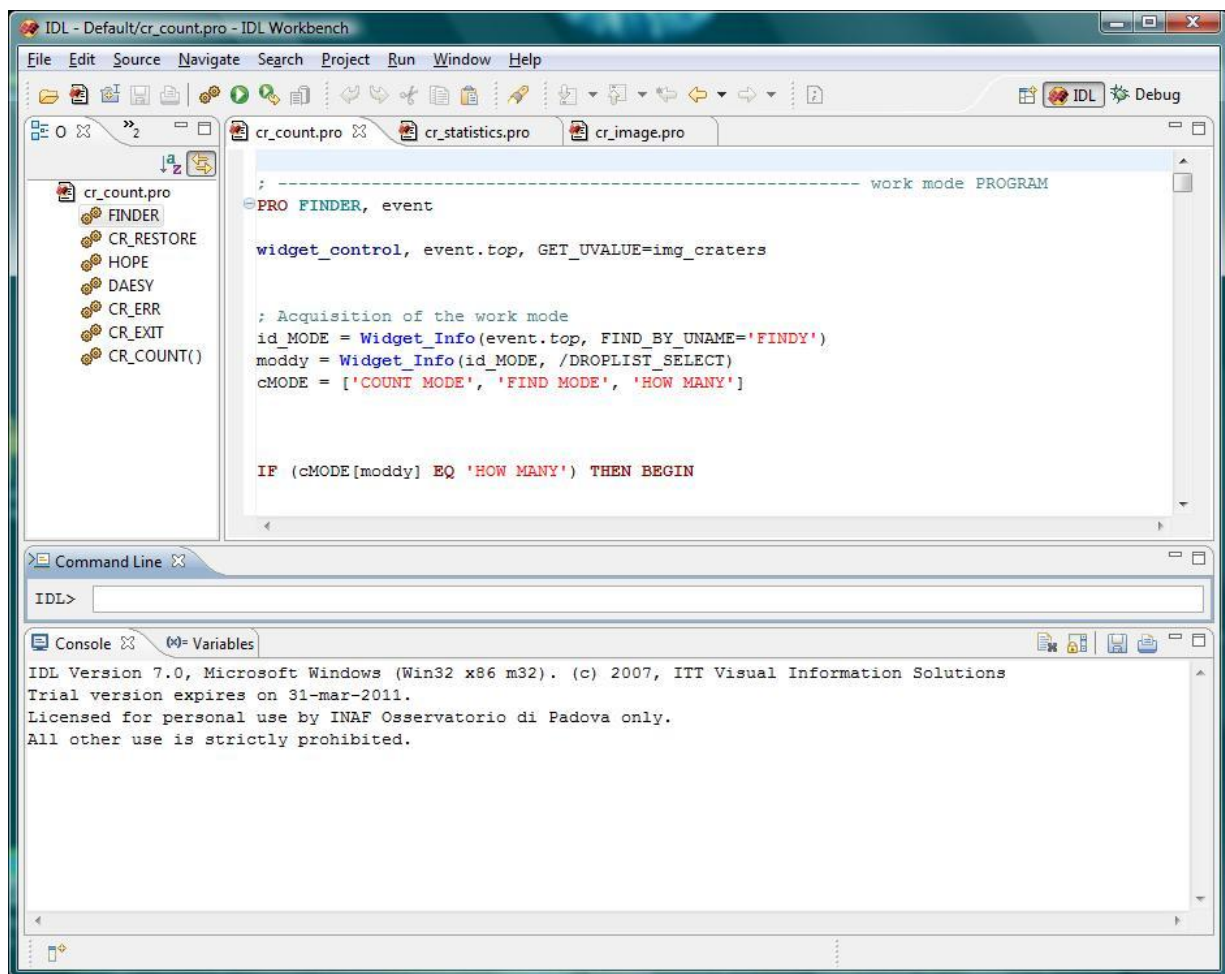


Fig. 4.6.1. IDL Workbench.

The main features, besides the application bar with menu for the opening of commands, are (from top to bottom in Fig. 4.6.1):

1. a project directory containing source code files and other resources, such as e.g., data, image files and documentation, which is useful as logical container for related source code and resource files;
2. an editor where IDL programs are displayed, created ex novo and compiled;
3. a command line to perform ad hoc analyses, compile and launch applications, and create main-level-programs;

4. “views”, that are movable windows inside the IDL Workbench to display data, do analyses, and allow to interact with the command line interpreter and compiled programs (e.g., the command line is placed inside a view);
5. the console view, which displays output from both the IDL command line and compiled programs;
6. the variable view, which displays all the objects in use.

The crater counting software concept relies on marking on the rim of each crater three points, that are used to compute the crater coordinates center and radius of the circle that best fit it, since only one circle pass through three points. By replacing the acquired coordinates in the equation of a circle:

$$x^2 + y^2 + ax + by + c = 0$$

I find a system of three equations in the unknown a , b and c . Once solved this system with the Cramer method, these three variables are used to compute the circle parameters:

$$C = (x_0, y_0) = \left(-\frac{a}{2}; -\frac{b}{2}\right)$$

$$R = \sqrt{\left(-\frac{a}{2}\right)^2 + \left(-\frac{b}{2}\right)^2 - c}$$

The error on diameter is computed from the fact that the stratigraphic uplift defining the crater rim has a finite thickness, 0.6 crater radii (Melosh, 1989).

The realization of this program in IDL was accomplished by the opening of a working window facility (Fig. 4.6.2) with the following features:

1. The working type functionality is selected from a drop list of three options: (1) the “*COUNT MODE*” to perform crater counting, (2) the “*FIND MODE*” mode to retrieve the parameters of a crater already counted when it is selected with the mouse, and (3) “*HOW MANY*” to know the number of craters of a given typology counted up to that moment.
2. The planetary surface selected is displayed, along with the corresponding 2–magnified image to better identify small features; further devices are included to make easier the counting, such as a grid overdrawn both the images and a red point overprinted craters counted. Moreover, the “*TAKE AGAIN*” button was conceived to count again the last crater, if any carelessness yields to errors in the procedure.
3. The “*RESTORE*” button allows to call data of a previous count, allowing to accomplish the counting in different time spans.

4. A second drop list is come in handy to select the typology of the crater marked, i.e. if it is primary, secondary, volcanic, etc.
5. A space of the window is reserved to display the crater characteristics as they are stored in a file.
6. The last button, “EXIT”, saves all the data collected and closes the window.

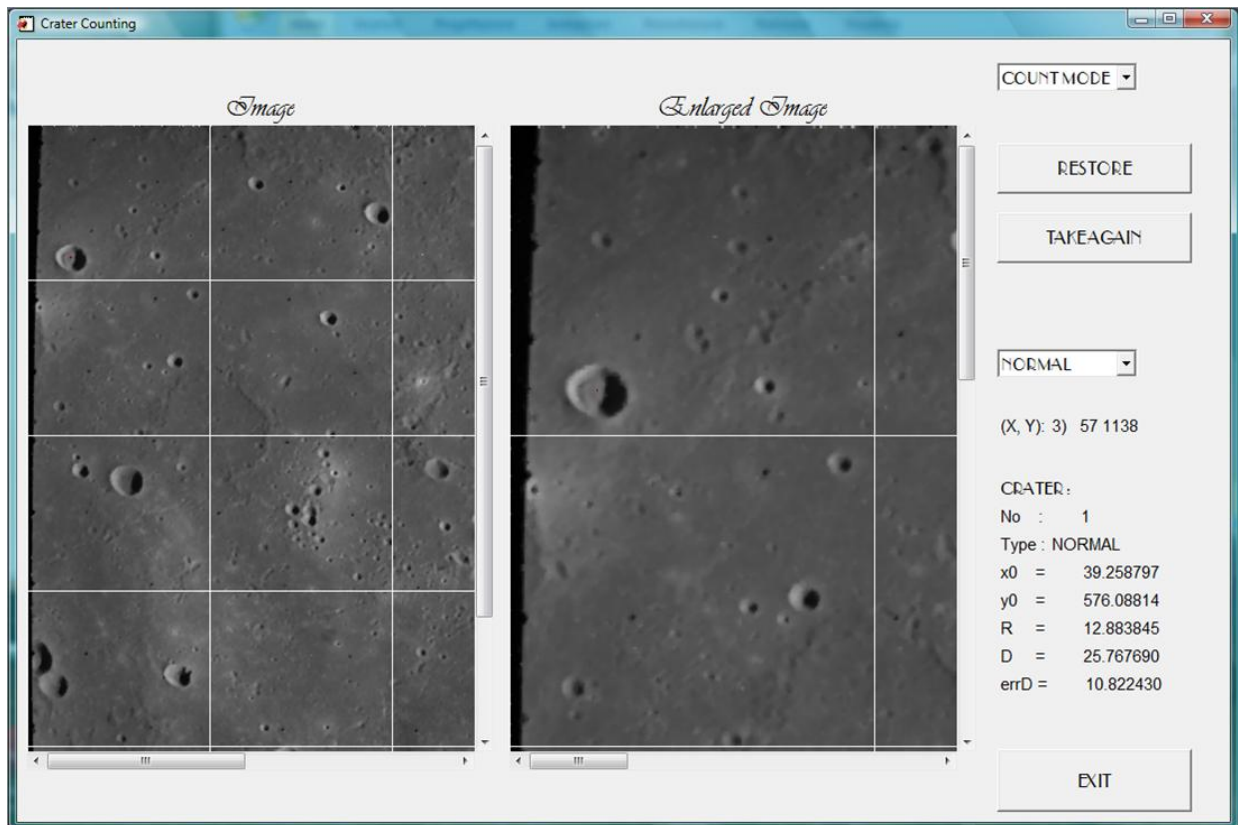


Fig. 4.6.2. Working window facility where crater counting is performed.

At this point, the data have to be organized in a standard representation, i.e. cumulative plot or R-plot (see also § 4.1) (Arvidson et al., 1979), to be of any usefulness in planetary chronology. Hence, a second IDL software has been written to generate both the graphs displaying the data collected. In particular, the mostly used cumulative plot is generated by sorting the obtained crater diameters into 18 bins per diameter decade (i.e., in the interval $1 \leq D \leq 10$ the steps are 1.0, 1.1, 1.2, 1.3, 1.4, 1.5, 1.7, 2.0, 2.5, 3.0, 3.5, 4.0, 4.5, 5.0, 6.0, 7.0, 8.0, 9.0, 10.0: from Hiesinger et al. (2000)), and then finding the total number of all the craters, belonged to a chosen property, larger than or equal to a certain diameter per area measured. An important trick introduced to make the final result more reliable is that only the craters with a minimum diameter value greater than 4 pixels enter the statistics (e.g., Oberst et al., 2008).

Chapter 5

Numerical Modelling

5.1 Introduction to *Hydrocodes*

Impact cratering is a geological process very important for the origin and evolution of the Solar System, planets and their satellites, but even poorly understood up to now (Melosh, 1989). Our understanding of impacts has been advanced through: (1) observational studies of impact craters on Earth and other planets; (2) small-scale laboratory impact experiments and high energy explosions; (3) numerical modelling.

The analysis of the impact craters size–frequency distribution from spacecraft images is of high importance to infer the impact rate and the role of impacting bodies in shaping the planetary surfaces (§ 4). A complementary ground–truth data set on the crater subsurface structures has come from the geologic and geophysical investigation of terrestrial impact craters (e.g., Pierazzo et al., 2008). However, the environmental consequences of meteorite impacts can be understood if the kinetic energy of the body is known, quantity that it is not easy to estimate for a given crater. The few known direct observations of Solar System impact events in recorded history are those of the impact of comet Shoemaker–Levy–9 on Jupiter, the recent Deep Impact cratering of comet Temple I (e.g., Richardson et al., 2005a) and various artificial impactors striking the Moon, such as SMART–1 (e.g., Burchell et al., 2010) and LCROSS (e.g., Korycansky et al., 2009; Schultz et al., 2010).

On the other hand, laboratory experiments can give some insights in the formation process, in particular as regards the influence of the impacting body properties, such as dimensions, velocity, impact angle and material, on the final crater size and morphology. In the past decades, a number of experiments

has been performed to interpret the impact process and the features involved under controlled conditions (e.g., Burchell et al., 2005; Gault & Greeley, 1978; Greeley et al., 1980), and the effect of impact angle and direction on both ejecta blanket evolution and geometry (Gault & Wedekind, 1978), but they could provide only a limited window into the dynamics of impact cratering. These experiments do have limitations as velocities and projectile sizes, which are far to reach the dimensions needed to form the kilometer-sized craters on Solar System (e.g., Holsapple, 1993; Housen & Holsapple, 2003). Similarly, underground nuclear explosions, although extremely valuable in elucidating the principal features of the excavation stage, do not have as well an appropriate scale (e.g., Oberbeck, 1971). In particular, the largest uncertainties regard the crater collapse stage, as it cannot be reproduced in laboratory scale, being gravity and not strength the leading feature (Collins et al., 2004), whereas processes like shock melting and vaporization, which involve extreme pressures and temperatures, are not easily reproduced in tests using conventional explosives or typical laboratory-scale impact experiments. To overcome this problem, many authors performed explosive cratering experiments on a geotechnical centrifuge in order to develop scaling rules for very large energy events, on the basis that a small-scale experiment will correctly reproduce an event n -times larger conducted at n -times the normal gravity level (e.g., Holsapple, 1987; Housen & Holsapple, 2003; Schmidt, 1978, 1980; Schmidt & Holsapple, 1979, 1980; Schmidt & Housen, 1987).

Computer modelling is a powerful complement and extension to laboratory experiments, which on the contrary cannot yet be reliably extrapolated to planetary scales. Numerical modelling of impacts can simulate conditions beyond the reach of experiments (e.g., velocity, size) (Pierazzo & Collins, 2004). In fact, it can investigate in its entirety the complex crater collapse on planetary scale, and the individual effect of any variable in the model, such as porosity or internal friction (Elbeshhausen et al., 2009; Wünnemann et al., 2006), in addition to verify the physics of the process. Although numerical modelling through hydrocodes has reached a high degree of sophistication and validation (Pierazzo et al., 2008), hydrocodes rely on the availability of accurate material models to describe the reaction of the target during impact, so that some authors continue to still prefer laboratory-based experiments (Burchell et al., 2001).

Hydrodynamic computer codes, or *hydrocodes*, are sophisticated computer programs that can be used to simulate numerically highly dynamic events, and in particular handle the propagation of shock waves as well as the behaviour of geologic materials over a broad range of stress states and of deformation rates (Anderson, 1987; Pierazzo et al., 2008). Over the last few decades, rapid improvement of computer capabilities has allowed impact cratering to be modeled with so increasing complexity and realism that also 3D simulations are fulfilled (Pierazzo & Collins, 2004).

To correctly describe the dynamics of continuous media during the impact process, hydrocodes can predict the material's behaviour to internal and external forces on the basis of the Newton's laws of motion, sometimes called the Navier–Stokes equations, and the constitutive equations (e.g., Anderson,

1987; Collins, 2002; Pierazzo et al., 2008). All hydrocodes utilize similar forms of the equations of motion, but material models come in a wide variety of typologies, all addressed to either the material's response in bulk (equation of state) and either the response to the deviatoric deformations (strength) (Pierazzo et al., 2008).

Computer modelling represents the only practical way of solving these equations, but in the meanwhile it is still limited by a finite memory allocation. Thus, the approach adopted by a hydrocode is the *discretization* (e.g., Collins, 2002). This process is based on subdividing the continuous media under investigation into elementary pieces, called *cells*. In this way, the snapshot of the impact event of interest was approximated by a mesh, where cells are usually defined by three or four vertices connected by straight lines to form a triangle or a quadrilateral, respectively.

The implementation of the discretization yields to the choice of the resolution, in space and time, at which a simulation is carried out. On one hand, any simulation should be conducted with a high enough resolution to resolve all the important flow variations both in space and time. On the other hand, this requirement has to be balanced by the available computer power and the time needed to complete the simulation (e.g., Pierazzo & Collins, 2004). In particular, both computer storage and simulation time have a strong dependence on the number of cells, the dimensionality of the hydrocode and the number of time-steps adopted. However, to avoid integration instabilities, the computational time-step Δt is chosen to satisfy the *Courant-Friedrichs-Lewy stability condition* (Anderson, 1987). It states that no signal can propagate across the shortest dimension of a cell in one time-step. This implies that the number of time-steps will be proportional to the number of cells. Hence, if N is the number of cells in each mesh dimension, d the number of dimensions and M the number of time-steps, the computer storage needed for a simulation is proportional to N^d , whereas the simulation run time is approximately proportional to $N^d \times M \sim N^{d+1}$ (Pierazzo & Collins, 2004).

A further concern regarding the implementation of a discretization to represent the impact event consists on the instabilities introduced by the “discontinuous” nature proper of shock waves. To stabilize the process, an *artificial viscosity* is introduced as a dissipative mechanism able to spread the shock over a few cells.

Once further feature has to be set before a simulation can run, that is the choice of the approach used to describe the event (Fig. 5.1.1), i.e. a coordinate system fixed in space (Fig. 5.1.2a) or one moving with the material (Fig. 5.1.2b) (cf. Tab. 5.1.1) (e.g., Anderson, 1987).

The *Eulerian* formulation (Fig. 5.1.2a) (e.g., Anderson, 1987) corresponds to the spatial description. It relies on material flowing through the mesh, which remains fixed with time and must define the entire space in which the event is contained. Mass, momentum and energy flow across cell boundaries. The quantities of flow into and out of a cell are used to compute the new mass, pressure, velocity, energy, etc., of that cell. In this formulation, the cell volume is an invariant since points remain fixed in space, while density may change as a consequence of changes in cell's mass.

The major limitation of this approach regards the fact that material interfaces are not totally well established at all times during the impact computation. This leads to the introduction of mixed cells of multiple materials, containing the average of state variables in single materials, which have undergone advection. As a consequence, the accuracy in the determination of material interfaces and free surfaces depends on the resolution of the mesh: the finer the mesh, the more accurately the boundary is represented. Moreover, as the material moving through the mesh will only partially occupy some cells, the free surface cannot be tracked exactly, yielding to problems regarding the definition of some features, e.g. the viscosity (Pierazzo & Collins, 2004).

The *Lagrangian* formulation (Fig. 5.1.2b) (e.g., Anderson, 1987) corresponds to the material description. The grid points are attached to the material and hence move with the local material velocity with respect to a fixed spatial coordinate system. As time progresses, all the variables of interest, as velocity, pressure, density, temperature, etc., are computed for each discrete point in the continuum. Cells defined by adjacent vertices become deformed in shape and size due to the forces acting on them and the constitutive relations between force and deformation. Mass, momentum and energy are transported by material flow. In this formulation, mass within a cell is an invariant, while density may change as a consequence of changes in cell's volume, i.e. expansion or compression.

This approach, computationally more efficient, allows both free surfaces and contact surfaces between different materials to remain distinct throughout all the calculation. The major limitation of the Lagrangian approach is the inaccuracy of the finite approximation when the cells are significantly distorted, as cells can even fold over themselves. This problem can be resolved by rezoning the old distorted computational grid with a new undistorted one, but on the other hand it is a time-consuming process, not needed in the Eulerian approach (Pierazzo & Collins, 2004).

A hybrid method is the *arbitrary Lagrange–Eulerian (ALE)* approach. It foresees the computation to remain Lagrangian until some condition is met, at which point the material is allowed to advect, while the mesh is transformed dynamically according to user defined rules. Here, Eulerian refers to the advection process; the mesh is not necessarily fixed over the duration of the simulation. This approach allows better tracking of interfaces without the cell distortion problem (Pierazzo et al., 2008).

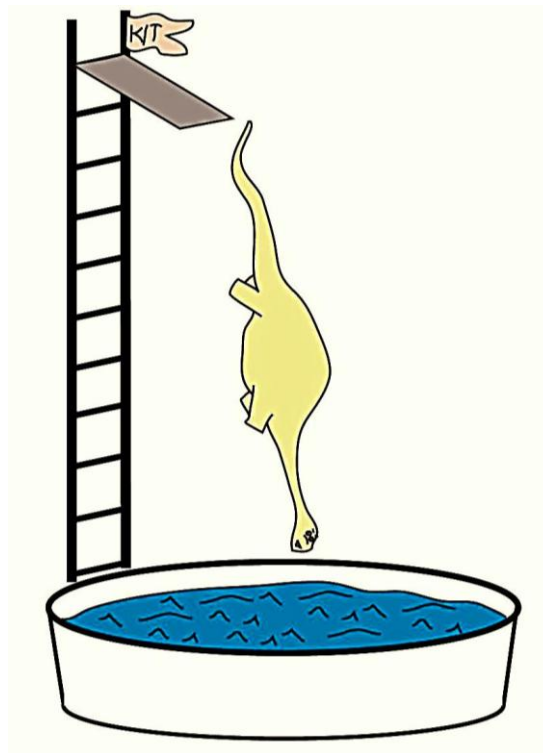


Fig. 5.1.1. Illustration of the dinosaur diving from the K/T diving board, as example of “impact event”. From Collins (2002).

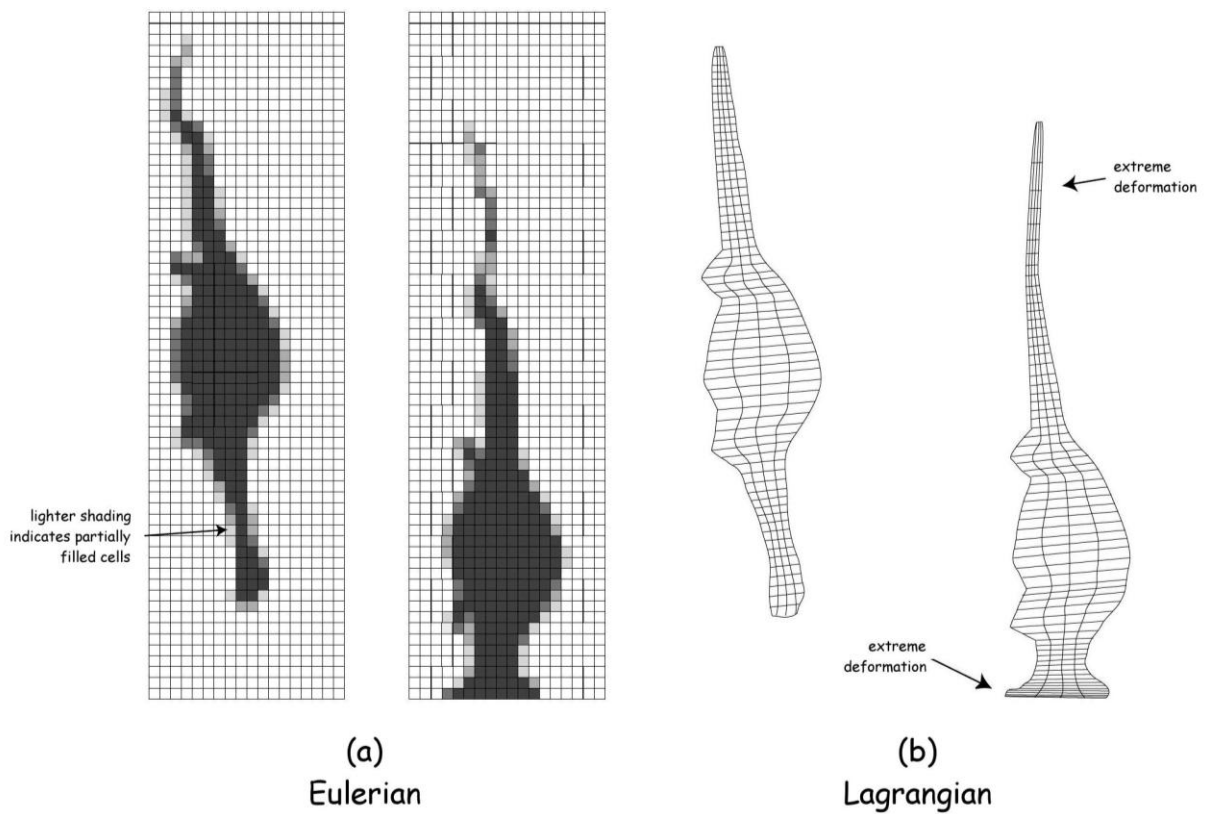


Fig. 5.1.2. Eulerian (a) and Lagrangian (b) descriptions used in hydrocodes to represent the dinosaur diving from the K/T diving board. From Collins (2002).

Eulerian	Lagrangian
<ul style="list-style-type: none"> ☒ material flows through a static mesh 	<ul style="list-style-type: none"> ☒ cells follow the material
<ul style="list-style-type: none"> ☒ cell volume is constant 	<ul style="list-style-type: none"> ☒ the mesh itself moves ☒ cell volume changes
<ul style="list-style-type: none"> ☒ cell mass changes with time 	<ul style="list-style-type: none"> ☒ cell mass is constant
<ul style="list-style-type: none"> ⊙ time evolution limited only by total mesh size 	<ul style="list-style-type: none"> ⊙ free surfaces and interfaces are well defined
<ul style="list-style-type: none"> ✗ material interfaces are blurred 	<ul style="list-style-type: none"> ✗ mesh distortion can end the simulation very early

Tab. 5.1.1. Comparison between the Eulerian and Lagrangian descriptions.

The impact event can be then simulated, as already noticed, through the equations of motion and the constitutive models.

The differential equations of motion (Collins, 2002) are established through the application of the principles of conservation of mass, momentum and energy from a macroscopic point of view. If a Lagrangian approach is set, they are formulated by relating the material density ρ , the velocity v_i , the specific internal energy E , the stress tensor σ_{ij} , which is composed of a hydrostatic component, the pressure p , the deviatoric stress Π_{ij} , the external body forces per unit mass f_i and the deviatoric strain rate $\dot{\epsilon}'_{ij}$:

$$\begin{aligned}
 \text{Conservation of Momentum} \quad & \frac{Dv_i}{Dt} = f_i + \frac{1}{\rho} \frac{\partial \sigma_{ji}}{\partial x_j} \\
 \text{Conservation of Mass} \quad & \frac{D\rho}{Dt} + \rho \frac{\partial v_i}{\partial x_i} = 0 \\
 \text{Conservation of Energy} \quad & \frac{DE}{Dt} = -\frac{p}{\rho} \frac{\partial v_i}{\partial x_i} + \frac{1}{\rho} \Pi_{ij} \dot{\epsilon}'_{ij}
 \end{aligned}$$

As noticed, the complete representation of a material's response to stress requires the conservation equations to be accompanied by other relations that accounts for the specific material properties governing the response of materials for nominally the same impact conditions. These relations consist of an equation of state and a constitutive model (e.g., Anderson, 1987).

The equation of state (EoS) (e.g., Collins, 2002; Pierazzo et al., 2008), which is characteristic for a given material, describes its thermodynamic state over a wide range of pressures, internal energies and densities, and is mathematically expressed by:

$$\textit{Equation of State} \quad p = p(\rho, E)$$

where p is the pressure, ρ the density and E the specific internal energy.

The EoS relates a material's instantaneous pressure, mass density and internal energy, and usually temperature and entropy. In addition, it defines compressibility, thermal expansion, wave speeds and other thermodynamic properties, and may also include descriptions of phase changes such as solid–solid, melt and vaporization.

Whereas the equation of state is important to describe the material's response during the early stages of the impact, when stresses are very large compared to yield stress, the strength models are critical for the modelling of the late stages of impact cratering, when material strength determines the final shape and characteristics of the crater (e.g., Anderson, 1987).

Strength, or rheologic, model is a set of equations that approximates the behaviour of a given material when subjected to stresses, which induce deviatoric deformations or changes of shape. They can be mathematically formulated as a relation between stresses σ_{ij} and a combination of strain ϵ_{ij} , strain rate effects $\dot{\epsilon}_{ij}$, internal energy E and damage D characteristics of the material in hand (Collins, 2002):

$$\textit{Constitutive Model} \quad \sigma_{ij} = g(\epsilon_{ij}, \dot{\epsilon}_{ij}, E, D)$$

The typical constitutive model used in hydrocodes, when simulating the early stages of an impact event, is elastic–perfectly plastic; that is, the material loads elastically to the yield stress and then it begins to permanently deform plastically. However, for a correct interpretation of the late stages of the impact process, the complicated rheology of the post–shock target, including heating, fracturing, shaking and deformation, had to be considered (Pierazzo & Collins, 2004).

The critical stress at which permanent deformation occurs in a given material is defined as the strength, whose value depends on the orientation of the applied stress, i.e., compression, tension or shear (Holsapple, 2009; Jaeger et al., 2007). In particular, the yield strength, which is the stress at the onset of failure, is a function of damage, confining pressure, temperature and strain rate.

At pressures and temperatures below the melting point, intact rocks have a finite yield strength, termed cohesion, and a tensile strength. However, rocks are usually fractured via faulting or fragmentation due to the activation, growth and coalescence of pre–existing cracks and flaws. Those processes are often modeled using a strain–rate dependent model such as the Grady-Kipp model. Those

processes and their modelling often introduce phenomena of bulking (increased volume during fracture growth) and a degraded ability to withstand stress. The degradation of strength is often characterized by a damage parameter D which varies from zero (intact) to one (fully damaged, no tensile strength).

Hence, geological materials are described by a mass of irregular debris blocks (e.g., Stesky et al., 1974), whose strength depends upon the strength of the intact blocks and their freedom of movement (Hoek, 1983). The freedom of movement depends on the number, orientation, shear strength and spacing of the surfaces separating the blocks, which may or may not be coated with weaker material (Hoek, 1983).

Hence, as regards fragmented rocks, yield strength is approximately linearly proportional through the coefficient of friction to the confining pressure (Byerlee, 1978), whereas in absence of overburden pressure, fragmented rock materials have no strength (Collins et al., 2004). As pressures increase, the yield strength of intact rocks rises. As the local slope of the yield curve in function of pressure, called coefficient of internal friction, declines with increasing confining pressure (Lundborg, 1968), the yield strength asymptotically approaches a constant value called the von Mises plastic limit (Collins et al., 2004).

On the other hand, as temperatures increase to the melting point value, the strength of both intact and fragmented rocks drops down, declining steadily to zero (e.g., Collins et al., 2004). In effect, the cohesion and the coefficient of friction are reduced by increasing temperature.

Thermal effects on strength are often included by multiplying the yield strength at a given reference temperature by a function of internal energy, which decreases monotonically from one at the reference temperature to zero at one chosen “melt” energy (Pierazzo et al., 2008).

5.2 iSALE hydrocode

iSALE — *impact*–SALE — is a multi–material, multi–rheology shock physics code, based on the SALE hydrocode, i.e. Simplified Arbitrary Lagrangian Eulerian.

The original code was developed by Amsden et al. (1980) for simulating single–material Newtonian–fluid flow, by using either, or a combination, of the Lagrangian and Eulerian descriptions (e.g., Collins, 2002), but since the 1990s, it has been modified to include extensions, correction and enhancements, giving rise to a “family” (e.g., Wünnemann et al., 2006) of SALE extensions.

The first extended release was SALEB, a simple versatile hydrocode, capable of simulating impact events from the first contact of the impactor with the target, to cessation of the final gravity driven collapse of the craters (e.g., Ivanov, 2005; Ivanov & Artemieva, 2002). Melosh et al. (1992) implemented an elasto–plastic constitutive model in tandem with the viscous model, and incorporated the Grady–Kipp fragmentation algorithm and several equations of state for impacts, including the Tillotson equation of state (Tillotson, 1962). Ivanov et al. (1997) advanced the underlying solution algorithm by incorporating free–surface and material–interface tracking in Eulerian mode, improved the constitutive model by incorporating damage accumulation and strain–weakening, and implemented into the code the semi–analytical equation of state ANEOS (Thompson and Lauson, 1972).

A second release was SALES-2, in which Melosh’s Lagrangian version of the original SALE was improved to include a wider range of possible rheological models (Collins et al., 2002).

A further release was iSALE. The major improvements of this version were significant changes to the code needed to perform simulations in pure Eulerian mode (Wünnemann & Lange, 2002), the introduction of a third target material (Wünnemann & Ivanov, 2003; Wünnemann et al., 2005), refinements to the constitutive model (Collins et al., 2004) and the incorporation of the ϵ –alpha model porous–compaction model (Wünnemann et al., 2006). More recently, a routine has been added to construct a self–consistent central gravity field for simulation of giant impacts onto spherical planetary bodies (Davison et al., 2010).

At the same time, a three–dimensional version of iSALE, i.e. iSALE–3D (Elbeshausen et al., 2009), has been developed from the original SALE–3D code (Amsden & Ruppel, 1981), including all the capabilities introduced for the 2D version, as well as the incorporation of custom made in–memory compression routines for efficient data output and access (Schmalzl, 2003).

The code is well tested against laboratory experiments at low and high strain–rates (Wünnemann et al., 2006) and other hydrocodes (Pierazzo et al., 2008). It has also been used in the previous numerical simulation of several terrestrial impacts (*Chicxulub*: Collins et al., 2002, 2008a; *Chesapeake Bay*: Collins & Wünnemann, 2005; *Ries*: Wünnemann et al., 2005; *Haughton*: Collins et al., 2008b; *Sierra Madera*: Goldin et al., 2006).

5.2.1 Discretization

Discretization, as already stated, is the basis of all shock codes, accounting for the computer finite memory allocation.

Cell (Fig. 5.2.1a) is the elementary element storing the scalar impact-related parameters, such as mass, energy and density, which remain constant within the cell in hand, whereas, vector quantities as velocity are assigned to the cell vertices (nodes) (e.g., Bray, 2009).

Internal and external forces, like gravity, pressure stress, etc., are applied to each node of the cell considered over a time-step, at the end of which the magnitude and direction of the resultant acceleration are calculated (Fig. 5.2.1b). However, when adopting a purely Lagrangian description, extreme deformation may occur, leading to spurious results (such as negative volumes) and the simulation is forced to stop. To avoid these complications, iSALE incorporates an optional second step in which the cell properties at the end of each time-step are remapped back to an undistorted mesh by *advecting* the “overlap” material into adjacent cell (Fig. 5.2.1c) (e.g., Bray, 2009).

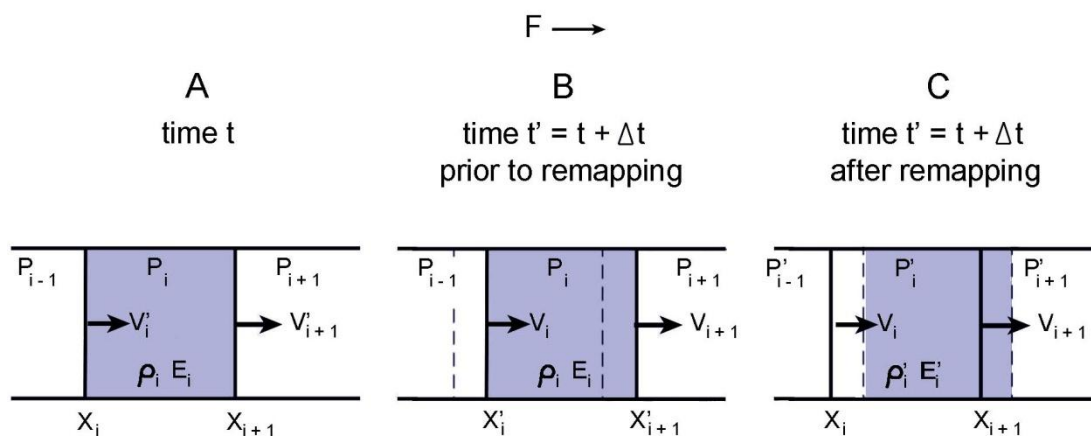


Fig. 5.2.1: Schematic illustration of a 1D hydrocode computation. From Bray (2009).

(A) At time t , a mesh cell i (shaded) with solid-lines boundaries is considered. Position (x) and velocity (V) are defined at the cell vertices, while mass, internal energy (E) and density (ρ) are assigned to the center of the cell. Density is calculated from the mass within the cell as the volume is constant. The pressure is calculated from the density and internal energy using an equation of state of the form $P(\rho, E)$.

(B) The codes advances from time t to $t+\Delta t$ as a result of the application of the net force F on each vertex. The new velocity V' is computing from acceleration of the vertices, in turn obtained by using the Newton's laws of motion. The momentum at both vertices is averaged to calculate a cell-centered momentum.

(C) To avoid accumulated cell distortion, the cell-centered properties are remapped back to an undistorted mesh by transferring the ‘overlap’ material and its properties to the appropriate adjacent cell. The new mass, density ρ' , internal energy E' and pressure P' are calculated and assigned, ready for the beginning of the new time-step. The remapped vertex velocities are updated according to the new cell-centered momenta.

5.2.2 Equations of State

The equation of state closes the system of equations of motion for a continuous medium, by relating pressure P to material density ρ and internal energy E located in each cell of the computational grid at a given time t . iSALE supports two EoS types: parameters defining the Tillotson analytical EoS and data tables produced by ANEOS (e.g., Ivanov, 2005).

The *Tillotson EoS* for high-speed impact computations was conceived to reproduce a wide range of pressures and densities. It duplicates the linear shock-particle velocity relation at low pressures while approaches the Thomas-Fermi limit at high (infinite limit) pressures. This equation of state also includes parameters that allow it to describe the unloading of shocked material into the vapor phase (Tillotson, 1962; Ahrens & O'Keefe, 1977).

The Tillotson EoS takes different formulations according to whether the material experiences compression, to higher density than its zero-pressure form ($\rho/\rho_0 \geq 1$), or expansion, to lower density ($\rho/\rho_0 \leq 1$), accounting also for the value of internal energy with respect to the vaporization state, i.e. incipient ($E < E_{iv}$), partial ($E_{iv} < E < E_{cv}$) or complete ($E > E_{cv}$):

$$\frac{\rho}{\rho_0} \geq 1 \quad E < E_{iv} \quad P = \left[a + \frac{b}{E/(E_0\eta^2) + 1} \right] \rho E + A\mu + B\mu^2 \quad (5.2.1)$$

$$\frac{\rho}{\rho_0} \leq 1 \quad \begin{cases} E_{iv} < E < E_{cv} & P = a\rho E + \left[\frac{b\rho E}{E/(E_0\eta^2) + 1} + A\mu e^{-\beta(\rho_0/\rho-1)} \right] e^{-\alpha(\rho_0/\rho-1)^2} \\ E > E_{cv} & P = \frac{(E - E_{iv})P_E + (E_{cv} - E)P_C}{(E_{cv} - E_{iv})} \end{cases} \quad (5.2.2)$$

where:

- P = the pressure
- E = the density energy
- $\eta = \frac{\rho}{\rho_0}$, with ρ_0 and ρ the initial and final densities, respectively
- $\mu = \eta - 1$
- $V = \frac{1}{\rho}$ = the specific volume
- a, b, A, B, E_0 are the empirically-derived Tillotson parameters, specific for each material
- α, β are constants that control the rate of convergence of the equation, and are included to the perfect gas law.

Eq. (5.2.1) describes the state of a material undergoing compression and for cold expanded states where the energy density is less than the energy of incipient vaporization E_{iv} . On the other hand, rapid expansion causes partial vaporization of the material if its internal energy exceeds the energy required for

vaporization to begin (E_{iv}). The extent of vaporization depends on the internal energy E , relative to the E_{iv} and the energy of complete vaporization E_{cv} . The expansion of cold ($E < E_{iv}$), partially vaporized ($E_{iv} < E < E_{cv}$) and entirely vaporized ($E > E_{cv}$) materials is considered separately, employing respectively Eq. (5.2.1), Eq. (5.2.2) and Eq. (5.2.3).

Tillotson EoS provides good results for metals and for some relatively simple rock types where solid state phase modifications are negligible (e.g., Weiss & Wünnemann, 2007). However, it provides no information about how to compute the temperature or the entropy of a material and is unable to model melting and vaporization (Pierazzo et al., 2008).

More recent trend in equations of state is toward the use of increasingly complex computer codes to generate an equation of state that relies on different physical approximations in different domains of validity. One of the best such equations of state is the ANalytical Equation Of State (ANEOS) (Thompson, 1970; Thompson & Lauson, 1972), that is a thermodynamically consistent analytic equation of state package used by various shock codes, iSALE included.

The ANEOS, once input data are known for the material in hand, is used to prepare tables and to describe the material pressure and temperature vs. density and internal energy in a wide range of both parameters (Ivanov & Artemieva, 2002).

One major advantage of this code over the Tillotson EoS is that, in ANEOS, pressures, temperatures and densities are derived from the Helmholtz free energy and are, hence, thermodynamically consistent. Explicit treatment of melt and vapor is included. Although clearly superior to prior analytical equations of state, the original ANEOS has several limitations, such as the treatment of gases as monoatomic species, which causes it to overestimate the liquid–vapor phase curve and the critical point of most complex materials. In addition, it treats high–pressure phase transitions as a modification of only the cold part of the Helmholtz free energy (Thompson & Lauson, 1972), whereas the low– and high–pressure phases depend on temperature in the same way. This implies that the pressure at which phase transition occurs depends only weakly on temperature, behaviour that is instead not observed (e.g., Melosh, 2007). The nearly fixed–pressure phase transformation also prevents ANEOS from reliably locating the liquid/solid phase boundary, implying that the liquid and solid states cannot be distinguished when a high–pressure phase transformation is introduced, and hence that the latent heat of melting cannot be accounted for.

Since the representation of liquid/solid phase transition in ANEOS is problematic, iSALE was implemented with the Simon equation (e.g., Poirier, 1994) to determine the melt temperature T_m as a function of pressure:

$$T_m = T_0 \left(\frac{P}{a} + 1 \right)^{1/c}$$

where T_0 is the melt temperature at normal pressure, while a and c are material constants.

5.2.3 Materials Models

Rheological models describe material response to stress or deformation and are fundamental for modelling the late stages of impact cratering, when material strength determines the final shape and characteristics of the crater. iSALE is a “multi-rheologic” code, as it includes more than one rheologic models, and precisely, the elastic, viscous and elasto-plastic ones.

The various strength models implemented in iSALE prescribe different formulations for defining the yield strength Y as a function of pressure, strain rate, temperature, etc. To take into account pressure effects on yield strength, the intact material strength Y_i is formulated using a smooth Lundborg (1968) approximation:

$$Y_i = Y_{i0} + \frac{\mu_i P}{1 + \frac{\mu_i P}{Y_{im} - Y_{i0}}}$$

where Y_{i0} is the shear strength at zero pressure (cohesion), Y_{im} the limiting strength at high pressure (von Mises plastic limit) and μ_i the coefficient of internal friction, all for intact material, whereas the damaged material strength Y_d is defined by:

$$Y_d = \min(Y_{d0} + \mu_d P, Y_{dm})$$

where Y_{d0} is the cohesion, Y_{dm} , the limiting strength at high pressure and μ_d the coefficient of internal friction, all for damaged material.

It is to note that the amount of target damage caused by impact is highest close to the impact site and decreased with radial distance from the crater center (e.g., Kenkmann, 2002). Hence, the strength of the target material increases from the fully damaged strength at the crater center to the intact strength at larger distances (Bray, 2009). iSALE accounts for the target fracturing by means the damage parameter D ($0 =$ intact, $1 =$ fully damaged), as the yield strength Y is defined as following (Ivanov et al., 1997):

$$Y = (1 - D)Y_i + DY_d$$

Another strength model to be mention is the one proposed by *Johnson-Cook strength model* (Johnson & Cook, 1983), more appropriate for impact on metals, when large strains, high strain rates and high temperatures are applied. It is mathematically expressed by:

$$Y = (A + B\varepsilon^N)(1 + C \ln\dot{\varepsilon}) \left[1 - \left(\frac{T - T_{ref}}{T_m - T_{ref}} \right)^M \right]$$

where ε is the equivalent plastic strain, $\dot{\varepsilon}$ the strain rate and T the temperature, while A, B, C, N, M, T_{ref} are model parameters characteristics of the metal in hand, computed from laboratory experiments.

Whatever the strength model adopted, the procedure for implementing the elasto–plastic scheme is to compare an invariant measure of stress in a cell with the prescribed yield stress. The stress invariant used in iSALE is the second invariant of the deviatoric stress tensor J_2 , given by:

$$J_2 = \frac{1}{6} [(\sigma_{e1} - \sigma_{e2})^2 + (\sigma_{e2} - \sigma_{e\theta})^2 + (\sigma_{e\theta} - \sigma_{e1})^2] + \sigma_{12}^2$$

where σ_{ei} are the elastic principal stresses in cylindrical coordinates. The elastic principal stresses are computed from the elastic deviatoric stresses, which are defined by the elastic deviatoric strain components. These are updated each time step by first assuming that all deformation is elastic.

If $\sqrt{J^2}$ exceeds the yield strength Y , then shear failure occurs: the updated elastic deviatoric stress components (and deviatoric elastic strain components) must be reduced to the yield envelope by multiplying by the factor $Y/\sqrt{J_2}$. The remaining strain (the difference between the elastic deviatoric strain components before and after the yield correction is applied) is the plastic strain. This plastic strain is then recorded and subsequently used to compute the shear damage.

Damage may take place by means of two different mechanisms, the shear deformation D_s and the tensile failure D_t . The shear damage can be defined as the total plastic strain ε_{tot} (in turn being the sum over all the time steps of a invariant measure of the plastic strain rate accumulated in the time step each cycle) divided by the accumulated plastic strain at the point of failure ε_f , which is known to be a function of pressure, temperature, and material type (Johnson & Holmquist, 1993):

$$D_s = \min\left(1, \frac{\varepsilon_{tot}}{\varepsilon_f}\right) \quad \text{where:} \quad \varepsilon_{tot} = \sum_{n=1}^{n_{tot}} \dot{E}_n \Delta t_n$$

$$\dot{E}_n = \left(\frac{1}{6} [(\dot{\varepsilon}_{1,n} - \dot{\varepsilon}_{2,n})^2 + (\dot{\varepsilon}_{2,n} - \dot{\varepsilon}_{\theta,n})^2 + (\dot{\varepsilon}_{\theta,n} - \dot{\varepsilon}_{1,n})^2]\right)^{1/2}$$

where Δt_n is the duration of the n^{th} time step, \dot{E}_n the invariant measure of the plastic strain rate in that step in cylindrical coordinates, and $\dot{\varepsilon}_{i,n}$ are the principal plastic strain rate components for the n^{th} cycle.

5.2.4 Acoustic Fluidization

Crater is a roughly parabolic pit excavated by an impact, whose subsequent modification depends on its dimension (Melosh, 1982). If it is large enough, it becomes unstable and collapse under gravity, immediately after excavation, when large amounts of elastic energy are still present in the rock surrounding the crater.

However, the standard strength models for rocks are not able to account simultaneously the uplift of material from beneath the crater floor as well as the slumping of the transient crater walls (e.g., Dent, 1973; Melosh, 1977; McKinnon, 1978; O'Keefe & Ahrens, 1993; Melosh & Ivanov, 1999; Collins et al., 2002; Ivanov & Artemieva, 2002). In fact, to reproduce the observed morphologies of complex craters, collapse requires significant, but temporary, weakening of the target material beneath the crater floor, but at the same time without losing its plastic properties (Melosh, 1982).

The target material is hence better described as a *Bingham fluid*, i.e. a material that responds elastically to stress until a critical strength (the yield strength or cohesion) is reached, while, once this limit is exceeded, it flows as a viscous fluid (Bingham, 1916).

Melosh (1979) proposed, following existing models of earthquake-induced landsliding (Seed & Goodman, 1964), that the presence of a strong, random acoustic field could cause rock debris to flow as a viscous flow. In fact, subsequent explosions experiments (Gaffney & Melosh, 1982) suggested that the strong shaking produced during crater excavation might play a major role in affecting the rheology of the debris surrounding the crater (Melosh & Gaffney, 1983).

The basic idea behind acoustic fluidization, as prefaced above, relies on the fact that rock debris can flow like a fluid if subjected to strong vibrations (Fig. 5.2.3), which are transmitted as a sound wave via rock-to-rock contacts (Melosh, 1989; Melosh & Ivanov, 1999). The pressure of any point in the mass of rock debris fluctuates rapidly about the mean overburden pressure ρgz , where z is the depth below the surface (Melosh & Gaffney, 1983). In the absence of an acoustic field, the rock debris moves only under an applied shear stress $\tau = \tau_{static} = \mu\rho gz$, where μ is the coefficient of friction. However, in presence of acoustic fluctuations of wavelength λ , there is a finite probability that the overburden pressure drops briefly below the level necessary for sliding to begin under an applied shear stress τ over a region roughly $\lambda/2$ in diameter. Hence, in area where the strength of the rarefaction waves does equal or exceed the overburden pressure, debris blocks are able to move relative to one another.

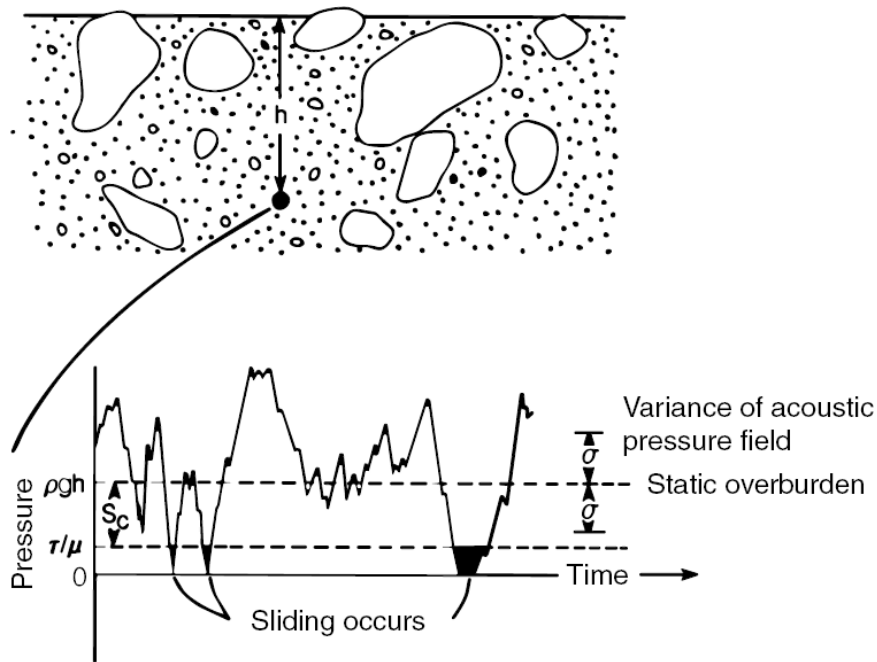


Fig. 5.2.3. Schematic diagram of the pressure variations as a function of time (*lower sketch*) at depth h in a mass of rock debris (*upper sketch*). The pressure at any given point at depth h randomly oscillates about the static overburden $\rho g z$ as sound waves pass by, with pressure deviation equal to s_c . Sliding occurs when the pressure falls to within τ/μ of zero (τ is the applied shear stress and μ is the coefficient of friction). From Melosh (1979).

The central equation of the acoustic fluidized model of Melosh (1979) describes the dependence of the strain rate $\dot{\epsilon}$ on the applied shear stress τ :

$$\dot{\epsilon} \approx \frac{\tau}{\rho \lambda c} \left[\frac{2}{\text{erfc}(\chi)} - 1 \right]^{-1} \tag{5.2.4}$$

where ρ is the bulk density, λ the wavelength of the acoustic vibrations, c the bulk sound speed of the granular debris, erfc the complementary error function, and

$$\chi = \frac{1 - \Omega}{\Sigma}$$

where, in turn $\Omega = \tau/\tau_{static}$ is a dimensionless measure of the driving stress, ranging from 0 to 1 ($\tau_{static} = \mu p$ is the stress required to initiate failure when no vibrations are present), while:

$$\Sigma = \frac{\sigma}{s_c}$$

is a dimensionless measure of the amplitude of the vibrations, in which σ is the variance of the pressure fluctuations, assumed to be distributed according to a Gaussian law (Crandall & Mark, 1973), and s_c is given by:

$$s_c = p - \frac{\tau}{\mu}$$

The flow law governed by Eq. (5.2.4) predicts that, from a macroscopic point of view, a mass of granular material behaves as a fluid when internal pressure vibrations are present. The continuum explanation is valid if the vibration wavelength λ is shorter than the fluidized region but much greater than the grain size, d , of the granular media, i.e. $\lambda \gg d$.

The effective viscosity of the fluidized debris η_{eff} is defined as the ratio of the shear stress to the net strain rate and can be approximated as follows if $\Omega=1$:

$$\eta_{\text{eff}} = \frac{\rho\lambda c}{2} \left[\frac{2}{\text{erfc}(\chi)} - 1 \right] \approx \rho\lambda c \quad (5.2.5)$$

The mean energy density in an acoustic pressure field is given by:

$$\mathcal{E} = \frac{\sigma^2}{2K}$$

where K is the appropriate elastic modulus. The temporal behaviour of this energy is controlled by the differential equation representing the energy balance equation for a unit volume of acoustically fluidized material (Melosh, 1996):

$$\frac{d\mathcal{E}}{dt} = \frac{\xi}{4} \nabla^2 \mathcal{E} - \frac{c}{\lambda Q} \mathcal{E} + e \frac{\epsilon \tau}{2}$$

The first term on the right-hand side is the scattering term, where ξ is the scattering diffusivity. The second term parameterizes conversion of elastic energy into heat, in which Q is defined as the ratio of the energy stored per cycle to the energy dissipated in the same period. The last term quantifies the energy generation during flow, where e is the fraction of the released acoustic energy that is available to regenerate the vibrations. Thus, a potentially important aspect of this full model is that energy dissipated by shear in the flowing debris could itself generate acoustic energy. In static regions, the vibrations might dissipate quickly by friction and the effective viscosity in those regions would rapidly rise; however, in flowing regions, the regeneration of acoustic energy could allow flow to continue until the driving stresses are relieved.

A major limit of this model is that it does not predict the wavelength of the vibrations dominating the flow and thus cannot be used to make quantitative predictions of the rheology of the material without further assumptions (Melosh & Ivanov, 1999). In addition, implementing this model of acoustic fluidization in shock codes it is not an easy task, as the equations governing the mechanism are non linear (e.g., Bray, 2009).

A simple approximation of the *acoustic fluidization* model (AF) developed by Melosh (1979, 1996), suitable to be incorporated into hydrocodes, is the *Block-model* (BM), developed by Ivanov (Ivanov & Kostuchenko, 1997; Ivanov & Artemieva, 2002; Melosh & Ivanov, 1999). The comparison between the two different rheologies underlying the two models is reported in Fig. 5.2.4.

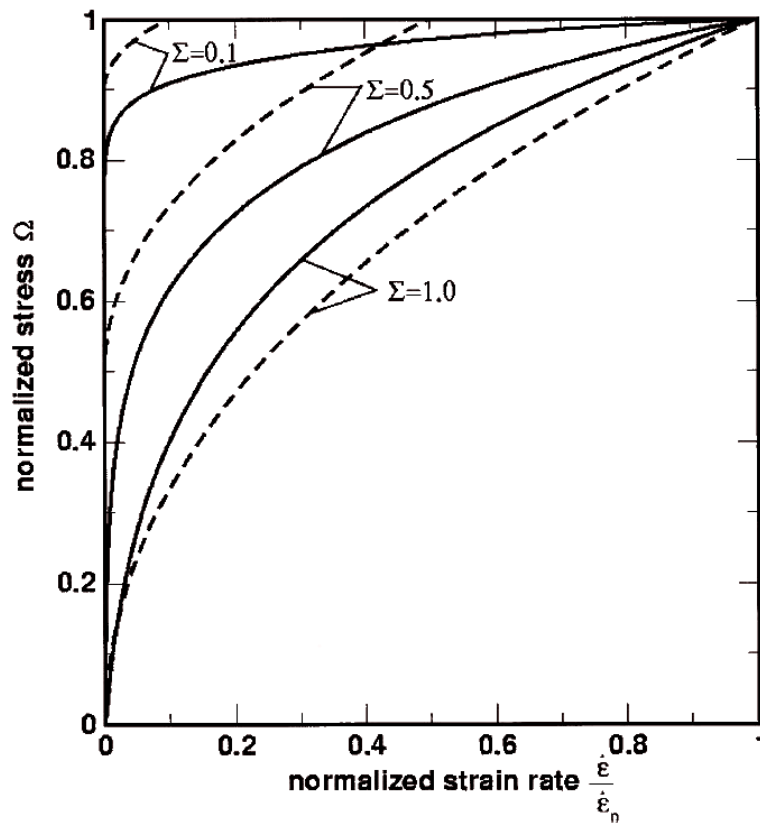


Fig. 5.2.4. Rheologies of the AF model (*solid lines*) and the BM one (*dashed lines*) for the flow of strongly vibrated rock debris. The plot illustrated the relation between the applied stress, normalized by the static sliding stress, and the strain rate, normalized by the maximum strain rate $\dot{\epsilon} = (\mu T p) / (\rho h^2)$ (cf. Eqs. 5.2.4 and Eq. 5.2.6). From Wünnemann & Ivanov (2003).

The basic idea behind this model relies on the fact that rocks material deforms as a system of discrete rock fragments (*blocks*): the low-frequency oscillations of these blocks periodically decrease contact forces between adjacent blocks; hence, the friction is decreased and slip occurs if oscillations are strong enough (Ivanov & Artemieva, 2002).

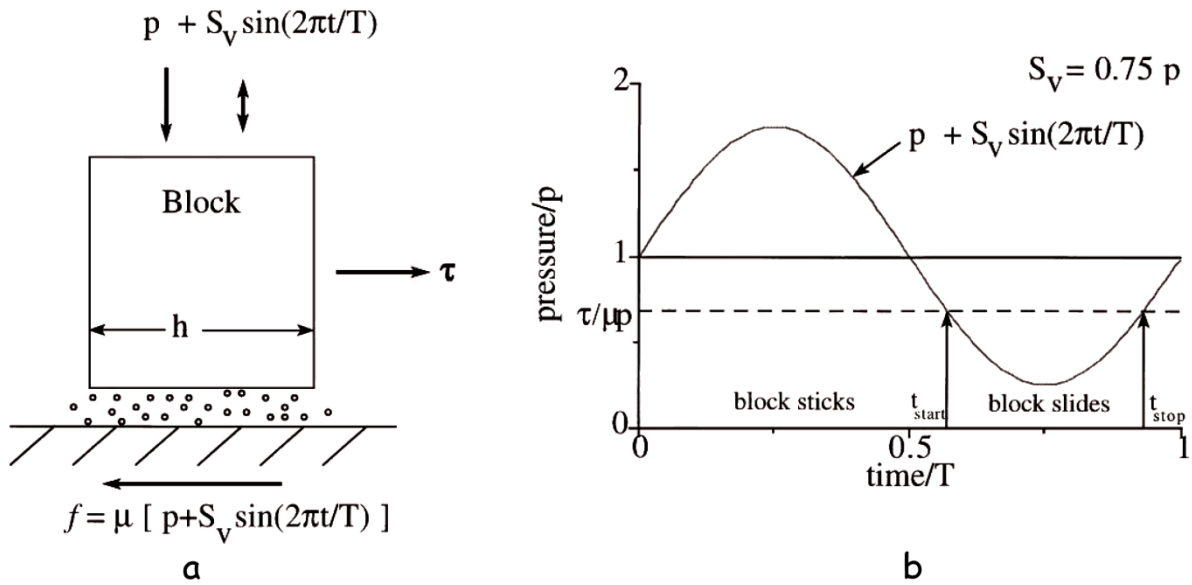


Fig. 5.2.5. (a) Schematic illustration of a block sliding along the underlying surface. The block, of size h , is under a static pressure p , a traction stress τ and a friction stress f . The varying acoustic pressure is indicated with a double-ended arrow. (b) Plot of the net pressure, relative to the overburden pressure, against time for one period of oscillation. The region addressed to “block slides” represents times at which the block is free to slide along the underlying surface. *From Melosh & Ivanov (1999).*

The central equation of the block-model (Ivanov & Kostuchenko, 1997) describes the flow of an acoustically fluidized system of rock debris in sinusoidal vibration (cf. Fig. 5.2.5):

$$\dot{\epsilon} = \frac{(\tau - Y_B)T}{2\pi^2 \rho h^2} \Phi \tag{5.2.6}$$

where τ is the driving stress, T the period of the block oscillation, h the block dimension, ρ the density of the block–matrix system, Y_B is a kind of Bingham yield strength:

$$Y_B = \mu(p - V_p)$$

where, in turn, μ is the coefficient of friction, p the overburden pressure and V_p the amplitude of the pressure vibration caused by the oscillating block; finally, Φ is given by:

$$\left(\sqrt{\frac{1+\chi}{1-\chi}} - \frac{\chi}{1-\chi} \cos^{-1} \chi \right) \cos^{-1} \chi$$

where, χ is assumed to be the same expression as in the AF model:

$$\chi = \frac{1-\Omega}{\Sigma}$$

whereas, in this case, Σ is given by:

$$\Sigma = \frac{V_p}{p}$$

The effective viscosity for the fluidized debris in the block model is again defined as the ratio of the stress to strain rate, that in a strong acoustic pressure field ($\Sigma \sim 1$, the Bingham yield strength is negligible and $\Phi \sim \pi/2$) becomes:

$$\eta_{\text{eff}} = \frac{\pi^2 \rho h^2}{T\Phi} \approx \frac{2\pi \rho h^2}{T} \quad (5.2.7)$$

To implement the idea of AF and BM models in iSALE, further simplifications have to be introduced. Eq. (5.2.4) and Eq. (5.2.5) express that the rheology of rock fragments under vibration is similar to the one of a viscous fluid. The difference between the AF model (or the BM one), and a Bingham fluid consists in the non-linearity of the AF (BM) rheology in comparison to the Bingham rheology. Hence, an assumption is introduced, i.e., rock debris under vibration behaves like a Bingham substance with cohesion Y_B and viscosity η .

The vibration state of the fragmented rocks is a temporal feature. A reasonable approach to implement the AF process into numerical models is to assume, that V_p decreases exponentially with time, like a free damped oscillation (Melosh & Ivanov, 1999; Collins et al., 2002):

$$V_p = V_{p,t=0} e^{-t/T_{dec}}$$

where $V_{p,t=0}$ is a function of maximum particle velocity, density and sound speed, while T_{dec} is the damping factor (decay time).

The viscosity η is assumed to be proportional to density ρ , sound speed c and a length parameter comparable to the block size h (Wünnemann & Ivanov, 2003). Drilling in impact structures and estimation from underground explosions (e.g., Ivanov et al., 1996; Kocharyan et al., 1996) suggested that the block length parameter for the determination of η could be scaled by some linear scale. If the block system under a growing crater is activated during the crater growth process, the block characteristic size seems to be proportional to the transient cavity depth (Ivanov & Artemieva, 2002) or diameter (Collins, 2001). However, the transient cavity depth itself depends on the value of η . If the projectile size r is considered to reproduce the fragment-size scale of a cratering event, the viscosity η becomes:

$$\eta = \gamma_{\eta} (c r \rho)$$

Thus, the length parameter (block size or wavelength) is scaled by the projectile radius r and a dimensionless scaling parameter γ_{η} . On the other hand, the duration and the damping of the vibration is considered as well to be linearly correlated to the radius of the projectile through the factor γ_T :

$$T_{dec} = \gamma_T \left(\frac{r}{c} \right)$$

γ_{η} and γ_T represents exactly the input parameters controlling the fluidization mechanism on iSALE (Wünnemann & Ivanov, 2003).

5.2.5 Porosity Model

A number of impact experiments and numerical studies pointed out that the growth of the transient cavity is mainly controlled by strength and gravity (e.g., Holsapple & Schmidt, 1987; O’Keefe & Ahrens, 1993). On the other hand, thermodynamic properties can become less marginal if the material involved in the impact possesses a significant amount of porosity. In fact, the crushing of pore space is an efficient mechanism for absorbing shock waves and results in higher post-shock temperatures than observed in impacts into nonporous rocks (e.g., Zel’dovich & Raizer, 2002). Although, the presence of void spaces can be considered negligible during large-scale impact events on planets, it strongly influences the crater formation on asteroids and comets, as porosity might reach values as high as 75–80% (Britt et al., 2002; Housen et al., 1999; Asphaug et al., 2002).

The behaviour of porous materials is different to that of fully consolidated material when a compressive stress is applied, because it had to consider the *compaction*, i.e. closing of pore space, in addition to the *compression* of the solid component. It was described by a number of models, one among them is the P-alpha model (Hermann, 1969; Kerley, 1992), which computes the compaction of void space in porous material from the applied pressure P , by introducing a new parameter, called *distension parameter* α , that is a function of the applied pressure P , i.e. $\alpha(P)$.

If ϕ is the porosity, it can be defined as the volume fraction of void space:

$$\phi = \frac{V - V_S}{V} = \frac{V_V}{V}$$

where V is the volume, V_S is the volume of the solid component and V_V of the pore space. A 0 porosity implies that no void is present, whereas a porosity of 1 implies that no solid component is present, and hence:

$$\rho = \rho_S (1 - \phi)$$

where ρ is the bulk density of the porous material and ρ_S the density of the solid component. In this context, the distension parameter is defined as:

$$\alpha = \frac{1}{1 - \phi} = \frac{V}{V_S} = \frac{\rho_S}{\rho}$$

However, the P-alpha model cannot be easily included in numerical modelling (Housen & Holsapple, 2000), as changes in pressure are caused by changes in density ρ and internal energy E , in addition to the α parameter. Moreover, computations become time consuming, since subroutines have to be introduced to update the distension parameter prior to the pressure calculation.

Wünnemann et al. (2006) proposed a new model, named ε -alpha model. It is a physics-based approach, since it deals with the “compaction of porosity”, that significantly controls the crater growth (Housen & Holsapple, 2003).

In the ε -alpha model (Wünnemann et al., 2006), the distension α is defined as a function of the volumetric strain ε_V , which, being a state variable, allows the distension to be updated prior to the pressure calculation. The volumetric strain is defined as the change in volume of an elementary cell divided by the initial volume, provided that the change in volume is small. In addition, if we consider an ideal case, all the void space is crushed out before any compression of the material solid component takes place. Hence, given the initial volume V_0 and the updated volume V' , the volumetric strain ε_V is related to distension α by the following expression:

$$\varepsilon_V = \int_{V_0}^{V'} \frac{dV}{V} = \ln\left(\frac{V'}{V_0}\right) = \ln\left(\frac{V' V_S}{V_S V_0}\right) = \ln\left(\frac{\alpha}{\alpha_0}\right)$$

from which, if α_0 is the initial distension before compaction starts, the compaction function is derived:

$$\alpha = \alpha_0 e^{\varepsilon_V}$$

However, during compression of material, both compaction of pore space, which is also accompanied by some frictional resistance as rearrangement of grains takes place, and compression of the matrix occur. To account for these effects, a parameter $\kappa \leq 1$ is introduced to control the compaction rate, i.e. the rate of change of distension with respect to volumetric strain, of pore closure in the compaction regime. Moreover, impact experiments on porous media have evidenced that, for samples with a cohesive strength, the crushing-out and closure of pores do not begin until a critical threshold ε_e of the volumetric strain is reached. Accounting for both these effects, the compaction function becomes:

$$\alpha = f(\varepsilon_V) = \begin{cases} \alpha_0 & |\varepsilon_V > \varepsilon_e \\ \alpha_0 e^{\kappa(\varepsilon_V - \varepsilon_e)} & |\varepsilon_V < \varepsilon_e \end{cases}$$

Taking in mind the fact that the compressive strain is negative, the progressive porous material compaction can be described as follows (cf. Fig. 5.2.6). At the early stages, compaction is in a first regime, described by the function $\alpha = f(\varepsilon_V)$, in which the void space is crushed out by grain rearrangement. As the grains become closer and closer together, the resistance becomes as great as further compaction would be possible only by fracturing individual grains. Compaction enter a second regime, described by $\alpha = g(\varepsilon_V)$, for volumetric strains less than a certain transition strain ε_X .

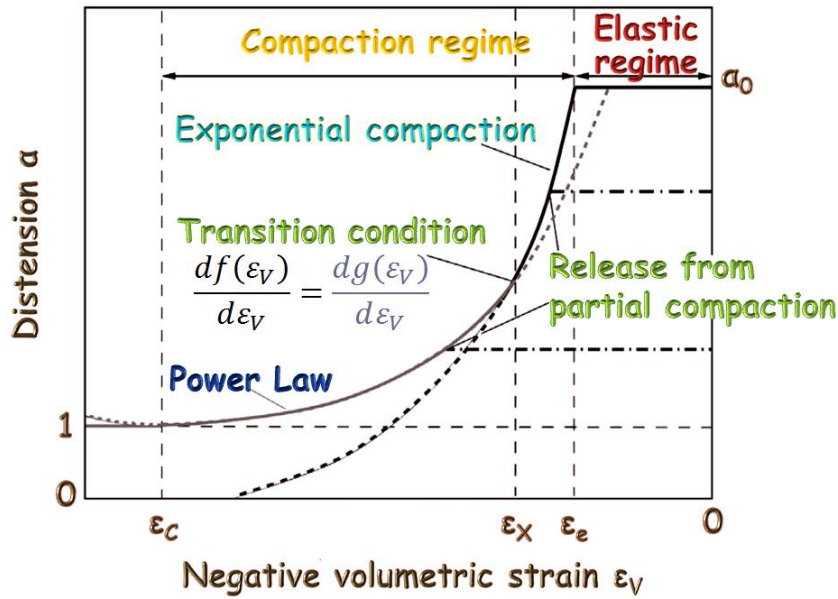


Fig. 5.2.6. Illustration of the ϵ - α porous-compaction model. The distension α (solid line) is represented as a function of the volumetric strain ϵ_V , which increases negatively. Vertical dashed line marks the boundary between the possible compaction regimes (elastic, exponential and power-law). As the distension crosses the different regimes, it is described by different types of curves. The first compaction regime is an exponential, because void space is crushed out by grain rearrangement, while the second should be represented by a power law, as it had to satisfy the following properties: (1) the power-law regime curve should be effectively a less steep curve than the exponential one, as it is more difficult to crush out pore space in this regime than in the exponential compaction one; (2) the transition between the two regimes is smooth; (3) the compaction curve should approach the line $\alpha = 1$ smoothly. From Wünnemann et al. (2006).

The two compaction regimes are defined as exponential and power-law, and are definitively expressed by the following functions:

$$\alpha = f(\epsilon_V) = \alpha_0 e^{\kappa(\epsilon_V - \epsilon_e)} \quad \left| \begin{array}{l} \kappa \leq 1, \\ \epsilon_e > \epsilon_V > \epsilon_X \end{array} \right. \quad (5.2.8)$$

$$\alpha = g(\epsilon_V) = 1 + (\alpha_0 e^{\kappa(\epsilon_V - \epsilon_e)}) \left(\frac{\epsilon_C - \epsilon_V}{\epsilon_C - \epsilon_X} \right)^2 \quad \left| \begin{array}{l} \epsilon_X > \epsilon_V > \epsilon_C \end{array} \right. \quad (5.2.9)$$

$$\alpha = g(\epsilon_V) = 1 \quad \left| \begin{array}{l} \epsilon_V < \epsilon_X \end{array} \right. \quad (5.2.10)$$

Eq. (5.2.10) represents the elastic region, in which the crushing is reversible. However, the elastic component of compaction is relatively small and can be neglected for large-stress processes like shock wave compression.

The free parameters of this porous model are the elastic-plastic transition strain ϵ_e , the threshold strain ϵ_X for the transition between the two compaction regimes, the exponential compaction rate κ and the initial distension α_0 , while the volumetric strain ϵ_C at which all pore space is crushed out can be derived for a given ϵ_X .

5.3 Validation to laboratory experiments

To evaluate and to apply the existing codes to various scientific problems, it is necessary to know the code reliability. Recently, Pierazzo et al. (2008) presented a work of benchmarking and validating a number of shock codes widespread in the impact community. The codes validation testing involves the evaluation of shock codes through comparison of simulations with laboratory experiments, which have been conducted under well-known conditions and provide direct information on impact events.

Among the experiments described in the paper, I focused the attention to the one performed by Prater (1970). A 6.35-mm-diameter aluminum sphere impacts perpendicularly at about 7 km/s onto various aluminum alloy cylinders. Material strength was varied by employing targets of 1100-O, 6061-T6, 7075-T6 and 7075-T0 aluminum alloys. Flash X-ray techniques were used to measure accurately the rate at which the crater grew during the impact process.

I simulate this experiment, choosing alloy 6061-T6 (insensitive to strain rate), employed in Pierazzo et al. (2008), to have in addition a comparison chance with other modelers (Fig. 5.3.1). The simulations have been carried out with varying resolutions. The resolution of an impact model is usually defined as the number of computational cells per projectile radius (*cppr*) (Wünnemann et al., 2008). I have performed runs at 10, 20 and 50 *cppr*. Fixed input conditions included the projectile size, impact velocity and angle, shape and material, target material and mesh size, which is set large enough to consider the target as “infinite”. The adopted equation of state is the Tillotson EoS, while the strength model used is the Johnson-Cook one. In Tab. 5.3.1, I report the input material parameters set for this simulation.

In Fig. 5.3.2, I report the evolution, as time passes, of the radius and the depth of the crater simulated (colored lines), showing as well experimental data (red points) for comparison. Numerical simulations are found to be in relatively good agreement with the experiment values, showing however a deviance from the experiments, and precisely an underestimation of the crater radius, whereas an overestimation of the crater depth. Similar results have been noticed also in other shock codes simulations (Fig. 5.3.1). Both deviance from the experimental data are within ~13%, depending from the resolution, which turns to have a very important role in performing numerical modelling.

The higher resolution of the computational mesh (and hence, a higher number of cells defining the projectile), the closer the modeled projectile comes to approximate a perfect sphere. Consequently, the projectile has slightly more mass in high resolution runs than for lower resolution runs. This additional mass can lead to different final crater morphologies. Hence, employing “lower” resolution will produce deviations in final crater dimensions relative to higher results. Fig. 5.3.2 demonstrates, in fact, an overall increase both in crater radius and depth for higher resolutions, although it is the volume of material experiencing a certain peak pressure to be the very sensitive parameters on resolution (Wünnemann et al., 2008).

JOHNSON-COOK MODEL for Al 6061-T6			TILLOTSON EoS for Aluminum	
<i>Symbol</i>	<i>Definition</i>	<i>Value</i>	<i>Symbol</i>	<i>Value</i>
ν	Poisson ratio	0.33 MPa	ρ_0	2700 kg m ⁻³
A	JC strain coeff.	324 MPa	a	0.5
B	JC strain coeff.	114	b	1.63
n	JC strain exponent	0.42	A	75.2 GPa
C	JC strain rate coeff.	0.002	B	65 GPa
m	JC thermal softening	1.34	E_0	5 MJ kg ⁻¹
T_{ref}	JC reference temp.	293 K	α	5
T_m	Melt temperature	933 K	β	5
C_p	Specific Heat Capacity	896 J kg ⁻¹ K ⁻¹	E_{iv}	3.0 MJ kg ⁻¹
			E_{cv}	13.9 MJ kg ⁻¹

Tab. 5.3.1. Table reporting the material parameters adopted for the simulation of an aluminum alloy sphere onto a target of equal composition. The Johnson–Cook model parameters have been found on Rule (1997), while the Tillotson EoS ones in Melosh (1989).

In all my simulations, a 10 *cppr* cell resolution is chosen as “starting point”, because it allows better approximation of a perfectly spherical projectile in comparison to lower resolution options, but it allows as well a less computation time in comparison to higher resolution options.

Finally, in Fig. 5.3.3 I report the snapshots at different time steps of density and pressure beneath the Al 6061–T6 crater, that point out pressure values exceeding 5 GPa.

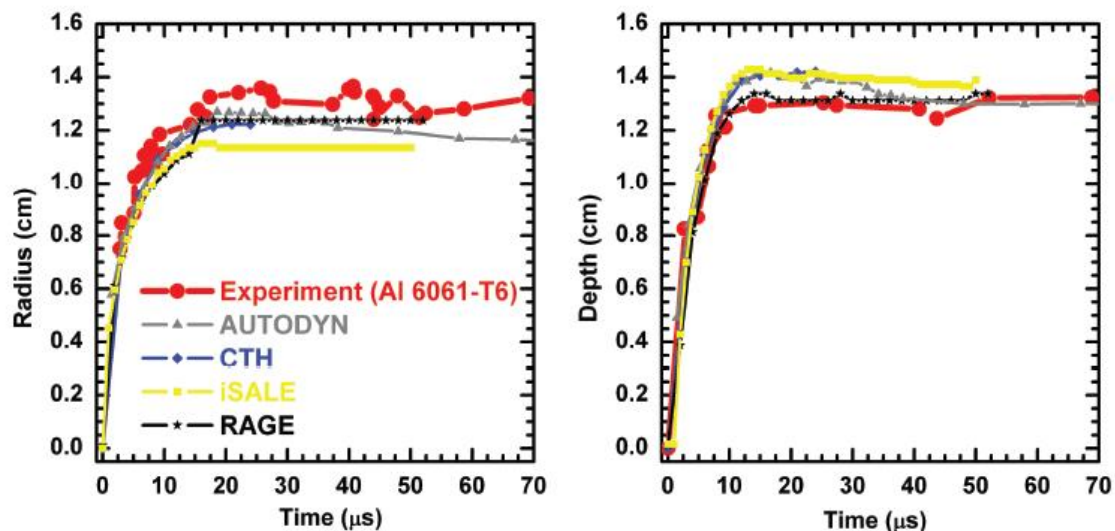


Fig. 5.3.1. Intra-codes validation of the Al 6061-T6 laboratory experiment, reporting estimates of temporal evolution of crater radius and depth in comparison to experimental data. From Pierazzo et al. (2008).

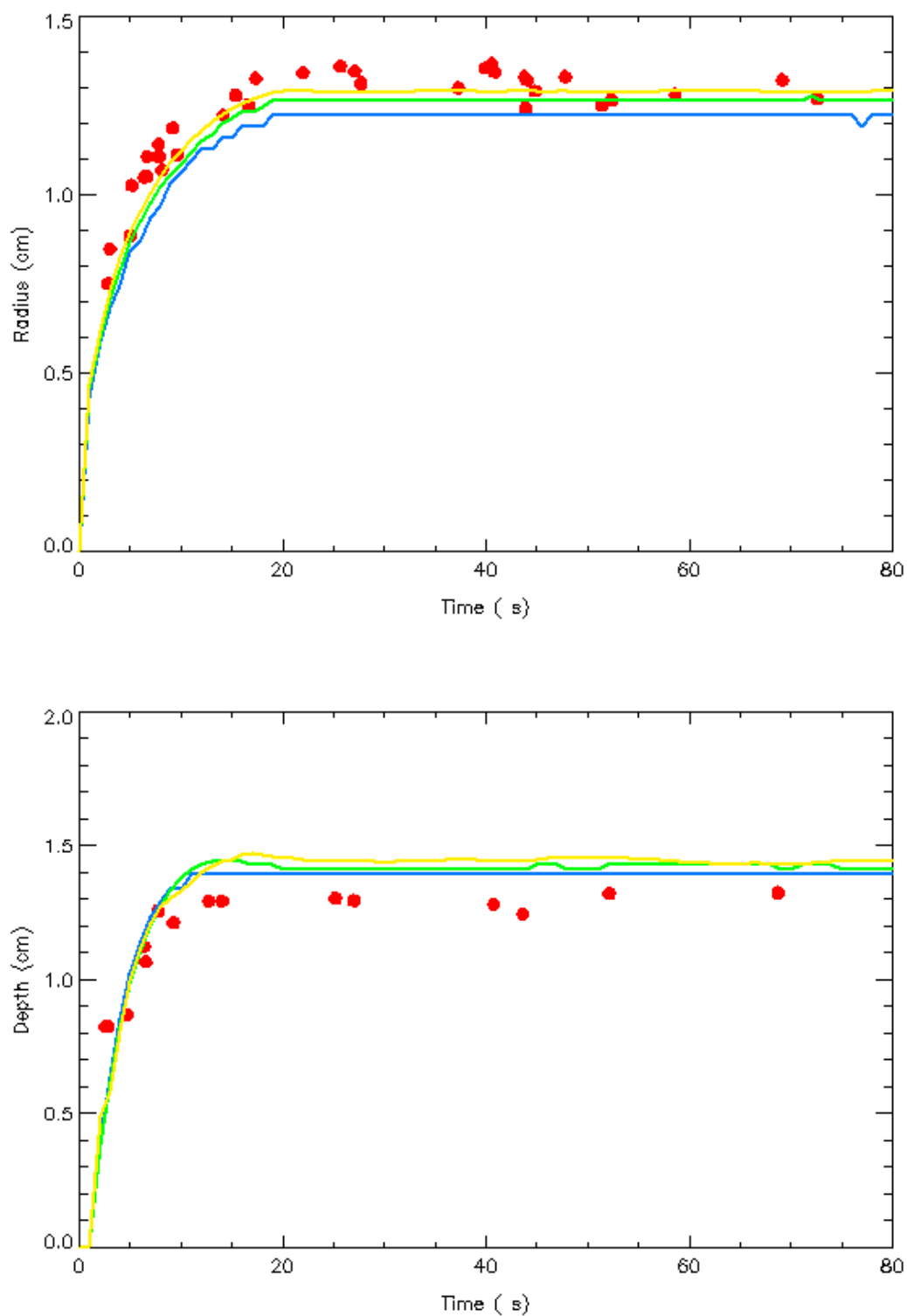


Fig. 5.3.2. Temporal evolution of crater radius (*top*) and depth (*bottom*) for the impact of an aluminum projectile on a target made of Al 6061-T6 compared to the experimental data (red points): different resolutions have been analyzed: 10 (*blue*), 20 (*green*) and 50 (*yellow*) *cpr*.

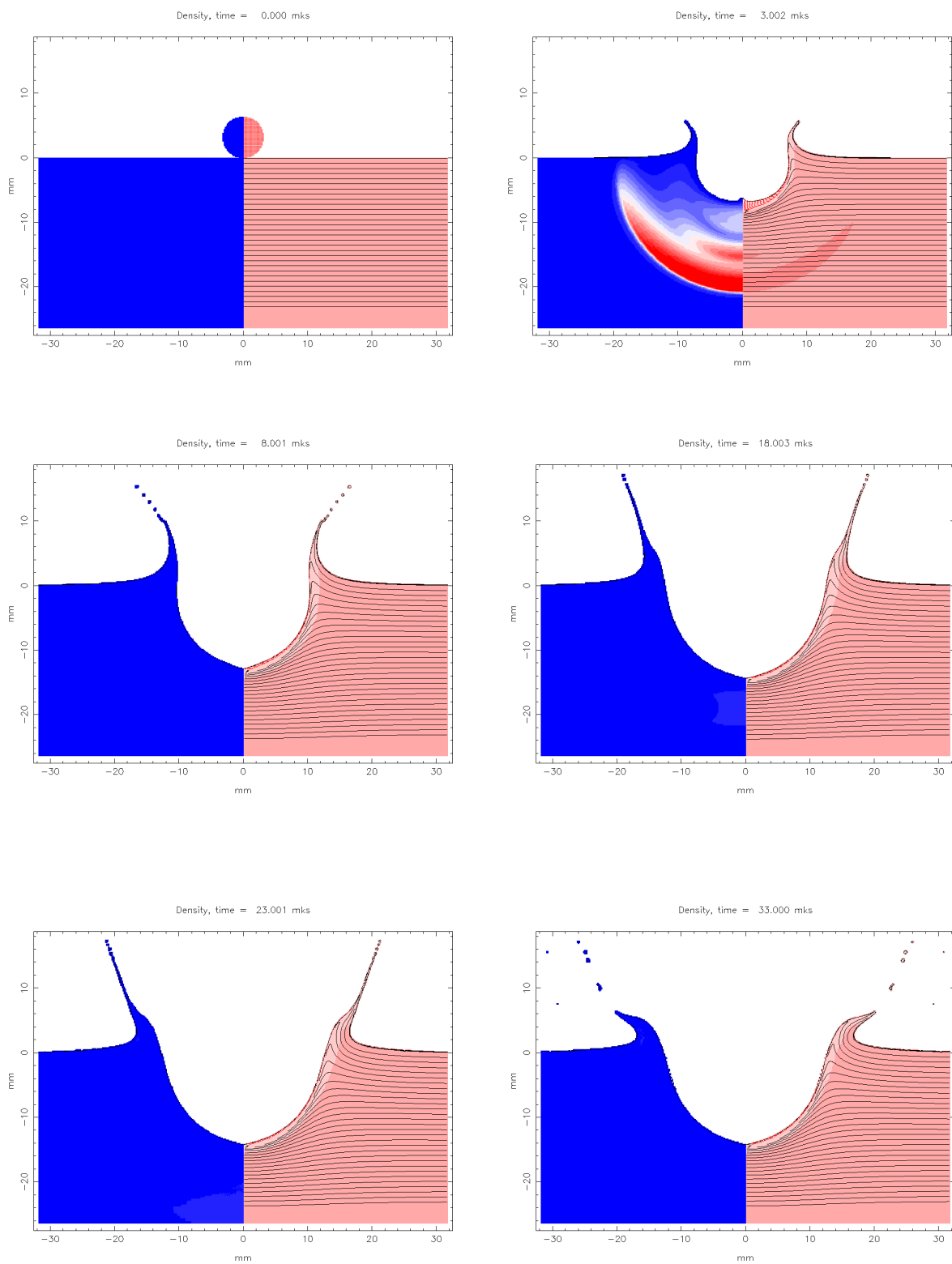


Fig. 5.3.3. Density (*right*) and Pressure (*left*) beneath Al 6061-T6 crater, at several times during crater formation, for the numerical run at 20 *cpr*.

Chapter 6

Space Missions

6.1 Introduction

It is not much more than fifty years since the Sputnik became the first artificial satellite of the Earth. The October 4th, 1957 was a starting Era in the way of facing up the investigation of the Solar System. The knowledge of the Earth itself, to what concern atmosphere, ocean, continents and their changes with time, was improved from space non-stop observations. On the other hand, the terrestrial planets turned from largely astronomically perceived objects observed by Earth-based telescope to intensely studied world. The increasingly amount of data and level of details let come us to understand the basic range of processes differentiating planetary interiors, creating planetary crusts and forming and modifying planetary surfaces and to advance the relationship of surface geology to internal processes and thermal evolution (Head et al., 2001).

Space missions, therefore, have turned to be an essential tool in studying our surrounding world. In this chapter, I will introduce the BepiColombo mission, with particular regard to the STC/SIMBIOSYS instrument. Then, I will briefly outline two missions, MESSENGER and Rosetta, whose data I have used in my research.

6.2 BepiColombo

This PhD research has been performed in the scientific activities of the STC/SIMBIOSYS instrument onboard of the BepiColombo mission, which is the fifth cornerstone mission of ESA, foreseen to be launched in August 2014 with the aim of studying in great detail Mercury, the innermost planet of the Solar System.

For more than thirty years, our poorly knowledge of Mercury came from the data collected by Mariner 10 during its three flybys in 1974 and 1975. Mariner 10 imaged about 45% of the surface at an average resolution of about 1 *km* and less than 1% of the surface at better than 500-*m* resolution (Murray, 1975). Further, Mariner 10 discovered the planet's internal magnetic field (Ness et al., 1974, 1975), measured the ultraviolet signatures of H, He, and O in Mercury's atmosphere (Broadfoot et al., 1974, 1976), documented the time-variable nature of Mercury's magnetosphere (Ogilvie et al., 1974; Simpson et al., 1974), and determined some of the physical characteristics of Mercury's surface materials (Chase et al., 1974). Important subsequent ground-based discoveries include the Na, K, and Ca components of the atmosphere (Potter and Morgan, 1985, 1986; Bida et al., 2000) and the radar-reactive polar deposits (Slade et al., 1992; Harmon and Slade, 1992).

A substantially improved knowledge of the planet Mercury is nonetheless critical to our understanding of how the terrestrial planets formed and evolved. However, this planet is a difficult body for study. In fact, both earth-based astronomical observations and space imaging systems, like the Hubble Space Telescope, are not so conclusive because of direct observations near the Sun must be avoided. On the other hand, Mercury poses severe thermal and dynamical challenges to observation by spacecraft (e.g., Solomon et al., 2001; Strom & Sprague, 2003).

Key questions regards the origin of its 3:2 spin-orbit resonance, the origin of Mercury's high density, the composition and structure of its crust, the timing of volcanism, the nature of the polar deposits, the nature and dynamics of the thin atmosphere and Earth-like magnetosphere, and finally the interior structure, in particular whether the outer core is molten and can then be responsible for generating the magnetic field (e.g., Solomon et al., 2001, 2003). A further context in which to regard Mercury's unusual attributes is provided by the recent discovery of planets and planetary systems in orbit about other stars (Marcy & Butler, 2000). While the extrasolar planets documented to date are all analogues to the gas giant planets of our Solar System, the orbital parameters of Mercury fall within those of known extrasolar planets, and Mercury provides our nearest laboratory for studying planetary system processes in the vicinity of a star. Furthermore, a variety of efforts are under way to detect and characterize extrasolar Earth-like planets (Seager, 2003), and Mercury will provide a relevant point of comparison with those less than 1 AU from their parent star (Solomon et al., 2003).

BepiColombo is an interdisciplinary mission devoted to fully characterize Mercury through a partnership between ESA and Japan's Aerospace Exploration Agency (JAXA) (Schulz and Benkhoff, 2006). The mission has been named in honour of Giuseppe Colombo (1920–1984), who made many contributions to planetary research, in particular Mercury, and to celestial mechanics, including the development of new space flight concepts, like the interplanetary trajectory using gravity assist. The Scientific objectives of this mission are:

- Origin and evolution of a planet close to the parent star
- Mercury as a planet: form, interior, structure, geology, composition and craters
- Mercury's vestigial atmosphere (exosphere): composition and dynamics
- Mercury's magnetized envelope (magnetosphere): structure and dynamics
- Origin of Mercury's magnetic field
- Test of Einstein's theory of general relativity

BepiColombo will complement the work of MESSENGER (cf. § 6.3) by providing a highly accurate and comprehensive set of observations of Mercury, through two complementary modules that will study the planet and its environment from their dedicated orbits. The Mercury Planet Orbiter (MPO) (e.g., Benkhoff et al., 2010), realized in Europe, will be carrying remote sensing and radio science experiments, to map the entire surface of the planet, to study the geological evolution of the body and its inner structure. The Mercury Magnetospheric Orbiter (MMO) (e.g., Hayakawa et al., 2004), realized by JAXA in Japan, will be carrying field and particle science instrumentation, to study the magnetosphere and its relation with the surface, the exosphere and the interplanetary medium.

The MPO orbital characteristics, i.e. elliptical polar orbit with periherm and apoherm altitudes of 400 km and 1500 km respectively, and 2.3 hours orbital period, are mainly determined by the need for the remote sensing instruments to have high spatial resolution not changing too much all over the surface during the one year nominal mission lifetime, and are extremely challenging due to the thermal constraints on the S/C. For a continuous observation of the planet surface during the mission, the S/C is 3-axis stabilized with the Z-axis, corresponding to payload boresight direction, pointing to nadir.

Crucial information to analyze the geological and mineralogical characteristics of the Mercury surface and exosphere will come from the integrated package Spectrometer and Imagers for MPO BepiColombo Integrated Observatory SYStem (SIMBIOSYS) (Flamini et al., 2010). SIMBIOSYS (Fig. 6.2.1) investigation can count on a very high spatial resolution and coverage, strict complementarity on the spectral range for mineralogical mapping, and high accuracy for the stereo-derived topography. Furthermore, STC will cover approximately all of Mercury's surface, including the north polar regions and the southern hemisphere. SIMBIOSYS will, thus, provide the global view of the planet corroborated by high-resolution data at local scale to unambiguously reconstruct the overall evolution of the planet. A synoptic view of the scientific objectives of SIMBIOSYS is listed in Tab. 6.2.1 and related to the main Science themes of the BepiColombo mission.

BepiColombo main theme	SIMBIOSYS science theme
Origin and evolution of a planet close to its parent star	<p>Definition of the impact flux in the inner Solar System: based on the impact crater population records</p> <p>Understanding of the accretional model of an end member of the Solar System: based on the type and distribution of mineral species</p>
Mercury as a planet: form, interior, structure, geology, composition and craters	<p>Reconstruction of the surface geology and stratigraphic history: based on the combination of stereo and high- resolution imaging along with compositional information coming from the spectrometer</p> <p>Relative surface age by impact craters population density and distribution: based on the global imaging including the high- resolution mode</p> <p>Surface degradation processes and global resurfacing: derived from the erosional status of the impact crater and ejecta</p> <p>Identification of volcanic landforms and style: using the morphological and compositional information</p> <p>Crustal dynamics and mechanical properties of the lithosphere: based on the identification and classification of tectonic structures from visible images and detailed DTM</p> <p>Surface composition and crustal differentiation: based on the identification and distribution of mineral species as seen by the NIR hyperspectral imager</p> <p>Soil maturity and alteration processes: based on the measure of the spectral slope derived by the hyperspectral imager and the colour capabilities of the stereo camera</p> <p>Determination of moment of inertia of the planet: the high- resolution imaging channel as landmark pairs of surface features that can be observed on the periside as support for the libration experiment</p>
Mercury's exosphere: composition and dynamics	<p>Surface–Atmosphere interaction processes and origin of the exosphere: knowledge of the surface composition is also crucial to unambiguously identify the source minerals for each of the constituents of the Mercury's exosphere</p>

Tab. 6.2.1. Synoptic table of SIMBIOSYS science themes. From Flamini et al. (2010).

SIMBIOSYS is made up by:

1. the high resolution imaging channel (HRIC), that will provide images at a spatial resolution of 5 m/pixel at the periherm,
2. the VIS–NIR spectrometer (VIHI) that will provide the mineralogical global mapping of Mercury's surface in the spectral range $400\text{--}2200\text{ nm}$, with a spectral sampling of 6.25 nm , and a spatial resolution of 400 m/pixel at the periherm, and allowing local spectra at 100 m/pixel ,
3. the stereo imaging channel (STC) that will provide panchromatic 3D global mapping and colour imaging of selected regions of the Hermean surface, with a spatial resolution lower than 110 m .

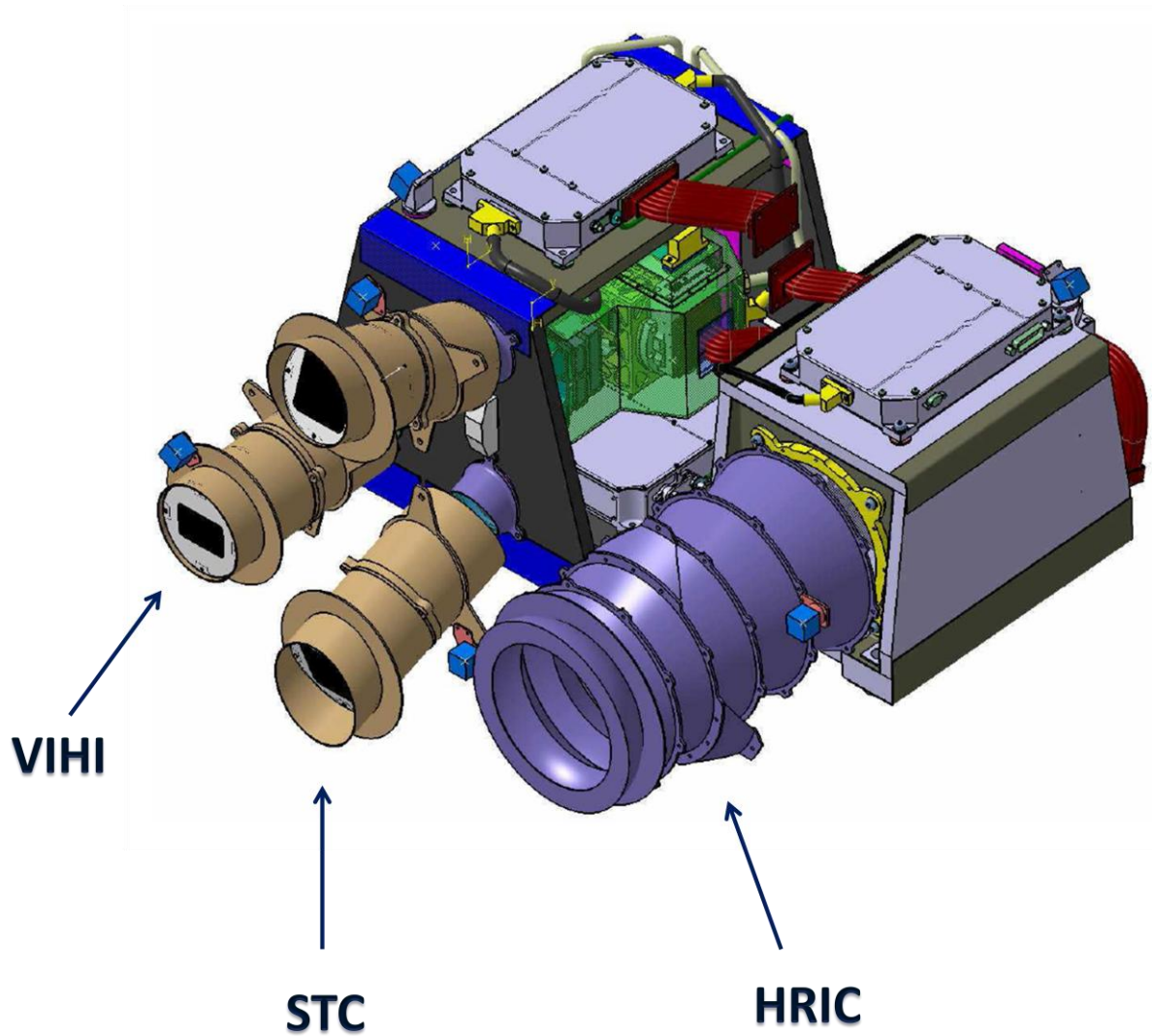


Fig. 6.2.1. SIMBIOSYS package. From Flamini et al. (2010).

STC is a double wide angle camera designed to image each portion of the Mercury surface from two different perspectives; it provides panchromatic stereo image pairs required for reconstructing the Digital Terrain Model (DTM) of the planet surface (Fig. 6.2.2) and colour images of selected areas. With respect to classical two- or single-camera designs, this solution allows to reach good stereo performance with general compactness, saving of mass, volume and power resources.

STC is based on a completely new optical design and acquisition technique. The push-frame has been adopted instead of the push-broom adopted in other missions, as for instance the Mars Express camera HRSC, because it can improve the stereo reconstruction as a reduced number of larger images to mosaic will be used, increasing the tie points on the same stereo pair and taking into account possible small drifts of the satellite pointing (Cremonese et al., 2009).

STC is mainly composed by 3 sub–units (Cremonese et al., 2010):

1. a focal Plane Assembly with dedicated Proximity Electronics to pilot detector in terms of integration time, windowing and binning,
2. an optical Module in which the optical elements are kept in stable position by means of a dedicated optical bench able to guarantee the optical stability after launch, and
3. external and internal baffling system.

The scientific requirements and characteristics of the design are summarized in Tab. 6.2.2, while the optical system could be well described by Fig. 6.2.2 (Da Deppo et al., 2010).

	Parameter	Value
Nominal Performances	<i>Scale factor</i>	50 <i>m/px</i> at periherm
	<i>Swath</i>	40 <i>km</i> at periherm
	<i>Stereoscopic properties</i>	±21°.4 stereo angle with respect to nadir both images on the same detector
	<i>Vertical accuracy</i>	80 <i>m</i>
	<i>EE</i>	> 70% inside 1 <i>pixel</i>
	<i>MTF</i>	> 60% at Nyquist frequency
	<i>Wavelength coverage</i>	410–930 <i>nm</i> (5 filters)
Optical Parameters	<i>Filters</i>	Panchromatic (700 ± 100 <i>nm</i>) 420 ± 10 <i>nm</i> 550 ± 10 <i>nm</i> 750 ± 10 <i>nm</i> 920 ± 10 <i>nm</i>
	<i>Optical concept</i>	Catadioptric: modified Schmidt telescope plus folding mirrors fore–optics
	<i>Stereo solution (concept)</i>	2 identical optical channels; Detector and most of the optical elements common to both channels
	<i>Focal length (on-axis)</i>	95 <i>mm</i>
	<i>Pupil size (diameter)</i>	15 <i>mm</i>
	<i>Focal ratio</i>	<i>f</i> /6.3
	<i>Mean image scale</i>	21.7 <i>arcsec/px</i> (105 <i>μrad/px</i>)
	<i>FoV (cross track)</i>	5.3°
	<i>FoV (along track)</i>	2.4° panchromatic 0.4° color filters
	<i>Detector</i>	Si_PIN (format: 2048 × 2048; 10 <i>μm</i> squared pixel). 14 bits dynamic range

Tab. 6.2.2. Summary of the nominal performances and optical parameters of the STC. *From Da Deppo et al. (2010).*

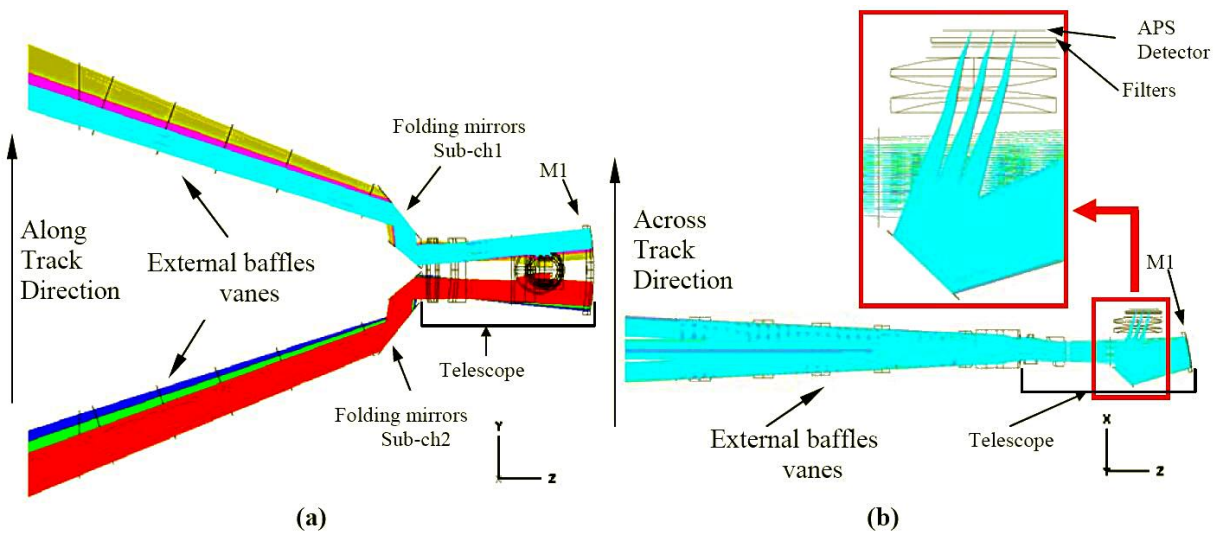


Fig. 6.2.2. STC optical layout. (a) The configuration viewed in the plane defined by the along track and nadir directions. (b) The projection in the orthogonal plane, the one including across track and nadir directions, is given. In the inset, an enlarged view of the focal plane shows the focalization of rays on the APS detector. From Da Deppo et al. (2010).

The optical solution is composed by two independent elements: a fore-optics, consisting of two folding mirrors per each channel, and a common telescope unit, which is an off-axis portion of a modified Schmidt design. The telescope mirror is off-axis because of the need to have a free back focal length sufficient to easily integrate the Focal Plane Assembly (FPA), maintaining at the same time the required optical performance.

For each sub-channel, it is possible to acquire simultaneously three quasi-contiguous areas of Mercury surface in different colors and without using movable elements; however, while the nominal FoV of each sub-channel is $5.3^\circ \times 4.8^\circ$, the scientific useful FoV is actually smaller, i.e. $5.3^\circ \times 3.2^\circ$. At perihelion, each panchromatic strip corresponds to an area of about $40 \times 19 \text{ km}^2$ on the Mercury surface and each colored strip to an area of about $40 \times 3 \text{ km}^2$ (Fig. 6.2.3).

The selected detector is a hybrid APS Si_PIN device. This type of detector has been preferred to the more classical CCD because of its radiation hardness, a very critical point given the hostile Mercury environment. Moreover, its capability of snapshot image acquisition allows both to avoid the use of a mechanical shutter, and to easily obtain the millisecond exposure times that are necessary to avoid possible image smearing due to the relative motion of the S/C with respect to Mercury surface

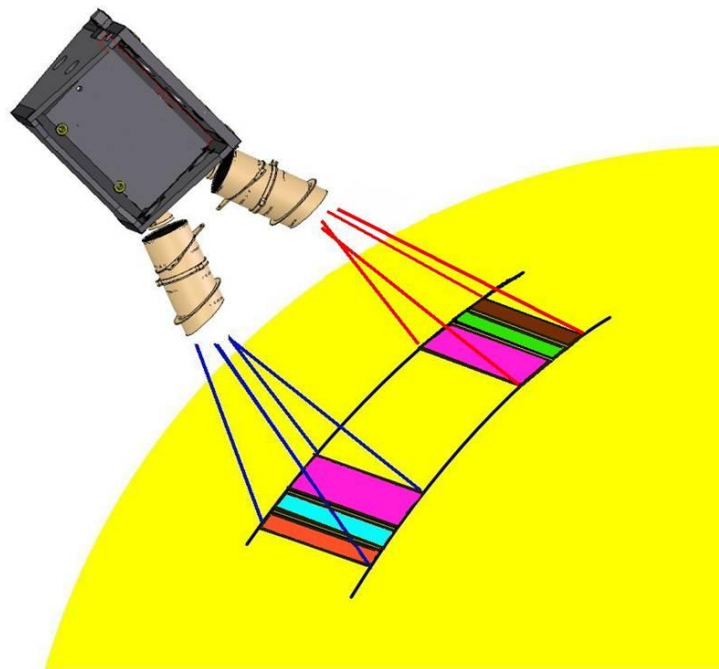


Fig. 6.2.3. The STC acquisition concept. The ground-track swath is about 40 km. From Cremonese et al. (2010).

The STC configuration (Cremonese et al., 2010) takes into account five filters in 400–1000 nm spectral range. One broad-band filter for stereoscopic acquisition is centered at 700 nm with 200nm full-width at half- maximum (FWHM). Four filters for low-resolution spectral observations are centered at 420, 550, 750 and 920 nm; the first two filters are sensitive to iron charge transfer processes in silicate and conduction band transitions in sulphides, the others are able to detect the presence of iron crystal field transitions in mafic minerals. The generation of a high-accuracy and high-resolution DTM is the main target of the stereo reconstruction by STC. In order to provide the scientific requirements for the optical design and the thermo-mechanical calculations, we simulated the STC performance in the DTM generation, taking into account the up-to-date spacecraft accuracies and the maximum allowed ground spatial scale of 50 m/pixel at the periherm on the equator.

6.3 MESSENGER

MESSENGER (*ME*rcury *S*urface, *S*pace *EN*vironment, *GE*ochemistry, and *R*anging) is a NASA mission belonged to the Discovery Program and designed to orbit Mercury as well, for one year after completing three flybys of that planet (e.g., Solomon et al., 2001, 2007).

The scientific objectives outlined for BepiColombo are partly shared by MESSENGER, and are briefly compared in Tab. 6.3.1.

M	MESSENGER questions	Mapping	B	BepiColombo questions
1	What planetary formational processes lead to the high metal/silicate ratio in Mercury	M1 → B1	1	The dense planet: Why is Mercury's density so high?
2	What is the geological history of Mercury?	M2, B3	2	The magnetic field: What is the origin of Mercury's magnetic field?
3	What are the nature and origin of Mercury's magnetic field?	M3 → B2, B6	3	Geology: How has Mercury evolved geologically?
4	What are the structure and state of Mercury's core?	M4 → B1, B2	4	Detecting water ice: Is there water ice in the polar regions?
5	What are the radar-reflective materials at Mercury's poles?	M5 → B4	5	Mercury's exosphere: What are the constituents of Mercury's exosphere?
6	What are the important volatile species and their sources and sinks on the near Mercury?	M6 → B5	6	Magnetic field interaction: How does the planetary magnetic field interact with the solar wind in the absence of any ionosphere?
			7	Testing general relativity: Can we take advantage of the Sun's proximity to test general relativity with improved accuracy?

Tab. 6.3.1. Science questions to be addressed by the two missions. From McNutt Jr et al. (2004).

At the time of editing this thesis, the MESSENGER spacecraft completed its third flyby with Mercury on 29 September 2009 and is now en route to insertion into orbit about the planet on 18 March 2011 (Solomon et al., 2007). During these encounters, the cameras imaged ~91% of the surface, at a resolution of 500 m/pixel or better. Investigation on the new data points out the dominance of both volcanic features, suggesting long lasting internal activity, and lobate scarps, which records the global contraction associated with cooling of the planet (e.g., Solomon et al., 2008; Head et al., 2008; Prockter et al., 2010). In addition, MESSENGER data confirmed the presence of a liquid iron-rich outer core, coupled through a dominantly dipolar magnetic field to the surface, exosphere and magnetosphere, all of which interacting with the solar wind (e.g., Slavin et al., 2008, 2010).

6.3.1 Mission Overview

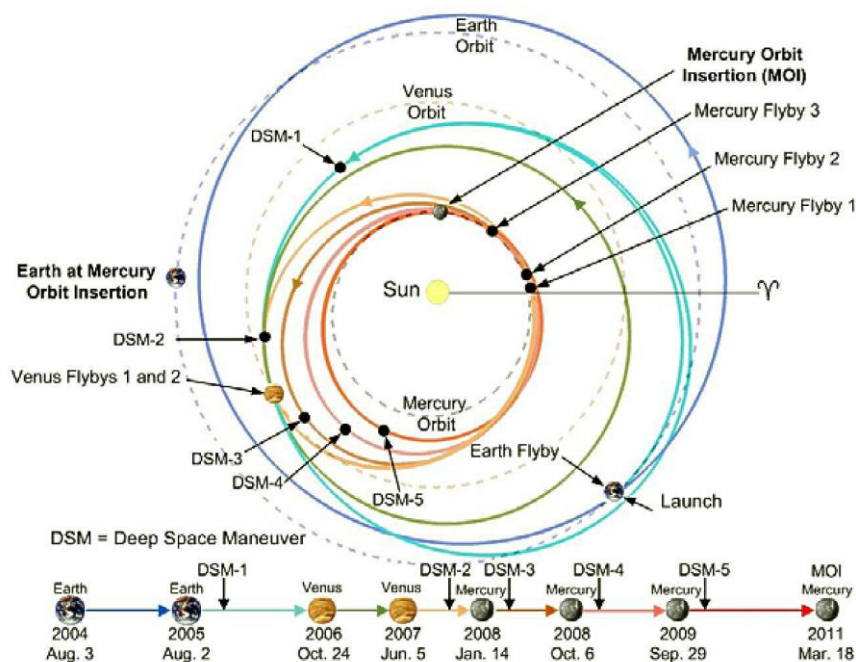


Fig. 6.3.1. MESSENGER cruise trajectory from the Earth to Mercury with annotation of flybys and maneuver events. Courtesy of NASA.

Delta II 7925H-9.5 rocket on August 3, 2004 from Cape Canaveral Air Force Station (McAdams et al., 2007). The major milestones from launch to orbit insertion are summarized in Fig. 6.3.1. The cruise phase covers six gravity assists from three planets —one with Earth, two with Venus and three with Mercury— as well as a number of propulsive corrections to the trajectory (deep-space manoeuvres, DSMs), in such a way that the spacecraft will accelerate from an average speed around the Sun of 30 *km/s* to 48 *km/s*. The cruise phase of the mission concludes in March 2011, when the spacecraft will encounter Mercury and execute the orbit insertion (Mercury orbiting insertion, MOI) maneuver, slowing down to be captured into an orbit around Mercury.

Within a few days of orbit insertion, the spacecraft will be in its mapping orbit, starting at 200 *km* above the surface at the periaapsis and 15,193 *km* at the apoapsis, with a 12-hour orbit period. The plane of the orbit will be inclined about 82.5° to Mercury's equator, and the low point of the orbit comes initially at 60°N latitude. During the orbit around Mercury the observations are staged by altitude and time of day so as to maximize scientific return among all scientific instruments, subject to restrictions on spacecraft attitude set by the need to maintain sunshade pointing within small angular deviations in yaw and pitch of the sunward direction. MESSENGER will orbit Mercury twice every 24 hours during the 12-month orbital mission covering four Mercury years. MESSENGER will obtain global mapping data from the different instruments during the first day and focus on target science investigations during the second.

6.3.2 Spacecraft & Payload

MESSENGER spacecraft was designed and constructed to withstand the harsh environment associated with achieving and operating in Mercury orbit (Leary et al., 2007). A ceramic-cloth sunshade, passive heat radiators and a mission design limiting time over the planet’s hottest regions protect MESSENGER from the harsh environment near the Mercury dayside.

The structure, primarily lightweight composite material, is a three-axis stabilized body, 1.42 m tall, 1.85 m wide and 1.27 m deep. Power is provided by two specially designed 2.6-m² solar arrays consisting of two-thirds mirrors and one-third solar cells for thermal management. The propulsion is provided by one bipropellant thruster for large manoeuvres and 16 hydrazine-fueled thrusters for small trajectory adjustments and attitude control. Telecommunications are provided by redundant transponders, solid-state power amplifiers, and a diverse antenna suite that includes two phased-array antennas, the first electronically steered antennas designed for use in deep space.

The measurement objectives for MESSENGER are met by a payload consisting of seven instruments plus radio science, for a total of 47.2 kg (Fig. 6.3.2) (e.g., Solomon et al., 2007; Leary et al., 2007).

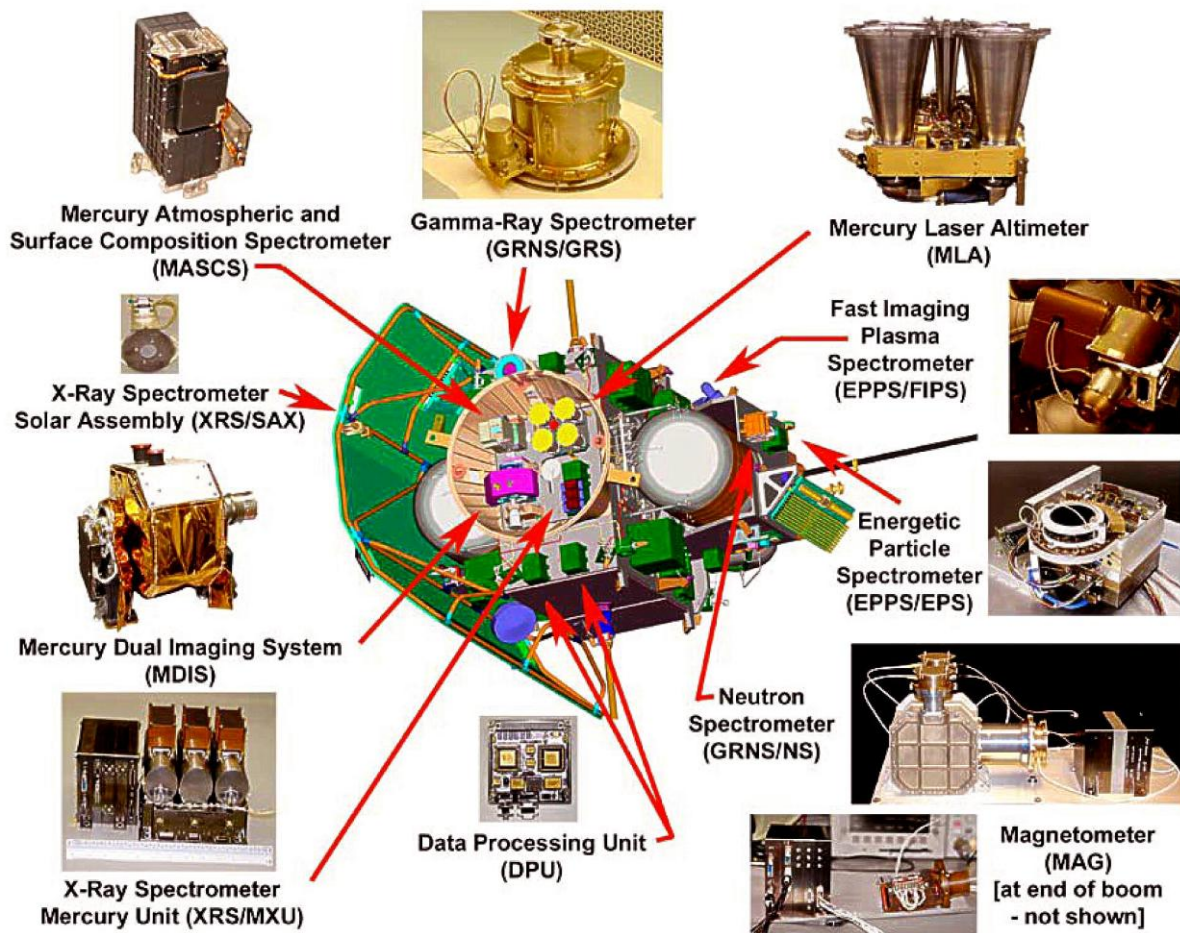


Fig. 6.3.2. MESSENGER payload and their locations on the spacecraft. From Solomon et al. (2007).

The instruments include the Mercury Dual Imaging System (MDIS), the Gamma-Ray and Neutron Spectrometer (GRNS), the X-Ray Spectrometer (XRS), the Magnetometer (MAG), the Mercury Laser Altimeter (MLA), the Mercury Atmospheric and Surface Composition Spectrometer (MASCS), and the Energetic Particle and Plasma Spectrometer (EPPS). The instruments communicate to the spacecraft through fully redundant Data Processing Units (DPUs).

The payload was selected by balancing the challenging of providing the full set of measurements required to satisfy the MESSENGER science objectives and the availability of mission resources for mass, power, mechanical accommodation, schedule and cost. In this case, payload mass was limited to 50 kg because of the propellant mass needed for orbit insertion. The instrument mechanical accommodation was difficult because of the unique thermal constraints faced during the mission; instruments had to be mounted where Mercury would be in view but the Sun would not, and they had to be maintained within an acceptable temperature range in a very harsh environment. In addition, the payload instrumentation has been selected to provide functional redundancy across scientific objectives to give both complementarity of observations in case of problems and consistency checks of results (cf. Tab. 6.3.2).

Guiding Questions	Science Objectives	Measurements Objectives
What planetary formational processes lead to the high metal/silicate ratio in Mercury?	Map the elemental and mineralogical composition of Mercury's surface	Surface elemental abundance: GRNS and XRS Spectral measurements of surface: MASCS-VIRS
What is the geological history of Mercury?	Image globally the surface at a resolution of hundreds of meters or better	Global imaging in color: MDIS-WAC Targeted high-resolution imaging: MDIS-NAC Global stereo: MDIS Spectral measurements of geological units: MASCS-VIRS Northern hemisphere topography: MLA
What are the nature and origin of Mercury's magnetic field?	Determine the structure of the planet's magnetic field	Mapping the internal field: MAG Magnetospheric structure: MAG, EPPS
What are the structure and state of Mercury's core?	Measure the libration amplitude and gravitational field structure	Gravity field, global topography, obliquity, libration amplitude: MLA, RS
What are the radar-reflective materials at Mercury's poles?	Determine the composition of the radar-reflective materials at Mercury's poles	Composition of polar deposits: GRNS Polar exosphere: MASCS-UVVS Polar ionized species: EPPS Altimetry of polar craters: MLA
What are the important volatile species and their sources and sinks on the near Mercury?	Characterize exosphere neutrals and accelerated magnetosphere ions	Neutral species in exosphere: MASS-UVVS Ionized species in magnetosphere: EPPS Solar wind pick-up ions: EPPS Elemental abundances of surface sources: GRNS, XRS

Tab. 6.3.2. The guiding questions, science objectives and measurement objectives for the MESSENGER mission. Each question will be answered by observations from two or more elements of the payload, while the observations from each instrument will address multiple questions. *From Solomon et al. (2007).*

6.3.3 MDIS

The MDIS instrument (Hawkins et al., 2007) includes both a wide-angle camera (WAC) and a narrow-angle camera (NAC) with an onboard pixel summing capability. That combination of features was chosen to provide images of a nearly uniform horizontal resolution throughout MESSENGER's elliptical orbit while minimizing downlink requirements. Because of the geometry of the orbit and limitations on off-Sun pointing by the spacecraft, the WAC and NAC are mounted on opposite sides of a pivoting platform to provide for optical navigation and planetary mapping during the Mercury flybys. MDIS is the only MESSENGER instrument with a pointing capability independent of the spacecraft attitude. The MDIS pivot can point from 50° toward the Sun to 40° anti-sunward centered on nadir, where it is co-aligned with the other optical instruments, all of which are mounted on the spacecraft lower deck (cf. Fig. 6.3.3). The pivot platform drive has a redundant-winding stepper motor system and a resolver to measure the platform rotation to a precision $< 75 \mu rad$.

The thermal design for MDIS faced the challenge that the instrument must work in cold space and yet be able to point at the $> 700\text{-K}$ sub-solar region of Mercury for extended periods and still produce high-quality images. Throughout this range of environmental conditions, the charge-coupled device (CCD) camera heads are maintained between -10 and -40°C to minimize their dark noise. The MDIS thermal protection system includes high-heat-capacity beryllium radiators, diode heat pipes to shut off thermal conduction when viewing the hot planet, phase-change "wax packs" to limit temperatures during hot periods, and flexible thermal links to tie these elements together.

The WAC is a refractive design with a 10.5° field of view (FoV) and a 12-position filter wheel to provide full-colour mapping. The NAC is an off-axis reflective design with a 1.5° FOV and a single band-limiting filter. The passband is a compromise between limiting the light at Mercury to keep the exposure times reasonable and providing high throughput for stellar imaging required for optical navigation.

The CCD camera heads use highly integrated, low-mass electronics with 12-bit intensity resolution. The CCD detectors are $1,024 \times 1,024$ *pixel* frame-transfer devices with electronic shuttering. There is no mechanical shutter. There are both manual and automatic exposure controls, and the exposure range is from 1 ms to $\sim 10\text{ s}$. The cameras can be commanded to perform on-chip summing of 2×2 *pixels* for 512×512 *pixel* images as required. The imager hardware can also compress the images from 12-bit to 8-bit quantization with a variety of look-up tables. Images are sent directly to the spacecraft solid-state recorder. They are later read back into the main spacecraft processor for additional image compression as commanded on an image-by-image basis.

6.4 Rosetta

The International ROSETTA Mission is the third planetary cornerstone mission ESA's long-term programme Horizon 2000. Rosetta was approved in November 1993 by the Science Programme Committee of the ESA, as a follow-up mission of ESA's previous mission, GIOTTO, to comet 1P/Halley (Reinhard, 1986), and was established as a cooperative project between ESA, various European national space agencies and NASA.

Comets have been selected as the target of a planetary ESA cornerstone because they are widely considered to contain the least processed material in our Solar System since their condensation from the proto-solar nebula. Most likely even pre-solar grains have been preserved in these bodies. The physical and compositional properties of comets may therefore be a key to their formation and evolution, hence to the formation of the Solar System. The primary scientific objectives of Rosetta are therefore to investigate the origin of the Solar System by studying both the origin of comets and the relationship between cometary and interstellar material (Schwehm & Schulz, 1999).

Our current knowledge came largely from data acquired from telescopic observations, while only recent times saw devoted space missions, i.e. Deep-Space I to comet 19P/Borrelly, Stardust to 81P/Wild2 and Deep Impact to 9P/Tempell (Glassmeier et al., 2007). Cometary activity is rather localized at the nucleus surface with only minor parts being active and the activity being highly constant in short time scales. However, sometimes outbursts with dramatic increase of activity but unclear genesis occur. The dominant component is not water ice and a more proper characterization of the nucleus would be as an "icy dirtball". Organic material, that is CHON particles, has been observed, whereas some isotopic ratios and most elemental abundance differ from solar ones. Their surfaces can be evolved with very different landforms visible; impact structures have been observed. The Deep Impact results even suggest a layered structure with different physical characteristics, which led to the development of a layered pile model (Belton et al., 2006). Furthermore, some minerals must have been processed in hot ($T \sim 2000$ K) environment near the Sun or other stars. All the present results indicate that cometary nuclei are unique, have their own history, and are not entirely pristine.

On the other hand, many physicochemical processes, like sublimation, photochemical reactions and interactions with the solar wind and the high energy radiation in space alter the material originally present in the nucleus. The species observable from Earth and even in situ during flyby missions are consequently not representing the immediate molecular composition of the nucleus from formation times, although the currently available information already demonstrates the low level of evolution of cometary material (Glassmeier et al., 2007).

To get insight regarding cometary nucleus composition and alteration, Rosetta will rendezvous in 2014 with comet 67P/Churyumov-Gerasimenko close to its aphelion, which will be studied through two different strategies for more than one year until it reaches perihelion. On one hand, the comet's evolution

along the orbit with decreasing heliocentric distance will be investigated with the orbiter instruments by monitoring the physical and chemical properties of the nucleus and in situ analysis of the near-nucleus environment. On the other hand, Rosetta will release a lander, PHILAE, that will provide ground truth by directly analyzing the nucleus material (Glassmeier et al., 2007). The measurement goals of Rosetta include (Schwehm & Schulz, 1999):

- global characterization of the nucleus and determination of its dynamic properties;
- surface morphology and composition;
- determination of chemical, mineralogical and isotopic compositions of volatiles and refractories in a cometary nucleus;
- determination of the physical properties activity and interrelation of volatiles and refractories in a cometary nucleus;
- study of the development of cometary activity and the processes in the surface layer of the nucleus and inner coma, i.e. dust/gas interaction;
- study of the evolution of the interaction region of the solar wind and the outgassing comet during perihelion approach.

6.4.1 Mission Overview

The original target of the ROSETTA mission was comet 46P/Wirtanen. A failure of an Ariane rocket in December 2002 forced ESA to postpone the initially scheduled January 2003 launch and to re-target ROSETTA, now heading for comet 67P/Churyumov-Gerasimenko. ROSETTA was finally launched by an Ariane-5 G+ launch vehicle from the Guyana Space Center in Kourou, French Guyana, on March 2, 2004 (Glassmeier et al., 2007).

On its way to 67P/Churyumov-Gerasimenko (Fig. 6.4.1) the spacecraft employed four planetary gravity assist manoeuvres (Earth-Mars-Earth-Earth) to acquire sufficient energy to reach the comet. In addition, it flew by two asteroids of the Main Belt, (2867) Steins and (21) Lutetia, that represents the rocky targets of the mission and have been both recently visited at the time of editing this thesis. Rosetta is now enter in hibernation up to January 2014, when it is scheduled to start a series of rendezvous manoeuvres for comet 67P/Churyumov-Gerasimenko in May 2014.

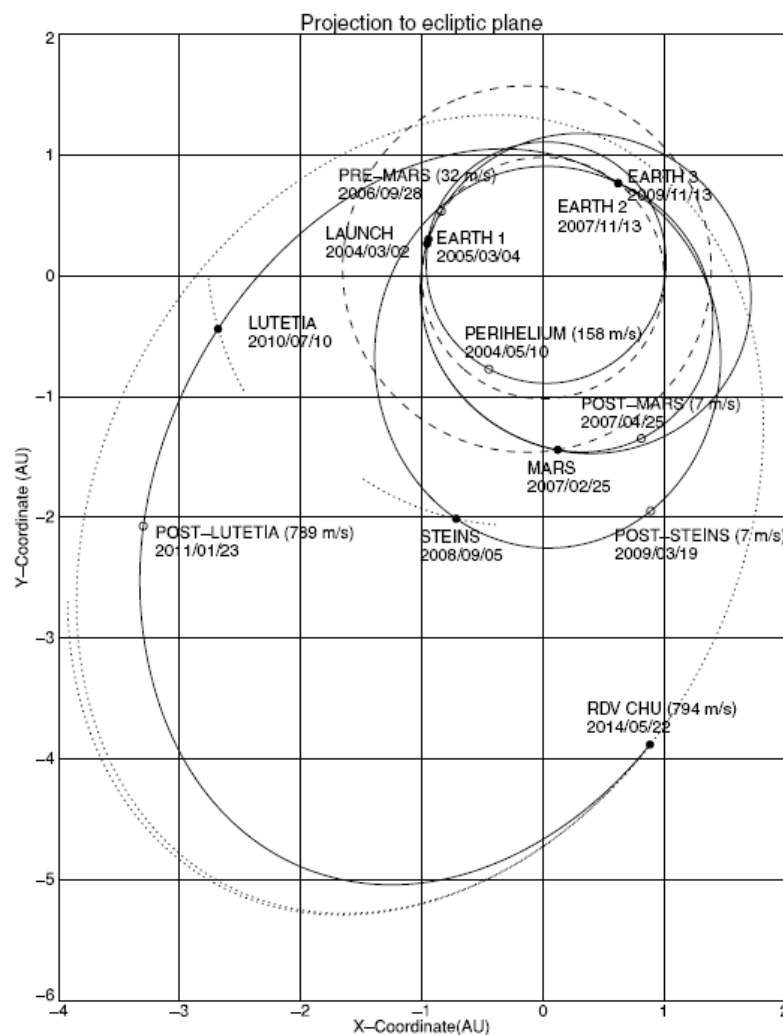


Fig. 6.4.1. ROSETTA's journey to 67P/Churyumov–Gerasimenko. *Courtesy of ESA, taken from Glassmeier et al. (2007).*

The rendezvous manoeuvre relies on lowering the spacecraft velocity relative to that of the comet to about 25 m/s and put it into the near comet drift phase, starting May 22, 2014 until the distance is about $10,000 \text{ km}$ from the comet. The final point of the near-comet drift phase, the comet acquisition point, is reached at a Sun distance of less than 4 AU . Changes in trajectories will be performed on the basis of a ground-based determination of the orbit from dedicated astrometric observations, before the comet is detected by the on-board cameras. The first camera images will dramatically improve calculations of the comet's position and orbit, as well as its size, shape and rotation. The relative speeds of the spacecraft and comet will gradually be reduced, slowing to 2 m/s after about 90 days.

At about 25 comet radii a capture manoeuvre will close the orbit. Polar orbits at 5 to 25 comet nucleus radii will be used for mapping the nucleus; this global mapping will start on August 22, 2014. After global studies of the nucleus are completed, about five areas ($500 \times 500 \text{ m}^2$) will be selected for close observation at a distance down to 1 nucleus radius.

At the end of the close observation phase, the landing site for PHILAE will be selected on the basis of the collected data. The lander will be delivered from an eccentric orbit and will touchdown at a maximum relative velocity of 1 m/s. Once it will be anchored to the nucleus, the lander sends back high-resolution images and the information acquired on the nature of the comet's ices and organic crust. The data are relayed to the orbiter, which stores them for transmission back to Earth at the next period of contact with a ground station.

The orbiter continues to orbit Comet 67P/Churyumov–Gerasimenko, observing what happens as the icy nucleus approaches the Sun and then travels away from it. The mission will end in December 2015. Rosetta will once again pass close to Earth's orbit, more than 4000 days after the launch.

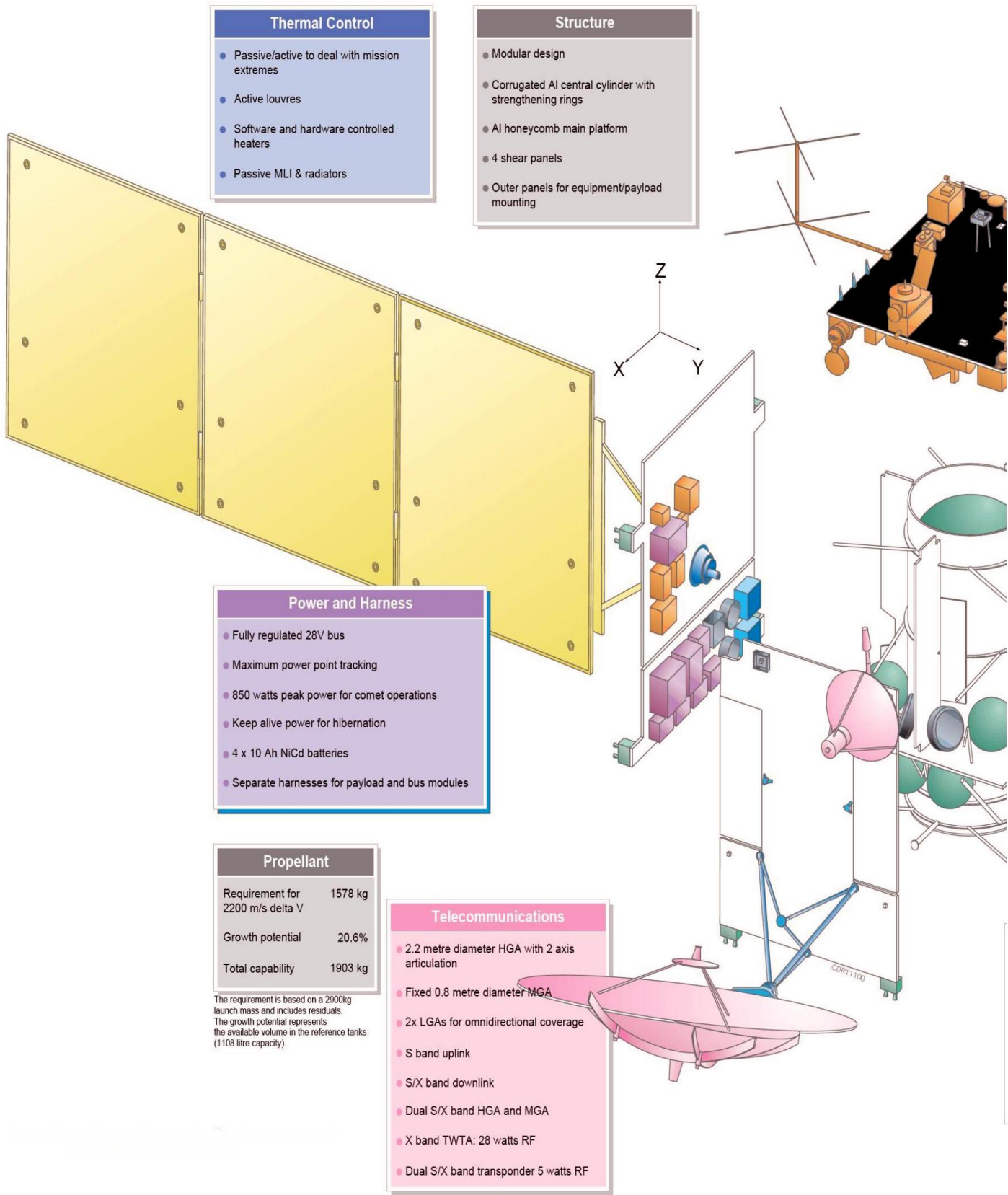
6.4.2 Spacecraft & Payload

Rosetta spacecraft is schematically represented in Fig. 6.4.2. It consists on 3-axis stabilized rectangular box of about $2 \times 2 \times 2$ m in size (Koschny et al., 2007). This central structure is completed by solar arrays as power source and a steerable high 2-m antenna as frequency linker with the Earth both in S and X band. Thrusters are used both for the attitude control and the trajectory changes manoeuvres.

Thermal control is a critical aspect for Rosetta, as the spacecraft has to sustain extreme conditions, both cold when approaching the comet, and hot when the distance to the Sun will decrease down to about 1 AU and all scientific instruments will operate. Thermal control is achieved by means of thermal insulation, radiators with louvers, thermostatic controlled heaters.

The payload includes a complement of remote sensing instruments, a set of composition analysis instruments, an instrument for nucleus large scale structure, an instrument for dust flux/mass distribution measurements and a package of instruments for comet plasma environment and solar wind interaction measurements, as well as the capability to perform radio science investigations. The lander payload comprises instruments of the comet composition, the comet physical properties, for large scale properties analyses and for cometary activity investigation.

Fig. 6.4.2 (Following pages) Exploded view of the Rosetta spacecraft. From Verdant & Schwehm (1998).



Thermal Control

- Passive/active to deal with mission extremes
- Active louvres
- Software and hardware controlled heaters
- Passive MLI & radiators

Structure

- Modular design
- Corrugated Al central cylinder with strengthening rings
- Al honeycomb main platform
- 4 shear panels
- Outer panels for equipment/payload mounting

Power and Harness

- Fully regulated 28V bus
- Maximum power point tracking
- 850 watts peak power for comet operations
- Keep alive power for hibernation
- 4 x 10 Ah NiCd batteries
- Separate harnesses for payload and bus modules

Propellant

Requirement for 2200 m/s delta V	1578 kg
Growth potential	20.6%
Total capability	1903 kg

The requirement is based on a 2500kg launch mass and includes residuals. The growth potential represents the available volume in the reference tanks (1108 litre capacity).

Telecommunications

- 2.2 metre diameter HGA with 2 axis articulation
- Fixed 0.8 metre diameter MGA
- 2x LGAs for omnidirectional coverage
- S band uplink
- S/X band downlink
- Dual S/X band HGA and MGA
- X band TWTA: 28 watts RF
- Dual S/X band transponder 5 watts RF

Mass (kg)	
Structure	198.9
Thermal	40.7
Mechanisms	38.6
Solar Array	169.7
Power	90.4
Harness	55.2
Propulsion	171.5
Telecommunications	44.8
Total	809.8

All masses include contingencies at equipment level, based on development status

Power Consumption (W)			
	Active Cruise X Band	Hibernation	Near Comet
Telecommunications	102 ⁽⁵⁾	8	102
AOCS/Propulsion *	89 ⁽¹⁾	0	134
DMS *	66	29	66
SADM/E	18 ⁽⁴⁾	0	18
Power	26	22	30
Thermal	100 ⁽²⁾	190 ⁽³⁾	40 ⁽²⁾
Payload *	0	0	270
Total	401W	249W	660W

The Solar Arrays and Power Subsystems can satisfy the total power required in all stages of the mission

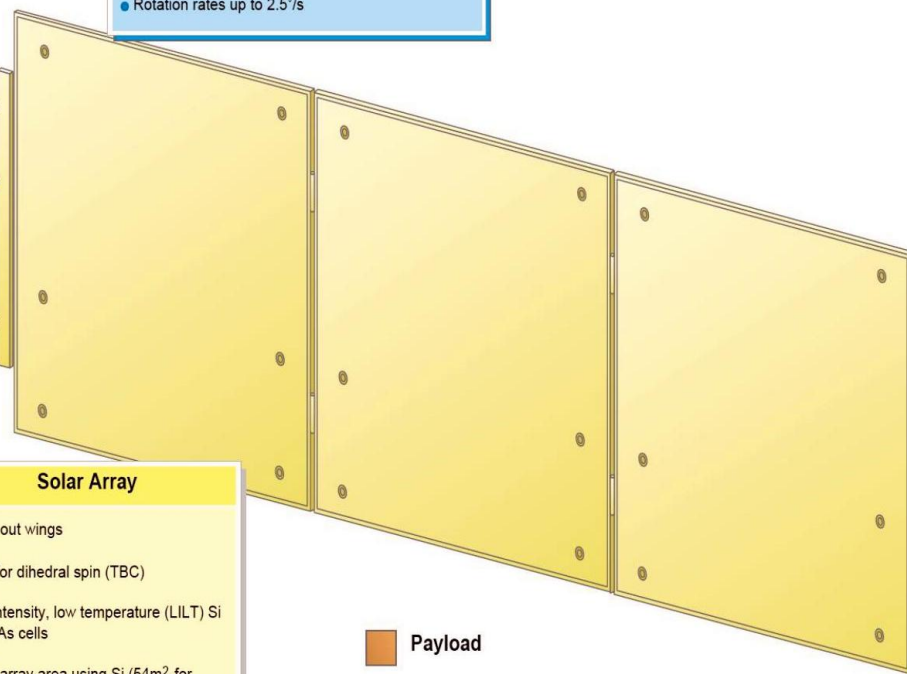
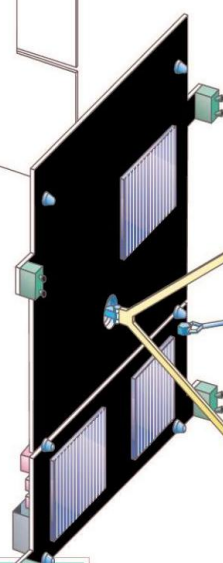
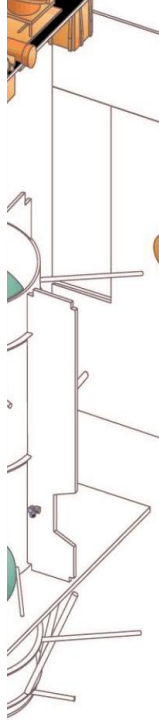
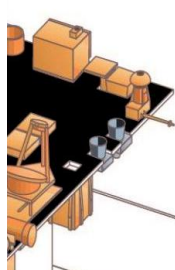
Notes: Figures represent "typical" mean consumptions. Actual figures vary throughout the mission.

- 1) AOCS/Propulsion increase by approx. 15W during manoeuvres
- 2) Typical thermal values - will vary according to sun distance and operational scenario
- 3) Represents aphelion worst case hibernation value. This is the solar array sizing case (353W output)
- 4) SADM/E power falls to zero when wings are not rotating
- 5) 54W for S band operations

*: Figures as specified in the ITT

Mechanisms

- 2 axis HGA pointing mechanism ($\pm 180^\circ$ azimuth 0 to 210° elevation)
- 2 SADM's (-90 to $+270^\circ$)
- 2 payload boom deployment mechanisms
- Flexible harness across rotating parts
- $< 0.04^\circ$ control
- Rotation rates up to $2.5^\circ/s$



Propulsion

- 2 x 1108 litre propellant tanks
- 4 x 35 litre pressurant tanks
- Pressure regulated and blow down operational modes
- 24 x 10N thrusters
- Usable propellant capacity 1571 kg

Solar Array

- 2 fold out wings
- Cant for dihedral spin (TBC)
- Low intensity, low temperature (LILT) Si or GaAs cells
- 68m² array area using Si (54m² for GaAs)
- 850 watts at 3.4 AU
- 353 watts at 5.2 AU

Payload
 Avionics

6.4.3 OSIRIS

OSIRIS (Optical Spectroscopic and Infrared Remote Sensing Imaging System) is the scientific imaging system onboard Rosetta, and is devoted to study the physical properties of the surface that may give origin to the cometary activity, and the way such activity influences the surface itself (Thomas et al., 1998; Keller et al., 2007).

Since Rosetta will act in close proximity to the cometary nucleus, OSIRIS was developed including both a narrow- and a wide-FoV imaging system. NAC (Narrow Angle Camera) will see in great detail portions of the surface of the comet, thus allowing the investigation of the nucleus physical properties, whereas WAC (Wide Angle Camera) will image large parts of the comet limb and of the inner coma, giving important information about the outflow of dust and gas directly above the nucleus surface (Naletto et al., 2002). The basic parameters of these two cameras are listed in Tab. 6.4.1.

	NAC	WAC
Optical design	3-mirror off-axis	2-mirror off-axis
Detector type	2k × 2k CCD	2k × 2k CCD
Angular resolution ($\mu\text{rad px}^{-1}$)	18.6	101
Focal length (mm)	717.4	140(sag)/131(tan)
Mass (kg)	13.2	9.48
Field of Views ($^{\circ}$)	1.20 × 2.22	11.35 × 12.11
<i>F</i> -number	8	5.6
Spatial scale from 1 km (cm px^{-1})	1.86	10.1
Typical filter bandpass (nm)	40	5
Wavelength range (nm)	250-1000	240-720
Number of filters	12	14
Estimated detection threshold (m_V)	21-22	18

Tab. 6.4.1. Optical characteristics of the OSIRIS camera.

Chapter 7

Results

7.1 Introduction to Applications

In this chapter, I am going to present the results I have achieved both in planetary age analysis and impact formation process modelling. In the following, a brief background to the work performed.

Age analysis (§ 7.2) has been focused on Mercury, one of the most enigmatic among the terrestrial planets (e.g., Strom and Sprague, 2003), caused also by the paucity of information collected about this body. For more than three decades, the major findings rise from the Mariner 10 data acquired during its three flybys in 1974–1975. However, relatively low average resolution, incomplete coverage, and limited spectral range of the image data left open some questions about its origin, the nature and evolution of its interior, and the geological processes that shaped its surface (Solomon et al., 2007; Head et al., 2007).

Only during these last years, a new mission has been devoted to visit Mercury. The MESSENGER took three gravity assists with the planet, providing a great deal of information pending its orbit insertion in 2011, first of all an extensive imaging of a portion of Mercury's surface never seen before. Up to the third flyby on 29 September 2009, 91% of the surface was imaged by MESSENGER cameras, raising to 98% the total surface recorded by both Mariner 10 and MESSENGER missions, at a resolution greater than 500 *m/px* (Prockter et al., 2010).

MESSENGER images revealed that (1) smooth plains are characterized by a range of compositions (Robinson et al., 2008; Denevi et al., 2009), (2) many occurrences of smooth plains are of volcanic origin (Head et al., 2008; Murchie et al., 2008; Strom et al., 2008), (3) Mercury displays evidence for a diversity of volcanic landforms and eruptive styles, such as flood basalt, small shield-building, and

explosive pyroclastic (Head et al., 2008, 2009a, 2009b), and (4) interior volatiles were present in some magmatic source regions (Kerber et al., 2009).

In particular, age analysis has been carried out for two new basins, that stand out for their peculiar post-impact evolution and their relation to volcanic processes. They are the “R-duet” (fig. 7.1.1): Raditladi (1st flyby, e.g., Strom et al., 2008), and Rachmaninoff (3rd flyby, e.g., Prockter et al., 2010).

Raditladi and Rachmaninoff (~300 *km* in diameter) soon appeared to be remarkably young because of the small number of impact craters seen within their rims (Strom et al., 2008; Prockter et al., 2010), likely formed well after the end of the late heavy bombardment of the inner Solar System at ~3.8 *Ga* (Strom et al., 2008; Massironi et al., 2009). In particular, Raditladi was pointed out to be as young as 1 *Ga* (Strom et al., 2008; Prockter et al., 2009).

A first aspect of interest regarding the presumed young age of Raditladi and Rachmaninoff basins together with their large sizes is connected to the formation of such large and young basins. The average impact velocity for NEOs striking Mercury is about 40 *km/s* Marchi et al. (2005). Considering a most probable impact angle of $\pi/4$ and the Holsapple and Housen (2007) crater scaling law, the projectiles responsible for the formation of the Raditladi and Rachmaninoff basins had diameters in the range 20–25 *km*. This result poses some puzzles, since only two NEOs, namely Eros and Ganymede, are presently known to have comparable sizes. It is not clear, therefore, how such basins could have formed given the paucity of impactors.

A second aspect is related to the fact that Rachmaninoff inner floor has been recognized to be volcanic in origin, as it is spectrally distinct with respect to the surroundings. The estimate of the temporal extent of the volcanic activity and in particular the timing of the most recent activity may represent a key element in our understanding of the global thermal evolution of Mercury, and it helps the analysis of the duration of the geologic activity on the planet in light of the new data provided by MESSENGER.

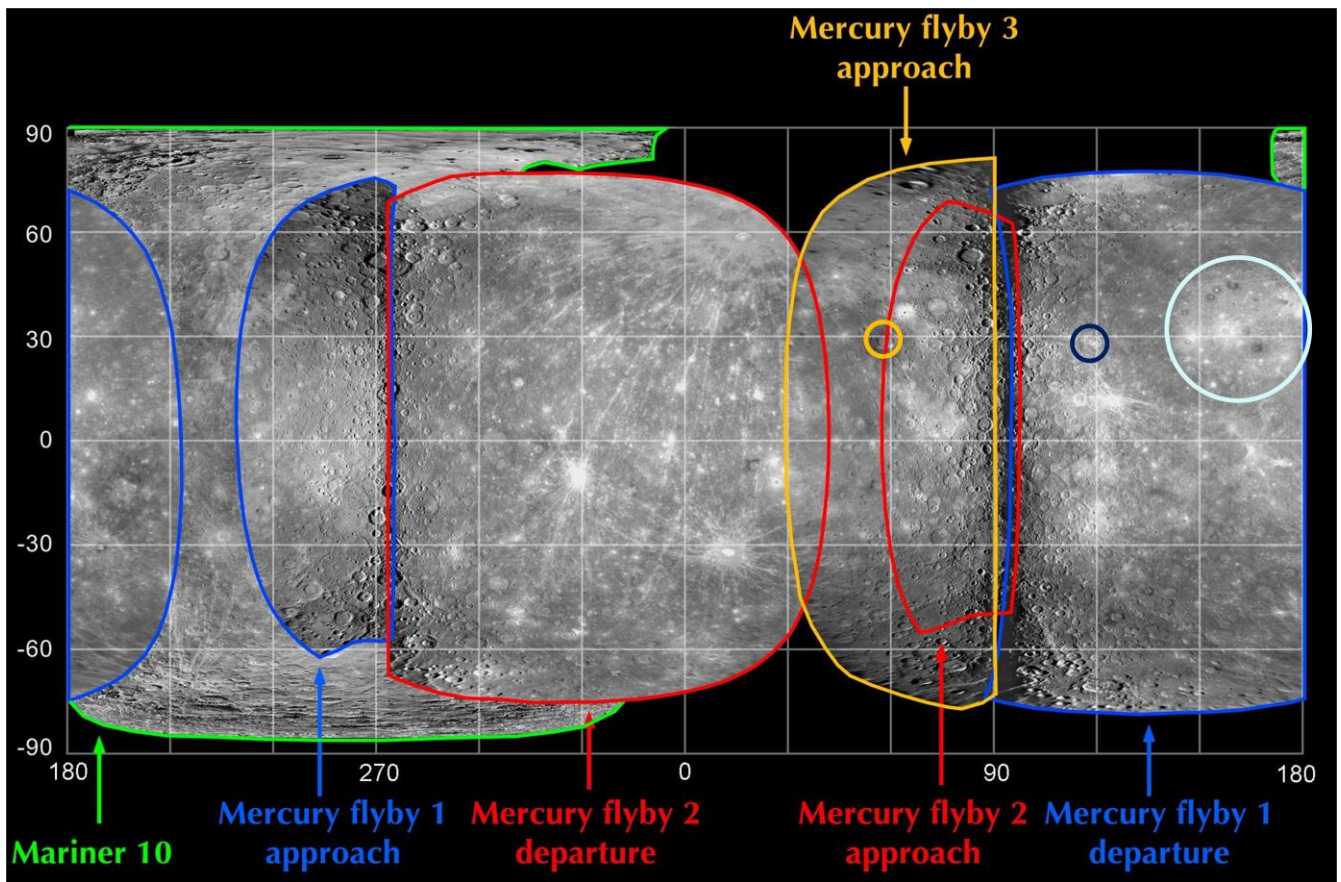


Fig. 7.1.1. Map of the Mercury total surface imagined up to now by the two NASA missions, Mariner 10 (1974-1975) and MESSENGER (2008-2009). The colored circles indicate the impact basins that are analyzed with age determination purpose in this thesis: Raditladi (yellow) and Rachmaninoff (dark blue). Caloris (light blue) is shown as well in the map for reference. *Modified after NASA image.*

Numerical modelling (§ 7.3) of the impact process is the second task of this thesis. It represents a recently widespread approach to investigate the formation of planetary-scale impact structures, since it allows to explore a wider range of crater size, to reach conditions not achievable in laboratory scale and to study the effects of each variable acting during the process.

My group started the study of the ring feature of suspected impact origin Omeonga, a ~40 km-diameter structure, located in the Central Africa (Martellato, 2010; Monegato, 2010). The area is hardly accessible for on-field investigations, hence, in the next future, sample collection to undoubtedly confirm the impact origin is not foreseen from our group. Up to now, extensive geomorphological and remote sensing analysis integrated with a stratigraphic and geological review of the area has been accomplished. The numerical modelling of Omeonga structure has the aim of integrate the geological observations in favour of the impact origin.

The last issue of this chapter regards asteroids, that appeared to be of highlight importance in a widespread of fields regarding planetary science (§ 7.4). I have focused my attention to two asteroids, recently observed by Rosetta spacecraft, on its way towards its final destination foreseen for 2014, the comet 67/Churyumov–Gerasimenko (e.g., Bar-Nun et al., 1993; Schwehm & Schulz, 1999).

The asteroids observed are (2867) Steins (~5 km in diameter) and (21) Lutetia (~100 km in diameter), that were flown by on 5th September 2008 and 10th July 2010, respectively. During both flybys, the wide and narrow angle cameras of the OSIRIS instrument on board Rosetta revealed the unique nature of these two bodies, as they do not resemble any other explored by previous space missions.

On one side, there is Steins. Despite only low resolution images were available because of acquisition problems occurred, a peculiar 2.1-km-diameter impact crater was identified on its surface, rising some hypotheses both on the following cratering record evolution and the consequences that a so huge impact can mean for a body as small as Steins.

On the other side, Lutetia, a puzzling asteroid already from ground observations (e.g., Belskaya et al., 2010), that is the largest asteroid visited by a spacecraft. The large amount of OSIRIS high resolution images revealed a complex world, made up by craters, mega-boulders deposits, linear features, exposed sliding surfaces and outcropping bedrocks, only to mention the most important characterizing structures.

In the extent of my thesis, Steins and Lutetia are differently investigated. Steins analysis regards the crater statistical analysis with age determination purpose. As the images collected for Steins all display a surface non orthogonal with respect to the camera, the IDL semi-automatic program (cf. § 4.6) was not suitable to determine craters dimensions. In this case, to minimize the uncertainty given from the asteroid curvature, crater sizes were obtained beginning from the shape of Steins.

On the other hand, the widespread of many large craters on Lutetia surface has whetted the idea of performing numerical modelling of a 21-km-diameter crater. This investigation was mainly addressed to provide important clues to the recently settled properties of Lutetia, in particular to what regards its composition and structure, but also to provide some input on the origin and evolution of the asteroid.

7.2 Crater Retention Age Determination: “*R-duet*”

Age analysis can be meaningful only for areas belonged to the same geological units, that have undergone similar endogenic and exogenic processes (e.g., Neukum & Ivanov, 1994). Hence, to accomplish age determination, a geological analysis has been assessed before.

The geological maps for the “*R-duet*” basins were constructed considering both floors and ejecta (Marchi et al., 2011). For the floor terrains, the geological units have been distinguished on the base of their different surface morphologies and spectral characteristics, i.e. albedo, joined with an analysis of their stratigraphic relationships. The ejecta units, surrounding the basins, were outlined considering exclusively the area of continuous ejecta blankets, which are easily detectable thanks to their typical hummocky surface. The geological maps take into account also the tectonic-related features affecting the areas.

Cratering age determination is based on the primary craters, i.e. formed by impacts with objects in heliocentric orbits (in the following, they can be addressed also as “bonafide craters”, in antithesis with “crater-like features” that include both impact and non-impact structures). Hence, a crucial point in assessing crater retention age is to avoid all secondary craters, that are mostly recognizable from their occurrence in loops, clusters and chains. Elliptical craters are not considered as they are most probably secondary, since grazing impacts are infrequent. In addition, craters with asymmetric shape have been taken as secondary, since their irregularity is likely due to interference with other adjacent secondaries and/or a relatively low impact velocity (Melosh, 1989).

7.2.1 Raditladi

During MESSENGER’s first flyby of Mercury, a 265-*km*-diameter double-ring impact basin, located at 27.0° N, 119.0° E west of the Caloris basin, was discovered (Strom et al., 2008; Prockter et al., 2009; Marchi et al., 2011). Raditladi (Fig. 7.2.1) on one way closely resembles lunar craters such as Schrödinger as well as similar-sized crater on Mercury such as Mozart, but on the other hand it soon appears to be very young.

The image-mosaic used for Raditladi has a spatial resolution of 280 *m/pixel* and the component images were obtained by the MESSENGER’s Mercury Dual Imaging System (MDIS) narrow-angle camera, while the color images, with a resolution of 5 *km/pixel*, have been obtained with the 11 filters of the MDIS wide-angle camera, which are centered on wavelengths from 430 to 1020 *nm* (Hawkins et al., 2007).



Fig. 7.2.1. Raditladi (27.0° N, 119.0° E) is a 265-km -diameter impact basin imagined for the first time during the 1st flyby of MESSENGER on Mercury. Characteristic features for such a basin are the peak ring structure and the terraced walls, but mainly it appeared very young. *Courtesy of APL.*

Raditladi contains an interior peak–ring structure that is slightly offset and $\sim 125\text{ km}$ in diameter (Head et al., 2009b; Prockter et al., 2009). The basin walls appear to be degraded, with terraces more pronounced within the north and west sides of the rim (Prockter et al., 2009). The hummocky continuous ejecta blanket with no visible system of rays surrounds the basin and extends up to 225 km from the basin rim.

The geological map of Raditladi (Fig. 7.2.2) was obtained following Prockter et al. (2009), considering two different units for the floor material: the smooth and the hummocky plains. Smooth plains may have a volcanic origin, as appear to be the case for plains in the nearby Caloris basin (Head et al., 2009a; Robinson et al., 2008). However, no clear stratigraphic relation with the hummocky plains has been found, suggesting that all the different terrains within Raditladi basin may be coeval and directly related to the impact.

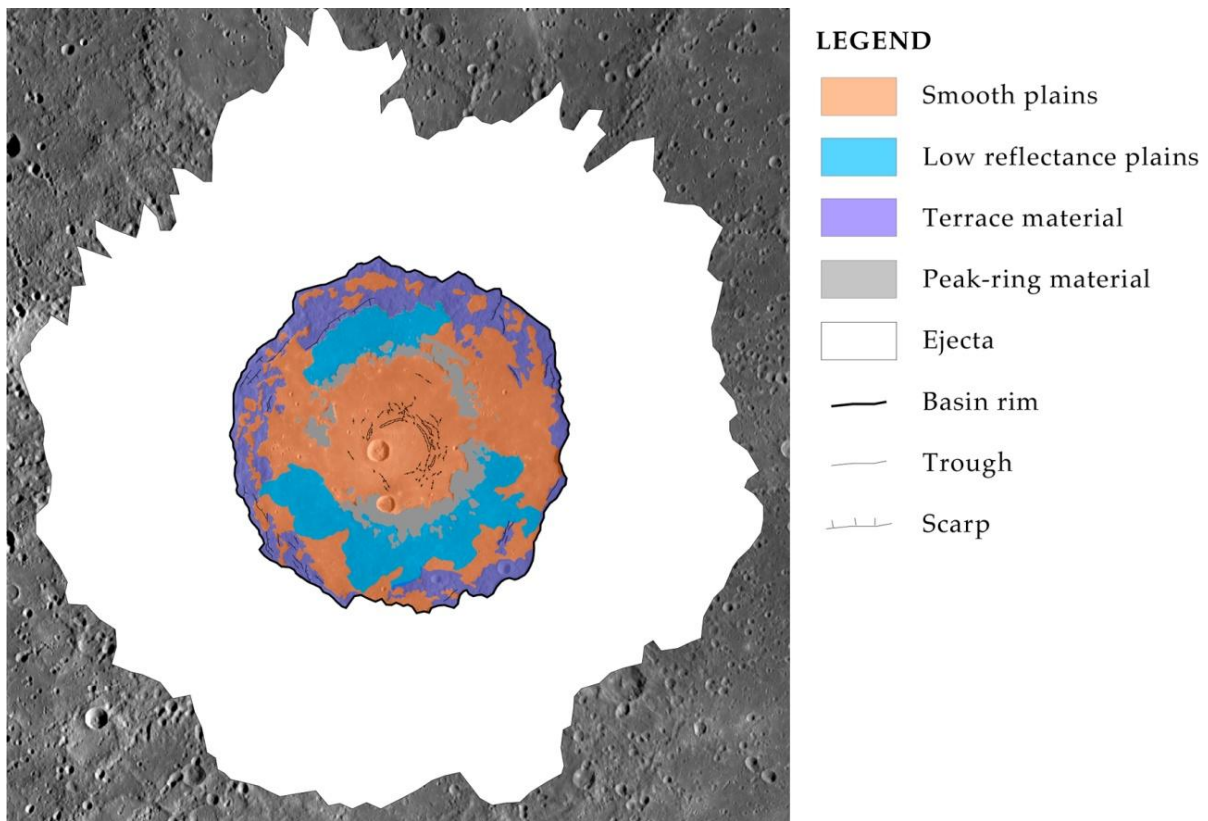


Fig. 7.2.2. Geological map of Raditladi, obtained following Prockter et al. (2009). The floor is mainly subdivided into two different units: the smooth and the hummocky plains, that do not display any clear stratigraphic relation, suggesting that all the different terrains within Raditladi basin may be coeval and directly related to the impact. *From Marchi et al. (2011).*

The multispectral images of the basin show that smooth, bright reddish plains material partially fill the basin floor mostly within the inner ring, but embaying also the rim and the central peak ring (Blewett et al., 2009; Prockter et al., 2009). The floor fracturing is found close to the center of the basin and consists of a series of narrow troughs arranged in a partially concentric pattern, ~70 km in diameter. This features are interpreted either as graben resulting from post-impact uplift of the basin floor, or as circular dikes possibly representing fissural feeding vents (Head et al., 2009b; Prockter et al., 2009).

The northern and southern sectors of the basin floor consist of dark, relatively blue hummocky plains material confined between the rim and the peak ring, and, as noted, embayed by the smooth plains material (Prockter et al., 2009). Evidence of impact melt, occurring as smooth reddish material, has been found on top of the ejecta blanket, which, because of its location, cannot have a volcanic origin. This observation gives strength to the assertion that the smooth plains may have an impact origin.

The impact origin was supported as well by the crater retention age analysis performed by Strom et al. (2008), since they pointed out that the density of small craters on Raditladi's ejecta deposits is similar to that of its floor. Hence, to understand the different processes that had shaped this basin, crater counts

and dating was carried out for the inner plains and the annular units within the basin, separately. The first one corresponds to the smooth plains located inside the peak ring, while the exterior region corresponds to the remaining areas enclosed between the basin rim and the peak ring. Counts were performed for the ejecta blankets as well.

The resulting statistics of both all crater-like features and bonafide craters greater than or equal to 1.12 km (4 pixels) (§ 4.6) for the three different units, i.e. inner plains, annular unit and ejecta blanket, are summarized in Tab. 7.2.1.

	All crater-like Features	Bonafide Feature
Inner Plains	71	56
Annular Plains	257	78
Ejecta Blanket	1565	421

Tab. 7.2.1. Crater statistics of both all crater-like features and bonafide craters greater or equal to 1.12 km for the inner plains, the annular unit and the ejecta blanket of Raditladi basin.

Crater retention ages will be based only on bonafide craters (shown in Fig. 7.2.3), as they are the only ones related to the impactor flux, and hence apt to date surfaces (§ 4). All the other features neglected in the statistics include both secondary impact craters and tectonic features (Fig. 7.2.4). Clusters and chains of secondaries are present on the annular plains. Within the inner plains, numerous small graben-related pits up to 5 km in diameter were found and recognized to be most probably tectonically-originated features and/or volcanic vents. Specifically, two peculiar pits (Fig. 7.2.4b) in the northern inner plains were interpreted as volcanic vents for the dark material on the crater floor (Head et al., 2009b). The ejecta blanket is characterized by numerous secondary craters, variously occurring mainly in clusters and chains. Isolating primaries from all the non-bonafide craters within the crater field was sometimes difficult to achieve.

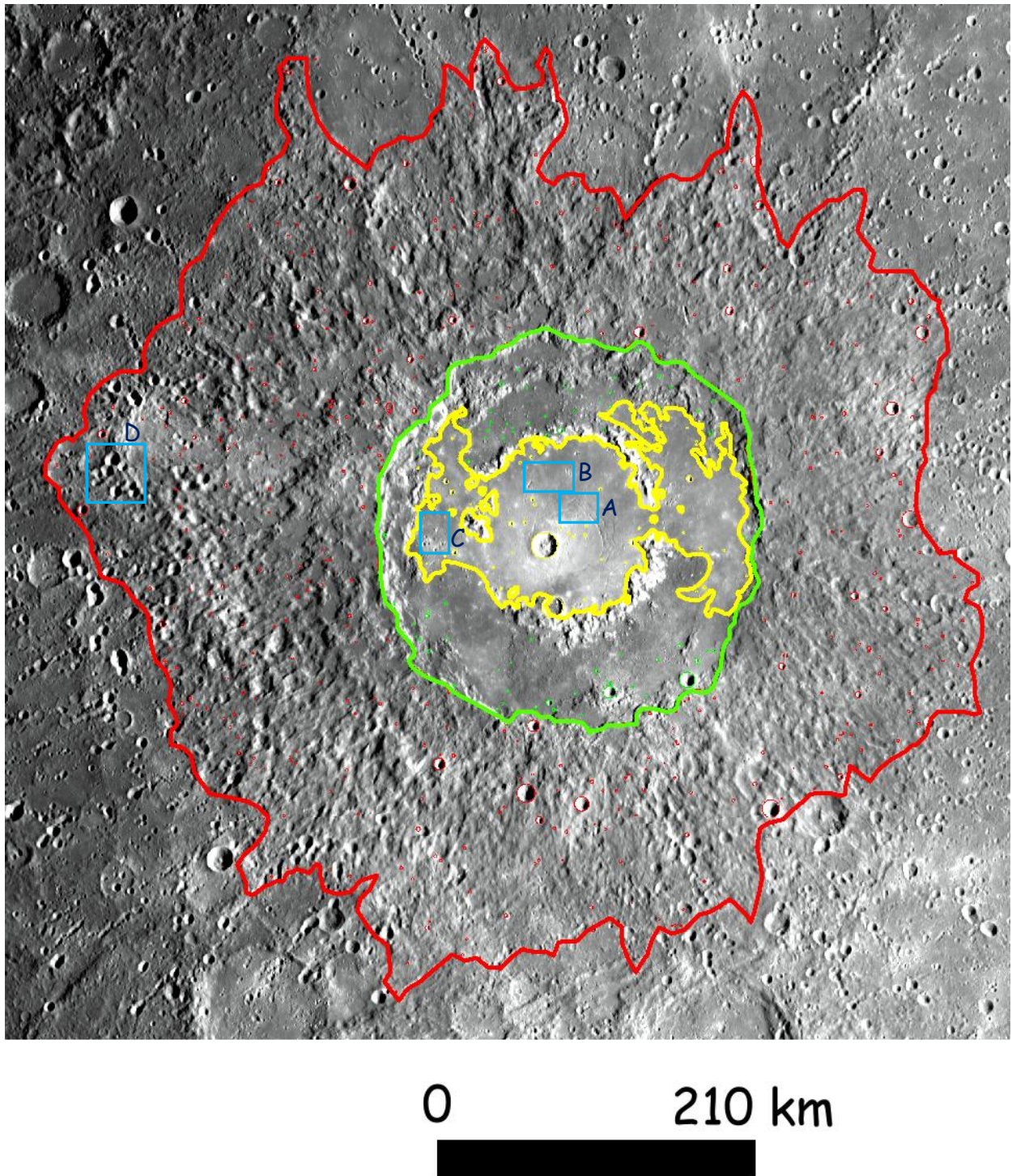


Fig. 7.2.3. Bonafide craters statistics in Raditladi basin and its surrounding ejecta, distinctly marked out on the base of the unit they belong to: inner plains (*yellow*), annular units (*green*) and ejecta blanket (*red*). The boxes indicate some interesting regions, represented enlarged in Fig. 7.2.4.

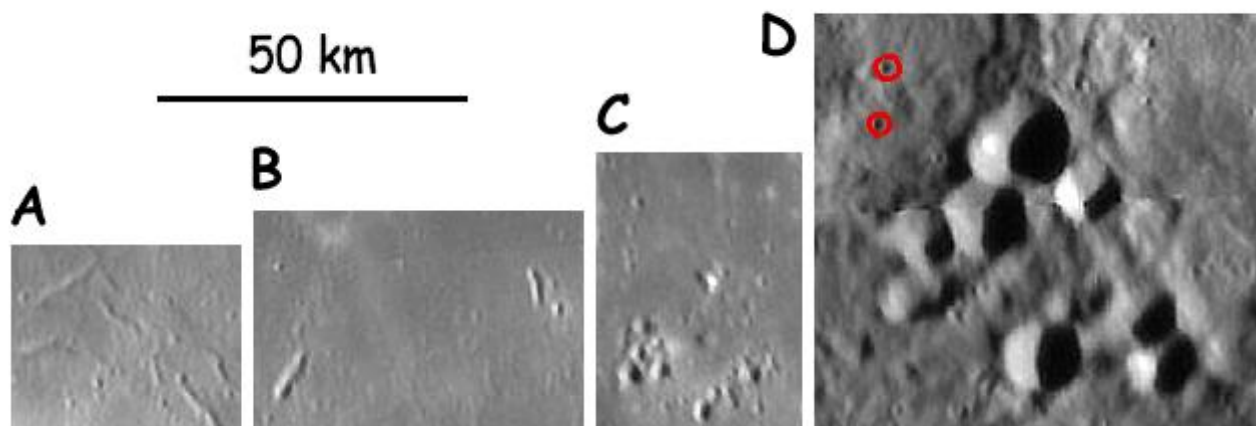


Fig. 7.2.4. Example of crater-like features on Raditladi basin. They are interpreted as of endogenic origins (volcanic or tectonic pits) (A, B), or secondary craters (chains and clusters) (C, D).

The cumulative crater SFD for different terrains of the Raditladi basin are shown in fig. 7.2.5a, along with the MPF model ages. The best fit for the annular units is achieved using a surficial fractured layer thickness of $D_t = 3 \text{ km}$. The resulting age is 0.98 Ga . As regards the inner plains, the poor statistics mean that the crater SFD cannot be used to constrain D_t . Hence, MPF age was derived by considering two different thicknesses, once time taking the value as for the annular units ($D_t = 3 \text{ km}$), and in the second case assuming a negligible thickness ($D_t \sim 0$). The ages resulted 1.53 Ga and 0.56 Ga , respectively. It is noteworthy that the former assumption of 3 km for the fractured layer implies that inner plains would be older than annular units. This is a paradox given that the annular units are certainly at least coeval with the basin formation and it is mainly due to the presence of two large craters ($D > 10 \text{ km}$) within the inner plains.

Since Raditladi do not show any particular albedo, color or overlapping relationship on its units, (Prockter et al., 2009), the inner plains were suggested to be likely coeval with the unit between the peak-ring and the basin rim emplaced during the impact event. In this case, it is appropriate to consider the crater SFD of the whole basin floor. The resulting model age is 1.37 Ga (Fig. 7.2.5b). The MPF age is in agreement with the age supposed by Strom et al. (2008) on the basis of a relative-chronology approach.

Concerning the ejecta blanket, the measured crater SFD is consistent with the basin floor therefore it implies a similar age. However, it is not easily modeled by MPF (Fig. 7.2.5c), most probably due to the rough texture of the ejecta blanket that makes the identification of craters very difficult.

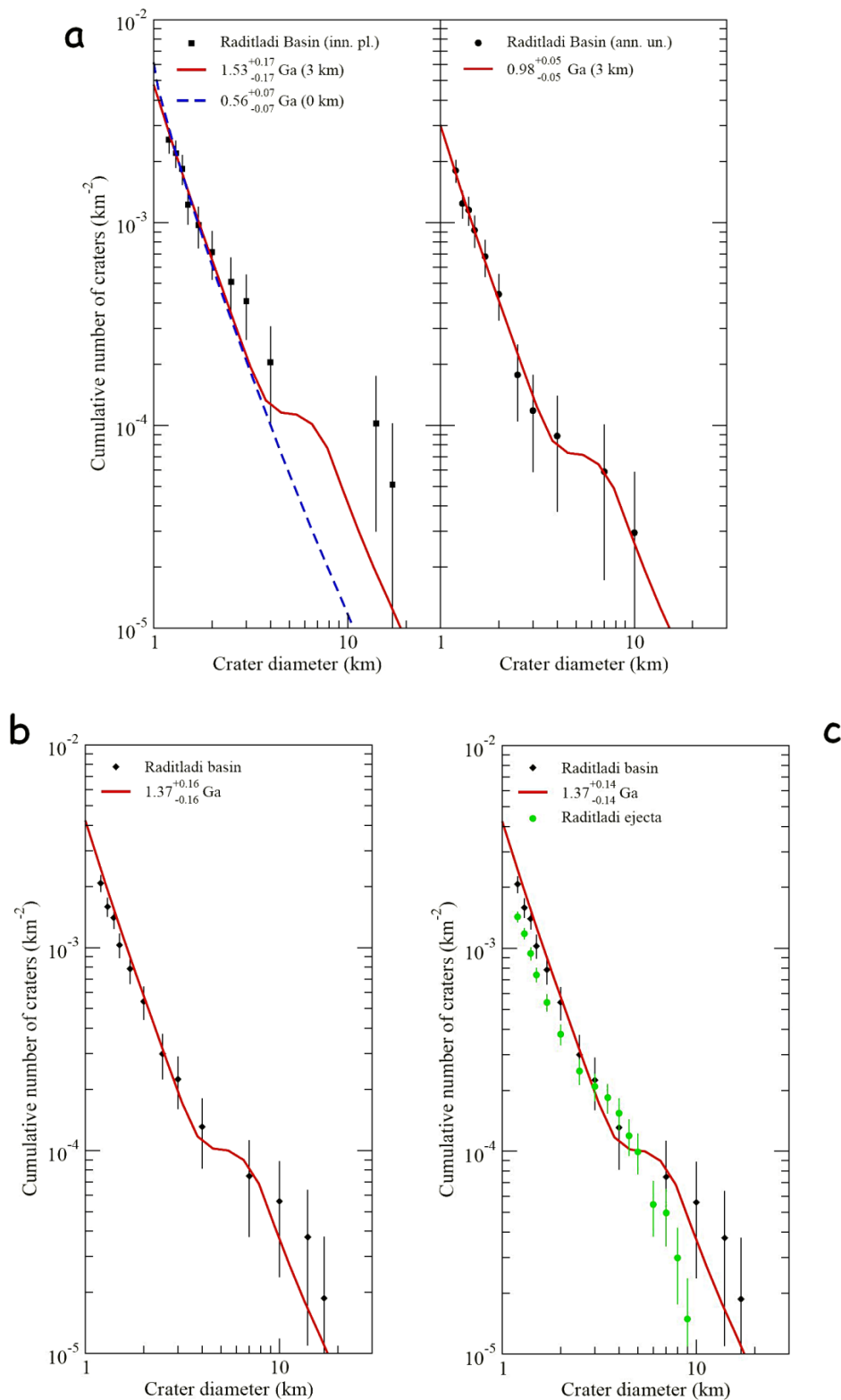


Fig. 7.2.5. (A) MPF ages for Raditladi inner plains (left panel) and annular units (right panel). In the latter case, the best fit is obtained with $D_t = 3.0$ km, while in the former one with both $D_t = 3.0$ km and $D_t \sim 0$ km. (B) MPF ages for the whole Raditladi floor (inner plains and annular units) achieved with $D_t = 3.0$ km. (C) Raditladi ejecta crater SFD compared to basin floor crater SFD and corresponding MPF best fit. From Marchi et al. (2011).

7.2.2 Rachmaninoff

The first two MESSENGER flybys allowed to collect a wealth of data, yielding to deepen many aspects regarding the surface, first of all the role of volcanism since it is a key element in our understanding of the global thermal evolution of Mercury (Prockter et al., 2010). Before the MESSENGER flybys the knowledge was based on the Mariner 10 data interpretation, that was in favour of a geological evolution lasting up to around the Caloris Basin, since both the Mansurian and Kuiperian systems seem to show evidence only of impact crater deposits, assuming no regional volcanic or tectonic activity (Spudis & Guest, 1988).

During MESSENGER's third flyby of Mercury, a 290-km-diameter double-ring impact basin, located at 27.6° N, 57.6° E, was discovered (Prockter et al., 2010; Marchi et al., 2011). Rachmaninoff (Fig. 7.2.6) appears to be relatively young among peak-ring basins on Mercury, as Raditladi itself, to which the new basin closely resembles in terms of size and morphology, demonstrated to be. It is surrounded by a continuous ejecta blanket, but no rays system has been detected. It shows a rim crest crisp and well preserved, while most of the basin walls are modified into terraces. In its interior, it includes a 136-km-diameter peak-ring structure and extended smooth plains filling its floor.

The image-mosaic used for Rachmaninoff and its ejecta has a spatial resolution of 500 *m/pixel* and the component images were obtained by the MESSENGER's Mercury Dual Imaging System (MDIS) narrow-angle camera (Hawkins et al., 2007).

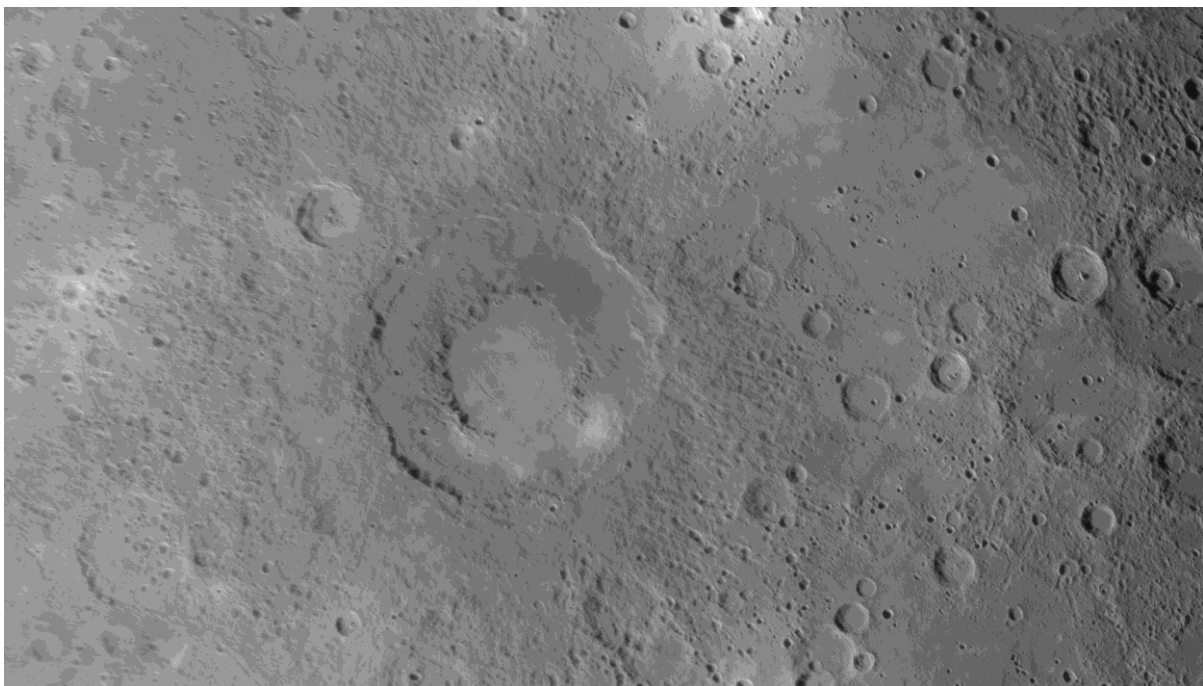


Fig. 7.2.6. Rachmaninoff (27.6° N, 57.6° E) is a 290-km-diameter impact basin imaged for the first time during the 3rd flyby of MESSENGER on Mercury. As the case of Raditladi, to whom it closely resembles, Rachmaninoff appears to be very young as well. *Courtesy of APL.*

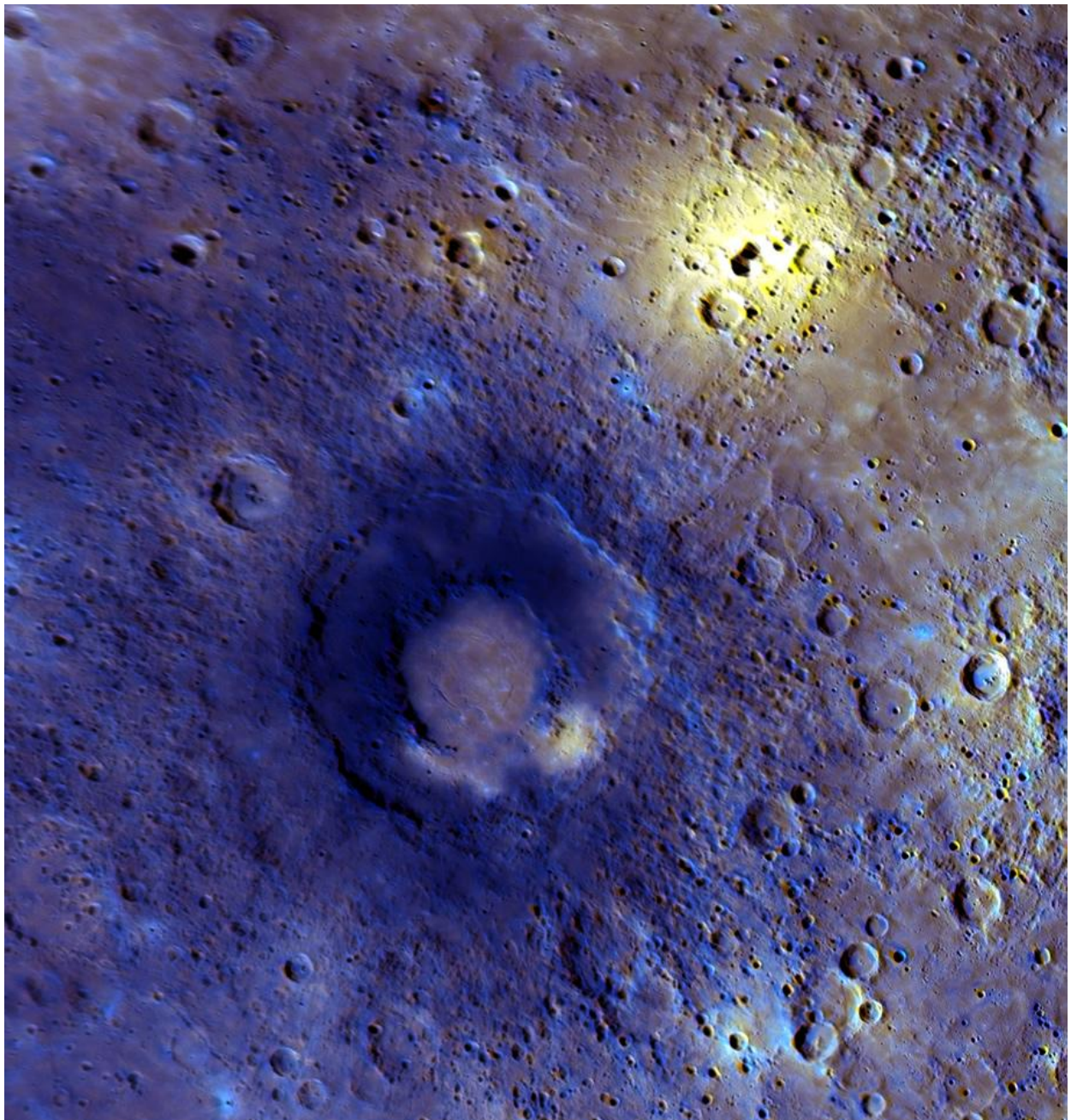


Fig. 7.2.7. Enhanced-color view (second and first principal component and 430-nm/1000-nm ratio in red, green, and blue, respectively) of Rachmaninoff, observed during MESSENGER's third flyby of Mercury. Lower-resolution wide-angle camera observations (5 km/pixel) were merged with the higher-resolution narrow-angle camera mosaic (430 m/pixel) to display color variations with geologic terrain. *Courtesy of APL.*

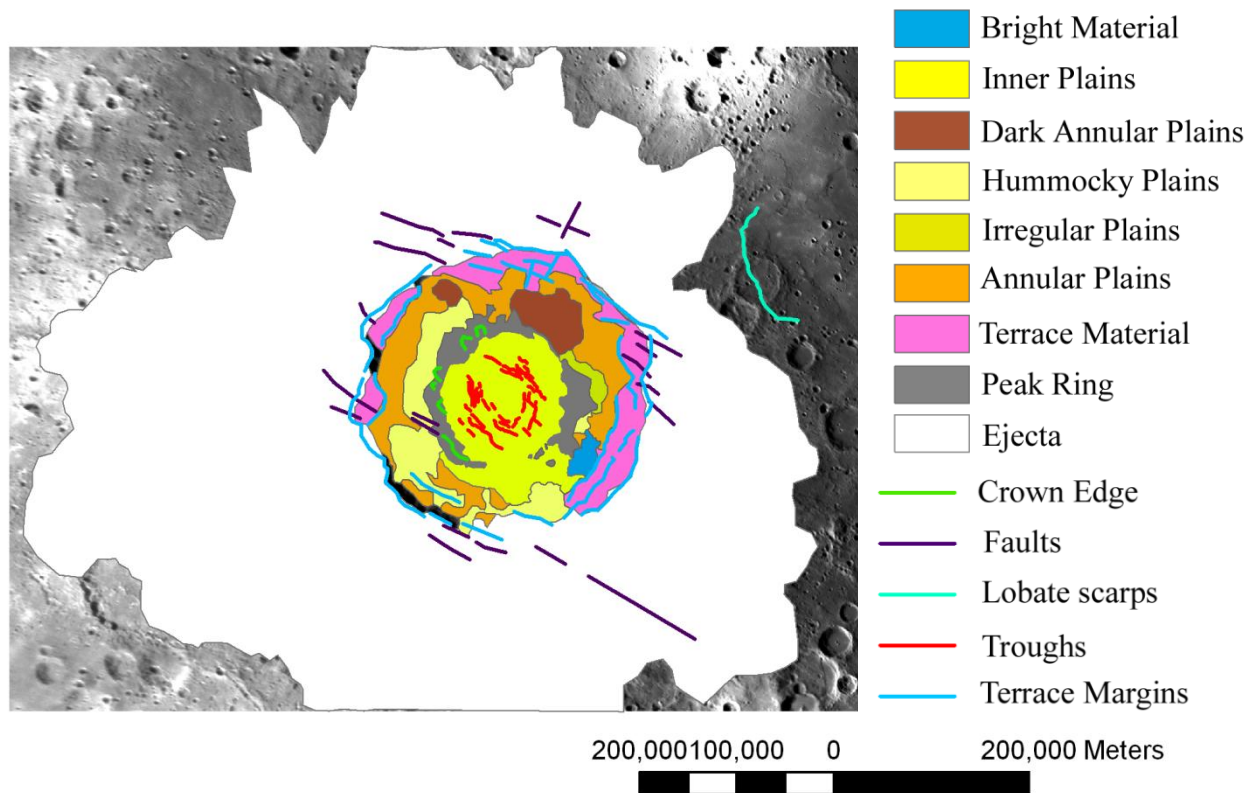


Fig. 7.2.8. Geological map of Rachmaninoff. The different relative albedo and surface texture of the floor revealed several terrains, that have been re-organized into two principal units: the smooth and the hummocky plains. Ejecta blanket is considered as well. From Marchi et al. (2011).

The geological map of Rachmaninoff (Fig. 7.2.7) revealed several different terrains inside the floor on the base of their different relative albedo and surface texture. The WAC enhanced–color image (Fig. 7.2.8) shows a yellow to reddish tone for the smooth plains, which stands out from the darker and bluer color of the other units within the basin and surrounding regions (Prockter et al., 2010). This strongly supports the different composition and origin of inner smooth plains from hummocky plains, suggesting a recent volcanic emplacement vs. an impact–related origin for the two terrains.

The inner smooth plains, mostly encircled by the peak ring, appear to have covered the other units (Marchi et al., 2011). Several discontinuous and concentric troughs possibly due to the uplift and extension of the basin floor, affect the area enclosed by the peak ring. These structures, interpreted as graben, are largely basin–concentric forming a nearly completing ring and basin–radial, and both typologies together form polygonal patterns similar to those seen in Caloris and Rembrandt basins (Prockter et al., 2010). The cumulative length of imaged graben is ~460 km, larger than in Raditladi, suggesting that the Rachmaninoff floor experienced greater extensional strain. The source of the extensional stress field in the interiors of Rachmaninoff is not known, but the confining of the extensional troughs to the central volcanic plains suggests that volcanism and deformation may have been related (Prockter et al., 2010).

The annular region between the peak ring and the rim basin includes seven different units. The most prominent one is made up of bright materials, apparently younger than all the other units and possibly related to explosive volcanism (Prockter et al., 2010). Peak ring and terrace material boundaries stand out for their relief, whereas hummocky, dark, irregular and annular smooth plains do not show unequivocal stratigraphic relationships with each other (Prockter et al., 2010). This suggests an almost coeval origin of these units that should consist of impact melts and breccias. This is furthermore confirmed by the WAC images, where annular units do not reveal any color variations and are characterized by a uniform blue color similar to the surrounding terrain. The rough-textured, hummocky annular deposits are concentrated outside of the uplifted peaks of the peak ring (Marchi et al., 2011).

To shed more light on the origin of the floor material, dating of the Rachmaninoff basin was performed by making crater counts for annular units and inner plains separately. Bright material was neglected in crater count due to its limited extension. Craters in the ejecta blanket were counted as well (Fig. 7.2.6).

The resulting statistics of both all crater-like features and bonafide craters greater than or equal to 2 km (4 pixels) for the three different units, i.e. inner plains, annular units and ejecta blanket, taken into account are summarized in Tab. 7.2.2.

	All crater-like Features	Bonafide Features
Inner Plains	50	8
Annular Plains	174	44
Ejecta Blanket	1183	175

Tab. 7.2.2. Crater statistics of both all crater-like features and bonafide craters greater or equal to 1.12 km for the inner plains, the annular units and the ejecta blanket of Rachmaninoff basin.

Crater retention ages will be based only on bonafide craters (shown in Fig. 7.2.8), as they are the only ones related to the impactor flux, and hence apt to date surfaces (§ 4). All the other features neglected in the statistics include both secondary impact craters and tectonic features (Fig. 7.2.9). Secondary craters have not been detected within the Rachmaninoff inner plains but numerous pits up to 3.5 km in diameter have been found in close proximity to the concentric grabens. These features are very unlikely to be impact craters and in my interpretation are most probably of tectonic and/or volcanic origin. For this reason, they were neglected during the counting procedure. Clusters and chains of secondaries with irregular and elliptical shapes were recognized in the western sector of the annular units and are numerous within the ejecta blanket.

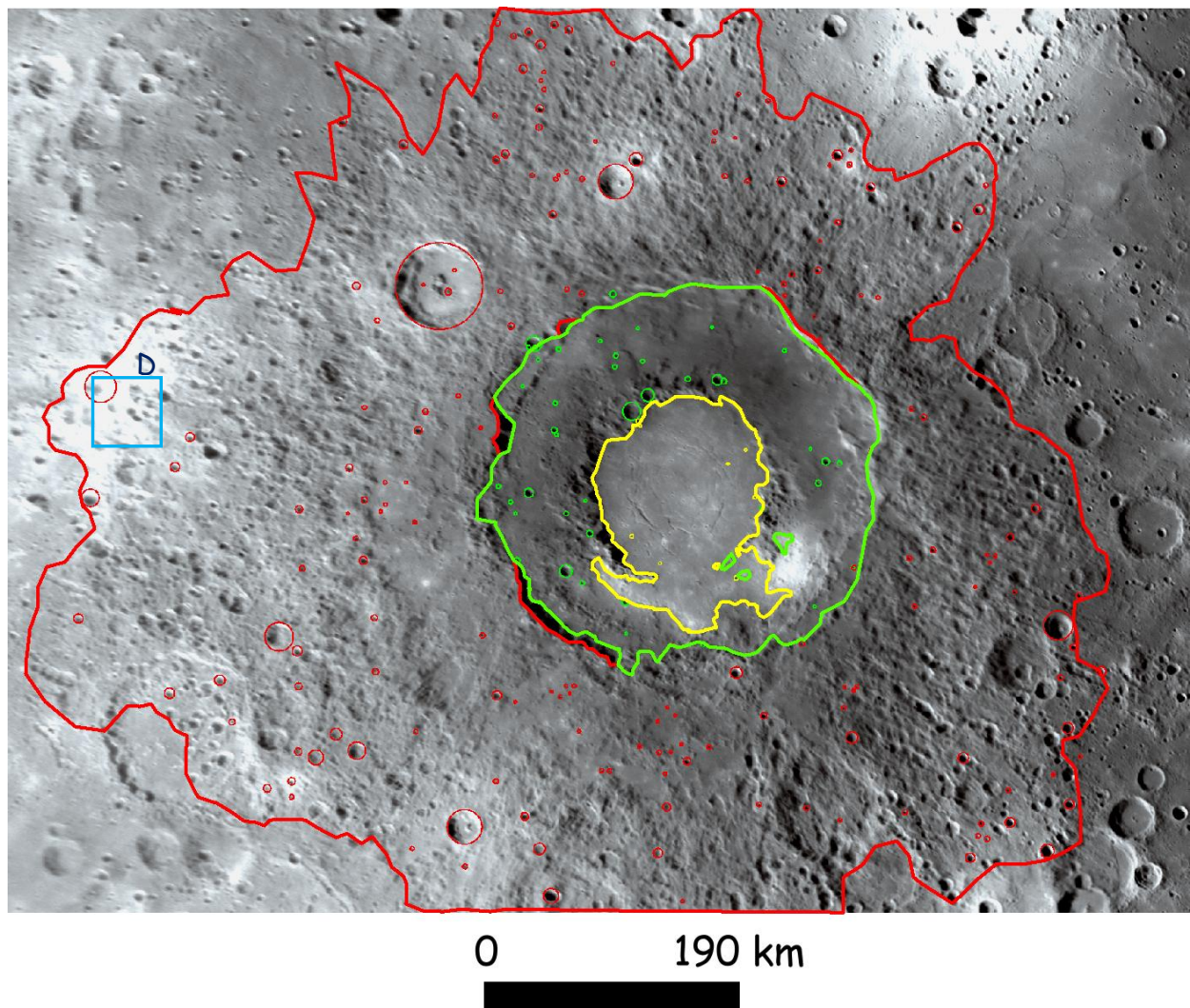


Fig. 7.2.8. Bonafide craters statistics in Rachmaninoff basin and its surrounding ejecta, distinctly marked out on the base of the unit they belong to: inner plains (yellow), annular units (green) and ejecta blanket (red). The boxes indicate some interesting regions, represented enlarged in Fig. 7.2.9.

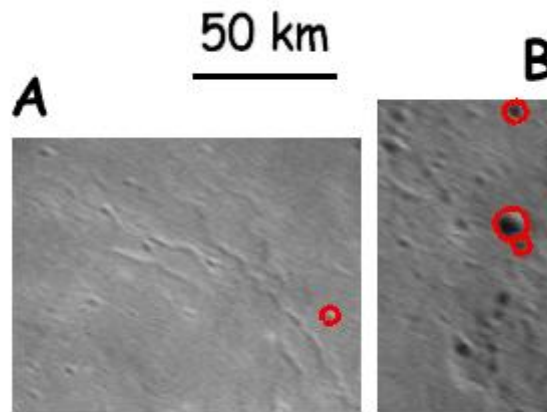


Fig. 7.2.9. Example of crater-like features on Rachmaninoff basin. They are interpreted as of endogenic origin (A), or secondary craters (B).

Fig. 7.2.10 shows the distribution of bonafide primary impact craters detected on the ejecta blanket. The plot in Fig. 7.2.10b reports also the MPF best fit age, achieved with a surficial fractured layer thickness of $D_t = 10.5 \text{ km}$. This value is consistent with values already determined for other large basins on Mercury (Massironi et al., 2009). The model best fit age is $\sim 3.42 \text{ Ga}$.

In Fig. 7.2.10a the bonafide crater SFD on inner plains and annular units are shown. The plot also shows the MPF model ages. For the annular units, I report the best fit using the same D_t of the ejecta, obtaining an age of $\sim 3.48 \text{ Ga}$. However, as proved by a lower χ_r^2 of the best fit, a better fit is achieved using $D_t = 4.5 \text{ km}$. In this case, the resulting model age is $\sim 3.39 \text{ Ga}$. The thickness of the fractured layer is consistent with the supposed brecciated nature of this terrain, possibly more or less welded by impact melt at depth, due to the formation of the basin. Notably, the model age is affected marginally by such variation in D_t , therefore the age of the annular units can be fixed to about 3.4 Ga .

Regarding the inner plains, the statistics are poorer, therefore the crater SFD cannot be used to infer D_t . Nevertheless, geological analysis suggests that the inner plains are younger volcanic flows on the basis of their different albedo, colour and overlapping relationship with respect to the unit emplaced between the peak-ring and the basin rim (Prockter et al., 2010). This would make possible also the scenario in which the former megaregolith horizon was completely hardened by lavas and the subsequent impacts were able only to create a very thin regolith layer, negligible to affect the formation of the sparse and relatively large craters detected. In this case the derived model age is 0.36 Ga . For comparison, the model age using $D_t = 4.5 \text{ km}$ as for the annular units yields to an age of 0.92 Ga (larger D_t would not affect the age determination). In either case, the inner plains turn out to be remarkably young, and demonstrate that a recent volcanic activity occurred within the basin.

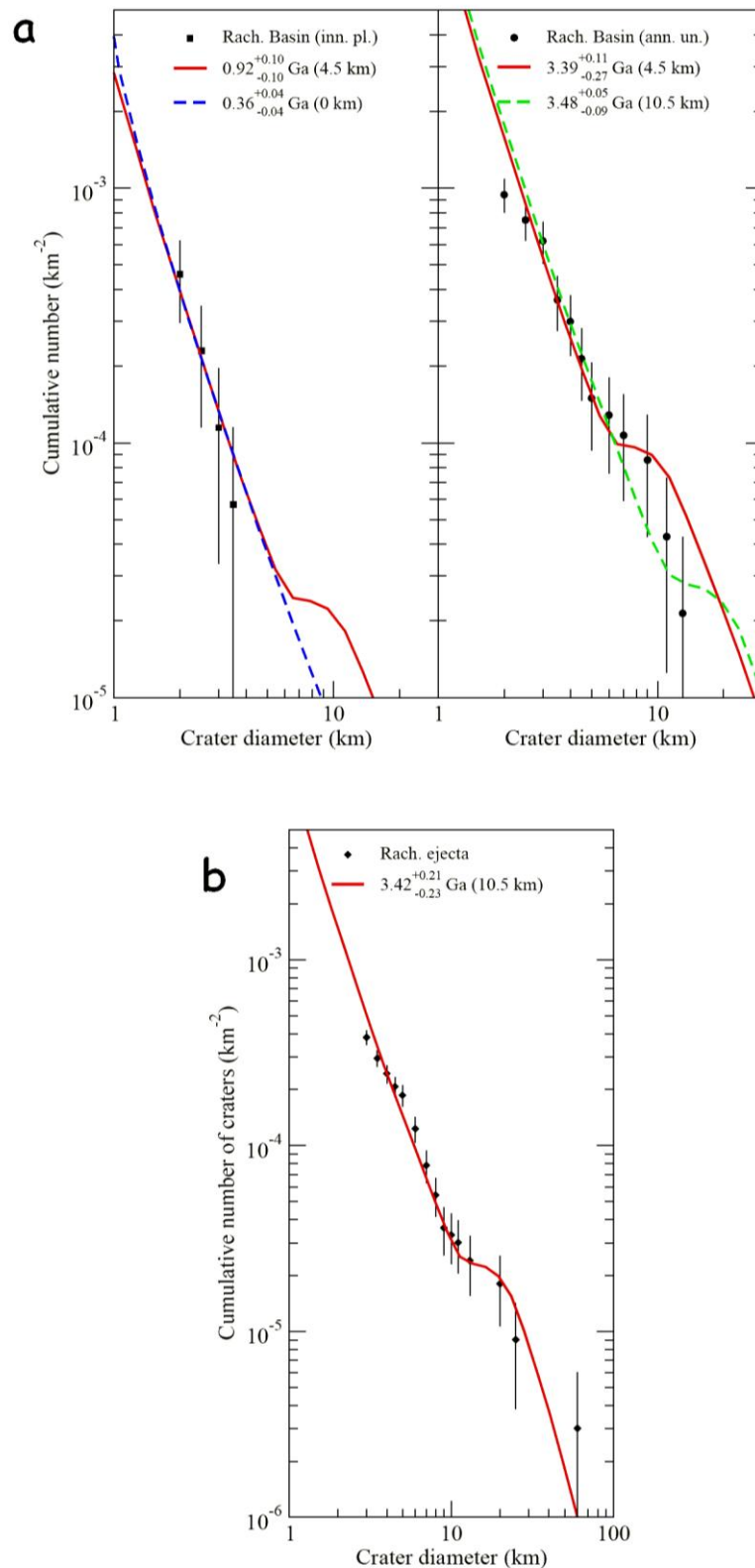


Fig. 7.2.10. (A) MPF ages for Rachmaninoff inner plains (*left panel*) and annular units (*right panels*). For the inner plains, the best fit achieved with $D_t \sim 0$ and $D_t = 10.5$ km (same as for ejecta) are shown. For the annular units, the best fit achieved for $D_t = 4.5$ and $D_t = 10.5$ km are reported. (B) MPF best fit of the age for the Rachmaninoff ejecta, assuming $D_t = 10.5$ km. From Marchi et al. (2011).

7.3 Numerical Modelling: Omeonga

I have focused the attention on a not yet studied ring structure found in the rain forest of the Central Africa and reported as a suspected impact crater in 2006 (Rajmon, 2006). The feature in hand is Omeonga, a structure formed within the Cenozoic stratigraphic unit (it cuts the Kwango Formation) of the Eastern Kasai and is therefore likely of the Cenozoic age, and hence formed within the last 65 *Myr*. If it is an impact crater, it would be a peak-ring basin, as the diameter measured on satellite images should be at least of 36 *km* (e.g., Melosh, 1989; French, 1998).

The aim of this analysis is to discuss the characteristics of this structure and the reliability of the impact origin on the base of a geological review of all the endogenic circular structures, the remote sensing interpretation and the available stratigraphic, geomorphological and geological information. However, no rock sample can be retrieved from this structure, and hence an ultimate word regarding its origin can not be established. To test the impact origin, I have performed numerical modelling of this structure and compared the model predictions with the DTM obtained from satellite images.

7.3.1 Background

The crater records of the Earth (Fig. 7.3.1) are still incomplete since the impact structures are difficult to be recognized because of the cumulative effects of fluvial erosion and transport and vegetation cover, that are particularly severe in warm climates. For this reason, craters are more easily recognizable in landscapes like deserts and prairies, rather than in rainforest areas, as testified in many databases (Spray, EID website: <http://www.passc.net/EarthImpactDatabase/index.html>; Rajmon, Impact Database website: <http://impacts.rajmon.cz>; Moilanen, Impact Structures of the World website: <http://www.somerikko.net/impacts/database-ref.php>).

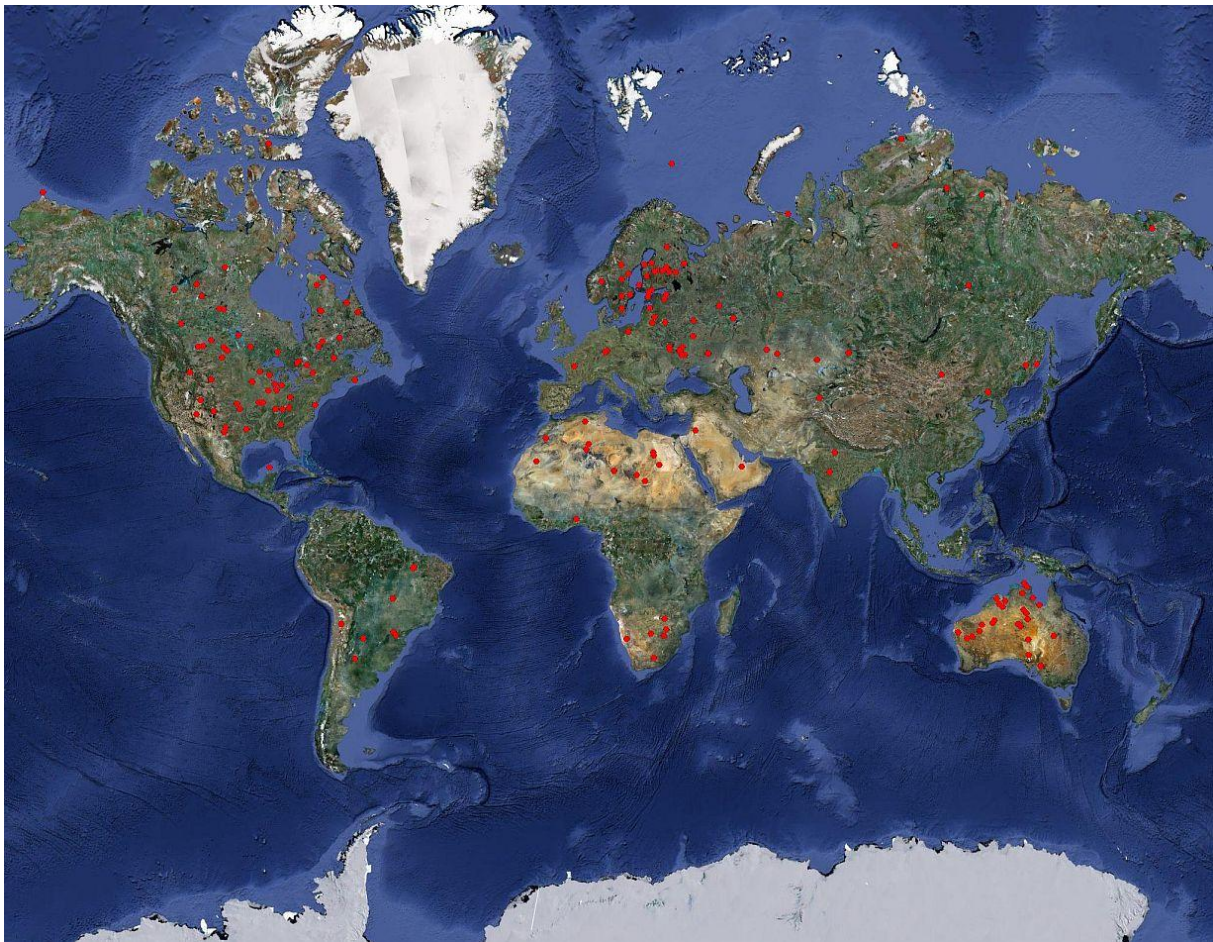


Fig. 7.3.1. Earth Impact Database, showing all the confirmed impact structures. *Courtesy of PASSC, EID database.*

7.3.1 Omeonga description and geological setting



Omeonga (Fig. 7.3.2) is a ring structure located in the Eastern Kasai province (D.R. Congo), centered at $3^{\circ}37'50''\text{S}$, $24^{\circ}31'00''\text{E}$, near the village of Omeonga, 37 km north of the Wembo–Nyama site in the Central African rain forest.

Fig. 7.3.2. GoogleEarth image of Omeonga, a ring structure located in the Congo Basin, which is suspected to be impact in origin.

The structure is recognizable in satellite images for the perfect roundness of the ring underlined by the Unia River, a tributary of the Lomami River. The ring formed by the river has a total diameter of 36 km. If Omeonga will turn out an impact structure, it should be classified as a peak ring, due to its large dimensions. To this extent, the Unia River would correspond to the crater floor, while the crater rim would be represented by the first hills chain defining the external side of the river. In the rim of the structure, one finds also the location of -the springs of the Tshuapa and Lukenia rivers, flowing into the main Congo River far westwards (Fig. 7.3.3c).

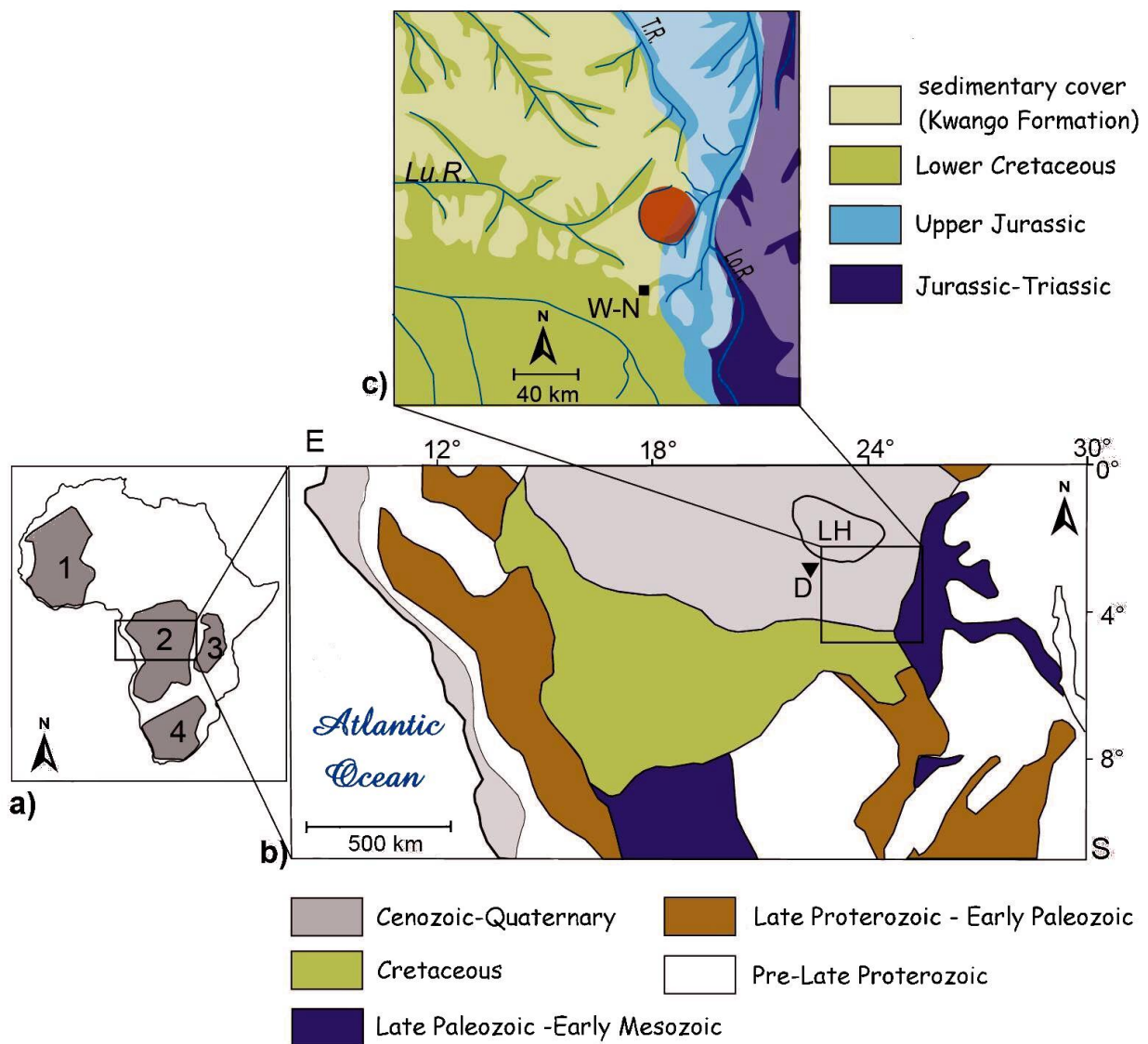


Fig. 7.3.3. (a) Distribution of the African Cratons: 1) West African Craton, 2) Congo-Kasai Craton, 3) Tanzania Craton, 4) Kalahari Craton. (b) Geological map of the central Africa, in which it is indicated the Dekese borehole (D) and the Lokonia Uplift (LH); *Modified after Giresse (2005)*. (c) Zoom on the geological map holding Omeonga (red); Lu.R.: Lukenia River, T.R.: Tshuapa River, Lo.R.: Lomami River, W-N: Wembo-Nyama village; *Modified after Choubert & Faure-Muret (1986)*.

Omeonga structure is located, as said, in the Eastern Kasai (Fig. 7.3.3), which is dominated by aeolian sandstones (Kwango Fm.), occurring in a few–tens–meters cover unit (Fig. 7.3.3c) (Choubert & Faure Muret, 1986). The Eastern Kasai region is in turn located the Cuvette Central of the Congo Basin (Cahen, 1954), one of the largest cratonic basins of the Earth, with a surface of about 1.2 million km^2 (Fig. 7.3.3a).

The stratigraphy of the Congo Basin can be likely described by the Dekese well, about 300 km westwards of the structure (Fig. 7.3.3b) (Downey & Gurnis, 2009), as both the seismic lines and the tectonic map seem to suggest. The upper layering of this area is schematically represented in Fig. 7.3.4, which points to a ~1800 m sequence of mainly sandstones, laying above the Precambrian basement of the Congo Craton (Batumike et al., 2009; Cahen et al., 1960; Daly et al., 1992). The underlying lithosphere is characterized by the presence of a high dense region, located at 200 km depth and consistent with a large positive upper mantle shear wave velocity anomaly, that gives origin to a large negative free–air gravity anomaly and a topographic depression of the Congo basin’s surface (Downey & Gurnis, 2009; Hartley & Allen, 1994; Sahagian, 1993).

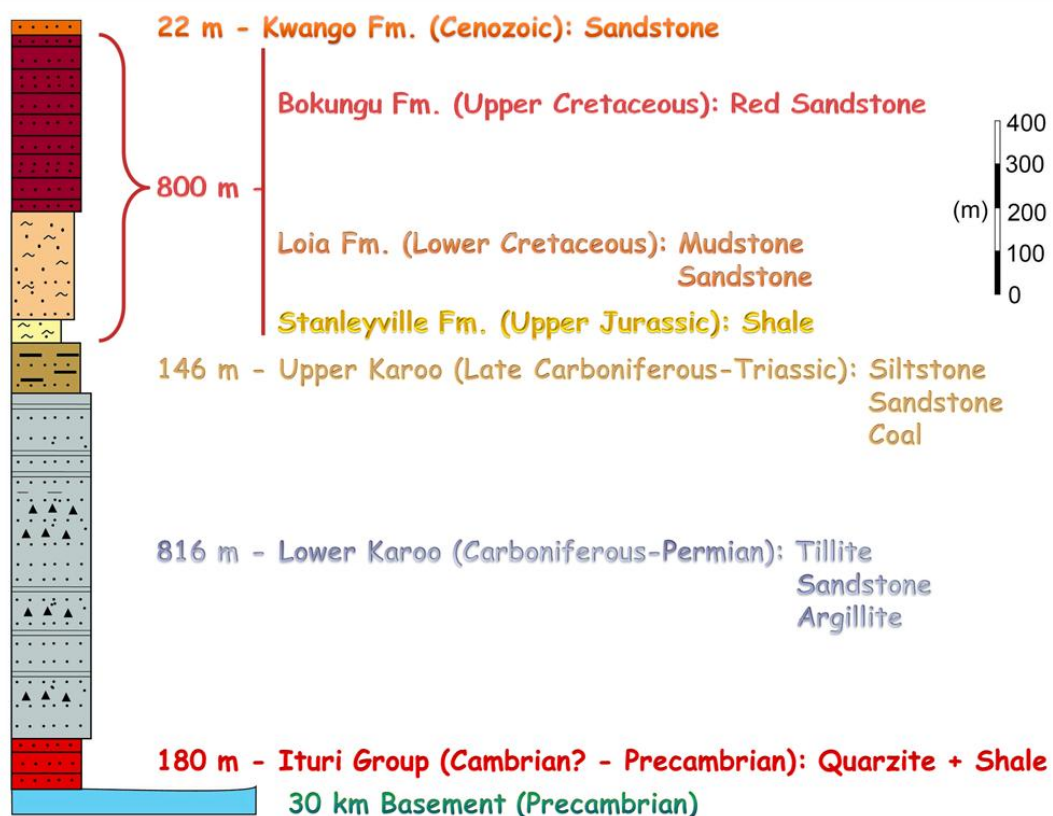


Fig. 7.3.4. Stratigraphy of the Dekese borehole modified after Cahen et al. (1960) and geological interpretation after Daly et al. (1992).

7.3.2 Remote sensing analysis

The remote sensing analysis was carried out on both LANDSAT 7 ETM and ASTER DEM (Digital Elevation Model) data, by using ENVI 4.7 and ARC-GIS software packages.

The LANDSAT 7 ETM scenes, i.e. 176-062 and 176-063 (Fig. 7.3.5), were acquired respectively on 05/02/2003 and 07/04/2002 and downloaded from the website <http://glovis.usgs.gov/>. These two images were orthorectified and superimposed on the ASTER DEM applying the WGS84-UTM projection, but have not been atmospherically corrected because the area of interest was clear enough and on such a vegetated environment no spectral analysis for the geological interpretation was required.

The adopted ASTER DEM was downloaded from the Global DEMs site (<http://www.gdem.aster.ersdac.or.jp/>), which collects DEMs derived from ASTER stereo-pair images. These DEMs have a grid resolution of about 29 *m/px* and an estimated accuracy of 20 *m* at 95% confidence for elevation and 30 *m* at 95% confidence for horizontal coordinates.

Most of the geological interpretation was performed on the LANDSAT RGB 7-4-2 false color composites sharpened using the panchromatic band 8, which is characterized by a higher ground-resolution with respect to the visible and short wave infrared bands of the ETM sensor (15 *m/px* vs. 30 *m/px*).

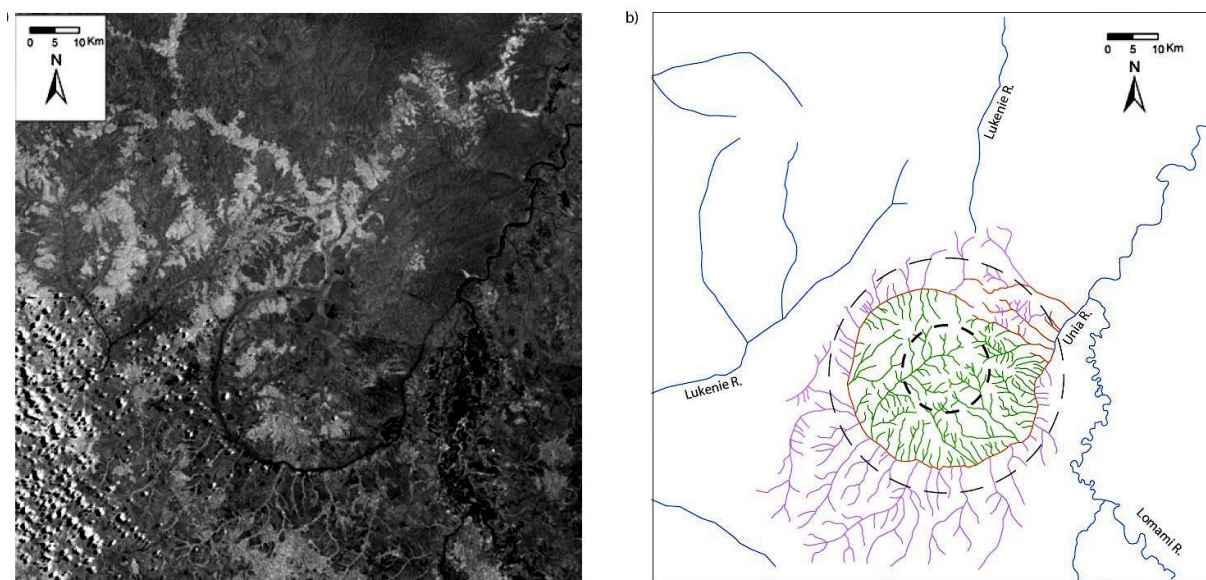


Fig. 7.3.5. (a) LANDSAT of the study area. (b) line-drawing of the drainage network in the study area, where the Unia river is emphasized (red line). Thin dashed circle: interpolation of the crater rim; Thick dashed circle: interpolation of the peak-ring.

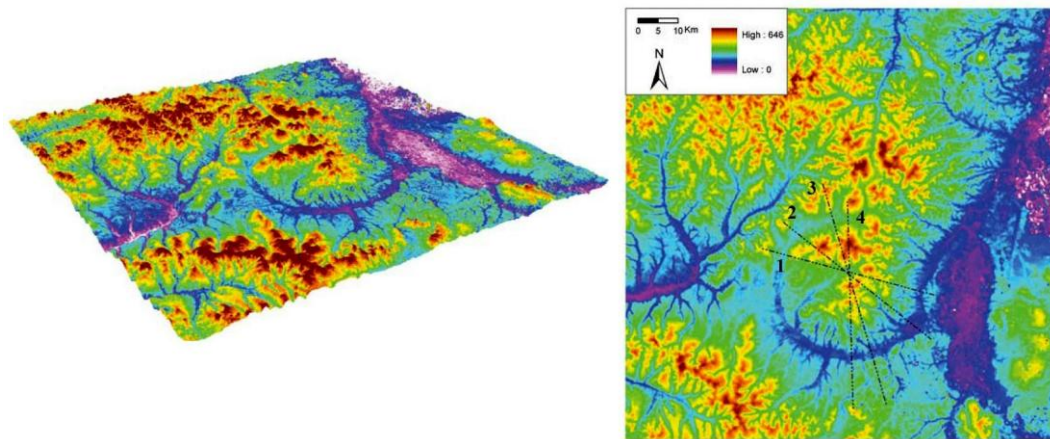


Fig. 7.3.6. ASTER DEM of the study area in which are drawn the traces of the profiles of Fig. 7.3.7.

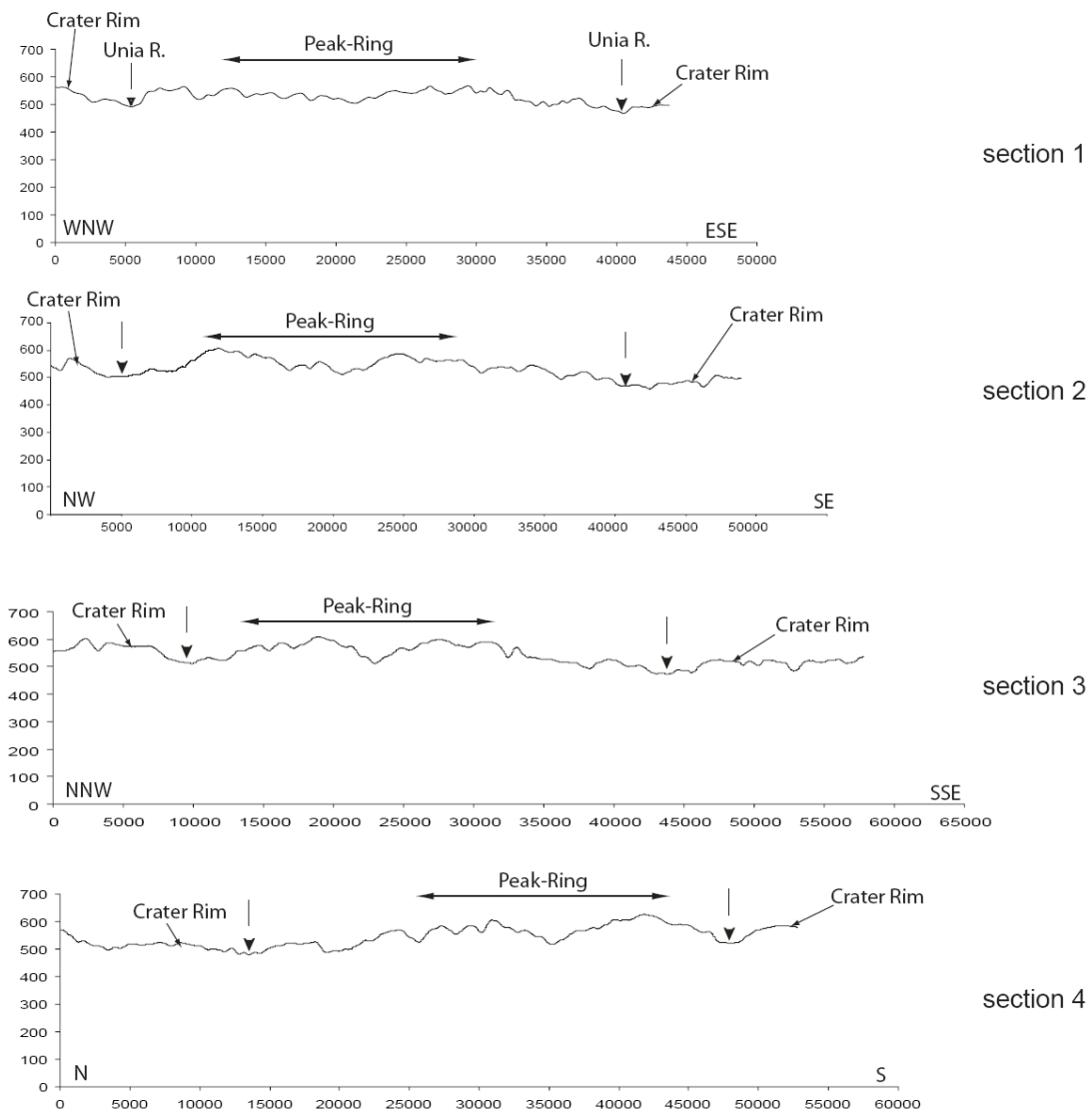


Fig. 7.3.7. Topographic profiles of the ring structure with the location of the Unia River and the inferred rim and peak-ring. The directions are given in Fig. 7.3.6.

The morphological analysis was carried out on the ASTER DEM and the related topographic profiles (Fig. 7.3.6a). These profiles were realized by smoothing the images with a mean filter based on a 15×15 grid kernel. In addition, hill-shades were included to emphasize the minor radial drainage. I used the circular Sun shading algorithm developed by Cooper (2003), which depends on two parameters, and precisely an origin and a value for the Sun elevation. I assumed the center of the Omeonga ring structure as origin and a value of 20° as Sun elevation. This setting provides images with sunshades both radial and tangential to the circular structure, enhancing features respectively parallel or perpendicular to radial vectors passing through the selected origin (Fig. 7.3.6b, c). This filter was preferred instead of the Hough transform, often used in crater detection, because it is less time consuming, as it does need only the position of the circle center, but not the radius value (Cooper, 2003).

ASTER DEM topography evidence a 36-km -diameter ring structure, continuous for about 280° , except for the north-east area, where a series of small tributaries complete the circular flow (Fig. 7.3.5b). If Omeonga is an impact structure, this ring where the Unia River flows would represent the floor of the crater between the basin rim and the peak ring.

The internal morphology has an average elevation of 550 m a.s.l. , $60\text{--}70\text{ m}$ higher than the ring depression where the Unia River flows, whereas the highest hill reaches 624 m a.s.l. (Fig. 47.3.6). Both radial sun-shade and topographic profiles do evidence an inner ridge. The diameter of this internal structure is estimated to be $13\text{--}20\text{ km}$, depending if either the ridge crest or the external slope is considered (Fig. 7.3.6). Small watercourses show a bent shape within the inner ridge, whose central part is cut by a Unia River tributary; this marks the central depressed area in the profiles of Fig. 7.3.7. Many small radial tributaries flow from the inner ridge to the trunk river in a centrifugal pattern (Fig. 7.3.5b). If Omeonga is an impact structure, this inner ridge represents the peak-ring.

Externally, the landscape has an average elevation of about 560 m a.s.l. , forming a continuous arched ridge towards the south-west and an irregular topography to the north (Fig. 7.3.6). However, a centripetal drainage network is clearly visible all around the circle of the Unia River (Fig. 7.3.5b). The tangential sun-shade clearly shows an uneven distribution of the external radial features, which are of limited length in the NW and SE quadrants, but instead can reach an extension of up to 27 km from the Unia River circular structure in the NE and SW quadrants. The enhanced erosion associated with the big Lomami River has partly obliterated the eastern external sector leaving just small and discontinuous hills (maximum elevation of 521 m a.s.l.) still displaying an arched trend (Fig. 7.3.6).

If Omeonga is an impact structure, the continuous arch formed by the 85-km long Unia River and its northern tributaries (Fig. 7.3.5b) can be interpreted as the inner margin of the crater rim, which is estimated to be 47 km in diameter.

7.3.3 Impact or non-impact origin?

Omeonga has been proposed to be an impact crater, but circular structures can be of either endogenic either regional tectonic origin. In the following, a number of different volcanic and intrusive circular-features-originating processes are discussed to understand whether they can likely create a so large structure, that is not so common in geological records.

Volcanic calderas and batholiths can display or exceed dimensions similar to those of Omeonga ($\geq 36 \text{ km}$) (Johnson et al., 2002), as for example the Meugueur-Meugueur ring structure of the Air Massif, which reaches 65 km in diameter (Moreau et al., 1986; Ritz et al., 1996). Nevertheless, the volcanic activity seems to have not affected the Omeonga region, as the East African Rift System is 300 km to the east of the studied area (Cahen, 1954; Master, 2010; Morgan, 1983; Choubert & Faure-Muret, 1986).

Kimberlitic pipes (Cox, 1978) have been detected in the south of the studied area (Milesi et al., 2006), but they are characterized by relatively low dimensions (about 4 km in diameter; Jacques et al., 1998) and a wide central depression not seen in the Omeonga structure.

Salt diapirs or domes are mostly located in tectonic active belts and frequently circular shaped, but they are characterized as well by moderate dimensions (up to 15 km in diameter; Aslop et al., 2000), as for example the salt diapirs of the Great Kavir (Jackson et al., 1990). Karst sinkholes can be excluded as well because either carbonate and/or sulphate successions in the area are negligible either no central peak-ring like feature is present within their structure.

All these presented geological arguments suggest that igneous intrusion, volcanic activity, salt diapirism or karst dissolution are not likely mechanisms for Omeonga structure, highlighting the possibility of an impact origin for the structure. On the other hand, the concentric path of the river together with the tributary river networks of Omeonga is similar to the drainage pattern found in many confirmed large impact structures (Mihalyi et al., 2008). Examples of concentric path of a trunk river are Popigai (Siberia) (e.g., Deutsch et al., 2000) and Carswell (Canada) (e.g., Pagel et al., 1985), whereas examples of drainage around a pronounced peak-ring structure are Gosses Bluff (Australia) (e.g. Milton et al., 1996), and finally examples of tributary river networks are Manicouagan (Canada) (e.g., Floran et al., 1978) and West Clearwater (Canada) (e.g., Grieve, 1978). Complex drainage patterns with both centripetal and concentric small rivers draining the central uplift and the external rim have been found as well in the Brazilian tropical region (e.g., Reimold et al., 2006).

However, the non-impact origin can not completely ruled out because, as already noticed (§ 3.4), remote sensing is not enough to firmly confirm the impact origin of a circular structure: positive identification can come only from petrographic and geochemical evidence contained in the rocks of the structure or the discovery of meteorites (e.g., French & Koeberl, 2010). Hence, to query regarding the possibility of an impact origin for Omeonga, numerical modelling of the related impact formation process that would originate this *crater* is performed by using iSALE hydrocode.

7.3.4 Numerical modelling of Omeonga

Let assume Omeonga to be an impact structure. A number of runs by using iSALE has been carried out to investigate the formation process of Omeonga and to compare the final morphology obtained through numerical modelling with the observed data.

In all the simulations, I use a purely Eulerian approach, which describes the instantaneous state of the material in each fixed cell, but is unable to follow a point in the material through the mesh, and hence losing information regarding the thermodynamic history of these points, as the state (pressure, temperature, etc.) of each grid cell at a given time represents only the state of that spatial location (Artemieva et al., 2004). To track the information regarding both the movement the state of material elementary components, Lagrangian tracer particles are implemented (Collins et al., 2008b). These are massless particles that move with material flow without interacting with it and record the position and changing state of the material.

The mesh where the impact is simulated has dimensions large enough to avoid spurious shock waves reflection in the target at the boundaries. The simulation starts with the projectile being in contact with the target surface. The atmosphere was not included in this modelling.

To develop a consistent model for the formation of the Omeonga, the pre-impact surface was modeled by using the known information regarding the stratigraphy of the Congo basin (§ 7.3.1). The halfspace representing the target is made up two lithological units, i.e. a crystalline basement of about 30-*km*-thickness of granite, which is in turn covered by 1.8-*km*-layer of sandstone. The basement was set with no porosity, while the sandstone with 25% of porosity. This last value was set accordingly to many investigations regarding the Coconino sandstone at Meteor Crater (Arizona) (e.g., Kieffer, 1971; Kring, 2007), that point out the high heterogeneity of porosity distribution on samples, ranging from 10% to values as high as 25%.

Here, it is to call that a not insignificant amount of shocks wave energy will be spent for the compaction of void space, before the compression of material can occur (§ 5.2.5), leading to reduced shock magnitudes, unusually high target heating and more rapid shock decay, in turn causing the final crater to be smaller with respect to a crater forming in a dense rock with the same bulk density (Wünnemann et al., 2008).

The projectile was chosen to be of asteroidal origin, as it represents the most likely impactor population on Earth (> 90%; Chyba, 1991; Pierazzo & Chyba, 2006). I take a granite composition for the impactor, as possible representative of meteoroids (e.g., Artemieva et al., 2004), because, unlike basalt, it has a well-defined EoS and constitutive model and the strength model parameters for granite and basalt are similar (Davison & Collins, 2007), along with the convenience of reducing the number of different materials in the model (Collins et al., 2008b). Porosity can range over a large span of values, as asteroids

could be found either coherent either rubble piles. I take a porosity of 10%, derived from the average values for the meteorite types proposed by Britt et al. (2002) (Tab. 2 wherein).

The impactor size to be used as input is computed applying scaling relationships to the inferred crater diameter. However, it is to note here that Omeonga structure has been interested by a high degree of erosion. From the remote sensing analysis, the Unia River and its northern tributaries was interpreted to be the inner margin of the crater rim, and a value of 47 km for the diameter was proposed.

First, I apply the Croft (1985) relation, derived from the reconstruction of large lunar craters, to infer the diameter D_{tr} of the transient cavity:

$$D_{tr} = D_{sc}^{0.15} D^{0.85}$$

where, D_{sc} is the critical value above which crater collapse occurs and hence, complex morphologies are encountered. In the case of Earth, D_{sc} is about 4 km for crystalline rocks (Neukum & Ivanov, 1994). Hence, the transient crater diameter for Omeonga would be expected up to about 30 km.

Then, I used the Schmidt & Holsapple (1987) scaling law, obtained from small-scale hypervelocity and nuclear explosion experiments:

$$D_{tr} = 1.16 \left(\frac{\rho_p}{\rho_t} \right)^{1/3} D_p^{0.78} v_i^{0.44} g^{-0.22}$$

where ρ_p and ρ_t are the densities of projectile and target, respectively, D_p is the projectile diameter, v_i the impact velocity, and g the acceleration of gravity.

A word of note regarding this equation is that, from this set up, $\rho_p/\rho_t \sim 1$, and hence mostly of the crater growth is expected to take place in the granitic basement. In fact, as the transient cavity is approximately a paraboloid of revolution (Dence, 1973), with a depth-diameter ratio between 0.25 and 0.33 (Melosh, 1989), the corresponding depth of the Omeonga transient cavity ranges between 9.5 and 12.54 km.

The last assumption regards the impact velocity, since this scaling relation implies that, keeping constant projectile and target materials, the same transient cavity may be produced by both a high-velocity small projectile or a low-velocity larger body. The difference may be important for melt production estimates, as the melt volume is proportional to the projectile volume for a given impact velocity (Artemieva et al., 2004).

iSALE has a 2D capability (Collins et al., 2008b), and thus limits impact events to normal incidence angles. However, perpendicular impact is not common in nature, being 45° the most probable angle of impact (Gilbert, 1983; Shoemaker, 1962). In fact, the probability of a meteoritic impacting a given surface at an angle between ϑ and $\vartheta + d\vartheta$ (ϑ measured from the vertical) is:

$$dP \propto 2 \sin \vartheta \cos \vartheta d\vartheta$$

Moderately oblique impacts, ranging between 40 and 50°, are six times more probable than near-normal incidence angles. In addition, meteoroids have a higher concentration near the ecliptic plane in orbits, with low inclinations, causing probabilities to skew to smaller angles of incidence with respect to an isotropic flux model. Hence, shallow angle trajectories result to be more frequent, but, on the other hand, impact craters result circular for impact angles greater than ~15° to the horizontal (Gault & Wedekind, 1978).

At last, I consider an impact velocity of 12 km s^{-1} , which approximates the vertical component of an 18 km s^{-1} impact at 45° angle, as it has been proposed after laboratory experiments (Gault & Wedekind, 1978). In addition, for such a value of impact velocity, the volume of vaporized material remains relatively small to prevent a useless consume of CPU time, as the expansion of vapour plume have little effect on the late stage mechanics of the cratering process investigated (Wünnemann & Ivanov, 2003).

Adopting these input parameters, the projectile diameter turns out to be up to 5 km , value that has been implemented in my model setup.

The thermodynamic behaviour of each material in the model is described by an equation of state (§ 5.2.1). I use Tillotson EoS for both granite (Melosh, 1989), to represent both crystalline basement rocks and impactor, and sandstone (Kenkman et al., 2005), to represent the sedimentary sequence (Tab. 3.5.2). The strength model used in my numerical simulations is the standard rock strength algorithm implemented in iSALE, that accounts for changes in material shear strength that result from changes in pressure, temperature and both shear and tensile damage (Tab. 3.5.2) (§ 5.2.3) (Melosh et al., 1992; Ivanov et al., 1997; Collins et al., 2004).

TILLOTSON EoS		
<i>Symbol</i>	<i>Sandstone</i>	<i>Granite</i>
$\rho_0 \text{ (kg m}^{-3}\text{)}$	2460	2660
a	0.5	0.5
b	0.6	1.3
A (GPa)	30	18
B (GPa)	10	18
$E_0 \text{ (MJ kg}^{-1}\text{)}$	10	16
α	5	5
β	5	5
$E_{iv} \text{ (MJ kg}^{-1}\text{)}$	3.5	3.5
$E_{cv} \text{ (MJ kg}^{-1}\text{)}$	20	18

Tab. 5.3.1. Tillotson EoS parameters for the material used in the simulation: sandstone (taken from Kenkman (2005)) and granite (taken from Melosh (1989)).

INPUT PARAMETERS			
	<u>Projectile</u>	<u>Target</u>	
		<i>Sediments</i> <i>(sandstone)</i>	<i>Basement</i> <i>(granite)</i>
Impactor radius (km)	2.5		
Impact velocity (km/s)	12		
Impactor material	granite		
Impactor density (kg m ⁻³)	2660		
Impactor porosity	10%		
Thickness layer (km)		1.8	30
Target density (kg m ⁻³)		2460	2660
Porosity	10%	25%	0%
Poisson ration	0.25	0.30	0.25
Cohesion (Yield strength at zero pressure; <i>MPa</i>)	50	20	50
Coefficient of internal friction	1.5	0.95	1.5
von Mises plastic limit (theoretical yield strength at infinite pressure; <i>GPa</i>)	2.5	1	2.5
Cohesion (initial damaged material; <i>kPa</i>)	1	0.01	1
Coefficient of friction (damaged material)	0.6	0.5	0.6
yield strength at infinite pressure (damaged material; <i>GPa</i>)	2.5	1	2.5
Melt temperature (°K)	1600	1750	1600
Thermal softening parameter	1.2	1.2	1.2
Kinematic viscosity of acoustically fluidized region (<i>m²/s</i>)	50,000	0.	50,000
Decay time of acoustic vibrations (<i>s</i>)	50	0.	50

Tab. 5.3.2. Numerical model setup and parameters.

However, a further transient mechanism of weakening had to be considered to facilitate deep-seated gravitational collapse of the initial bowl-shaped cavity (e.g., Melosh, 1989). It is the acoustic fluidization model, that explains the temporary liquid-like behaviour of rocks in the vicinity of the crater (Melosh, 1979).

The acoustic fluidization algorithm implemented in iSALE is the “Block Model” (BM) (§ 5.2.4). The behaviour of acoustically fluidized matter is mainly determined by the viscosity η and the decay time τ , that are both strongly linked with the fragmentation state of the rocks beneath the structure (Wünnemann & Ivanov, 2003; Wünnemann et al., 2005).

As the final output depends on the choice of the BM parameters, in the following is presented a brief discussion describing the influence of each parameter individually. The definitive choice of BM parameters, which I differently set for either the crystalline basement and the above sediments, was thus based on a number of runs devoted to better reproduce Omeonga structure.

EFFECTS OF DECAY TIME

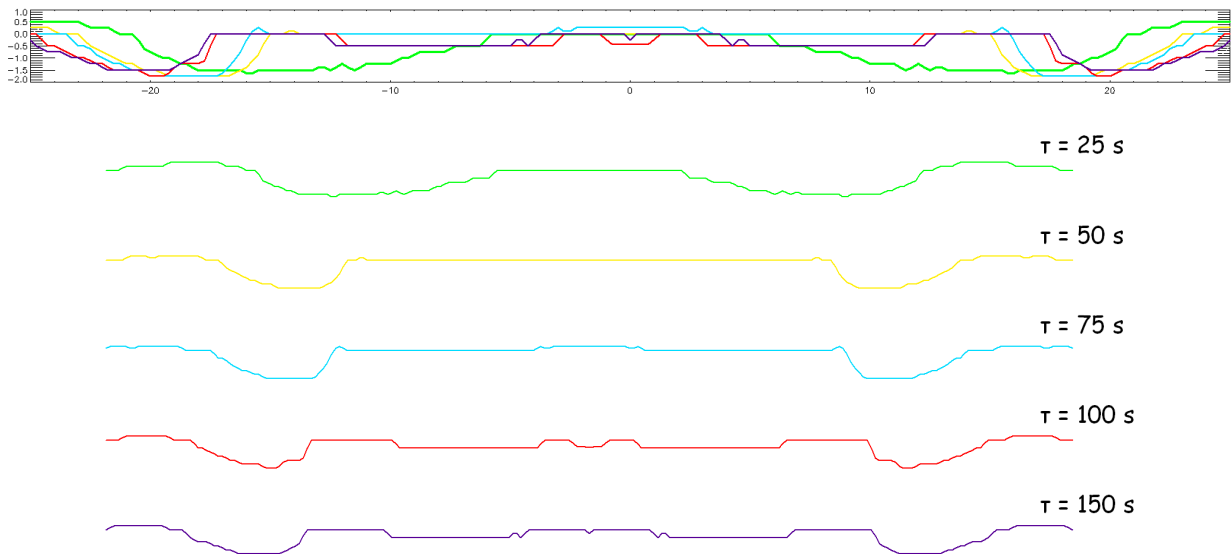


Fig. 3.7.8. This plot shows the influence of decay time on the final crater morphology. Adopting a kinematic viscosity is set to $50,000 \text{ m}^2/\text{s}$, the crater was modeled for different values of the damping time. The plot shows all the profiles obtained, overlaid for comparison (profile on the top), and splitted for each case (profiles on the bottom).

The decay time of the pressure vibrations controls the rate at which this fluidized region contracts in size, i.e. the length of time before the fluidization process is halted and crater morphology is “frozen”.

Fig. 3.7.8 illustrates the effect of block–oscillation decay time on the final simulated crater morphology. The rate of collapse is limited by inertia: the transient crater cannot collapse faster than its free–fall time under gravity ($t_{\text{free}} = \sqrt{2H_t/g}$). For a transient crater depth of $\sim 4 \text{ km}$ (as the case of Omeonga), this corresponds to a minimum collapse time of $\sim 30 \text{ s}$ on Earth. For decay time less than the free–fall time, the collapse is arrested to a final morphology containing a central peak or mound. For simulations with a longer decay time, the uplifted central mound overshoots the original target surface and becomes unstable itself.

EFFECTS OF VISCOSITY

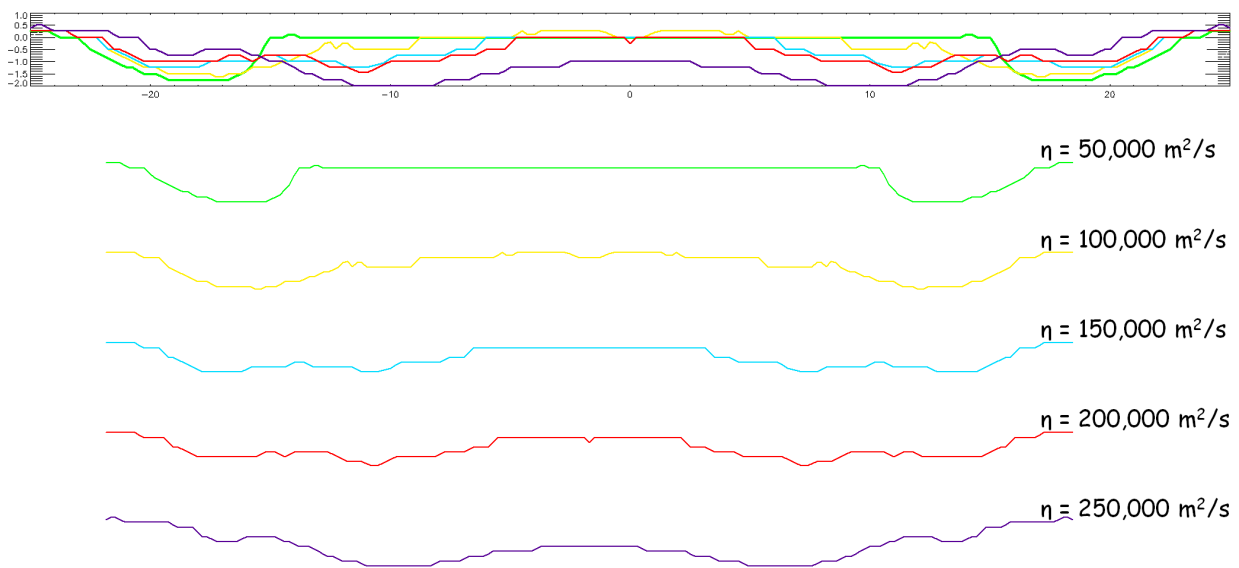


Fig. 3.7.9. This plot shows the influence of kinematic viscosity (where, $\eta_{\text{eff}} = \rho \eta_{\text{kin}}$) on the final crater morphology. Adopting a decay time of 50 s , the crater was modeled for different values of the kinematic viscosity. The plot shows all the profiles obtained, overlaid for comparison (profile on the top), and splitted for each case (profiles on the bottom).

The effective viscosity of the fluidized region influences the dynamics of the collapse; both the maximum height of the central uplift and the velocity of the collapse increase with decreasing viscosity. However, Collins et al. (2002) found that the value of 10^9 Pa s may be considered as an upper limit for the effective viscosity of the fluidized debris, above which damping of the collapsing cavity is so abrupt that overshoot of the central uplift is prevented.

Fig. 3.7.9 illustrates the final morphology for simulations with various kinematic viscosities for the fluidized region, well below the upper limit proposed by Collins et al. ($10^6 \text{ m}^2/\text{s}$). The increasing viscosity yields to a decrease in both the final crater and peak diameter.

The block model relates the kinematic viscosity η of the fluidized debris to the size h of the oscillating blocks and the period T of block oscillation (Ivanov & Kostuchenko, 1997; Ivanov & Artemieva, 2002; Melosh & Ivanov, 1999):

$$\eta_{\text{kin}} = \frac{2\pi h^2}{T}$$

Assuming a period of block-oscillation of a few seconds, the best fit viscosity (cf. Tab. 5.3.2) corresponds to a block size of $\sim 120 \text{ m}$ (Collins et al., 2008b). This hypothesis may represent, if confirmed by on-ground drilling in Congo, a possible feature either to give credit to the impact origin or to favour later improvements in this model.

In Fig. 7.3.10, the sequence of the best-fit numerical model for Omeonga.

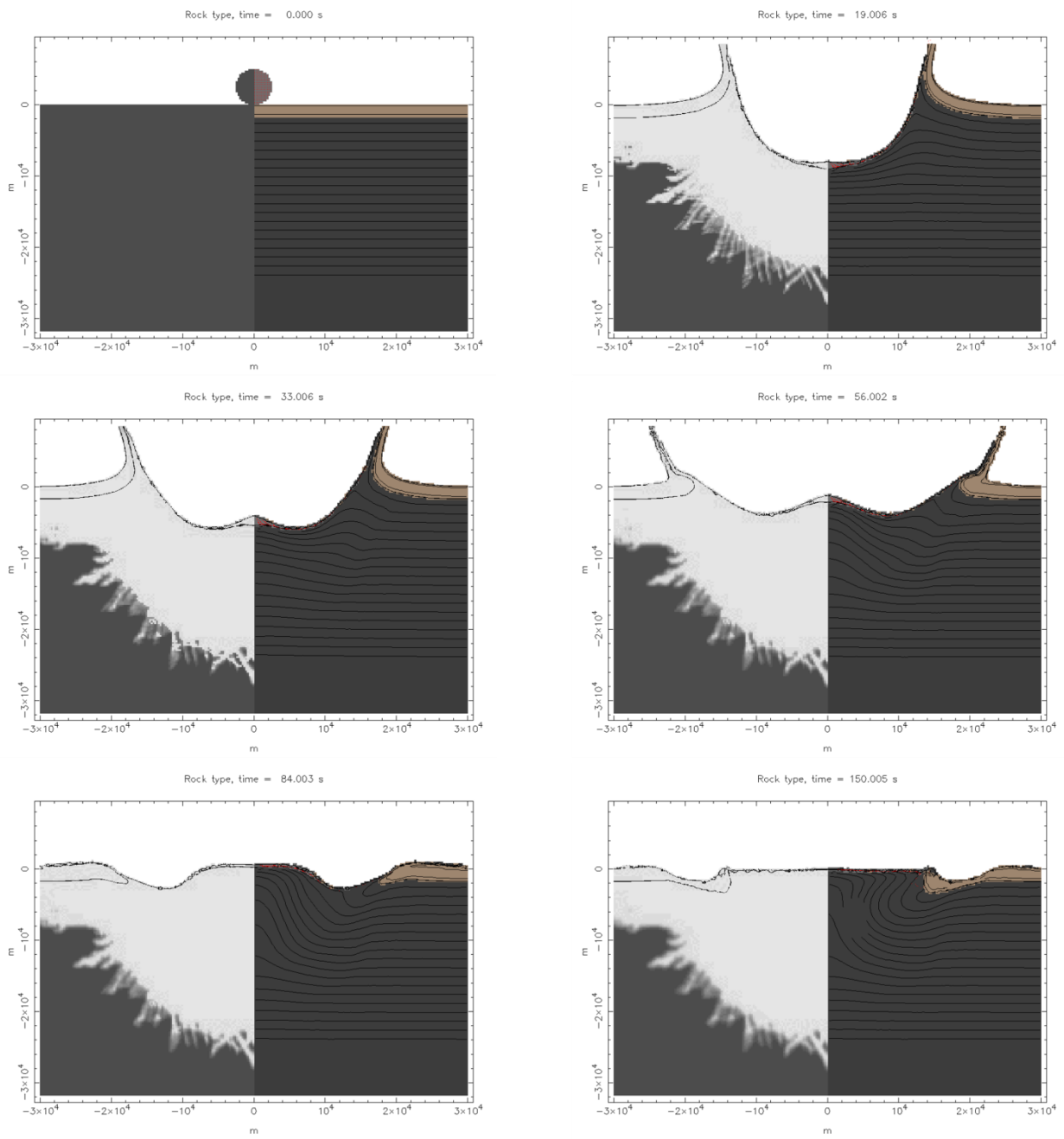


Fig. 7.3.10. Sequence of Omeonga formation simulation. *Right panel:* Material. *Left panel:* Damage distribution.

My best-fit numerical model crater has a diameter of 48 km, a depth of 1.750 km below the pre-impact surface and a rim height of 0.25 km above the pre-impact surface, while the central ring is 28 km in diameter. In this central ring area, the uplifted zone displays a lower-sequence sediments (brown) above crystalline basement (grey). The basement has got a higher position (< 2 km) in this central uplift relative to its position beneath the crater rim.

As already pointed out by Collins et al. (2008b) in a study of the Haughton crater (Canada), the sedimentary layer is thick enough to not allow the the granite basement to upturn: the overturning of the surface that follows the uplift involves only the mid-sedimentary sequence strata (Fig. 3.7.10).

The hard erosion at Omeonga makes extremely difficult a comparison of the final simulated crater with observation. I have considered only one of the profiles of Fig. 7.3.7 (No. 3). The comparison of the profiles obtained from the numerical model and observed through the DTM analysis is reported in Fig. 7.3.11. My best-fit model does appear to show a good correlation between the rim and peak-ring diameters, but, at the same time, to consistently overestimate the depth of the final simulated structure, by a value higher (~ 1 km deeper) than the expected mismatch of $\sim 20\%$. Hence, a considerable post-impact modification is invoked, due to erosion of the ridges, gravitational phenomena involving the rim and the peak-ring and sediments deposition at the thalweg of the Unia and the Lomami rivers.

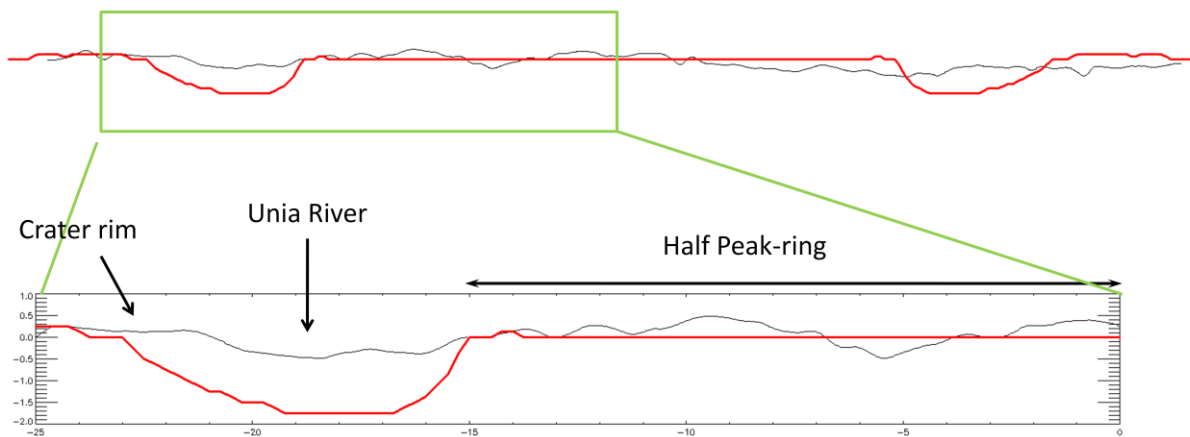


Fig. 7.3.11. Comparison between the profiles of the simulated crater (red) and of DTM reconstruction (black). The location of the main features of the structure, namely the crater rim, peak-ring, and Unia River (crater floor for the modeled structure) are provided.

7.4 Rosetta: A deciphering *Stone* for a so far away world

Asteroids.

It was not a long time ago that asteroids were merely star-like points of light in our telescopes, instead they are instead world by themselves with a unique history to be unraveled (Bottke et al., 2002b).

Asteroids, having small dimensions, complete their chemical and thermal evolution within the first 23 *Myr* of the Solar System history. Hence, they can be considered as a “deputy” of the early planetesimals population, bodies from which terrestrial planets has formed and undergone modifications since the time of planetary accretion (e.g., Bottke et al., 2002b; Gaffey et al., 2002).







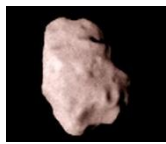
This means that they provide a relatively pristine record of conditions and processes which took place in the inner (~1.8–3.5 AU) region of the earliest Solar System. At the same time, they experienced subsequent events, including collisions, that have shaped their present-day physical and dynamical state (e.g., Bottke et al., 2002b). Consequently, their mineralogical and physical characterization (size, shape, spin, mass, density, internal structure, etc.) may be useful to constrain the processes that lead the inner solar nebula to evolve into the Solar System as well as the planetesimal to aggregate into terrestrial planets (Gaffey et al., 2002), and, in more recent time, the delivery of hydrated mineral to originate the Earth’s water (Rivkin et al., 2002).

During the two centuries since Ceres was discovered, ground-based telescopic observations have provided the main sources of data, along with some auxiliary data drawn from analyses of meteorites that reach the Earth. However, observations had showed to be inadequate to resolve even their shapes and the features characterizing their surface, such as impact craters (Chapman, 2002; Sullivan et al., 2002).

In the last twenty years, a considerable progress in the study and knowledge of asteroids has been achieved thanks to exploration and mainly the flybys of asteroids by space missions, that have allowed to acquire only limited information (Farquhar et al., 2002). In 1991, the *Galileo* spacecraft, on its way to Jupiter, obtained the first in-situ images of two Main-Belt asteroids, and precisely 951 Gaspra, 243 Ida and its moon Dactyl. From then, the NEAR *Shoemaker* spacecraft not only flew past 253 Mathilde and 433 Eros, but made touchdown on the surface of Eros itself (e.g., Sullivan et al., 2002). *Hayabusa*, the first mission with the purpose of collect sample from one asteroid (25143 Itokawa) and return them back to Earth, allows to have for studying some particles less than 10 μm . At the time of editing this thesis, one space mission, the last asteroid to be imaged is 21 *Lutetia* by the OSIRIS camera onboard of the *Rosetta* spacecraft, rising to seven the number of the asteroids visited by a spatial mission (Tab. 7.4.1).

The last section of my thesis is devoted to the two rocky targets of Rosetta mission, i.e. Steins and Lutetia. The images of these two asteroids have been taken by the imaging system onboard of Rosetta, named OSIRIS (Optical Spectroscopic and Infrared Remote Sensing Imaging System), which is made up by a narrow-angle (NAC, angular resolution 5 *arcsec/px*) and wide-angle (WAC, angular resolution 22 *arcsec/px*) cameras, and a group of 24 filters, ranging between 240 and 980 *nm*.

As anticipated in § 7.1, Steins and Lutetia distinctly fulfill the two topics of my thesis, the crater retention age determination and the numerical modelling investigation. These analysis will be presented in § 7.4.1 and § 7.4.2, respectively.

Asteroids	951 Gaspra	243 Ida	253 Mathilda	433 Eros	25143 Itokawa	2867 Steins	21 Lutetia
							
Mission	Galileo (1991)	Galileo (1997)	NEAR (1993)	NEAR (2000)	Hayabusa (2005)	Rosetta (2008)	Rosetta (2010)
	Res = 54 m/px	Res = 180 m/px	Res = 25 m/px	Res = cm/px	Res < 1 cm/px	Res ≥ 80 m/px	Res ≥ 60 m/px
Period	7.09 h	17.406 d	4.634 h	5.267 h	12.132 h	6.047 h	8.168 h
Size (km × km × km)	18 × 10 × 9	60 × 25 × 19	66 × 48 × 46	34 × 11 × 11	0.54 × 0.29 × 0.21	6.7 × 5.9 × 4.3	121 × 112 × 97
Type	S	S	C	S	S/Q	E	M/C
Composition	ordinary chondrite	carbonaceous chondrite	ordinary chondrite	ordinary chondrite	ordinary chondrite	aubrite	? enstatite or carbonaceous chondrite
Density (g/cm ³)	2.7	1.3	2.6	2.67	1.95	?	2.9- 3.5
Porosity	?	55 – 63 %	18 – 24 %	16 – 21 %	39 – 43 %	?	?
Age	200 Ma	2 – 4.5 Ga	1 Ga	2 Ga	1 – 100 Ma	100 – 150 Ma	2.7 – 3.6 Ga
Cratering	Production	Saturation	Saturation	Saturation	?	Production	Production

7.4.1 Steins

On 10th July 2010, ESA Rosetta mission flew by asteroid (2867) Steins, at the closest approach (CA) distance of 803 km, resolving approximately 60% of the surface (Fig. 7.4.1).



Fig. 7.4.1. Asteroid Steins at different snapshots near the close approach. Courtesy of ESA 2008 MPS for OSIRIS Team MPS/UPD/LAM/IAA/RSSD/INTA/UPM/DASP/IDA, No. SEM27ZO4KKF.

Before this close encounter, data available allowed only few speculations regarding the nature of this asteroid (e.g., Barucci et al., 2007). The first spectroscopic observations made at Spitzer (Barucci et al., 2005; Fornasier et al., 2007) suggested a similarity between Steins and E-type asteroids, a rare class of objects with properties similar to the enstatite achondrite meteorites. Such asteroids are quite small in size and orbit and mostly found in the inner part of the main asteroid belt. They probably originate from the mantle of larger asteroids destroyed in the early history of the Solar System, and are thought to be composed mainly of silicate minerals. In addition, polarimetric properties strengthened this classification for Steins (Fornasier et al., 2006). The derived albedo was 0.45 ± 0.1 (Fornasier et al., 2006), that in conjunction with an absolute visual magnitude $V = 13.18$ mag allowed to estimate the diameter of Steins as ~ 4.6 km (Fornasier et al., 2006).

The flyby with Rosetta confirmed these first findings. In the followings, a briefly discussion of the results come out from the encounter with the spacecraft. However, the data collected by OSIRIS allowed only a limited science investigation on Steins, as NAC stopped its automatic operation about 10 min before the CA, due to a shutter problem (Keller et al., 2010). Hence, we have only images at a relatively low resolution acquired by WAC.

The OSIRIS data confirmed that Steins is a member of subtype E[II] (Keller et al., 2010). Its disk-integrated geometric albedo at a wavelength of 632 nm, which was directly calculated from the radiance of the image obtained at the lowest phase angle (0.36°), is 0.40 ± 0.01 (Keller et al., 2010). On the other hand, no color variation larger than 4% at a 95% confidence level has been detected in a principal component analysis (Leyrat et al., 2010), suggesting either a complete alteration of the surface either a relatively insensitive response of the E type Steins surface to space weathering over time scales shorter than 150 Myr, which is the minimum age of the large craters (Keller et al., 2010).

The shape of Steins is that of a “diamond”, an oblate body rotating about its short axis, with overall dimensions $6.67 \times 5.81 \times 4.47$ km and an effective spherical diameter of 5.3 km (Keller et al., 2010). The surface of Steins is mostly covered by shallow craters, often with subdued, ambiguous rims. The overall crater shape and depth-to-diameter ratio (~ 0.12) are consistent with degradation caused by ejecta blanketing and regolith disturbance by impact seismic shaking (Richardson et al., 2005b). One of the most peculiar feature is a large, 2.1-km-diameter crater, located near the south pole (e.g., Keller et al., 2010). The numerical modelling of this impact structure suggest that before the impact, Steins must have been either a rubble pile with microporosity, or a monolithic body with or without microporosity. In all cases, the impact would have transformed Steins into a rubble pile structure (Jutzi et al., 2010).

In this context, I performed a statistical study of the impact structures present on Steins to derive the crater retention age. In addition, this analysis evidenced the importance of the 3D modelling into planetary sciences. In fact, initial cumulative distributions of crater counts performed in the highest resolution image showed large differences between each others, however only partially attributed to the low resolution and the paucity of the crater statistics. The major uncertainty on crater diameters, and then in the size-distribution, arose indeed from the methods applied, i.e. the computation of crater dimensions considering the features as circular while they can display an irregular shape, due to the non-orthogonality of the asteroid surface with respect to the camera. Hence, to achieve the most reliable crater size-frequency distribution, a new method is adopted, which uses the 3D reconstruction of Steins.

The 3D shape model of Steins, referred to a common coordinate system having its origin in the "middle" of the asteroid, was derived through the following steps (Simioni, 2011): define the cube containing the asteroid; detect the isosurface separating either internal or external part of the volume; apply the shape from the silhouettes defined by automatic segmentation. Finally, a correction is introduced to take into account the terminator, once known the direction of light. The input data were all the images acquired with filter F17, whereas the parameters taken into account are: the focal length (135.7 mm), the optical center —pixel coordinates corresponding to the boresight direction— (1043.937), the screw angle (0°), the parameters relative to the attitude and position of the camera in the static asteroid reference frame. These latter are provided by the satellite and instrument kernels, which give both the vector between the satellite and the body target and the camera attitude in the J2000 reference frame.

I considered three images acquired from WAC near the CA (Tab. 7.4.2), chosen by selecting different position and orientation between Rosetta and the asteroid.

Image Name	Distance (km)	Resolution (km/pix)	Visible Area (km²)	N^o craters > 4 pix
WAC_2008-09- 05T18.37.00.561Z_ID30_0166077025_F17	953.529	0.095	39.5406	12
WAC_2008-09- 05T18.38.02.520Z_ID30_0166089000_F17	800.099	0.079	47.8299	17
WAC_2008-09- 05T18.39.23.223Z_ID30_0166098003_F17	1069.893	0.106	64.5970	10

Tab. 7.4.2. The list of images chosen for the count. The first column reports the name of the image, the second the distance in km between Rosetta and the asteroid, the third the resolution in km per pixel, the fourth the total visible area in km^2 where the counts are performed, and finally the last column reports the total number of craters counted with diameter greater than or equal to 4 pixels.

Crater counts have been performed in each 2D image by using my semi-automatic program (§ 4.6). The subsequent statistical analysis would be based on the crater diameters after their conversion in km . This “trivial” step is underlined because the conversion of the diameter from pixel to km does not allow to find the “correct” diameter value. In fact, the value adopted for resolution represents only a mean value, because the curvature of Steins surface with respect to the OSIRIS images is not negligible. To minimize these uncertainties, craters —circular features— are projected onto the 3D model of Steins.

Craters are identified on the reconstructed shape by all the points of the 3D model that, once projected on the 2D image, corresponds to the respective craters. Then, the area of the region occupied by these points is computed to be used to extrapolate the corresponding crater diameter.

In the following, I report the results for each image analyzed, and precisely: (1) the table (Tab. 7.4.3) with the craters detected, each one with the value of both the diameter computed directly from the 2D image and the one corrected by the projection onto 3D model; here, it is worth noting that the diameters corrected are about 1.5 times, on average, greater; (2) the 2D (Fig. 7.4.2) and 3D model (Fig. 7.4.3) images of the asteroid, where the craters counted are drawn in; (3) the cumulative plots (Fig. 7.4.4) for both the set of diameters, for each image.

IMA GE	WAC_2008-09- 05T18.37.00.561Z_ID30_ 0166077025_F17		WAC_2008-09- 05T18.38.02.520Z_ID30_ 0166089000_F17		WAC_2008-09- 05T18.39.23.223Z_ID30_ 0166098003_F17	
	<i>Diameter counted (km)</i>	<i>Diameter corrected (km)</i>	<i>Diameter counted (km)</i>	<i>Diameter corrected (km)</i>	<i>Diameter counted (km)</i>	<i>Diameter corrected (km)</i>
No. Craters						
1	0.48	0.62	0.37	0.47	0.58	1.00
2	0.49	0.59	1.09	1.38	0.48	0.89
3	0.44	0.56	0.36	0.49	0.43	0.76
4	1.12	1.40	0.43	0.66	0.50	0.93
5	0.48	0.75	0.70	0.88	0.44	0.79
6	0.56	0.69	0.34	0.43	0.56	0.93
7	0.47	0.67	0.77	1.13	0.46	0.52
8	0.53	0.78	0.49	0.72	0.87	1.64
9	0.47	1.16	0.36	0.55	1.64	1.96
10	0.42	0.56	0.68	1.13	2.05	3.44
11	1.55	2.32	0.53	0.66		
12	2.01	2.57	0.45	0.69		
13			0.64	1.11		
14			0.35	0.47		
15			1.80	2.64		
16			0.35	0.45		
17			2.26	3.22		

Tab. 7.4.3. List of the craters counted in the three images taken at different time interval. Crater diameters are computed either as the best circle fitting the three points taken in the crater rim (§ 4.6) either from the projections of these measures onto the 3D model of Steins.

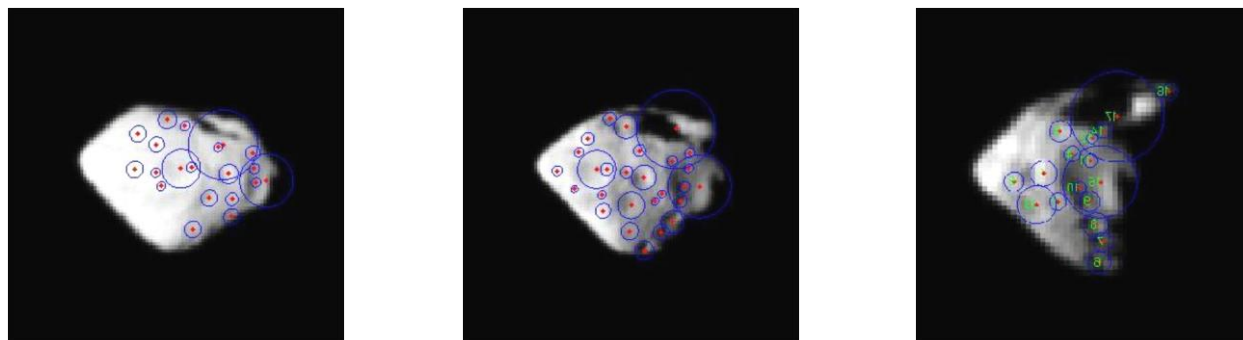


Fig. 7.4.2. 2D images of Steins taken at (a) UT = 18.37.00.561, (b) UT = 18:38:02.520, 18.37.00.561, (c) 18.39.23.223. Craters detected (listed in Tab. 7.4.3) are identified on it by a red point (center) and a blue circle (best circle that fit it).

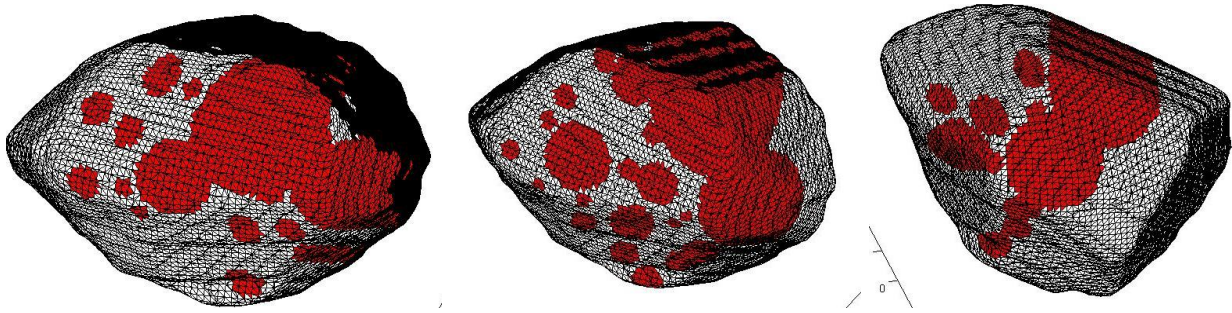


Fig. 7.4.3. 3D model of Steins, at the snapshots corresponding to Fig. 7.4.2. Craters detected are projected on it as red circles.

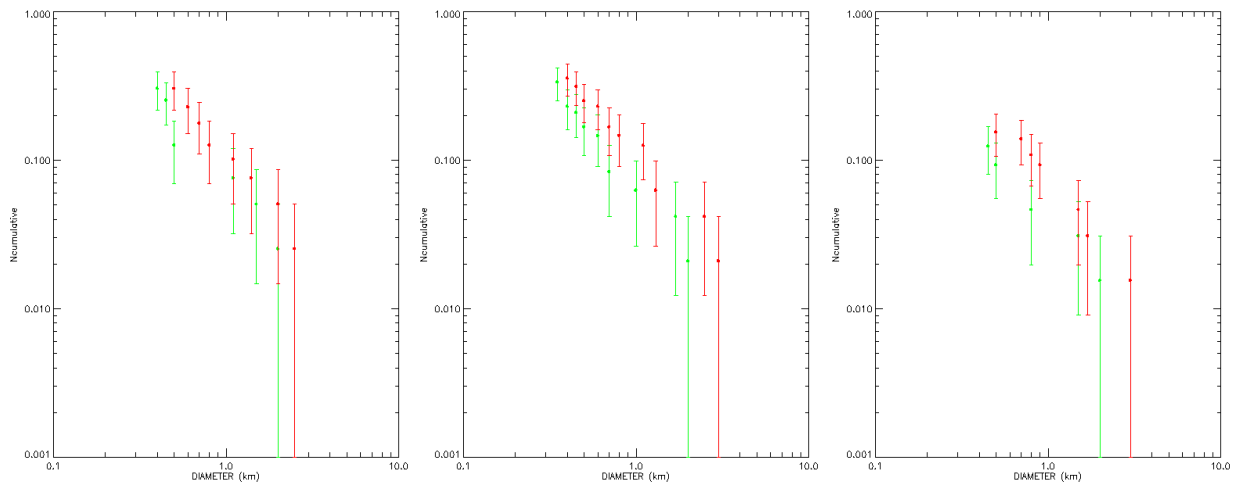


Fig. 7.4.4. Cumulative plots of crater counts performed in the three images used for this analysis (Tab. 7.4.2), considering the crater diameters with (*red*) or without (*green*) the 3D correction. Error bars are shown as well.

A natural improvement of this method relies in considering craters as features with the shape observed in the OSIRIS data, instead of a simple circle. Then, it is just this shape that is projected onto the 3D model of Steins.

A single image among the previous used is chosen, and precisely the one at the highest resolution (UT = 18:38:02.520). The working environment is ArcGIS, a standard-based platforms collecting GIS software products for visual interpretation. All crater rims have been contoured in the x2 pixelized image. The total crater-like features detected are 34 (Fig. 7.4.5).

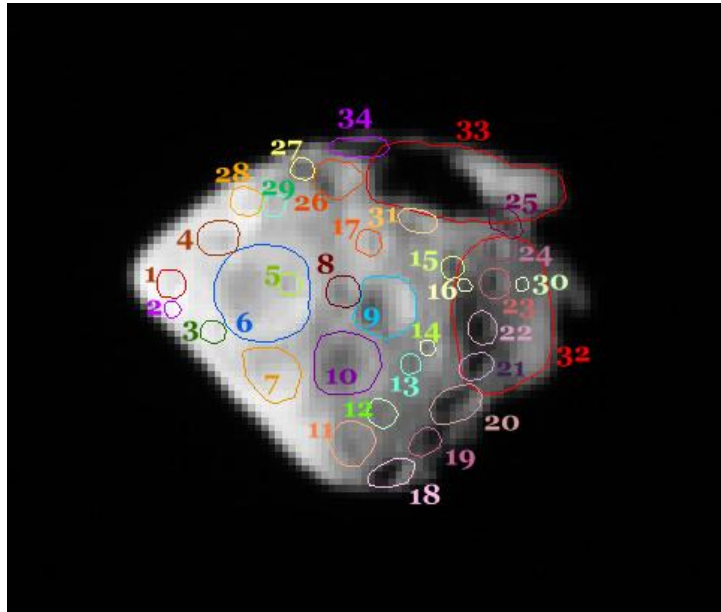


Fig. 7.4.5. Crater-like features counted on the image acquired at UT = 18:38:02.520. The area is 34.5254 km^2 , computed removing the shaded areas near the terminator seen by OSIRIS, since no crater is detected on them.

Each single crater shape is turned into raster data, to be projected onto the 3D model of Steins and fitted with an ellipse (Fig. 7.4.6). The best fit provides the estimate for the crater mean diameter. The result of this count is reported in Tab. 7.4.4.

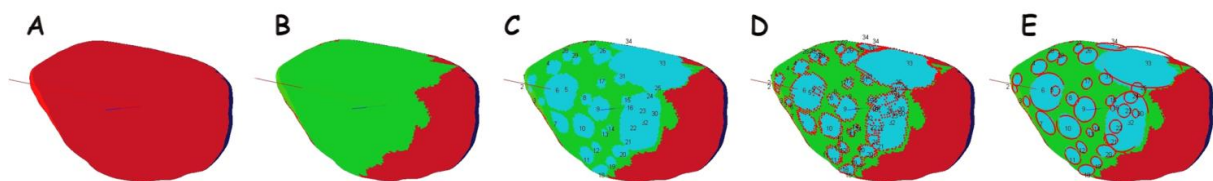


Fig. 7.4.6. Sequence of steps to derive the final crater dimensions through projecting crater masks onto the 3D model of Steins: (A) define region of interest by selecting the normal faces in relation to the direction of both the light and the spacecraft; (B) define their terminator by using the projected images; (C) define 3D craters by projecting the ArcGIS masks; (D) detect border vertices; (E) elliptical fit (LMS) and mean diameter estimation.

No	Type	2D SHAPE	3D SHAPE		
		<i>Mean Diameter (km)</i>	<i>Semi major axis (km)</i>	<i>Semi minor axis (km)</i>	<i>Mean Diameter (km)</i>
1	PRIMARY	0.22	0.22	0.18	0.40
2	?	0.53	0.13	0.14	0.27
3	PRIMARY	0.62	0.23	0.16	0.40
4	PRIMARY	0.94	0.30	0.26	0.56
5	PRIMARY	0.33	0.16	0.15	0.30
6	DEGRADED	1.20	0.65	0.59	1.24
7	ELLIPTIC	0.48	0.56	0.39	0.96
8	PRIMARY	0.29	0.24	0.20	0.44
9	DEGRADED	0.80	0.41	0.38	0.79
10	DEGRADED	0.78	0.59	0.41	1.01
11	PRIMARY	0.75	0.49	0.28	0.77
12	PRIMARY	0.72	0.31	0.19	0.50
13	PRIMARY	0.41	0.20	0.13	0.33
14	PRIMARY	0.34	0.13	0.11	0.25
15	PRIMARY	0.38	0.18	0.15	0.34
16	PRIMARY	0.80	0.10	0.08	0.17
17	PRIMARY	0.33	0.21	0.17	0.38
18	CHAIN	0.65	0.37	0.19	0.55
19	CHAIN	0.70	0.33	0.19	0.52
20	CHAIN	0.86	0.49	0.28	0.78
21	CHAIN	0.41	0.27	0.21	0.48
22	CHAIN	0.56	0.22	0.19	0.40
23	CHAIN	0.43	0.21	0.20	0.41
24	CHAIN	0.41	0.24	0.19	0.42
25	CHAIN	0.85	0.30	0.23	0.53
26	PRIMARY	0.52	0.50	0.30	0.80
27	PRIMARY	0.54	0.31	0.15	0.46
28	PRIMARY	0.27	0.27	0.20	0.47
29	PRIMARY	0.75	0.21	0.15	0.36
30	PRIMARY	0.40	0.11	0.13	0.24
31	ELLIPTIC	0.97	0.30	0.18	0.48
32	?	1.76	0.97	0.66	1.64
33	?	2.19	2.16	1.10	3.26
34	?	0.78	0.72	0.30	1.02

Tab. 7.4.4. List of craters-like features counted in the image UT = 18:38:02.520. The first column is the sequential number of the craters, referred to Fig. 7.4.5. The second is the classification of the crater-like features. The third is the mean diameter of the shape contour computed in ArcGIS. The next two columns are the semi major and semi minor axis of the ellipse best fitting data on the 3D Steins model. The last column is the mean diameter, subsequently used to derive crater size-frequency distribution.

The crater-like features as identified result to be 29 with diameter larger than 4 pixels (0.32 km). However, this list includes all the crater-features, while the crater retention age determination is based only on the primary impacts.

The ambiguous features to be excluded are a chain of eight pits, roughly similar in size, crossing a large degraded crater and extending almost from the south to the north pole of the asteroid (Keller et al., 2010). The low resolution does not allow to clarify whether or not these pits are impact in origin. However, the probability of occurrence of such a chain in a low gravity body is highly improbable. Instead, this feature may be linked to the impact that caused the large crater. It indicates partial drainage of loose surface material into a fracture within stronger, deeper material, possibly marking pre-existing physical inhomogeneities (Richardson et al., 2002; 2005b). This hypothesis is strengthened by the presence of a large elongated depression, imaged by NAC before the CA, opposite to the pits chain. Similar linear features were also observed on other small bodies, like Gaspra (Belton et al., 1992).

Crater retention age is inferred by adopting the Marchi et al. (2009) model (§ 4.4). The impactors flux is derived combining the impactor size-frequency distribution and the impact velocity distribution. The first is obtained from the average size distribution of the MBA of Bottke et al. (2005a, 2005b) in conjunction with the intrinsic probability of collision with Steins. The impact velocity distribution for Steins has been obtained applying the Farinella & Davis (1992) algorithm to the present population of asteroids intersecting Steins orbit. The crater size-frequency distribution is finally derived applying the Nolan et al. (1996, 2001) scaling law. In addition, to this nominal model the cratering erasing process is taken into account as well.

In Fig. 7.4.7, the cumulative distribution of both the all crater-like features and the bonafide ones are displayed. The best fit with the MPF (red line) has been performed only for bonafide craters with diameter larger than 0.7 km, because the smaller craters seem to be depleted. This kink has been recently observed, at a different diameter range ($D < 10$ m), on Itokawa (Hirata et al., 2009; Michel et al., 2009), and it is attributed to an episode of crater erasing. In the case of Steins, the 2-km crater likely caused the erase of the pre-existing craters smaller than 0.5–0.6 km. This finding turned out to be very important. Since small craters started to accumulate on the surface again after the formation of the 2-km impact, their distribution can be used to date this event. Hence, in Fig. 7.4.7, the best fit of the MPF (pink line) with craters ranging between 0.3 km and 0.6 km is reported as well.

The resulting model age for Steins is 127 ± 5 Myr (Fig. 7.4.7), while the 2-km impact craters turned out to have occurred 48 ± 3 Myr ago. Both these values may represent a lower limit, since the adopted scaling law overestimates cratering efficiency as it neglects the shear resistance of materials (Nolan et al., 1996).

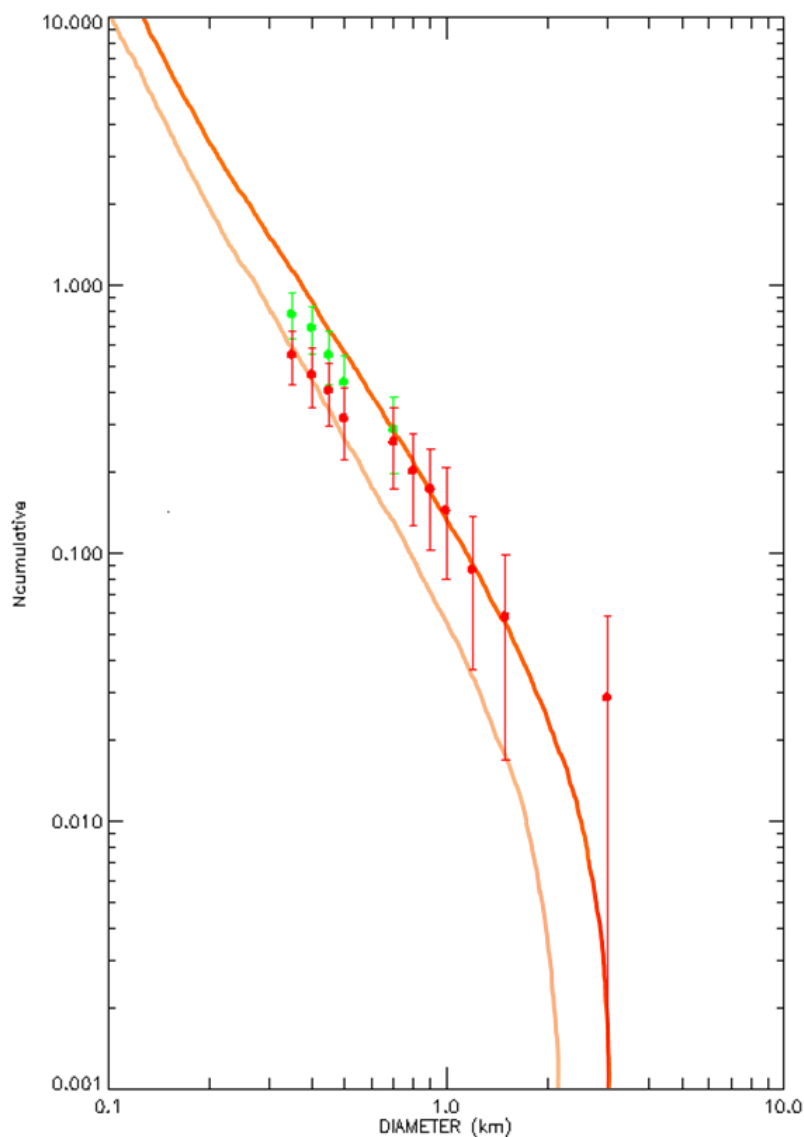


Fig. 7.4.7. Cumulative plot of the crater count performed in the image acquired at UT = 18:38:02.520 (cf. 7.4.5). Both crater like (green) and bonafide (red) features are shown. MPF model was applied to fit either bonafide craters larger than 0.7 km to derive Steins surface age (ref line), either small craters ($D < 0.6$ km) to derive the age of the 2.1-km impact event (pink line).

7.4.2 Lutetia

On 10th July 2010, ESA Rosetta mission flew by asteroid (21) Lutetia, at the closest approach distance of 3160 km, recording an amount of data of more than 50% of the asteroid (Fig. 7.4.8).

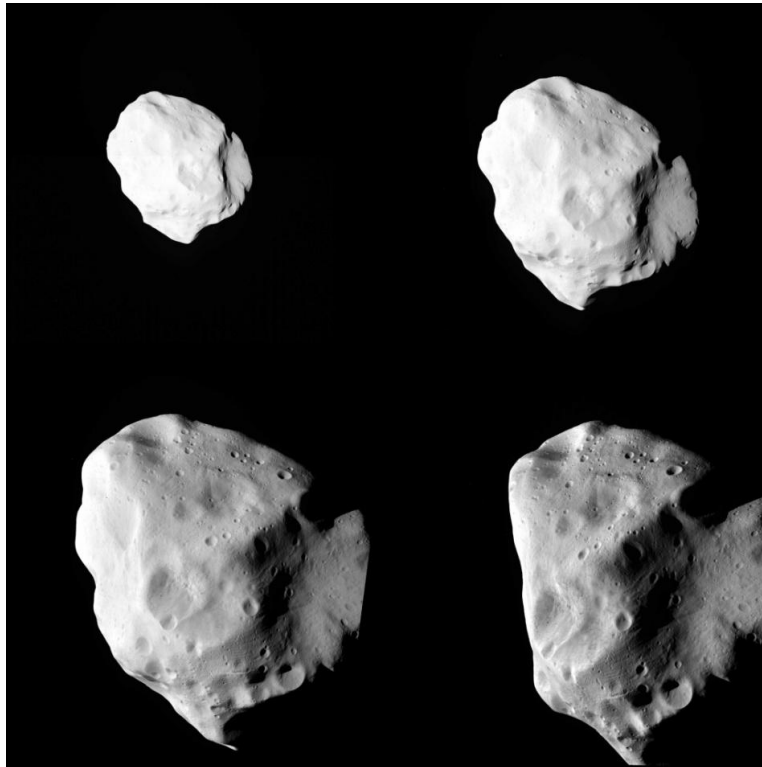


Fig. 7.4.8. Asteroid Lutetia at different snapshots near the close approach. *Courtesy of ESA 2010 MPS for OSIRIS Team MPS/UPD/LAM/IAA/RSSD/INTA/UPM/DASP/IDA, No. SEMSZCZOFBG.*

Before this close encounter, Lutetia has been extensively studied, with increasing interest since it was selected as target of the Rosetta mission in 2004 (Barucci et al., 2007), using spectroscopy in the visible, near- and mid-infrared and its albedo measured by polarimetry and thermal radiometry (e.g., Carry et al., 2010). However, the nature of this asteroid is still controversial. The outcome of these ground-based observations may be summarized as followings.

Lutetia displays a non-convex shape, probably due to large craters (Belskaya et al., 2010), along with a significant departure from an idealized ellipsoid (Drummond et al., 2010). This seems to be confirmed by recent visible spectroscopic observations, which exhibit surface variations of the spectral slope between 0.6 and 0.7 μm (Perna et al., 2010). Lutetia surface was found to be heterogeneous, probably due to variations in the texture and/or mineralogy related to the surface morphology, in part covered by a fine-grained regolith of particle size smaller than μm (Belskaya et al., 2010).

Telescopic images are processed with sizes estimate purpose. Drummond et al. (2009) used images taken at Keck Observatory to determine the asteroid triaxial ellipsoid diameters. Further improvements

of these values (e.g., Carry et al., 2010; Drummond et al., 2010) have been obtained using the “KOALA” (Knitted Occultation, Adaptive-optics, and Lightcurve Analysis) shape modelling technique. The asteroid dimensions, in conjunction with other properties such its shape and the spin, are computed by combining data set of optical lightcurves, stellar occultations and disk-resolved images obtained with adaptive optics (AO) imaging systems on the Keck and VLT telescopes. For Lutetia, a $124 \pm 5 \times 101 \pm 5 \times 80 \pm 15$ km has been proposed (Carry et al., 2010), yielding to a density of 3.5 ± 1.1 g cm⁻³ (Drummond et al., 2010).

The composition of Lutetia remained doubtful. In fact, its V+NIR spectral behaviour together with thermal emissivity obtained with the Spitzer space telescope pointed out to an analogue composition of the carbonaceous chondrites (e.g., Barucci et al., 2005), but, at the same time, the IRAS albedo (0.22 ± 0.02), obtained with radiometric measurements, leads Lutetia to be classified as an M-type asteroid, suggesting a metallic composition. On the other hand, the emissivity spectrum departs significantly from the typical metallic meteorites, so that the first M classification derived from its high IRAS albedo is not confirmed, whereas its emissivity in the 6–38 μ m range is similar to that of the CO3 and CV3 carbonaceous chondrites with a small grain size (Barucci et al., 2005). The CO carbonaceous chondrites consist of small chondrules and aggregates set in a fine-grained matrix consisting of a heterogeneous mixture of fine-grained, iron-rich olivine and hydrated silicates (Sandford, 1984). This similarity with the carbonaceous chondrites implies that Lutetia is a primordial body. Its surface has to be composed of particles of small size, with the possible presence of aqueous altered material that underwent slight thermal alteration (Barucci et al., 2005). More recently, Lazzarin et al. (2009), with NTT+EMMI at ESO–La Silla, find a behaviour similar to X-type asteroids and three absorption bands probably connected to pyroxenes. Vernazza et al. (2009), with laboratory irradiation experiment, suggest Lutetia as a possible parent body of enstatite chondrite meteorites, whereas Weaver et al. (2010), analyzing UV and visible observations with HST, found a Far–UV albedo of about 10%, too high for typical C–chondrite material (4%).

These last findings regarding Lutetia all emphasize the peculiarity of this asteroid, that however prevent a definitive knowledge of it. On the other hand, the Rosetta flyby was addressed to gain information about shape, volume, rotation, surface characteristics, number and shape of craters, light and phase curves, presence of satellites, dust and gas around the object. All the data acquired is in phase of study. In the following, a briefly discussion of the major recent findings, taking care of the physical and dynamical aspects then implemented in my numerical modelling.

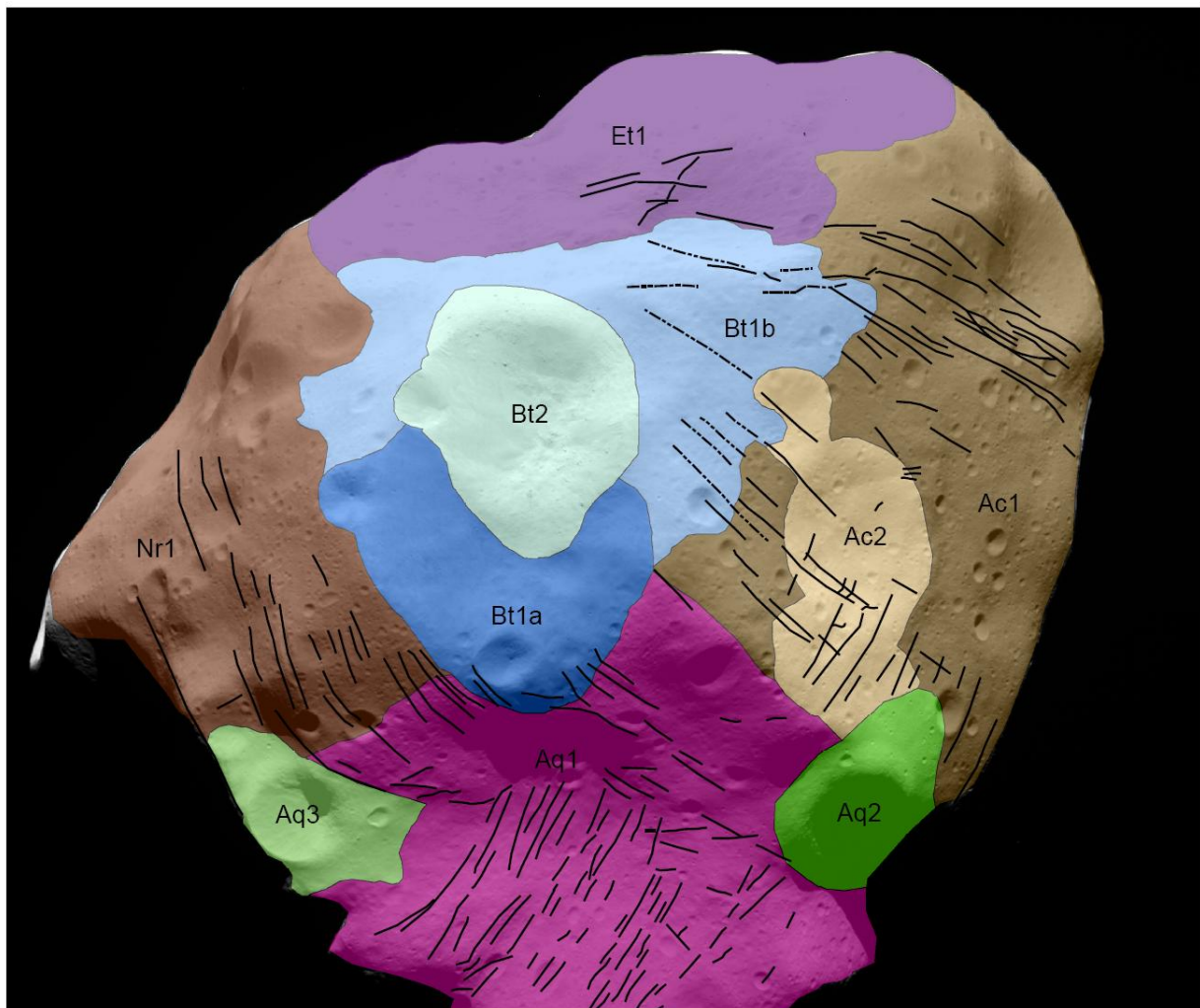
The OSIRIS images confirm the complex and diverse character of Lutetia asteroid, which was pointed to be a coherent body, not reassembled from broken fragments of preexisting asteroids (not a rubble pile), with an irregular shape due to its collisional history. The hypothesis of coherence was sustained by the presence of large-scale joints fractures and the presence of boulders relatively smaller than the size of the asteroid (Thomas et al., 2010).

Jorda et al. (2010) proposed $124 \times 112 \times 97 \text{ km}$ as best estimate of the sizes of Lutetia. This value has been derived by a model of Lutetia obtained as follows. Shape model from limb profiles is modified by the introduction of control point calculated by matching points of interest on several images by stereoscopy. From this model with concavities, a stereophotoclinometry method based on the selection of “maplets” will allow calculating the topography of the surface. The coordinates of the center of the maplets in the body-fixed frame will be calculated by stereoscopy after co-registering the images included in the analysis. The topography around the maplets will then be determined by photoclinometry. Finally, the topography of the maplets will be combined into a global topographic model.

As regards composition, both spectral and polarimetric observations point out that Lutetia’s surface composition can be likely particular types of carbonaceous chondrites (CO, CV, CH), although this is still matter of debate as an enstatite composition is not yet ruled out. In addition, it cannot be excluded that Lutetia could have a specific surface composition that is not representative among studied meteorites or has a mixed mineralogy, e.g. due to surface contamination. (Fornasier et al., 2010). The most interesting polarimetric characteristic feature of Lutetia is its wide branch of negative polarization with a large inversion angle. This may imply that at least part of Lutetia’s surface is covered by regolith composed of particles with a mean grain size smaller than $20 \mu\text{m}$. In addition, color variation is in favour to the presence of inhomogeneities in the surface, located especially in the equator (Fornasier et al., 2010).

The surface morphology is dominated by large impact craters, some of which having sizes comparable to the radius of the asteroid. Moreover, other geological features have been detected, including grabens, grooves, fault/cracks, pit-chain structures and irregular steps. In addition, there are numerous $\geq 200\text{-m}$ -diameter boulders related to the high end of the size distribution of ejecta from individual impacts. In the most extensive boulder field, the boulders appear to have been covered and possibly moved by landslides acting under the tenuous gravity ($\sim 50 \text{ m/s}$) (Thomas et al., 2010).

The preliminary geological analysis of the portion of Lutetia surface observed revealed the presence of seven principal units, on the basis of crater densities and contacts (Fig. 7.4.9). At the time of editing this thesis, the final name of the regions and craters have not established yet. The last proposal for the IAU is: Baetica, Achaia, Etruria, Aquitania, Noricum, Pannonia, Raetia (OSIRIS Team – IAU Proposal 14 January 2011).



10 5 0 10 Kilometers

- Baetica unit 2 (Bt2): deposits of the 21 km North polar crater and related landslides
 - Baetica unit1b (Bt1b): outer ejecta of the 32 km North polar crater
 - Baetica unit 1a (Bt1a): inner ejecta and deposits of the 32 km North polar crater
 - Aquitania unit 3 (Aq3): Patavium crater and ejecta
 - Aquitania unit 2 (Aq2):Francofurtum crater and ejecta
 - Aquitania unit 1 (Aq1): Aquitania crater (60 km)
 - Achaia unit 2 (Ac2):Burdigala and Lugdunum craters and ejecta
 - Etruria unit 1 (Et1): heavily cratered and partly lineated region
 - Noricum unit 1 (Nr1):heavily cratered and lineated region
 - Achaia unit 1 (Ac1): heavily cratered and lineated region
- linear features

- - - - - buried linear features

Fig. 7.4.9. Geological map of Lutetia.

In this intriguing context, my group has been focusing on the Baetica region. It was found to have the lowest crater density: 26 small ($< 0.5 \text{ km}$) craters, some of those with bright halos, signature of young ages. Preliminary age investigation has pointed out that Baetica is consistent with being formed by ejecta emplacement from other large crater, as recently as 30–100 *Ma* (Marchi et al., 2010). All the units surrounding Baetica are partially covered by smooth material, which is likely ejecta from recent impacts in this region. In fact, the defining feature of this region, is a clusters of craters, named *North Pole Crater Cluster* (NPCC), clearly visible in the closest approach image (Fig. 7.4.10).

It's a 21-*km*-diameter crater belonged to the NPCC the most recent large structure of the Baetica region (cf. Fig. 7.4.10). The crater interior shows a great variety of deposits, including mega-boulders, smooth and fine deposits and landslide accumulations, which seem to have exposed rocky outcrops. Hence, this crater has turned to be very interesting to be analyzed in more details, in particular to be modeled using iSALE. In the following paragraphs I will, address this crater as C-3PO.

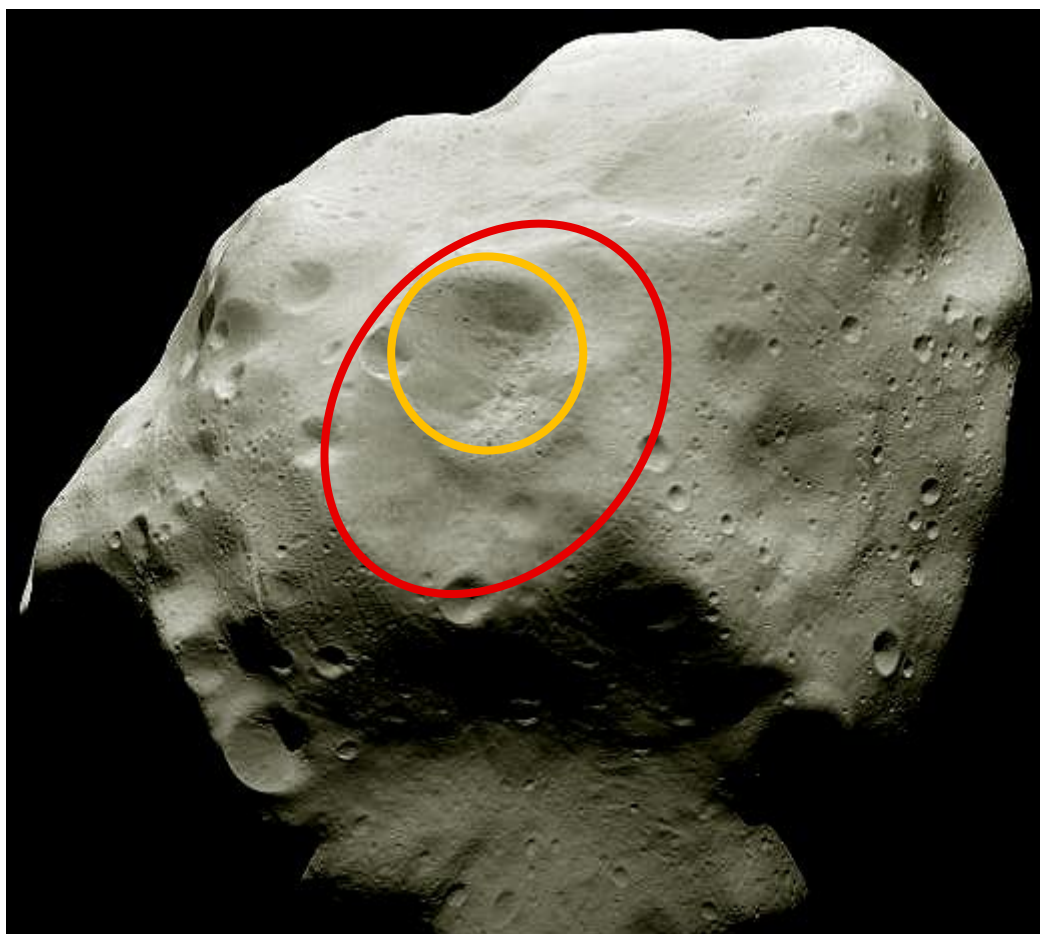


Fig. 7.4.10. CA image of Lutetia. The North Pole Crater Cluster (NPCC, *red line*) is the principal feature of Baetica, the youngest region of Lutetia. The crater studied in this thesis is a C-3PO (*yellow line*), a 21-*km* crater belonged to NPCC.

The principal aim of this investigation is to outline the crater morphology by comparing the numerical modelling outputs with the profiles obtained from the DTM generated by the DLR of Berlin, exploring a variety of materials for Lutetia. In fact, as mentioned in the previous section, an ultimate composition for this asteroid has not yet established, since spectral properties suggest a composition similar to carbonaceous or enstatite chondrite, whereas the albedo was found higher than the one expected for these type of meteorites. In addition, the determination of the size of the projectile originating C-3PO turns out to have implications on the probability formation of this structure.

To achieve this goal, numerical simulations of the impact have been performed to reproduce C-3PO, assuming different compositions for the asteroid. A discrete grid of cells is used to represent the region in which the collision occurs. The smaller the size of these cells, the more accurately the propagation of a shock wave can be resolved. However, this increase in resolution comes at the cost of computational time, so a suitable balance must be found. Hence, different cell dimensions have been considered, in order to explore the influence of resolution on the final morphology, although the crater sizes seem to be relatively insensitive to resolution (Wünnemann et al., 2008).

The usual set up (half space target) can not be kept any more, because it is not realistic for this context, as shock waves likely interfere with the asteroid boundaries. For these numerical runs, it would be more appropriate to simulate the impact as a collision of two independent bodies. Very recently, iSALE was updated with a routine to construct a self-consistent central gravity field for simulation of impacts onto spherical planetary bodies (Davison et al., 2010).

The mesh, where the impact is simulated, has dimensions suitable to contain both the colliding bodies and a surrounding “space” large enough to account either for eventual movement of the bodies with respect to their initial position and either for the ballistic launch of ejecta. I use a purely Eulerian approach, implementing as well Lagrangian tracers to track both the movement and the state of material elementary components (§ 7.3.1) (Collins et al., 2008b).

To develop a consistent model for the formation of C-3PO crater, a reliable representation of Lutetia had to be considered. The dimensions assumed are based essentially on the ones proposed by Carry et al. (2010) and Jorda et al. (2010), while composition ranges among the usual asteroid-like materials, such as dunite, basalt, granite, chondrite and olivine are employed. As Lutetia was found to be coherent with a high estimated bulk of density ($\sim 3.5 \text{ g cm}^{-3}$), only a small porosity (10%) has been set. In addition, some simulations have foreseen Lutetia to be made up by two layers. The upper layer, with a variable thickness up to 4 km, is set only of basaltic composition, because I want to investigate the influence an upper layer on the final morphology of C-3PO. In this case, a small porosity was assigned only to the core of Lutetia, while no porosity was set for the upper layer.

As I am searching for the most likely composition for Lutetia that accounts for the formation of C-3PO, all the other input parameters are taken constant. The projectile is treated for all the tested materials as a spherical dunite asteroid, 3.5 km in diameter, while the velocity was set to 4.3 km/s (most

probable asteroidal velocity in Lutetia region, Marchi pers. comm.). iSALE is a 2D hydrocode that employs axial symmetry. This limits impact events to normal incidence angles, and collisional events to a head-on, direct impact geometry (Davison et al., 2010).

The thermodynamic behaviour of each material in the model is described by an equation of state (§ 5.2.2). I use Tillotson EoS (Melosh, 1989; Benz & Asphaug, 1999; Marinova et al., 2008) for all the materials (Tab. 7.4.5), except the dunite, which is described by ANEOS.. Among the materials I have used, only granite and basalt Tillotson EOS parameters were provided by Melosh (1989) and Benz & Asphaug (1999), respectively. On the other hand, these values are not easy accessible. Marinova et al. (2008) provides the olivine EOS parameters, which they partially collected from literature sources and in part hypothesized as the average of those published for basalt, granite, anorthosite low- and high-pressure and andesite. I take into account this “methodology” to evaluate the Tillotson EOS parameters for the chondrite. My literature reference, Cintala & Grieve (1998) (hereafter, CG98), provided the parameters of Murnaghan EOS for a “Chondrite”, which approximated by a dense basalt. I use these parameters (listed in Tab. 1 in CG98) in conjunction to some assumptions and/or relations to derive the value of interest. The bulk modulus is given by CG98. The energies are taken equal to the basalt ones (Benz & Asphaug, 1999). The fitting parameters α , β and a are identical for all rocky material. b is computed from the Gruneisen parameter Γ :

$$a + b = \Gamma(p = 0)$$

$$S = \frac{1 + \Gamma_0}{2}$$

where S is a constant found in the linear shock-particle velocity equation: $U = C + Su_p$, where, in turn, U is the shock-wave velocity, u_p the particle velocity, while C corresponds to the bulk sound speed. Finally, B is computed from:

$$S = \frac{1}{2} \left[1 + \frac{B}{A} + \frac{a + b}{2} \right]$$

TILLOTSON EoS				
<i>Symbol</i>	<i>Basalt</i>	<i>Granite</i>	<i>Chondrite</i>	<i>Olivine</i>
ρ_0 (kg m ⁻³)	2650	2660	3580	3500
a	0.6	0.5	0.5	0.5
b	0.6	1.3	1.4	1.4
A (GPa)	53	18	19	131
B (GPa)	53	18	66	49
E_0 (MJ kg ⁻¹)	487	16	500	550
α	5	5	5	5
β	5	5	5	5
E_{iv} (MJ kg ⁻¹)	4.72	3.5	4.72	4.72
E_{cv} (MJ kg ⁻¹)	18.2	18	18.2	18.2

Tab. 7.4.5. Tillotson EoS parameters for the material used in the simulation (cf. explanation in the text from the references of the parameters).

The strength model used in my numerical simulations is the standard rock strength algorithm implemented in iSALE, that accounts for changes in material shear strength that result from changes in pressure, temperature and both shear and tensile damage (§ 5.2.3) (Melosh et al., 1992; Ivanov et al., 1997; Collins et al., 2004). The strength parameters adopted for all the materials are summarized in Tab. 7.4.6.

INPUT PARAMETERS

Projectile

Impactor radius (km)	3.5
Impact velocity (km/s)	4.3
Impactor material	dunite
Impactor density ($kg\ m^{-3}$)	3300
Impactor porosity	40%

Target

Lutetia semi-axes ($km \times km$)	60×40
Target material	variable
Target porosity	10%
Layer (km)	1, 2, 3, 4
Layer material	basalt
Layer density ($kg\ m^{-3}$)	2650
Layer porosity	0%

	<i>Dunite</i>	<i>Basalt</i>	<i>Granite</i>	<i>Chondrite</i>	<i>Olivine</i>
Target density ($kg\ m^{-3}$)	3300	2650	2658	3580	3500
Cohesion (Yield strength at zero pressure; <i>MPa</i>)	1	10	1	100	60
Coefficient of internal friction	0.6	1.2	2.0	0.85	1.2
von Mises plastic limit (theoretical yield strength at infinite pressure; <i>GPa</i>)	2.5	3.5	2.5	3.5	9
Cohesion (initial damaged material; <i>kPa</i>)	10	1000	1	1000	600
Coefficient of friction (damaged material)	0.6	0.6	0.6	0.6	0-6
yield strength at infinite pressure (damaged material; <i>GPa</i>)	2.0	3	2	3.5	8

Tab. 7.4.6. Numerical model setup and parameters.

The resulting crater morphologies obtained from the numerical simulations are compared with the crater morphology inferred from the OSIRIS images and related Digital Terrain Model. This latter (Fig. 7.4.11) has been obtained with respect to a 40 *km* sphere, with the origin in the asteroid center. However, comparison between the two model products has been carried out with some caution, because C-3PO is located on the wall of a underlying 40-*km* crater, and hence its final morphology is influenced by the pre-existing target topography (§ 3.1.2).

To improve the knowledge of the structure, profiles of different directions are considered (Fig. 7.4.12). Diameters range between 19 and 30 *km*, with a mean value of 23 *km*, while depth is up to 6 *km*. Due to the highly asymmetry of this impact structure, only few profiles have been subsequently used for the comparison. In addition, the results from the validation tests had to take in mind (§ 5.3): slightly underestimation of the crater diameter and overestimation of the crater depth.

The results of this analysis is reported in Fig. 7.4.13.

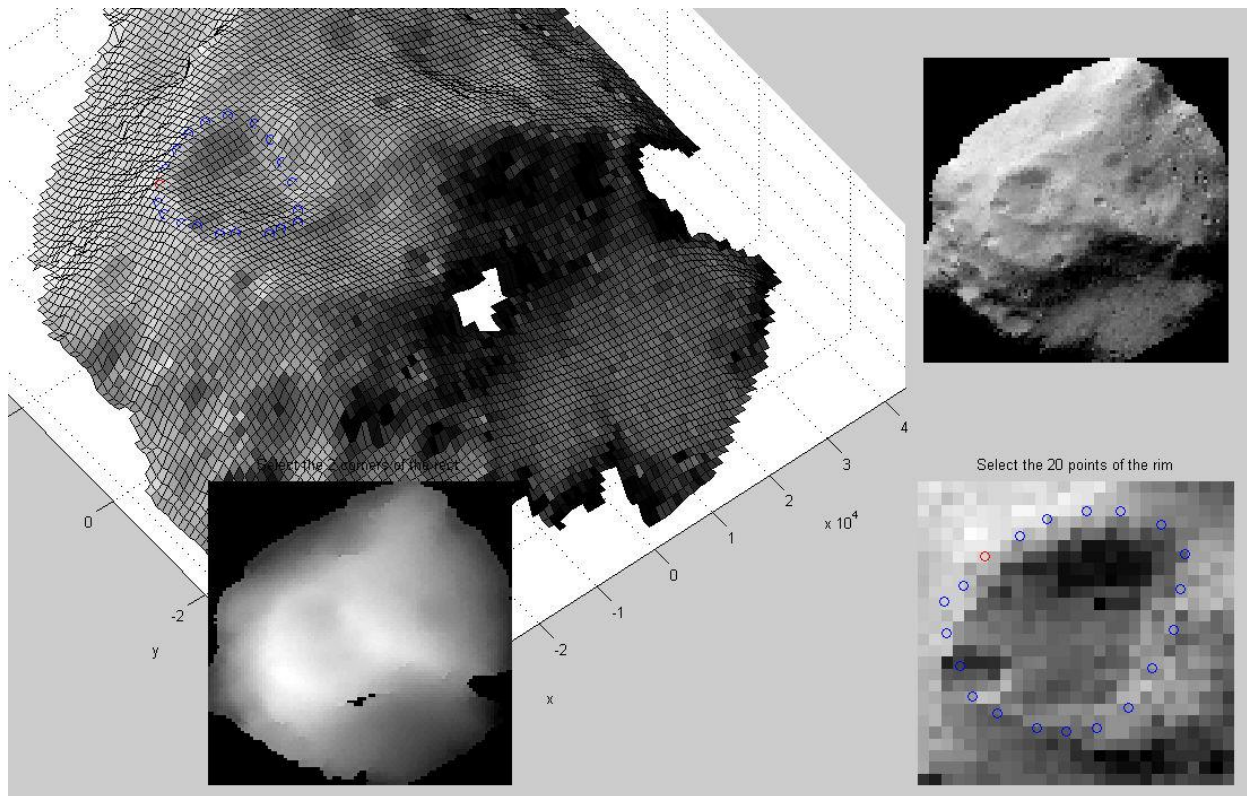


Fig. 7.4.11. DTM of the region of Lutetia where C-3PO lies. Elevations are given with respect to a 40-km sphere.

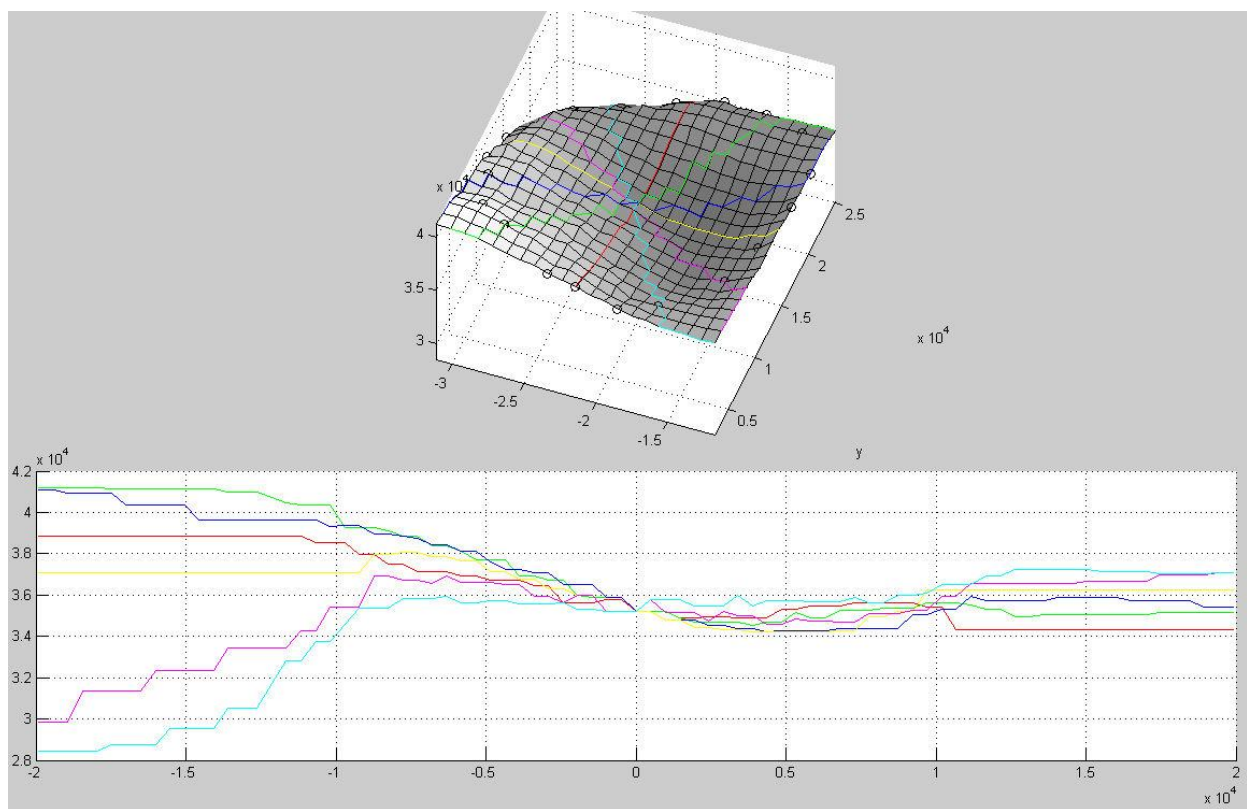


Fig. 7.4.12. DTM profiles of C-3PO for different directions. Values are given in meters.

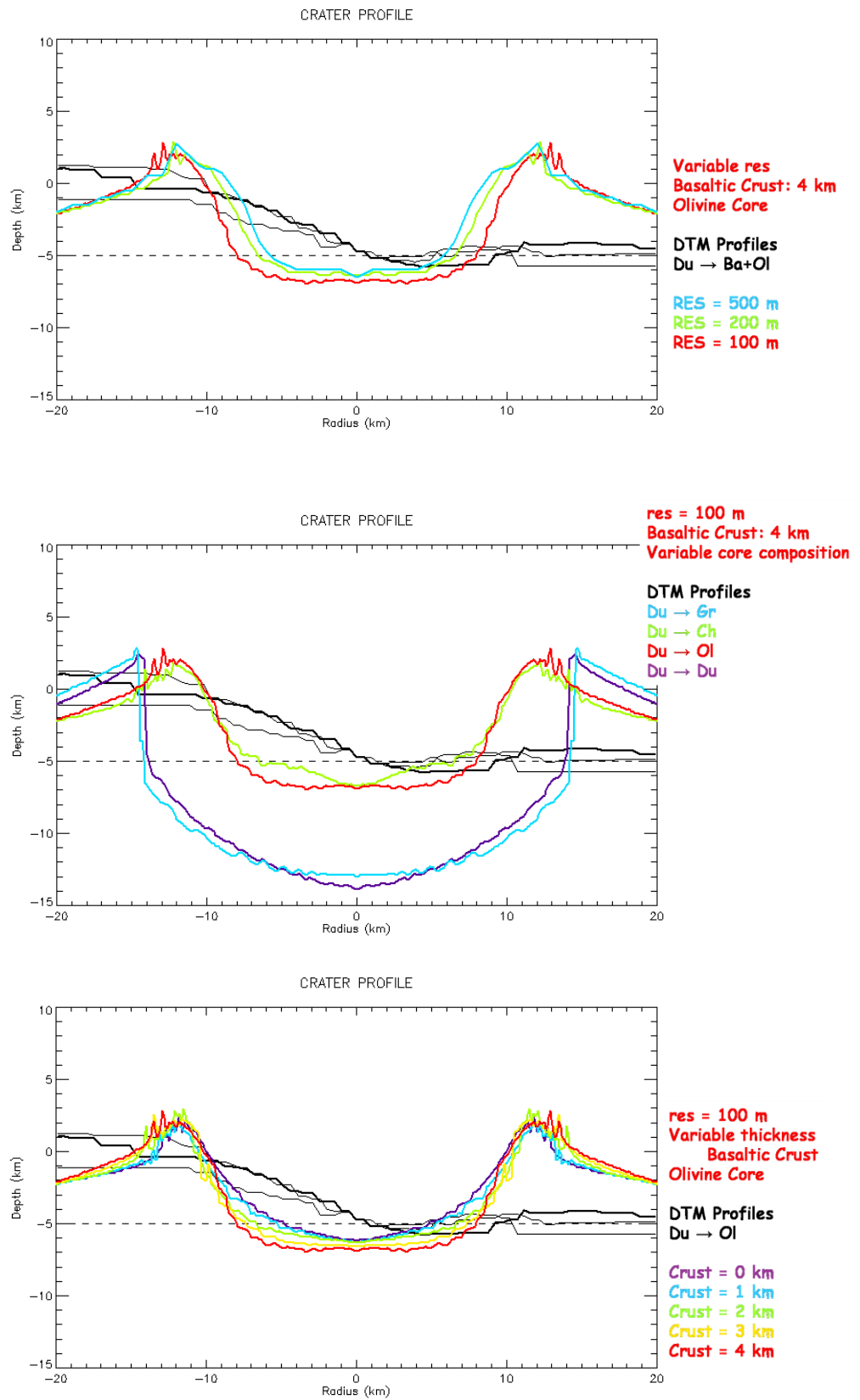


Fig. 7.4.13. Plots of the numerical simulations, with different resolution (a), materials (b) and crust thickness (c) (a, b, c are from the top to the bottom).

Some first findings can be drawn observing these plots.

Plot in Fig. 7.4.13a stresses the importance of the initial choice of the cell resolution: the adoption of saving-time lower resolutions can underestimate the final crater dimensions, hence a subsequent analysis have to consider also and thins aspect.

Plot in Fig. 7.4.13b shows the output from considering different composition for the core of Lutetia. Olivine and chondrite result the most suitable to reproduce the final crater morphology, as they gave a crater of ~ 22 km in diameter and ~ 7 km in depth. The difference in the depth can be explained both by the possible post-impact modification of the real structure, and the code error found against laboratory test ($\sim 10\%$ in the depth dimension).

Adopting an olivine composition, the effects of the upper crust is explored (Fig. 7.4.13c). The introduction of an upper layer does not seem to substantially affect the final dimensions of the crater, however, the morphology increasingly deviates from the bowl shape. In this case, only a qualitative comparison due to both poor DTM profiles and high post impact modifications.

This analysis points out an overall agreement between DTM and numerical modelling profiles. Hence, the input parameters are likely describing the projectile, in particular its sizes. According to the impactor population of Ivezic et al. (2001) and the collision probabilities of Bottke et al. (2005a), the impact event that originated C-3PO may take place every 2 Gyr.

Chapter 8

Conclusions

Impact cratering has been recognized to be the most intriguing process across the Solar System since the uniqueness of the conditions met during its occurring and the variety of morphologies it originates, but at the same time yet poorly understood. Craters, the result of this event, are ubiquitous features on the Moon, and more in general the terrestrial planets, and the asteroids, and reflect the complexity of this highly dynamic process, being hence an important *tool* in the investigation of planetary bodies.

The motivation behind this thesis was to deepen the understanding of the impact process and to explore a variety of aspects of the Solar System that can be improved by the investigation of impact craters. This analysis plays an important role as the craters are the most common feature that will be imagined on Mercury by the STC/SIMBIOSYS, to whose scientific activities this thesis belongs.

Two topics have been argued during my PhD, each one concerning different aspects of impact cratering. The first theme turns to impact craters not as an individual entity, but as a population of objects on planetary surfaces, in particular Mercury. The cratering records, being the result of a long–repeated meteorite bombardment history, can be used to infer surface age after the application of a chronological model to statistical analysis, based on the fact that the frequency of impact craters superimposed on a given geologic unit is directly correlated with geologic time.

The second theme of my thesis addresses the investigation of the impact formation process. The current understanding of impact cratering derived from extensive small–scale laboratory impact experiments and high energy explosions. Standing by to these methods of investigation, the rapid improvement of computer capabilities has allowed numerical modelling through hydrocodes to become

the favourite approach as more and more increasing complexity and realism is reachable. In fact, shocks codes represent one of the only feasible methods for studying impact craters, as they can simulate a large span of conditions beyond the reach of experiments, in addition to analyze the individual effect of any parameters acting during the impact event.

This chapter will draw together all the issues raised in this thesis regarding the investigation of craters as a *tool* to our understanding in planetary sciences.

CRATER RETENTION AGE

Age analysis has been focused on Mercury, the less known terrestrial planets (e.g., Strom and Sprague, 2003). Recently, new information have been collected by the MESSENGER mission, which took three gravity assists with the planet pending its orbit insertion in 2011. During this flyby, MESSENGER imaged up to 91% of the surface of Mercury, revealing new intriguing features, among which Raditladi and Rachmaninoff that soon appeared to be remarkably young, likely formed well after the end of the LHB, as the small number of craters in their rims testifies.

To perform crater retention age analysis, I have adopted a recent chronology model proposed by Marchi et al. (2009), who used the dynamical models of both the Main Belt Asteroids and Near Earth Objects (e.g., Bottke et al., 2002, 2005a) to derive the impactor flux, which is then converted via scaling law (Holsapple & Housen, 2007) into the MPF, in turn calibrated using the lunar rocks radiometric ages. Strength points of this model are the implementation of dynamical models, when they are available, to describe the impactors flux on a given planet, the possibility to simulate a non-constant impact flux through time and the geological interpretation of the upper crustal layering of the studied region (e.g., Massironi et al., 2009). In particular, the possibility to implement a layered planetary-like crust stands at the basis of the dating investigation performed in this thesis.

Age analysis for both Raditladi and Rachmaninoff began with the identification of the geological units that have undergone similar endogenic and exogenic processes, on the base of their different surface morphologies and spectral characteristics, i.e. albedo, joined with an analysis of their stratigraphic relationships. For sake of simplicity in deriving ages, geological units were classified into three main areas: inner plains, annular plains and ejecta. Then, crater counts was performed by an ad hoc facility written in IDL language. A crucial point in collecting these data is that only primary craters (originated by meteoroids coming from heliocentric orbits) enter the final statistics, while all the recognized secondary craters, volcanic features and tectonic structures must be avoided. The final ages for these basins were obtained by implementing different thickness values for the fractured upper layer, that is derived from the craters size-frequency distribution.

Let see Raditladi. The annular plains were found to be $0.98 Ga$, if a surficial fractured layer thickness of $D_t = 3 km$ is adopted. On the other hand, inner plains display a so poor statistics to not constrain D_t . Hence, MPF age was derived by considering two different thicknesses, once time taking the value as for the annular units ($D_t = 3 km$), and in the second case assuming a negligible thickness ($D_t \sim 0$). The ages resulted $1.53 Ga$ and $0.56 Ga$, respectively.

The finding of an age for the inner plains higher than the one of the annular plains, along with the absence of any particular albedo, colour or clear stratigraphic relationships within the basins, all these facts together seem to suggest that the inner plains were most probably coeval with the unit between the peak-ring and the basin rim emplaced during the impact event. In this case, it turned appropriate to consider the crater SFD of the whole basin floor. The resulting model age is $1.37 Ga$. The MPF age is in agreement with the age inferred by Strom et al. (2008) on the basis of a relative-chronology approach.

Concerning the ejecta blanket, the measured crater SFD is consistent with the basin floor, therefore it implies a similar age. However, it is not easily modeled by MPF, most probably due to the rough texture of the ejecta blanket that makes the identification of craters very difficult.

Let see Rachmaninoff. The ejecta blanket was found to be $\sim 3.42 Ga$, if a surficial fractured layer thickness of $D_t = 10.5 km$ is adopted. This value is consistent with values already determined for other large basins on Mercury (Massironi et al., 2009).

The annular plains were found to be $\sim 3.39 Ga$, if a surficial fractured layer thickness of $D_t = 4.5 km$ is adopted. This thickness is consistent with the supposed brecciated nature of this terrain, possibly more or less welded by impact melt at depth, due to the formation of the basin. On the other hand, if the fractured layer thickness value used for the ejecta blanket is adopted, the age of the annular units turned $\sim 3.48 Ga$, showing an only marginal influence of D_t , on the final result. Therefore the age of the annular units can be fixed to about $3.4 Ga$.

Regarding the inner plains, the statistics are poorer, therefore the crater SFD cannot be used to infer D_t . Nevertheless, geological analysis suggests that the inner plains are younger volcanic flows on the basis of their different albedo, colour and overlapping relationships with respect to the unit emplaced between the peak-ring and the basin rim (Prockter et al., 2010). This would make possible also the scenario in which the former megaregolith horizon was completely hardened by lavas and the subsequent impacts were able only to create a very thin regolith layer, negligible to affect the formation of the sparse and relatively large craters detected. In this case the derived model age is $0.36 Ga$. For comparison, the model age using $D_t = 4.5 km$ as for the annular units yields to an age of $0.92 Ga$. In either case the inner plains turn out to be remarkably young, demonstrating that a recent volcanic activity occurred within the basin.

NUMERICAL MODELLING

Numerical modelling of impact structures was performed through iSALE shock code (Amsden et al., 1980; Collins et al., 2004; Ivanov et al., 1997; Wünnemann et al., 2003, 2006). The model is based on the SALE hydrocode (Amsden et al., 1980), which was subsequently modified to include an elasto-plastic constitutive model, fragmentation models, various equations of state (EoS), and multiple materials (Melosh et al., 1992; Ivanov et al., 1997). The most recent advance was the implementation of a novel porosity compaction model, the so-called ε - α -model (Wünnemann et al., 2006). The code is well tested against laboratory experiments at low and high strain-rates (Wünnemann et al., 2006) and other hydrocodes (Pierazzo et al., 2008).

Numerical modelling was achieved for two craters, coming from a completely different environment, the Earth and one asteroid, recently observed by a space mission. In the first case, the knowledge of the surrounding area where the structure is located allowed to study in detail the impact crater collapse mechanism that origins a large crater. On the other hand, the good relatively knowledge of the formation of a simple crater allowed to investigate the composition and the structure of the asteroid. In both cases, the numerical modelling of the impact process have demonstrated to be a powerful *tool* to deepen our comprehension on the Solar System, and the related results are presented in the following.

OMEONGA.

Omeonga is a ~ 47 km-diameter ring structure suspected to be impact in origin. The area is hardly accessible for on-field investigations, hence up to now only extensive geomorphological and remote sensing analysis integrated with a stratigraphic and geological review of the area has been accomplished. The numerical modelling of Omeonga structure has had the aim of integrate the geological observations in favour of the impact origin.

To model Omeonga formation, I take an halfspace representing the target, which is made up by two lithological units, i.e. a crystalline basement of about 30-km-thickness of granite, in turn covered by 1.8-km-layer of sandstone, with a porosity of 0% and 25%, respectively. The impactor is set as a 5-km meteoroid having a granitic composition and an impact velocity of 12 km s^{-1} .

The thermodynamic behaviour of all the materials was described by the Tillotson equation of state, while the strength model is the standard rock strength algorithm implemented in iSALE, that accounts for changes in material shear strength resulting from changes in pressure, temperature and both shear and tensile damage.

In addition, the acoustic fluidization mechanism is implemented to facilitate deep-seated gravitational collapse of the initial bowl-shaped cavity. The behaviour of acoustically fluidized matter is mainly determined by the viscosity η and the decay time τ , that are both strongly linked with the fragmentation state of the rocks beneath the structure. Hence, a number of runs was carried out to find the couple of parameters that better reproduce Omeonga structure.

My best-fit numerical model crater has a diameter of 48 km, a depth of 1.750 km below the pre-impact surface and a rim height of 0.25 km above the pre-impact surface, while the central ring is 28 km in diameter. In this central ring area, the uplifted zone displays a lower-sequence sediments above the crystalline basement. As already pointed out by Collins et al. (2008b) in a study of the Haughton crater (Canada), the sedimentary layer is thick enough to not allow the the granite basement to upturn: the overturning of the surface that follows the uplift involves only the mid-sedimentary sequence strata.

The obtained modeled structure is compared with the ASTER-derived profiles, although the hard erosion at Omenga makes extremely difficult a comparison of the final simulated crater with observations. My best-fit model does appear to show a good correlation between the rim and peak-ring diameters, but, at the same time, to consistently overestimate the depth of the final simulated structure, by a value higher (~1 km deeper) than the mismatch of 20% expected from the validation test. Hence, a considerable post-impact modification is invoked, due to erosion of the ridges, gravitational phenomena involving the rim and the peak-ring, and sediments deposition at the thalweg of the Unia and the Lomami rivers.

C-3PO

C-3PO is a 21-km-diameter crater belonged to the North Pole Crater Cluster on Lutetia asteroid and was found to be the most recent large structure of the Baetica region. The crater interior shows a great variety of deposits, including mega-boulders, smooth and fine deposits and landslide accumulations, which seem to have exposed rocky outcrops.

The principal aim of this investigation is to outline the crater morphology by comparing the numerical modelling output with the profiles obtained from the DTM generated by the DLR of Berlin, exploring a variety of materials and layered structure for Lutetia.

To develop a consistent model for the formation of C-3PO crater, I take an ellipsoid 120×80 km to represent Lutetia, while composition ranges among the usual asteroid-like materials, such as dunite, basalt, granite, chondrite and olivine. As Lutetia was found to be coherent with an estimated high bulk of density ($\sim 3.5 \text{ g cm}^{-3}$), only a small porosity (10%) has been set. In addition, some simulations have foreseen Lutetia to be made up by two layers. In this case, the upper layer was set of basaltic composition with no porosity and a variable thickness from 1 km to 4 km.

The projectile is treated for all the tested materials as a spherical dunite asteroid, 3.5 km in diameter, while the velocity was set to 4.3 km/s.

The thermodynamic behaviour of the materials was described by the ANEOS equation of state for dunite, and the Tillotson one for all the other materials, while the strength model is the standard rock strength algorithm implemented in iSALE.

The resulting crater morphologies obtained from the numerical simulations are compared with the crater morphology inferred from the OSIRIS images and the related DTM, which provided a diameter of about 23 km and a depth up to 6 km. The findings of this comparison can be summarized as follows.

The resolution of the cell shows a negligible influence on the final diameter, while the depth increases of 30% from the lower to the higher resolutions tested in my simulations.

The profiles have been obtained varying the composition, showing that olivine and chondrite are the most suitable to reproduce the final crater morphology, as they gave a crater of about 22 km in diameter and 7 km in depth. The difference in the depth can be explained both by the possible post-impact modification of the real structure, and the code error found against laboratory test (10% in the depth dimension). Adopting an olivine composition, the effects of the upper crust is explored. The introduction of an upper layer does not seem to substantially affect the final dimensions of the crater, however, the morphology increasingly deviates from the bowl shape. In this case, only a qualitative comparison is possible, due to both poor DTM profiles and high post-impact modifications.

This analysis points out an overall agreement between DTM and numerical modelling profiles. Hence, the input parameters are likely describing the projectile, in particular its sizes. According to the impactor population of Ivezić et al. (2001) and the collision probabilities of Bottke et al. (2005a), the impact event that originated C-3PO may take place every 2 Gyr.

The overall findings of this investigation highlights crater modelling to a powerful *tool* in probing planetary surfaces, and it could be the starting point for a new intriguing travel across the Solar System.

Bibliography

- AHRENS, T.J., and O'KEEFE, J.D., 1977. Equations of state and impact-induced shock-wave attenuation on the Moon. In: D.J. Roddy, R.O. Pepin and R.B. Merrill (eds), *Impact and Explosion Cratering: Planetary and Terrestrial Implications*, Pergamon, New York, pp. 639–656.
- ALVAREZ, L.W., ALVAREZ, W., ASARO, F., and MICHEL, H.V., 1980. Extraterrestrial Cause for the Cretaceous-Tertiary Extinction. *Science*, Vol. **208**, pp. 1095–1108.
- AMSDEN, A.A., RUPPEL, H.M., and HIRT, C.W., 1980. SALE: A simplified ALE Computer Program for Fluid Flows at all speeds. Los Alamos National Laboratories, Report **LA-8095**.
- AMSDEN, A.A., and RUPPEL, H.M., 1981. SALE-3D: A simplified ALE Computer Program for calculating Three-Dimensional Fluid Flows. Los Alamos National Laboratories, Report **LA-8905**.
- ANDERS, E., 1964. Origin, age and composition of meteorites. *Space Sci. Rev.*, Vol. **3**, pp. 583–574.
- ANDERS, E. and ARNOLD, J.R., 1965. Age of craters on Mars. *Science*, Vol. **149**, 1494–1496.
- ANDERSON Jr, C.E., 1987. An overview of the theory of hydrocodes. *International Journal of Impact Engineering*, Vol. **5**, pp. 33–59.
- ANDERSON, D.L., 2007. *New Theory of the Earth*. Cambridge University Press. 384 p.
- ARNOLD, J.R., 1979. Ice in the lunar polar regions. *Journal of Geophysical Research*, Vol. **84**, pp. 5659–5668.
- ARTEMIEVA, N.A., 2005. Small primaries versus large secondaries on Mars—numerical approach. *Lunar Planet. Sci.* **36**, abstract #1589.
- ARTEMIEVA, N.A., KARP, T., and MILKEREIT, B., 2004. Investigating the Lake Bosumtwi impact structure: Insight from numerical modeling. *Geochemistry Geophysics Geosystem*, Vol. **5**, Q11016,1–20.
- ARVIDSON, R., BOYCE, J., CHAPMAN, M., CINTALA, M., FULCHIGNONI, M., MOORE, H., NEUKUM, G., SCHULZ, P., SODERBLOM, L., STROM, R., WORONOW, A., and YOUNG, R., 1979. Standard Techniques for Presentation and Analysis of Crater Size-frequency Data. *Icarus*, Vol. **37**, pp. 467–474.
- ASAY, J.R., and SHAHINPOOR, M., 1993. *High-pressured shock compression of solids*. Springer, New York, Berlin, Heidelberg, 393 p.

- ASLOP, G.I., BROWN, J.P., DAVISON, I., and GIBLING, M.R., 2000. The geometry of drag zones adjacent to salt diapirs. *Journal of the Geological Society, London*, Vol. **157**, pp. 1019–1029.
- ASPHAUG, E., MOORE, J.M., MORRISON, D., BENZ, W., NOLAN, M.C., and SULLIVAN, R.J., 1996. Mechanical and Geological Effects of Impact Cratering on Ida. *Icarus*, Vol. **120**, pp. 158–184.
- ASPHAUG, E., RYAN, E.V., and ZUBER, M.T., 2002. Asteroid interiors. In: W.K. Bottke Jr, P. Cellino, P. Paolicchi, R.P. Binzel (eds), *Asteroids III*, Univ. Arizona Press, Tucson, pp. 463–484.
- BAR-NUN, A., BARUCCI, A., BUSSOLETTI, E., et al., 1993. Rosetta comet rendezvous mission. *ESA SCI* **7**.
- BARLOW, N.G., 2004. Martian subsurface volatile concentrations as a function of time: Clues from layered ejecta craters. *Geophysical Research Letters*, Vol. **31**, L05703,1–4.
- BARUCCI, M.A., FULCHIGNONI, M., FORNASIER, S., DOTTO, E., VERNAZZA, P., BIRLAN, M., BINZEL, R.P., CARVANO, J., MERLIN, F., BARBIERI, C., and BELSKAYA, I.N., 2005. Asteroid target selection for the new Rosetta mission baseline. *Astronomy & Astrophysics*, Vol. **430**, pp. 313–427.
- BARUCCI, M.A., FULCHIGNONI, M., and ROSSI, A., 2007. Rosetta asteroid targets: 2867 Steins and 21 Lutetia. *Space Science Reviews*, Vol. **128**, pp. 67–78.
- BATUMIKE, J.M., GRIFFIN, W.L., O'REILLY, S.Y., BELOUSOVA, E.A. and PAWLITSCHKEK, M., 2009. Crustal evolution in the central Congo-Kasai Craton, Luebo, D.R. Congo: Insights from zircon U–Pb ages, Hf–isotope and trace–element data. *Precambrian Research*, Vol. **170**, pp. 107–115.
- BELSKAYA, I.N., FORNASIER, S., KRUGLY, Y.N., SHEVCHENKO, V.G., GAFTONYUK, N.M., BARUCCI, M.A., FULCHIGNONI, M., and GIL–HUTTON, 2010. Puzzling asteroid 21 Lutetia: our knowledge prior to the Rosetta fly–by. *Astronomy & Astrophysics*, Vol. **515**, pp. A29,1–8.
- BELTON, M.J., VEVERKA, J., THOMAS, P., HELFENSTEIN, P., SIMONELLI, D., CHAPMAN, C., DAVIES, M.E., GREELEY, R., GREENBERG, R., HEAD, J., MURCHIE, S., KLAASEN, K., JOHNSON, T.V., McEWN, A.S., MORRISON, D., NEUKUM, G., FANALE, F., ANGER, C., CARR, M., and PILCHER, C., 1992. Galileo Encounter with 951 Gaspra: First Pictures of an Asteroid. *Science*, Vol. **257**, pp. 1647–1652.
- BENKHOFF, J., SEIDENSTICKER, K.J., SEIFERLIN, K., and SPOHN, T., 1995. Energy analysis of porous water ice under space-simulated conditions: results from the KOSI-8 experiment. *Planet. Space Sci.*, Vol. **43**, pp. 353–361.
- BENKHOFF, J., van CASTEREN, J., FUJIMOTO, M., LAAKSO, H., NOVARA, M., FERRI, P., MIDDLETON, H.R., and ZIETHE, R., 2010. BepiColombo—Comprehensive exploration of Mercury: Mission overview and science goals. *Planetary and Space Science*, Vol. **58**, pp. 2–20.
- BENZ, W., SLATTERY, W.L., and CAMERON, A.G.W., 1988. Collisional Stripping of Mercury's Mantle. *Icarus*, Vol. **74**, pp. 516–528.
- BENZ, W., and ASPHAUG, E., 1999. Catastrophic Disruptions Revisited. *Icarus*. Vol. **142**, pp. 5–20.
- BIBRING, J.-P., LANGEVIN, Y., MUSTARD, J.F., POULET, F., ARVIDSON, R., GENDRIN, A., GONDET, B., MANGOLD, N., PINET, P., and FORGET, F., 2006. Global mineralogical and aqueous Mars history derived from OMEGA/Mars express data. *Science*, Vol. **312**, pp. 400–404.
- BIDA, T.A., KILLEN, R.M., and MORGAN T.H., 2000. Discovery of calcium in Mercury's atmosphere. *Nature*, Vol. **404**, pp. 159–161.
- BIERHAUS, E.B., 2004. Discovery that secondary craters dominate Europa's small crater population. PhD thesis. Univ. Colo. Boulder, 293 p.

- BIERHAUS, E.B., CHAPMAN, C.R., MERLINE, W.J., BROOKS, S.M., and ASPHAUG, E., 2001. Pwyll Secondaries and Other Small Craters on Europa. *Icarus*, Vol. **153**, pp. 264–276.
- BIERHAUS, E.B., CHAPMAN, C.R., and MERLINE, W.J., 2005. Secondary craters on Europa and implications for cratered surfaces. *Nature*, Vol. **437**, pp. 1125–1127.
- BINGHAM, E.C., 1916. An investigation of the laws of plastic flow. *Bull. Bur. Stand.*, Vol. **13**, pp. 309–53.
- BINZEL, R.P., LUPISHKO, D.F., DI MARTINO, M., WHITELEY, R.J., and HAHN, G.J., 2002. Physical Properties of Near–Earth Objects. In: W.K. Bottke Jr, P. Cellino, P. Paolicchi, R.P. Binzel (eds), *Asteroids III*, Univ. Arizona Press, Tucson, pp. 255–271.
- BIRCK, J.L., and ALLÈGRE, C.J., 1978. ^{87}Rb – ^{87}Sr age of soils and rock from Mare Crisium Luna 24. *Physics of the Earth and planetary Interiors*, Vol. **16**, pp. P10–P14.
- BLEWETT, D.T., ROBINSON, M.S., DENEVI, B.W., GILLIS–DAVIS, J.J., HEAD III, J.W., SOLOMON, S.C., HOLSDAW, G.M., and McCLINTOCK, W.E., 2009. Multispectral images of Mercury from the first MESSENGER flyby: Analysis of global and regional color trends. *Earth and Planetary Science Letters*, Vol. **285**, pp. 272–282.
- BOTTKE Jr, W.K., JEDICKE, R., MORBIDELLI, A., PETIT, J.–M., and GLADMAN, B., 2000. Understanding the Distribution of Near–Earth Asteroids. *Science*, Vol. **288**, pp. 2190–2194.
- BOTTKE Jr, W.K., MORBIDELLI, A., JEDICKE, R., PETIT, J.M., LEVISON, H.F., MICHEL, P., and METCALFE, T.S., 2002a. Debaised orbital and absolute magnitude distribution of the near Earth objects. *Icarus*, Vol. **156**, pp. 399–433.
- BOTTKE Jr, W.K., CELLINO, A., PAOLICCHI, P., and BINZEL., R.P., 2002b. An Overview of the Asteroids: The Asteroids III Perspective. In: W.K. Bottke Jr, P. Cellino, P. Paolicchi, R.P. Binzel (eds), *Asteroids III*, Univ. Arizona Press, Tucson, pp. 3–15.
- BOTTKE Jr, W.F., DURDA, D.D., NESVORNÝ, D., JEDICKE, R., MORBIDELLI, A., VOKROUHLICKÝ, D., and LEVISON, H., 2005a. The fossilized size distribution of the main asteroid belt. *Icarus*, Vol. **175**, pp. 111–140.
- BOTTKE Jr, W.F., DURDA, D.D., NESVORNÝ, D., JEDICKE, R., MORBIDELLI, A., VOKROUHLICKÝ, D., and LEVISON, H., 2005b. Linking the collisional history of the main asteroid belt to its dynamical excitation and depletion. *Icarus*, Vol. **179**, pp. 63–94.
- BOTTKE Jr, W.F., NESVORNÝ, D., and DURDA, D.D., 2005c. Are most small craters primaries or secondaries: insights from asteroid collisional/dynamical evolution models. *LPSC 36th*, abstract #1489.
- BOYCE, J.M., SCHABER, G.G., and DIAL Jr, A.L., 1977. Age of Luna 24 mare basalts based on crater studies. *Nature*, Vol. **265**, pp. 38–39.
- BRAY, V.J., 2009. Impact Crater Formation on the Icy Galilean Satellites. Doctoral Dissertation, Department of Earth Science and Engineering Imperial College, London.
- BRITT, D.T., YEOMANS, D., HOUSEN, K.R., and CONSOLOMAGNO, G., 2002. Asteroid density, porosity and structure. In: W.K. Bottke Jr, P. Cellino, P. Paolicchi, R.P. Binzel (eds), *Asteroids III*, Univ. Arizona Press, Tucson, pp. 485–500.
- BROADFOOT, A.L., KUMAR, S., BELTON, M.J.S., McELROY, M.B., 1974. Mercury's Atmosphere from Mariner 10: Preliminary Results. *Science*, Vol. **185**, pp. 166–169.

- BRUZZONE, L., LIZZI, L., MARCHETTI, P.G., EARL, J., and MILNES, M., 2004. Recognition and Detection of Impact Craters from EO Products. Proceedings of ESA–EUSC 2004, pp. 60.1.
- BSCHORR, O., 1970. Ratio of meteor fall to earth and moon. COSPAR Tagung, Leningrad, USSR.
- BUE, B.D., and STEPINSKI, T.F., 2007. Machine Detection of Martian Impact Craters from Digital Topography Data. IEEE Transactions on Geoscience and Remote Sensing, Vol. **45**, No. **1**, pp. 265–274.
- BURCHELL, M.J., GREY, I.D.S., and SHRINE, N.R.G., 2001. Laboratory investigations of hypervelocity impact cratering in ice. Adv. Space Res., Vol. **28**, pp. 1521–1526.
- BURCHELL, M.J., LELIWA–KOPPYSTŃSKI, J., and ARAKAWA, M., 2005. Cratering of icy targets by different impactors: Laboratory experiments and implications for cratering in the Solar System. Icarus, Vol. **179**, pp. 274–288.
- BURCHELL, M.J., ROBIN–WILLIAMS, R., and FOING, B.H., 2010. The SMART–1 lunar impact. Icarus, Vol. **207**, pp. 28–38.
- BUTLER, B.J., MUHLEMAN, D.O., and SLADE, M.A., 1993. Mercury: Full-disk images and the detection and stability of ice at the north pole. Journal of Geophysical Research, Vol. **98**, pp. 15,003–15,023.
- BYERLEE, J., 1978. Friction of rocks. Pure and Applied Geophysics, Vol. **116**, pp. 615–626.
- BYRNE, S., DUNDAS, C.M., KENNEDY, M.R., MELLON, M.T., SHEAN, D.E., DAUBER, I.J., CULL, S.C., SEELOS, K.D., MURCHIE, S.L., CANTOR, B., ARVIDSON, R.E., EDGETT, K.S., McEWEN, A.S., HARRISON, T., POSIOLOVA, L., SEELOS, F.P., and HiRISE Team, Ctx Team, Crism Team, 2009a. Excavation of subsurface ice on Mars by new impact craters. In: Lunar and Planetary Institute Science Conference Abstracts, Lunar and Planetary Institute, Technical Report, Vol. **40**, pp. 1831–1832.
- BYRNE, S., DUNDAS, C.M., KENNEDY, M.R., MELLON, M.T., McEWEN, A.S., CULL, S.C., DAUBER, I.J., SHEAN, D.E., SEELOS, K.D., MURCHIE, S.L., CANTOR, B., ARVIDSON, R.E., EDGETT, K.S., REUFER, A., THOMAS, N., HARRISON, T.N., POSIOLOVA, L.V., and SEELOS, F.P., 2009b. Distribution of mid-latitude ground ice on Mars from new impact craters. Science, Vol. **325**, pp. 1674–1676.
- CAHEN, L., 1954. Géologie du Congo belge. H. Vaillant-Carmanne, Liège, 577 p.
- CAHEN, L., FERRAND, J.J., HAARSMA, M.J., LEPERSONNE, J., and VERBEEK, T., 1960. Description du Sondage de Dekese (Résultats scientifiques des missions du Syndicat pour l'étude géologique et minière de la Cuvette congolaise et Travaux connexes. Géologie). Ann. Musée Royal du Congo Belge, Sc. Géol., Tervuren, Vol. **34**, 115 p., 3 planches.
- CARRY, B., KAASALAINEN, M., LEYRAT, C., MERLIN, W.J., DRUMMOND, J.D., CONRAD, A., WEAVER, H.A., TAMBLYN, P.M., CHAPMAN, C.R., DUMAS, C., COLAS, F., CHRISTOU, J.C., DOTTO, E., PERNA, D., FORNASIER, S., BERNASCONI, L., BEHREND, R., VACHIER, F., KRYSZCZYNSKA, A., POLINSKA, M., FULCHIGNONI, M., ROY, R., NAVES, R., RAYMOND, P., WIGGINS, P., 2010. Physical properties of ESA Rosetta target asteroid (21) Lutetia: Shape and flyby geometry. Astronomy & Astrophysics, Vol. **523**, pp. A94,1–19.
- CHAPMAN, C.R., 2002. Cratering on Asteroids from Galileo and NEAR Shoemaker. In: W.K. Bottke Jr, P. Cellino, P. Paolicchi, R.P. Binzel (eds), Asteroids III, Univ. Arizona Press, Tucson, pp. 315–330.
- CHAPMAN, C.R., 2004. The hazard of near–Earth asteroid impacts on earth. Earth and Planetary Sciences Letters, Vol. **222**, pp. 1–15.
- CHAPMAN, C.R., and HAEFNER, R.R., 1967. A critique of methods for analysis of the diameter–frequency relation for craters with special application to the Moon. J. Geophys. Res., Vol. **72**, pp. 549–557.

- CHAPMAN, C.R., RYAN, E.V., MERLINE, W.J., NEUKUM, G., WAGNER, R., THOMAS, P.C., VEVERKA, J., and SULLIVAN, R.J., 1996a. Cratering on Ida. *Icarus*, Vol. **120**, pp. 77–86.
- CHAPMAN, C.R., VEVERKA, J., BELTON, M.J.S., NEUKUM, G., and MORRISON, D., 1996b. Cratering on Gaspra. *Icarus*, Vol. **120**, pp. 231–245.
- CHAPMAN, C.R., 2004. Frontiers. The hazard of near–Earth asteroid impacts on earth. *Earth and Planetary Science Letters*, Vol. **222**, pp. 1–15.
- CHASE, S.C., et al., 1974. Preliminary Infrared Radiometry of the Night Side of Mercury from Mariner 10. *Science*, Vol. **185**, pp. 142–145.
- CHOUBERT, G., and FAURE–MURET, A., 1986. Carte géologique internationale de l’Afrique (International Geological Map of Africa). Published by CGMW and Unesco.
- CHYBA, C.F., 1991. Terrestrial mantle siderophiles and the lunar impact record. *Icarus*, Vol. **92**, pp. 217–233.
- CINTALA, M.J., and GRIEVE, R.A.F., 1998. Scaling impact melting and crater dimensions: Implications for the lunar cratering record. *Meteoritics & Planetary Science*, Vol. **33**, pp. 889–912.
- CLARK, R.N., 2009. Detection of Adsorbed Water and Hydroxyl on the Moon. *Science*, Vol. **326**, pp. 562–564.
- COHEN, B.A., SWINDLE, T.D., and KRING, D.A., 2000. Support for the lunar cataclysm hypothesis from lunar meteorite impact melt ages. *Science*, Vol. **290**, pp. 1754–1756.
- COHEN, B.A., SWINDLE, T.D., and KRING, D.A., 2005. Geochemistry and ^{40}Ar – ^{39}Ar geochronology of impact–melt clasts in feldspathic lunar meteorites: Implications for lunar bombardment history. *Meteorit. Planet. Sci.*, Vol. **40**, pp. 755–777.
- COLAPRETE, A., BRIGGS, G., ENNICO, K., WOODEN, D., HELDMANN, J.L., SOLLITT, L., ASPHAUG, E., KORYCANSKY, D., SCHULTZ, P., CHRISTENSEN, A., GALAL, K., BART, G.D., and the LCROSS Team, 2009. An overview of the Lunar Crater Observation and Sensing Satellite (LCROSS) mission – An ESMD mission to investigate lunar polar hydrogen. *Lunar Planet. Sci.* **40**, abstract #1861.
- COLAPRETE, A., SCHULTZ, P., HELDMANN, J.L., WOODEN, D., SHIRLEY, M., ENNICO, K., HERMALYN, B., MARSHALL, W., RICCO, A., ELPHIC, R.C., GOLDSTEIN, D., SUMMY, D., BART, G.D., ASPHAUG, E., KORYCANSKY, D., LANDIS, D., and SOLLITT, L., 2010. Detection of water in the LCROSS Ejecta Plume. *Science*, Vol. **330**, pp. 463–468.
- COLLINS, G.S., 2001. Hydrocode simulations of complex crater collapse. *LPSC 32th*, abstract #1752.
- COLLINS, G.S., 2002. Numerical Modelling of Large Impact Crater Collapse. Thesis submitted for the degree of Doctoral of Philosophy and Diploma, Department of Earth Science and Engineering Imperial College of Science, Technology and Medicine, University of London, London.
- COLLINS, G.S., MELOSH, H.J., MORGAN, J.V., and WARNER, M.R., 2002. Hydrocodes simulations of Chicxulub crater collapse and peak–ring formation. *Icarus*, Vol. **157**, pp. 24–33.
- COLLINS, G.S., MELOSH, H.J., and IVANOV, B.A., 2004. Modeling damage and deformation in impact simulations. *Meteoritics & Planetary Science*, Vol. **39**, pp. 217–231.
- COLLINS, G.S., and WÜNNEMANN, K., 2005. How big was the Chesapeake Bay impact? Insight from numerical modeling. *Geology*, Vol. **33**, pp. 925–928.

- COLLINS, G.S., MORGAN, J., BARTON, P., CHRISTESON, G.L., GULICK, S., URRUTIA, J., WARNER, M., and WÜNNEMANN, K., 2008a. Dynamic modeling suggests terrace zone asymmetry in the Chicxulub crater is caused by target heterogeneity. *Earth and Planetary Science Letters*, Vol. **270**, pp. 221–230.
- COLLINS, G.S., KENKMANN, T., OSINSKI, G.R., and WÜNNEMANN, K., 2008b. Mid-sized complex crater formation in mixed crystalline–sedimentary targets: Insight from modeling and observation. *Meteoritics & Planetary Science*, Vol. **43**, pp. 1955–1977.
- COOPER, G.R.J., 2003. Feature detection using sun shading. *Computer & Geosciences*, Vol. **29**, pp. 941–948.
- COX, K.G., 1978. Kimberlite pipes. *Scientific American*, Vol. **238**, pp. 120–132.
- CRANDALL, S.H., and MARK, W.D., 1973. *Random Vibration in Mechanical Systems*. New York: Academic. 166 p.
- CREMONESE, G., FANTINEL, D., GIRO, E., CAPRIA, M.T., DA DEPPO, V., NALETTO, G., FORLANI, G., MASSIRONI, M., GIACOMINI, L., SGAVETTI, M., SIMIONI, E., BETTANINI, C., DEBEI, S., ZACCARIOTTO, M., BORIN, P., MARINANGELI, L., and FLAMINI, E., 2009. The stereo camera on the BepiColombo ESA/JAXA mission: a novel approach. *Advances in Geosciences*, Vol. **15**, pp. 305–322.
- CREMONESE, G., DA DEPPO, V., NALETTO, G., MARTELLATO, E., DEBEI, BARBIERI, C., BETTANINI, C., CAPRIA, M.T., MASSIRONI, M., ZACCARIOTTO, M., 2010. Observing Mercury: from Galileo to the stereo camera on the BepiColombo mission. In: C. Barbieri, S. Chakrabarti, M. Coradini, M. Lazzarin (eds), *Proceedings of “Galileo’s Medicean Moons: their impact on 400 years of discovery”*, 6-9 January, Padova, Italy, IAU Symposium, No. **269**, pp. 213–218.
- CROFT, S.K., 1985. The scaling of Complex Craters. *Journal of Geophysical Research*, Vol. **90**, pp. 828–842.
- CULLER, T.S., BECKER, T.A., MULLER, R.A., and RENNE, P.R., 2000. Lunar impact history from ^{40}Ar – ^{39}Ar dating of glass spherules. *Science*, Vol. **287**, pp. 1785–1788.
- DA DEPPO, V., NALETTO, G., CREMONESE, G., CALAMAI, L., PAOLINETTI, R., DEBEI, S., and FLAMINI, E., 2010. Optical design performance of the stereo channel for SIMBIOSYS onboard the BepiColombo ESA mission. ICSO, International Conference on Space Optics, 4–8 October, 2010, Rhodes, Greece.
- DALY, M.C., LAWRENCE, S.R., DIEMU–TSHIBAND, K., and MATOUANA, B., 1992. Tectonic evolution of the Cuvette Centrale, Zaire. *Journal of the Geological Society*, Vol. **149**, pp. 539–546.
- DAVISON, T., COLLINS, G.S., and CIESLA, F.J., 2010. Numerical modelling of heating in porous planetesimal collisions. *Icarus*, Vol. 208, pp. 468–481.
- DAVISON, T., and COLLINS, G.S., 2007. The effect of the oceans on the terrestrial crater size–frequency distribution: Insight from numerical modeling. *Meteoritics & Planetary Science*, Vol. **42**, pp. 1915–1927.
- DENCE, M.R., 1965. The extraterrestrial origin of Canadian craters. *Ann. N. Y. Acad. Sci.*, Vol. **123**, pp. 941–969.
- DENCE, M.R., 1968. Shock zoning at Canadian craters: Petrography and structural implications. In: B.M. French and N.M. Short (eds), *Metamorphism of Natural Materials*, Mono Book Corp., Baltimore, pp. 169–184.
- DENCE, M.R., 1973. Dimensional analysis of impact structures. *Meteoritics*, Vol. **8**, abstract # pp. 343–344.
- DENCE, M.R., INNES, M.J.S., and ROBERTSON, P.B., 1968. Recent geological and geophysical studies of Canadian craters. In: B.M. French and N.M. Short (eds), *Metamorphism of Natural Materials*, Mono Book Corp., Baltimore, pp. 339–362.

- DENCE, M.R., GRIEVE, R.A.F., and ROBERTSON, P.B., 1977. Terrestrial impact structures: Principal characteristics and energy considerations. In: D.J. Roddy, R.O. Pepin and R.B. Merrill (eds), *Impact and Explosion Cratering: Planetary and Terrestrial Implications*, Pergamon, New York, pp. 247–275.
- DENEVI, B.W., ROBINSON, M.S., SOLOMON, S.C., MURCHIE, S.L., BLEWETT, D.T., DOMINIGUE, D.L., McCOY, T.J., ERNST, C.M., HEAD, J.W., WATTERS, T.R., and CHABOT, N.L., 2009. The Evolution of Mercury's Crust: A Global Perspective from MESSENGER. *Science*, Vol. **324**, pp. 613–618.
- DENT, B., 1973. Gravitationally Induced Stresses Around a Large Impact Crater. *EOS*, Vol. **54**, pp. 1207.
- DEUTSCH, A., MASAITIS, V.L., LANGENHORST, F. and GRIEVE, R.A.F., 2000. Popigai, Siberia — well preserved giant impact structure, national treasury, and world's geological heritage. *Episodes*, Vol. **23**, pp. 3–11.
- DOWNEY, N.J., and GURNIS, M., 2009. Instantaneous dynamics of the cratonic Congo basin. *Journal of Geophysical Research*, Vol. **114**, pp. B06401, 1–29.
- DRUMMOND, J.D., CONRAD, A., MERLINE, W. and CARRY, B., 2009. The Dimensions and Pole of Asteroid (21) Lutetia from Adaptive Optics Images. American Astronomical Society, **41st** DPS meeting, abstract #59.07.
- DRUMMOND, J.D., CONRAD, A., MERLINE, W.J., CARRY, B., CHAPMAN, C.R., WEAVER, H.A., TAMBLYN, P.M., CHRISTOU, J.C., and DUMAS, C., 2010. Physical properties of the ESA Rosetta target asteroid (21) Lutetia. 1. The triaxial ellipsoid dimensions, rotational pole, and bulk density of ESA Rosetta target asteroid (21) Lutetia. *Astronomy & Astrophysics*, Vol. **523**, pp. A93,1–8.
- DUNDAS, C.M., and McEWEN, A.S., 2007. Rays and secondary craters on Tycho. *Icarus*, Vol. **186**, pp. 31–40.
- DUVALL, G.E. and FOWLES, G.R., 1963. Shock waves. In: R.S. Bradley (eds), *High Pressure Physics and Chemistry*, Vol. II, Academic Press Inc., New York, pp. 209–291.
- EHLMANN, B.L., MUSTARD, J.F., MURCHIE, S.L., POULET, F., BISHOP, J.L., BROWN, A.J., CALVIN, W.M., CLARK, R.N., DES MARAIS, D.J., MILLIKEN, R.E., ROACH, L.H., ROUSH, T.L., SWAYZE, G.A., and WRAY, J.J., 2008. Orbital identification of carbonate-bearing rocks on Mars. *Science*, Vol. **322**, pp. 1828–1832.
- ELBESHAUSEN, D., WÜNNEMANN, K., and COLLINS, G.S., 2009. Scaling of oblique impacts in frictional targets: Implications for crater size and formation mechanisms. *Icarus*, Vol. **204**, pp. 716–731.
- FARINELLA, P., and DAVIS, D.R., 1992. Collision rates and impact velocities in the main asteroid belt. *Icarus*, Vol. **97**, pp. 111–123.
- FARINELLA, P., VOKROUHLICKY, D., and HARTMANN, W.K., 1998. Meteorite Delivery via Yarkovsky Orbital Drift. *Icarus*, Vol. **132**, pp. 378–387.
- FARQUHAR, R., KAWAGUCHI, J., RUSSELL, C.T., SCHWEHM, G., VEVERKA, J., and YEOMANS, D., 2002. Spacecraft Exploration of Asteroids: The 2001 Perspective. In: W.K. Bottke Jr, P. Cellino, P. Paolicchi, R.P. Binzel (eds), *Asteroids III*, Univ. Arizona Press, Tucson, pp. 367–376.
- FAURE, M., LAVALÉE, F., GUSOKUJIMA, Y., IYAMA, J.-T., CADET, J.-P., 1986. The pre-Cretaceous deep-seated tectonics of the Abukuma massif and its place in the structural framework of Japan. *Earth and Planetary Science Letters*, Vol. **77**, pp. 384–398.
- FELDMAN, W.C., MAURICE, S., BINDER, A.B., BARRACLOUGH, B.L., ELPHIC, R.C., and LAWRENCE, D.J., 1998. Fluxes of fast and epithermal neutrons from Lunar Prospector: Evidence for water ice at the lunar poles. *Science*, Vol. **281**, pp. 1496–1500.

- FELDMAN, W.C., LAWRENCE, D.J., ELPHIC, R.C., BARRACLOUGH, B.L., MAURICE, S., GENETAY, I., and BINDER, A.B., 2000. Polar hydrogen deposits on the Moon. *Journal of Geophysical Research*, Vol. **105**, pp. 4175–4195.
- FELDMAN, W.C., MAURICE, S., LAWRENCE, D.J., LITTLE, R.C., LAWSON, S.L., GASNAULT, O., WIENS, R.C., BARRACLOUGH, B.L., ELPHIC, R.C., PRETTYMAN, T.H., STEINBERG, J.T., and BINDER, A.B., 2001. Evidence for water ice near the lunar poles. *Journal of Geophysical Research*, Vol. **106**, pp. 23,231–23,251.
- FELDMAN, W.C., BOYTON, W.V., TOKAR, R.L., PRETTYMAN, T.H., GASNAULT, O., SQUYRES, S.W., ELPHIC, R.C., LAWRENCE, D.J., LAWSON, S.L., MAURICE, S., MCKINNEY, G.W., MOORE, K.R., and REEDY, R.C., 2002. Global distribution of neutrons from Mars: results from Mars Odyssey. *Science*, Vol. **297**, pp. 75–78.
- FELDMAN, W.C., AHOLA, K., BARRACLOUGH, B.L., BELIAN, R.D., BLACK, R.K., ELPHIC, R.C., EVERETT, D.T., FULLER, K.R., KROESCHE, J., LAWRENCE, D.J., LAWSON, S.L., LONGMIRE, J.L., MAURICE, S., MILLER, M.C., PRETTYMAN, T.H., STORMS, S.A., and THOMTON, G.W., 2004. Gamma-ray, neutron, and alpha-particle spectrometers for the lunar prospector mission. *Journal of Geophysical Research*, Vol. **109**, pp. E07S06,1–19.
- FERNANDES, V.A., and BURGESS, R., 2005. Volcanism in Mare Fecunditatis and Mare Crisium: Ar–Ar age studies. *Geochimica et Cosmochimica Acta*, Vol. **69**, pp. 4919–4934.
- FLAMINI, E., CAPACCIONI, F., COLANGELI, L., CREMONESE, G., DORESSOUNDIRAM, A., JOSSET, J.L., LANGEVIN, Y., DEBEI, S., CAPRIA, M.T., DE SANCTIS, M.C., MARINANGELI, L., MASSIRONI, M., MAZZOTTA EPIFANI, E., NALETTO, G., PALUMBO, P., ENG, P., ROIG, G.F., CAPORALI, A., DA DEPO, V., ERARD, S., FEDERICO, C., FORNI, O., SGAVETTI, M., FILACCHIONE, G., GIACOMINI, L., MARRA, G., MARTELLATO, E., ZUSI, M., COSI, M., BETTANINI, C., CALAMAI, L., ZACCARIOTTO, M., TOMMASI, L., DAMI, M., FICAI VELTRONI, J., POULET, F., HELLO, Y., and The SIMBIOSYS Team, 2010. SIMBIO-SYS: The spectrometer and imagers integrated observatory system for the BepiColombo planetary orbiter. *Planetary and Space Science*, Vol. **58**, pp. 125–143.
- FLORAN, R.J., GRIEVE, R.A.F., PHINNEY, W.C., WARNER, J.L., SIMONDS, C.H., BLANCHARD, D.P., and DENCE, M.R., 1978. Manicouagan impact melt, Quebec, 1, stratigraphy, petrology, and chemistry. *Journal of Geophysical Research*, Vol. **83**, pp. 2737–2759.
- FLYNN, G.J., 2004. Physical properties of meteorites and interplanetary dust particles: clues to the properties of the meteors and their parent bodies. *Earth, Moon, and Planets*, Vol. **95**, pp. 361–374.
- FORNASIER, S., BELSKAYA, I.N., FULCHIGNONI, M., BARUCCI, M.A., and BARBIERI, C., 2006. First albedo determination of 2867 Steins, target of the Rosetta mission. *Astronomy & Astrophysics*, Vol. **449**, pp. L9–L12.
- FORNASIER, S., MARZARI, F., DOTTO, E., BARUCCI, M.A., and MIGLIORINI, A., 2007. Are the E-type asteroids (2867) Steins, a target of the Rosetta mission, and NEA (3103) Eger remnants of an old asteroid family? *Astronomy & Astrophysics*, Vol. **474**, pp. L29–L32.
- FORNASIER, S., BARUCCI, M.A., BELSKAYA, I.N., and FULCHIGNONI, M., 2010. A portrait of the Rosetta targets 2867 Steins and 21 Lutetia. *EPSC 5th*, abstract #165.
- FRENCH, B.M., 1968. Shock metamorphism as a geological process. In: B.M. French and N.M. Short (eds), *Metamorphism of Natural Materials*, Mono Book Corp., Baltimore, pp. 1–17.
- FRENCH, B.M., 1998. *Traces of Catastrophe: A Handbook of Shock–Metamorphic Effects in Terrestrial Meteorite Impact Structures*. LPI Contribution No. 954, Lunar & Planetary Institute, Houston., 120 p.

- FRENCH, B.M., and KOEBERL, C., 2010. The convincing identification of terrestrial meteorite impact structures: What works, what doesn't, and why. *Earth–Science Reviews*, Vol. **98**, pp. 123–170.
- GAFFEY, M.J., CLOUTIS, E.A., KELLEY, M.S., and REED, K.L., 2002. Mineralogy of Asteroids. In: W.K. Bottke Jr, P. Cellino, P. Paolicchi, R.P. Binzel (eds), *Asteroids III*, Univ. Arizona Press, Tucson, pp. 183–204.
- GAFFNEY, E.S., and MELOSH, H.J., 1982. Noise and target strength degradation accompanying shallow-buried explosions. *Journal Geophysical Research*, Vol. 87, pp. 1871–1879.
- GAULT, D.E., 1970. Saturation and equilibrium conditions for impact cratering on the lunar surface: Criteria and implications. *Radio Science*, Vol. **5**, No. **2**, pp. 273–291.
- GAULT, D.E., QUAIDE, W.L., and OBERBECK, V.R., 1968. Impact Cratering Mechanics and Structures. In: B.M. French and N.M. Short (eds), *Shock Metamorphism of Natural Materials*, Mono, Baltimore, USA, pp. 87–99.
- GAULT, D.E., and GREELEY, R., 1978. Exploratory Experiments of Impact Craters Formed in Viscous–Liquid Targets: Analogs for Martian Rampart Craters? *Icarus*, Vol. 34, pp. 486–495.
- GAULT, D.E., and WEDEKIND, J.A., 1978. Experimental studies of oblique impact. *Proc. Lunar Planet. Sci. Conf.* **9th**, pp. 3843–3875.
- GILBERT, G.K., 1893. The moon's face: A study of the origin of its features. *Bull. Phil. Soc. Wash*, Vol. **12**, pp. 241–292.
- GIRESE, P., 2005. Mesozoic–Cenozoic history of the Congo Basin. *Journal of African Earth Sciences*, Vol. **43**, 301–315.
- GLADMAN, B., MIGLIORINI, F., MORBIDELLI, A., ZAPPALÀ, V., MICHEL, P., CELLINO, A., FROESCHLÉ, Ch., LEVISON, H., BAILEY, M., and DUNCAN, M., 1997. Dynamical lifetimes of objects injected into asteroid belt resonances. *Science*, Vol. **277**, pp. 197–201.
- GLADMAN, B., MICHEL, and FROESCHLÉ, Ch., 2000. The Near–Earth Object Population. *Icarus*, Vol. **146**, pp. 176–189.
- GLADSTONE, G.R., HURLEY, D.M., RETHERFORD, K.D., FELDMAN, P.D., PRYOR, W.R., CHAUFRAY, J.–Y., VERSTEEG, M., GREATHOUSE, T.K., STEFFL, A.J., THROOP, H., PARKER, J.W., KAUFMANN, D.E., EGAN, A.F., DAVIS, M.W., SLATER, D.C., MUKHERJEE, J., MILES, P.F., HENDRIX, A.R., COLAPRETE, A., and STERN, S.A., 2010. LRO–LAMP Observations of the LCROSS Impact Plume. *Science*, Vol. **330**, pp. 472–476.
- GLASSMEIER, K.-H., BOEHNHARDT, H., KOSCHNY, D., KURT, E., RICHTER, I., 2007. The Rosetta Mission: Flying Towards the Origin of the Solar System. *Space Science Reviews*, Vol. **128**, pp. 1–321.
- GOLDIN, T.J., WÜNNEMANN, K., MELOSH, H.J., and COLLINS, G.S., 2006. Hydrocode modeling of the Sierra Madera impact structure. *Meteoritics & Planetary Science*, Vol. **41**, pp. 1947–1958.
- GOMES, R., LEVISON, H.F., TSIGANIS, K., and MORBIDELLI, A., 2005. Origin of the cataclysmic Late Heavy Bombardment period of the terrestrial planets. *Nature*, Vol. **435**, pp. 466–469.
- GRAHAM, R.A., 1993. Solids under high–pressure shock compression — mechanics, physics and chemistry. Springer, New York, Berlin, Heidelberg, 221 p.
- GREELEY, R., and GAULT, D.E., 1970. Precision size–frequency distributions of craters for 12 selected areas of the lunar surface. *The Moon*, Vol. **2**, pp. 10–77.

- GREELEY, R., FINK, J., GAULT, D.E., SNYDER, D.B., GUEST, J.E., and SCHULTZ, P.H., 1980. Impact cratering in viscous targets: Laboratory experiments. *Proc. Lunar Planet. Sci. Conf.* **11th**, pp. 2075–2097.
- GRIEVE, R.A.F., 1978. Meteoritic component and impact melt composition at the Lac a L'Eau Claire/Clearwater/impact structures, Quebec. *Geochimica et Cosmochimica Acta*, Vol. **42**, pp. 429–431.
- GRIEVE, R.A.F., 1991. Terrestrial impact: the record in the rocks. *Meteoritics*, Vol. **26**, pp. 175–194.
- GRIEVE, R.A.F., 1993. Impact craters: Lessons from and for the Earth. *Vistas in Astronomy*, Vol. **36**, pp. 203–230.
- GRIEVE, R.A.F., and DENCE, M.R., 1979. The terrestrial cratering record. II – The crater production rate. *Icarus*, Vol. **38**, pp. 230–242.
- GRIEVE, R.A.F., and PILKINGTON, P.B., 1996. The signature of terrestrial impacts. *AGSO Journal of Australian Geology and Geophysics*, Vol. **16**, pp. 399–420.
- GUINNESS, E.A., and ARVIDSON, R.E., 1977. On the constancy of the lunar cratering flux over the past 3.3 billion yr. *Lunar Sci. Conf.* **8th**, pp. 3475–3494.
- GULICK, V.C., 2001. Origin of the valley networks on Mars: A hydrological perspective. *Geomorphology*, Vol. **37**, pp. 241–268.
- HAPKE, B., 1990. Coherent backscatter and the radar characteristics of outer planet satellites. *Icarus*, Vol. **88**, pp. 407–417.
- HARMON, J.K., and SLADE, M.A., 1992. Radar mapping of Mercury: Fulldisk Doppler delay images. *Science*, Vol. **258**, pp. 640–643.
- HART, R.J., HARGRAVES, R.B., ANDREOLI, M.A.G., TREDoux, M., and DOUCOURÉ, C.M., 1995. Magnetic anomaly near the center of the Vredefort structure: Implications for impact related magnetic signatures. *Geology*, Vol. **23**, pp. 277–280.
- HARTLEY, R.W., and ALLEN, P.A., 1994. Interior cratonic basins of Africa: relation to continental break-up and role of mantle convection. *Basin Research*, Vol. **6**, pp. 95–113.
- HARTMANN, W.K., 1964. On the distribution of lunar crater diameters. *Comm. Lunar Planet. Lab.*, Vol. **2**, pp. 197–203.
- HARTMANN, W.K., 1965. Terrestrial and lunar flux of meteorites in the last two billion years. *Icarus*, Vol. **4**, pp. 157–165.
- HARTMANN, W.K., 1966. Early lunar cratering. *Icarus*, Vol. **5**, pp. 406–418.
- HARTMANN, W.K., 1969. Lunar and interplanetary rock fragmentation. *Icarus*, Vol. **10**, pp. 201–213.
- HARTMANN, W.K., 1972. Paleocratering of the moon: Review of post–Apollo data. *Astrophysical and Space Science*, Vol. **17**, pp. 48–64.
- HARTMANN, W.K., 1973. Martian Cratering 4, Mariner 9 Initial Analysis of Cratering Chronology. *Journal of Geophysical Research*, Vol. **78**, No. **20**, pp. 4096–4116.
- HARTMANN, W.K., 1977. Relative Crater Production Rates on Planets. *Icarus*, Vol. **31**, pp. 260–276.
- HARTMANN, W. K., 1981, Discovery of multi-ring basins: Gestalt perception in planetary science. Multi-ring basins *Proc. Lunar Planet. Sci.*, Vol. **12A**, pp. 79–80.

- HARTMANN, W.K., 1984. Does crater “saturation equilibrium” occur in the Solar System?. *Icarus*, Vol. **60**, pp. 56–74.
- HARTMANN, W.K., 1995. Planetary cratering I: Lunar highlands and test of hypotheses on crater populations. *Meteoritics*, Vol. **30**, pp. 451–467.
- HARTMANN, W.K., 1999. Martian cratering VI. Crater count isochrons and evidence for recent volcanism from Mars Global Surveyor. *Meteoritics & Planet. Sci.*, Vol. **34**, pp. 167–177.
- HARTMANN, W.K., 2005. Martian cratering 8: Isochron refinement and the chronology of Mars. *Icarus*, Vol. **174**, pp. 294–320.
- HARTMANN, W.K., 2007. Martian cratering 9: Toward resolution of the controversy about small craters. *Icarus*, Vol. **189**, pp. 274–278.
- HARTMANN, W.K., and KUIPER, G.P., 1962. Concentric structures surrounding lunar basins. *Commun. Lunar and Planetary Lab., Univ. Arizona*, Vol. **1**, pp. 51–66.
- HARTMANN, W.K., et al., 1981. Chronology of planetary volcanism by comparative studies of planetary cratering. In: Basaltic Volcanism Study Project (eds), *Basaltic Volcanism on the terrestrial Planets*, Pergamon, New York, pp. 1049–1127.
- HARTMANN, W.K., and NEUKUM, G., 2001. Cratering chronology and the evolution of Mars. *Space Sci Rev.*, Vol. **96**, pp. 165–194.
- HARTMANN, W.K., QUANTIN, C., and MANGOLD, N., 2007. Possible long-term decline in impact rates 2. Lunar impact–melt data regarding impact history. *Icarus*, Vol. **186**, pp. 11–23.
- HARTMANN, W.K., NEUKUM G., and WERNER, S., 2008. Confirmation and utilization of the “production function” size–frequency distribution of Martian impact craters. *Geophysical Research Letters*, Vol. **35**, pp. L02205,1–5.
- HAYAKAWA, H., KASABA, Y., YAMAKAWA, H., OGAWA, H., and MUKAI, T., 2004. The BepiColombo/MMO model payload and operation plan. *Advance in Space Research*, Vol. **33**, pp. 2142–2146.
- HAWKINS, S.E., BOLDT, J.D., DARLINGTON, E.H., ESPIRITU, R., GOLD, R.E., GOTWOLS, B., GREY, M.P., HASH, C.D., HAYES, J.R., JASKULEK, S.E., KARDIAN, C.J., KELLER, M.R., MALARET, E.R., MURCHIE, S.L., MURPHY, P.K., PEACOCK, K., PROCKTER, L.M., REITER, R.A., ROBINSON, M.S., SCHAEFER, E.D., SHELTON, R.G., STERNER, R.E., TAYLOR, H.W., WATTERS, T.R., and WILLIAMS, B.D., 2007. The Mercury Dual Imaging System on the MESSENGER Spacecraft. *Space Sci. Rev.*, Vol. **131**, pp. 247–338.
- HEAD, J.N., MELOSH, H.J., and IVANOV, B.A., 2002. Martian meteorite launch: high-speed ejecta from small craters. *Science*, Vol. **298**, pp. 1752–1756.
- HEAD III, J.W., GREELEY, R., GOLOMBECK, M.P., HARTMAN, W.K., HAUBER, E., JAUMANN, R., MASSON, P., NEUKUM, G., NYQUIST, L.E., and CARR, M.H., 2001. Geological processes and evolution. *Space Science Reviews*, Vol. **96**, pp. 263–292.
- HEAD III, J.W., CHAPMAN, C.R., DOMINIGUE, D.L., HAWKINS III, S.E., McCLINTOCK, W.E., MURCHIE, S.L., PROCKTER, L.M., ROBINSON, M.S., STROM, R.G., and WATTERS, T.R., 2007. The Geology of Mercury: The View Prior to the MESSENGER mission. *Space Science Reviews*, Vol. **131**, pp. 41–84.

- HEAD III, J.W., MURCHIE, S.L., PROCKTER, L.M., ROBISON, M.S., SOLOMON, S.C., STROM, R.G., CHAPMAN, C.R., WATTERS, T.R., McCLINTOCK, W.E., BLEWETT, D.T., and GILLIS–DAVIS, J.J., 2008. Volcanism on Mercury: Evidence from the First MESSENGER flyby. *Science*, Vol. **321**, pp. 69–72.
- HEAD III, J.W., MURCHIE, S.L., PROCKTER, L.M., SOLOMON, S.C., CHAPMAN, C.R., STROM, R.G., WATTERS, T.R., BLEWETT, D.T., GILLIS–DAVIS, J.J., FASSET, C.I., DICKSON, J.L., MORGAN, G.A., and KERBER, L., 2009a. Volcanism on Mercury: Evidence from the first MESSENGER flyby for extrusive and explosive activity and the volcanic origin of plains. *Earth and Planetary Science Letters*, Vol. **285**, pp. 227–242.
- HEAD III, J.W., MURCHIE, S.L., PROCKTER, L.M., SOLOMON, S.C., STROM, R.G., CHAPMAN, C.R., WATTERS, T.R., BLEWETT, D.T., GILLIS–DAVIS, J.J., FASSET, C.I., DICKSON, J.L., HURWITZ, D.M., and OSTRACH, L.R., 2009b. Evidence for intrusive activity on Mercury from the first MESSENGER flyby. *Earth and Planetary Science Letters*, Vol. **285**, pp. 251–262.
- HEAD III, J.W., FASSETT, C.I., KADISH, S.J., SMITH, D.E., ZUBER, M.T., NEUMANN, G.A., and MAZARICO, 2010. Global Distribution of Large Lunar Craters: Implications for Resurfacing and Impactor Populations. *Science*, Vol. **329**, pp. 1504–1507.
- HERMANN, W., 1969. Constitutive equation for the dynamic compaction of ductile porous materials. *Journal of Applied Physics*, Vol. **40**, pp. 2490–2499.
- HIESINGER, H., JAUMANN, R., NEUKUM, G., and HEAD III, J.W., 2000. Ages of mare basalts on the lunar nearside. *Journal of Geophysical Research*, Vol. **105**, pp. 29,239–29,275.
- HIRATA, N., BARNOUIN–JHA, O.S., HONDA, C., NAKAMURA, R., MIYAMOTO, H., SASAKI, S., DEMURA, H., NAKAMURA, A.M., MICHIKAMI, T., GASKELL, R.W., SAITO, J., 2009. A survey of possible impact structures on 25143 Itokawa. *Icarus*, Vol. **200**, 486–502.
- HOEK, E., 1983. Strength of jointed rock masses. *Geotechnique*, Vol. **33**, pp. 187–223.
- HOLSAPPLE, K.A., 1987. The scaling of impact phenomena. *International Journal of Impact Engineering*, Vol. **5**, pp. 343–355.
- HOLSAPPLE, K.A., 1993. The scaling of impact processes in Planetary Sciences. *Annu. Rev. Earth Planet. Sci.*, Vol. **21**, pp. 333–373.
- HOLSAPPLE, K.A., and HOUSEN, K.R., 2007. A crater and its ejecta: An interpretation of Deep Impact. *Icarus*, Vol. **187**, pp. 345–356.
- HOLSAPPLE, K.A., 2009. On the “strength” of the small bodies of the solar system: A review of strength theories and their implementation for analyses of impact disruption. *Planetary and Space Sciences*, Vol. **57**, pp. 127–141.
- HOLSAPPLE, K.A., and SCHMIDT, R.M., 1987. Point–source solution and coupling parameters in cratering mechanics. *Journal of Geophysical Research*, Vol. **92**, pp. 6350–6376.
- HÖRZ, F., 1982. Ejecta of the Ries crater, Germany. In: L.T. Silver and P.H. Schultz (eds), *Geological Implications of Impacts of Large Asteroids and Comets on the Earth*, *Geol. Soc. Amer. Spec. Paper* Vol. **190**, pp. 39–55.
- HÖRZ, F., OSTERTAG, R., and RAINEY, D.A., 1983. Bunte Breccia of the Ries: Continuous deposits of large impact craters. *Rev. Geophys. Space Phys.*, Vol. **21**, pp. 1667–1725.
- HOUSEN, K.R., HOLSAPPLE, K.A., and VOSS, M.E., 1999. Compaction as the origin of the unusual craters on the asteroid Mathilde. *Nature*, Vol. **402**, pp. 155–157.

- HOUSEN, K.R., HOLSAPPLE, K.A., and VOSS, M.E., 2000. Numerical simulation of impact cratering in porous materials. *LPSC 31st*, abstract #1498.
- HOUSEN, K.R., and HOLSAPPLE, K.A., 2003. Impact cratering on porous asteroids. *Icarus*, Vol. **163**, pp. 102–119.
- IVANOV, B.A., 2005. Numerical modeling of the largest terrestrial meteorite craters. *Solar System Research*, Vol. **39**, pp. 381–409.
- IVANOV, B.A., 2006. Earth/Moon impact rate comparison: Searching constraints for lunar secondary/primary cratering proportion. *Icarus*, Vol. **183**, pp. 504–507.
- IVANOV, B.A., 2008. Size–frequency distributions of asteroids and impact craters: estimates of impact rate. In: V.V. Adushkin & I.V. Nemchinov (eds), *Catastrophic Events Caused by Cosmic Objects*, Springer, pp. 91–116.
- IVANOV, B.A., and KOSTUCHENKO, V.N., 1997. Block oscillation model for impact crater collapse. **28th** Annual Lunar and Planetary Science Conference, abstract # 631.
- IVANOV, B.A., and KOSTUCHENKO, V.N., 1997. Block oscillation model for impact crater collapse. *LPSC 28th*, abstract #1655.
- IVANOV, B.A., DENIEM, D., and NEUKUM, G., 1997. Implementation of dynamic strength models into 2D hydrocodes: Application for atmospheric breakup and impact cratering. *International Journal of Impact Engineering*, Vol. **20**, pp. 411–430.
- IVANOV, B.A., NEUKUM, G., and WAGNER, R., 1999. Impact craters, NEA, and Main Belt asteroids: Size–frequency distribution. *LPSC 30th*, abstract #1583.
- IVANOV, B.A., NEUKUM, G., and WAGNER, R., 2001. Size–frequency distribution of planetary impact craters and asteroids. In: M.Y. Marov and H. Rickman (eds), *Collisional Processes in the Solar System*, *Astrophys. Space Sci. Libr.*, Vol. **261**, pp. 1–34.
- IVANOV, B.A., and ARTEMIEVA, N.A., 2002. Numerical modeling of the formation of large impact craters. In: C. Koeberl, K.G. MacLeod (eds), *Catastrophic Events and Mass Extinctions: Impacts and Beyond*, Geological Society of America Special Paper **356**, Boulder, Colorado, pp. 619–630.
- IVANOV, B.A., NEUKUM, G., BOTTKE Jr., W.F., and HARTMANN, W.K., 2002. The Comparison of Size–Frequency Distributions of Impact Craters and Asteroids and the Planetary Cratering rate. In: W. K. Bottke Jr, P. Cellino, P. Paolicchi, R.P. Binzel (eds), *Asteroids III*, Univ. Arizona Press, Tucson, pp. 89–101.
- IVEZIĆ, Ž., TABACHNIK, S., RAFIKOV, R., LUPTON, R.H., QUINN, T., MANNERGREN, M., EYER, L., CHU, J., ARMSTRONG, J.C., FA, X., FINLATOR, K., GEBALLE, T.R., GUNN, J.E., HENNESSY, G.S., KNAPP, G.R., LEGGETT, S.K., MUNN, J.A., PIER, J.R., ROCKOSI, C.M., SCHNEIDER, D.P., STRAUSS, M.A., YANNY, B., BRINKAMANN, J., CSABAI, I., HINDSLEY, R.B., KENT, S., LAMB, D.Q., MARGON, B., MCKAY, T.A., SMITH, J.A., WADDEL, P., YORK, D.G., and the SDSS Collaboration, 2001. Solar System Objects Observed in the Sloan Digital Sky Survey Commissioning Data. *The Astronomical Journal*, Vol. **122**, pp. 2749–2784.
- JAEGER, J.C., COOK, N.G.W., and WIMMERMAN, R.W., 2007. *Fundamentals of Rock Mechanics*. Blackwell Publishing, 4th Edition. 475 p.
- JACKSON, M.P.A., CORNELIUS, R.R., CRAIG, C.H., GANSSER, A., STÖCKLIN, J., and TALBOT, C.J., 1990. Salt diapirs of the Great Kavir, Central Iran. *Geol. Soc. Am. Mem.*, Vol. **177**, 139 p.

- JACQUES, A.L., 1998. Kimberlite and lamproite diamond pipes. *AGSO Journal of Australian Geology & Geophysics*, Vol. **17**, pp. 153–162.
- JOHNSON, G.R., and COOK, W.H., 1983. A constitutive model and data for metals subjected to large strains, high strain rates and high temperatures. *Proceedings 7th International Symposium on Ballistics*. The Hague, The Netherlands.
- JOHNSON, G.R., and HOLMQUIST, T.J., 1993. An improved computational constitutive model for brittle materials. In: S.C. Schmidt, J.W. Shaner, G.A. Samara, M. Ross (eds), *High-pressure science and technology*, Woodbury, AIP Press, pp. 981–984.
- JOHNSON, S.E., SCHMIDT, K.L., and TATE, M.C., 2002. Ring complexes in the Peninsular Ranges Batholith, Mexico and the USA: magma plumbing systems in the middle and upper crust. *Lithos*, Vol. **61**, pp. 187–208.
- JORDA, L., LAMY, P., BESSE, S., CAPANNA, C., CARRY, B., FAURY, G., GASKELL, R., GESQUIRÈRE, G., GROUSSIN, O., KAASALAINEN, M., SPJUTH, S., and the OSIRIS team, 2010. The shape and physical properties of asteroid 21 Lutetia from OSIRIS images. *EPSC 5th*, abstract #200.
- JUTZI, M., MICHEL, P., and BENZ, W., 2010. A large crater as a probe of the internal structure of the E-type asteroid Steins. *Astronomy & Astrophysics*, Vol. **509**, pp. L2,1–4.
- KELLER, et al. 2007. Observations of Comet 9P/Tempel 1 around the Deep Impact event by the OSIRIS cameras onboard Rosetta. *Icarus*, Vol. **187**, pp. 87–103.
- KELLER, H.U., BARBIERI, C., KOSCHNY, D., LAMY, P., RICKMAN, H., RODRIGO, R., SIERKS, H., A'HEARN, M.F., ANGRILLI, F., BARUCCI, M.A., BERTAUX, J.-L., CREMONESE, G., DA DEPPO, V., DAVIDSSON, B., DE CECCO, M., DEBEL, S., FORNASIER, S., FULLE, M., GROUSSIN, O., GUTIERREZ, P.J., HVIID, S.F., IP, W.-H., JORDA, L., KNOLLENBERG, J., KRAMM, J.R., KÜHRT, E., KÜPPERS, M., LARA, L.-M., LAZZARIN, M., LOPEZ MORENO, J., MARZARI, F., MICHALIK, H., NALETTO, G., SABAU, L., THOMAS, N., WENZEL, K.-P., BERTINI, L., BESSE, S., FERRI, F., KAASALAINEN, M., LOWRY, S., MARCHI, S., MOTTOLA, S., SABOLO, W., SCHRÖDER, S.E., SPJUTH, S., and VERNAZZA, P., 2010. E-Type Asteroid (2867) Steins as Images by OSIRIS on Board Rosetta. *Science*, Vol. **327**, pp. 190–193.
- KENKMANN, T., 2002. Folding within seconds. *Geology*, Vol. **30**, pp. 231–234.
- KENKMANN, T., JAHN, A., SCHERLER, D., IVANOV, B.A., 2005. Structure and formation of a central uplift: A case study at the Upheaval Dome impact crater, Utah. In: *Large Meteorite Impacts III*, Geological Society of America Special Paper **384**, Boulder, Colorado, pp. 85–116.
- KERBER, L., HEAD III, J.W., SOLOMON, S.C., MURCHIE, S.L., BLEWETT, D.T., and WILSON, L., 2009. Explosive volcanic eruptions on Mercury: Eruption conditions, magma volatile content, and implications for interior volatile abundances. *Earth and Planetary Science Letters*, Vol. **285**, pp. 263–271.
- KERLEY, G.I., 1992. CTH equation of state package: Porosity and reactive burn models. Sandia National Laboratories, Report **SAND92-0553**.
- KIEFFER, S.W., 1971. Shock metamorphism of the Coconino sandstone at Meteor Crater, Arizona. *Journal of Geophysical Research*, Vol. **76**, pp. 5449–5473.
- KIEFFER, S.W., and SIMONDS, C.H., 1980. The role of volatiles and lithology in the impact cratering process. *Rev. Geophys. Space Phys.*, Vol. **18**, pp. 143–181.
- KIRSTEN, T., and HORN, P., 1974. Chronology of the Taurus–Littrow region III: Ages of mare basalts and highland breccias and some remarks about the interpretation of lunar highland rock ages. *Proc. Lunar Sci. Conf. 5th*, pp. 1451–1475.

- KOCHARYAN, G.G., KOSTUCHENKO, V.N., and IVANOV, B.A., 1996. Mechanics of rock massive disruption: implementation to planetary cratering process. LPSC 27th, abstract #677.
- KOEBERL, C., 2004. Remote sensing studies of impact craters: how to be sure? C. R. Geoscience, Vol. 336, pp. 959–961.
- KOLB, K.J., McEWEN, A.S., and PELLETIER, J.D., 2010. Investigating gully flow emplacement mechanisms using apex slopes. Icarus, Vol. 208, pp. 132–142.
- KORYCANSKY, D.G., PLESKO, C.S., JUTZI, M., ASPHAUG, E., and COLAPRETE, A., 2009. Predictions for the LCROSS mission. Meteoritics & Planetary Science, Vol. 44, pp. 603–620.
- KOSCHNY, D., DHIRI, V., WIRTH, K., ZENDER, J., SOLAZ, R., HOOFS, R., LAUREIJS, R., HO, T.-M., DAVIDSSON, B., and SCHWELM, G., 2007. Scientific Planning and Commanding of the Rosetta Payload. Space Science Reviews, Vol. 128, pp. 167–188.
- KRING, D.A., 2007. Guidebook to the Geology of Barringer Meteorite Crater, Arizona (a.k.a. Meteor Crater). LPI, Contribution No. 1355, 150 p.
- LANZA, N.L., MEYER, G.A., OKUBO, C.H., NEWSOM, H.E., WIENS, R.C., 2010. Evidence for debris flow gully formation initiated by shallow subsurface water on Mars. Icarus, Vol. 205, pp. 103–112.
- LAZZARIN, M., MARCHI, S., MOROZ, L.V., and MAGRIN, S., 2009. New visible spectra and mineralogical assessment of (21) Lutetia, a target of the Rosetta mission. Astronomy & Astrophysics, Vol. 498, pp. 307–311.
- LEARY, J.C., CONDE, R.F., DAKERMANJI, G., ENGELBRECHT, C.S., ERCOL, C.J., FIELHAUER, K.B., GRANT, D.G., HARTKA, T.J., HILL, T.A., JASKULEK, S.E., MIRANTES, M.A., MOSHER, L.E., PAUL, M.V., PERSONS, D.F., RODBERG, E.H., SRINIVASAN, D.K., VAUGHAN, R.M., and WILEY, S.R., 2007. The MESSENGER Spacecraft. Space Science Reviews, Vol. 131, pp. 187–217.
- LEFORT, A., RUSSEL, P.S., THOMAS, N., McEWEN, A.S., DUNDAS, C.M., KIRK, R.L., 2009. Observations of periglacial landforms in Utopia Planitia with the High Resolution Imaging Science Experiment (HiRISE). Journal of Geophysical Research, Vol. 114, pp. E04005.
- LEYRAT, C., FORNASIER, S., BARUCCI, M.A., MAGRIN, A., MAGRIN, S., LAZZARIN, M., FULCHIGNONI, M., JORDA, L., BELSKAYA, I.N., MARCHI, S., BARBIERI, C., KELLER, U., SIERKS, H., and HVIID, S., 2010. Search for Steins' surface inhomogeneities from OSIRIS Rosetta images. Planetary and Space Science, Vol. 58, pp. 1097–1106.
- LUNDBORG, N., 1968. Strength of rock-like materials. International Journal of Rock Mechanics and Mining Sciences, Vol. 5, pp. 427–454.
- MALIN, M.C., and EDGETT, K.S., 2000. Evidence for recent groundwater seepage and surface runoff on Mars. Science, Vol. 288, pp. 2330–2335.
- MARCHI, S., MORBIDELLI, A., and CREMONESE, G., 2005. Flux of meteoroid impacts on Mercury. Astronomy & Astrophysics, Vol. 431, pp. 1123–1127.
- MARCHI, S., MOTTOLA, S., CREMONESE, G., MASSIRONI, M., and MARTELLATO, E., 2009. A new chronology for the Moon and Mercury. The Astronomical Journal, Vol. 137, pp. 4936–4948.
- MARCHI, S., BARBIERI, C., BESSE, S., KUEPPERS, M., MARZARI, F., MASSIRONI, M., MOTTOLA, S., NALETTO, G., and SIERKS, H., 2010. ESA/Rosetta encounters the main belt asteroid (21) Lutetia: Analysis of Lutetia cratering history. EPSC 5th, abstract #119.

- MARCHI, S., CREMONESE, G., GIACOMINI, L., MARTELLATO, E., MASSIRONI, M., and PROCKTER, L.M., 2011. Age determination of young terrains on Mercury: the case of Raditladi and Rachmaninoff basins. PSS, Accepted pending revision
- MARCY, G.W., and BUTLER, R.P., 2000. Planets orbiting other suns. *Publ. Astron. Soc. Pacific*, Vol. **112**, pp. 137–140.
- MARINOVA, M.M., AHARONSON, O., and ASPHAUG, E., 2008. Mega–impact formation of the Mars hemispheric dichotomy. *Nature*, Vol. **453**, pp. 1216–1219.
- MARTELLATO, E., MASSIRONI, M., MONEGATO, G., and CREMONESE, G., 2010. Hydrocode Simulations of OMEONGA crater formation. EPSC 5th, abstract #558.
- MASSIRONI, M., CREMONESE, G., MARCHI, S., MARTELLATO, E., MOTTOLA, S., and WAGNER, R., 2009. Mercury’s geochronology revised by applying Model Production Function to Mariner 10 data: Geological implications. *Geophysical Research Letters*, Vol. **36**, pp. L21204,1–6.
- MASTER, S. 2010. Lac Télé structure, Republic of Congo: Geological setting of a cryptozoological and biodiversity hotspot, and evidence against an impact origin. *Journal of African Earth Sciences*, Vol. **58**, pp. 667–679.
- MCADAMS, J.V., FARQUHAR, R.W., TAYLOR, A.H., WILLIAMS, B.G., 2007. MESSENGER Mission Design and Navigation. *Space Science Reviews*, Vol. **131**, pp. 219–246
- MC EWEN, A.S., TURTLE, E., BURR, D., MILAZZO, M., LANAGAN, P., CHRISTENSEN, P., BOYCE, J., and The Themis Science Team, 2003. Discovery of a Large Rayed Crater on Mars: Implication for Recent Volcanic and Fluvial Activity and the Origin of Martian Meteorites. LPSC 34th, abstract #2040.
- MC EWEN, A.S., PREBLICH, B.S., TURTLE, E.P., ARTEMIEVA, N.A., GOLOMBEK, M.P., HURST, M., KIRK, R.L., BURR, D.M., and CHRISTENSEN, P.R., 2005. The rayed crater Zunil and interpretations of small impact craters on Mars. *Icarus*, Vol. **176**, pp. 351–81.
- MC EWEN, A.S., and BIERHAUS, E.B., 2006. The Importance of Secondary Cratering to Age Constraints on Planetary Surfaces. *Annu. Rev. Earth Planet. Sci.*, Vol. **34**, pp. 535–567.
- MC EWEN, A.S., ELIASON, E.M., BERGSTROM, J.W., BRIDGES, N.T., HANSEN, C.J., DELAMERE, W.A., GRANT, J.A., GULICK, V.C., HERKENHOFF, K.E., KESZTHELYI, L., KIRK, R.L., MELLON, M.T., SQUYRES, S.W., THOMAS, N., and WEITZ, C.M., 2007. Mars Reconnaissance Orbiter’s High Resolution Imaging Science Experiment (HiRISE). *Journal of Geophysical Research*, Vol. **112**, pp. E05S02,1–40.
- MC EWEN, A.S., BANKS, M.E., BAUGH, N., BECKER, K., BOYOD, A., BERGSTROM, J.W., BEYER, R.A., BORTOLINI, E., BRIDGES, N.T., BYRNE, S., CASTALIA, B., CHUANG, F.C., CRUMPLER, L.S., DAUBAR, I., DAVATZES, A., DEARDORFF, D.G., DeJONG, A., DELAMERE, W.A., DOBREA, E.N., DUNDAS, C.M., ELIASON, E.M., ESPINOZA, Y., FENNEMA, A., FISHBAUGH, K.E., FORRESTER, T., GEISSLER, P.E., GRANT, J.A., GRIFFES, J.L., GROTZINGER, J.P., GULICK, V.C., HANSE, C.J., HERKENHOFF, K.E., HEYD, R., JAEGER, W.L., JONES, D., KANEFSKY, B., KESZTHELYI, L., KING, R., KIRK, R.L., KOLB, K.J., LASCO, J., LEFORT, A., LEIS, R., LEWIS, K.W., MARTINEZ–ALONSOM, S., MATTSON, S., McARTHUR, G., MELLONM, M.T., METZ, J.M., MILAZZO, M.P., MILLIKEN, R.E., MOTAZEDIAN, T., OKUBO, C.H., ORTIZ, A., PHILIPPOFF, A.J., PLASSMANN, J., POLIT, A., RUSSELL, P.S., SCHALLER, C., SEARLSM, M.L., SPRIGGS, T., SQUYRES, S.W., TARR, S., THOMAS, N., THOMSON, B.J., TORNABENE, L.L., VAN HOUTEN, C., VERBA, C., WEITZ, C.M., and WRAY, J.J., 2010. The High Resolution Imaging Science Experiment (HiRISE) during MRO’s Primary Science Phase (PSP). *Icarus*, Vol. **205**, pp. 2–37.
- McKINNON, W.B., 1978. An investigation into the role of plastic failure in crater modification. *Proc. Lunar Planet. Sci. Conf.* 9th, pp. 3965–3973.

- McKINNON, W.B., and MELOSH, H.J., 1980. Evolution of planetary lithospheres: Evidence from multi-ringed basins on Ganymede and Callisto. *Icarus*, Vol. **44**, pp. 454–471.
- McNUTT, R.L., SOLOMON, S.C. GRARD, R., NOVARA, M., and TOSHIFUMI. An international program for Mercury exploration: synergy of MESSENGER and BepiColombo. *Advances in Space Research*, Vol. **33**, pp. 2126–2132.
- McSWEEN Jr, H.Y., 1999. *Meteorites and Their Parent Planets*. Cambridge University Press, 2nd Edition. 310 p.
- MELOSH, H.J., 1977. Crater modification by gravity: A mechanical analysis of slumping. In: D.J. Roddy, R.O. Pepin, R.B. Merrill (eds), *Impact and explosion cratering*, Pergamon Press, New York, pp. 1245–1260.
- MELOSH, H.J., 1979. Acoustic fluidization: A new geologic process? *Journal of Geophysical Research*, Vol. **84**, pp. 7513–7520.
- MELOSH, H.J., 1982. A schematic model of crater modification by gravity. *Journal of Geophysical Research*, Vol. **87**, No. **B1**, pp. 371–380.
- MELOSH, H.J., 1985. Impact cratering mechanics — Relationship between the shock wave and excavation flow. *Icarus*, Vol. **62**, pp. 339–343.
- MELOSH, H.J., 2007. A hydrocode equation of state for SiO₂. *Meteoritics & Planetary Science*, vol. **42**, p.2079–2098.
- MELOSH, H.J., 1989. *Impact cratering: A geologic process*. New York: Oxford University Press. 245 p.
- MELOSH, H.J., 1996. Dynamical weakening of faults by acoustic fluidization. *Nature*, Vol. **379**, pp. 601–606.
- MELOSH, H.J., and McKINNON, W.B., 1978. The mechanics of ringed basin formation. *Geophysical Research Letters*, Vol. **5**, pp. 985–988.
- MELOSH, H.J., and GAFFNEY, E.S., 1983. Acoustic Fluidization and the Scale Dependence of Impact Crater Morphology. *Proceedings of the 13th Lunar and Planetary Science Conference*, *Journal of Geophysical Research*, Vol. **88**, pp. A830–A834.
- MELOSH, H.J., and VICKERY, 1989. Impact erosion of the primordial atmosphere of Mars. *Nature*, Vol. **338**, pp. 487–489.
- MELOSH, H.J., RYAN, E.V., and ASPHAUG, E., 1992. Dynamic Fragmentation in Impact: Hydrocode Simulation of Laboratory Impacts. *Journal of Geophysical Research*, Vol. **97**, pp. 14,735–14,759.
- MELOSH, H.J., and IVANOV, B.A., 1999. Impact crater collapse. *Annu. Rev. Earth Planet. Sci.*, Vol. **27**, pp. 385–415.
- MICHAEL, G.G., 2003. Coordinate registration by automated crater recognition. *Planetary and Space Science* **51**, pp. 563–568.
- MICHEL, P., MORBIDELLI, A., and BOTTKE, W.F., 2005. Origin and dynamics of Near Earth Objects. *Comptes Rendus - Physique*, Vol. **6**, pp. 291–301
- MICHEL, P., O'BRIEN, D.P., ABE, S., HIRATA, N., 2009. Itokawa's cratering record as observed by Hayabusa: implications for its age and collisional history. *Icarus*, Vol. **200**, pp. 503–513.
- MIHÁLYI, K., GUCSIK, A., SZABÓ, J., 2008. Drainage patterns of terrestrial complex meteorite patterns: a hydrogeological overview. *LPSC 39th*, abstract #1200.

- MILESI, J.P., TOTEU, S.F., DESCHAMPS, Y., FEYBESSE, J.L., LEROUGE, C., COCHERIE, A., PENAYE, J., TCHAMENI, R., MOLOTO–A–KENGUEMBA, G., KAMPUNZU, H.A.B., NICOL, N., DUGUEY, E., LEISTEL, J.M., SAINT–MARTIN, M., RALAY, F., HEINRY, C., BOUCHOT, V., DOUMNANG MBAIGANE, J.C., KANDA KULA, V., CHENE, F., MONTHEL, J., BOUTIN, P. and CAILTEUX, J., 2006. An overview of the geology and major ore deposits of Central Africa: Explanatory note for the 1:4,000,000 map “Geology and major ore deposits of Central Africa”. *Journal of African Earth Sciences*, Vol. **44**, pp. 571–595.
- MILTON, D.J., GLIKSON, A.Y., and BRETT, R., 1996. Gosses Bluff — A latest Jurassic impact structure, central Australia. Part 1: Geological structure, stratigraphy, and origin. *AGSO Journal of Australian Geology & Geophysics*, Vol. **16**, pp. 453–486.
- MINTON, D.A., and MALHOTRA, R., 2010. Dynamical erosion of the asteroid belt and implications for large impacts in the Solar System. *Icarus*, Vol. **207**, pp. 744–757.
- MONEGATO, G., MASSIRONI, M., and MARTELLATO, E., 2010. LPSC **41st**, abstract #2148.
- MORBIDELLI, A., and GLADMAN, B., 1998. Orbital and temporal distribution of meteorites originating in the asteroid belt. *Meteoritics & Planetary Science*, Vol. **33**, pp. 999–1016.
- MORBIDELLI, A., BOTTKE Jr, W.F., FROESCHLÉ, C.H., and MICHEL, P., 2002. Origin and evolution of near–Earth objects. In: W. K. Bottke Jr, P. Cellino, P. Paolicchi, R.P. Binzel (eds), *Asteroids III*, Univ. Arizona Press, Tucson, pp. 409–422.
- MOREAU, C., BROWN, W.L., DEMAIFFE, D., DUPONT, P.-L., and ROCCI, G., 1986. Un des plus grands ring-dykes du monde: le Meugueur-Meugueur, massif de l’Aïr, République du Niger. *Comptes Rendus de l’Académie des Sciences Paris*, Vol. **302**, pp. 223–226.
- MORGAN, W.J., 1983. Hotspot tracks and the early rifting of the Atlantic. *Tectonophysics*, Vol. **94**, pp. 123–139.
- MUHLEMAN, D.O., BUTLER, B.J., GROSSMAN, A.W., and SLADE, M.A., 1991. Radar images of Mars. *Science*, Vol. **253**, pp. 1508–1513.
- MURCHIE, S.L., WATTERS, T.R., ROBISON, M.S., HEAD III, J.W., STROM, R.G., CHAPMAN, C.R., SOLOMON, S.C., McCLINTOCK, W.E., PROCKTER, L.M., DOMINIGUE, D.L., and BLEWETT, D.T., 2008. Geology of the Caloris Basin, Mercury: A view from MESSENGER. *Science*, Vol. **321**, pp. 73–76.
- MURCHIE, S.L., MUSTARD, J.F., EHLMANN, B.L., MILLIKEN, R.E., BISHOP, J.L., McKEOWN, N.K., NOE DOBREA, E.Z., SEELOS, F.P., BUCZKOWSKI, D.L., WISEMAN, S.M., ARVIDSON, R.E., WRAY, J.J., SWAYZE, G., CLARK, R.N., DES MARAIS, D.J., McEWEN, A.S., and BIBRING, J.-P., 2009. A synthesis of Martian aqueous mineralogy after 1 Mars year of observations from the Mars Reconnaissance Orbiter. *Journal of Geophysical Research*, Vol. **114**, pp. E00D06.
- MURRAY, B.C., STROM, R.G., TRASK, N.J., and GAULT, D.E., 1975. Surface History of Mercury: Implications for Terrestrial Planets. *Journal of Geophysical Research*, Vol. **80**, pp. 2508–2514.
- MURRAY, N., and HOLMAN, M., 1997. Diffusive chaos in the outer asteroid belt. *Astron. J.*, Vol. **114**, pp. 1246–1252.
- MUSTARD, J.F., MURCHIE, S.L., PELKEY, S.M., EHLMANN, B.L., MILLIKEN, R.E., GRANT, J.A., BIBRING, J.-P., POULET, F., BISHOP, J.L., NOE DOBREA, E.Z., ROACH, L., SEELOS, F., ARVIDSON, R.E., WISEMAN, S., GREEN, HASH, C., HUMM, D., MALARET, E., McGOVERN, J.A., SEELOS, K., CLANCY, T., CLARK, R.N., DES MARAIS, D.J., IZENBERG, N., KNUDSON, A., LANGEVIN, Y., MARTIN, T., McGUIRE, P., MORRIS, P., ROBINSON, M.S., ROUSH, T., SMITH, M., SWAYZE, G., TAYLOR, H., TITUS, T., and WOLFF, M., 2008. Hydrated silicate minerals on Mars observed by the Mars Reconnaissance Orbiter CRISM instrument. *Nature*, Vol. **454**, pp. 305–309.

- NAMIKI, N, and HONDA, C., 2003. Testing hypotheses for the origin of steep slope of lunar size–frequency distribution for small craters. *Earth Planets Space*, Vol. **55**, pp. 39–51.
- NESS, N.F., BEHANNON, K.W., LEPPING, R.P., WHANG, Y.C., and SCHATTEN, K.H., 1974. Magnetic field observations near Mercury: preliminary results from Mariner 10. *Science*, Vol. **185**, pp. 151–160.
- NESS, N.F., BEHANNON, K.W., LEPPING, R.P., WHANG, Y.C., and SCHATTEN, K.H., 1975. The magnetic field of Mercury. *Journal of Geophysical Research*, Vol. **80**, pp. 2708–2716.
- NESVORNÝ, D., FERRAZ–MELLO, S., HOLMAN, M., and MORBIDELLI, A., 2002. Regular and chaotic dynamics in the mean motion resonances: Implications for the structure and evolution of the asteroid belt. In: W. K. Bottke Jr, P. Cellino, P. Paolicchi, R.P. Binzel (eds), *Asteroids III*, Univ. Arizona Press, Tucson, pp. 379–394.
- NEUKUM, G., 1977a. Lunar cratering. *Philosophical Transactions of the Royal Society of London. Series A, Mathematical and Physical Sciences*, Vol. **285**, pp. 267–272.
- NEUKUM, G., 1977b. Different ages of lunar light plains. *The Moon*, Vol. **17**, pp. 383–393.
- NEUKUM, G., 1983. Meteoritenbombardement und Datierung planetarer Oberflächen. *Habilitationsschrift*, Univ. München, München, Germany.
- NEUKUM, G., KÖNIG, B., and ARKANI–HAMED, J., 1975a. A study of lunar impact crater size–distributions. *The Moon*, Vol. **12**, pp. 201–229.
- NEUKUM, G., KÖNIG, B., FECHTIG, H., and STORZER, D., 1975b. Cratering in the earth–moon system: Consequences for age determination by crater counting. *Proc. Lunar Sci. Conf.* **6th**, pp. 2597–2620.
- NEUKUM, G., and HORN, P., 1976. Effects of lava flows on lunar crater populations. *The Moon*, Vol. **15**, pp. 205–222.
- NEUKUM, G., and KÖNIG, B., 1976. Dating of individual lunar craters. *Proc. Lunar Sci. Conf.* **7th**, pp. 2867–2881.
- NEUKUM, G., and WISE, D.U., 1976. Mars: A Standard Crater Curve and Possible New Time Scale. *Science*, Vol. **194**, pp. 1381–1387.
- NEUKUM, G., and IVANOV, B.A., 1994. Crater size distributions and impact probabilities on Earth from lunar, terrestrial-planet, and asteroid cratering data. In: T. Gehrels (eds), *Hazard Due to Comets and Asteroids*, Univ. of Arizona Press, Tucson, pp. 359–416.
- NEUKUM, G., IVANOV, B.A., and HARTMANN, W.K., 2001a. Cratering records in the inner Solar System in relation to the lunar reference system. *Chronology and Evolution of Mars*, Vol. **96**, pp. 55–86.
- NEUKUM, G., OBERST, J., HOFFMANN, H., WAGNER, R., and IVANOV, B.A., 2001b. Geologic evolution and cratering history of Mercury. *Planetary and Space Science*, Vol. **49**, pp. 1507–1521.
- NIMMO, F., 2002. Constraining the crustal thickness on Mercury from viscous topographic relaxation. *Geophysical Research Letters*, Vol. **29**, pp. 1063,1–4.
- NIMMO, F., and WATTERS, T.R., 2004. Depth of faulting on Mercury: Implications for the heat flux and crustal and effective elastic thickness. *Geophysical Research Letters*, Vol. **31**, pp. L02701,1–5.
- NOLAN, M.C., ASPHAUG, E., MELOSH, H.J., and GREENBERG, R., 1996. Impact craters on asteroids: does gravity or strength control their size? *Icarus*, Vol. **124**, pp. 359–371.

- NOLAN, M.C., ASPHAUG, E., GREENBERG, R., and MELOSH, H.J., 2001. Impacts on Asteroids: Fragmentation, Regolith Transport, and Disruption. *Icarus*, Vol. **153**, pp. 1–15.
- OBERBECK, V.R., 1971. Laboratory Simulation of Impact Cratering with High Explosives. *Journal of Geophysical Research*, Vol. **76**, pp. 5732–5749.
- OBERBECK, V.R., and MORRISON, R.H., 1973. On the formation of the lunar herringbone pattern. *Proc. Sci. Conf.* **4th**, pp. 107–123.
- OBERST, J., SCHWARZ, G., BEHNKE, T., HOFFMANN, H., MATZ, K.-D., FLOHRER, J., HIRSCH, H., ROATSCH, T., SCHOLTEN, F., HAUBER, E., BRINKMANN, B., JAUMANN, R., WILLIAMS, D., KIRK, R., DUXBURY, T., LEU, C., and NEUKUM, G., 2008. The imaging performance of the SRC on Mars Express. *Planetary and Space Science*, Vol. **56**, pp. 473–491.
- OGILVIE, K.W., SCUDDER, J.D., HARTLE, R.E., SISCOE, G.L., BRIDGE, H.S., LAZARUS, A.J., ASBRIDGE, J.R., BAME, S.J., and YEATES, C.M., 1974. Observations at Mercury Encounter by the Plasma Science Experiment on Mariner 10. *Science*, Vol. **185**, pp. 145–151.
- O'KEEFE, J.D., and AHRENS, T.J., 1982. The interaction of the Cretaceous/Tertiary extinction bolide with the atmosphere, ocean, and solid earth. *Geological Society of America Special Papers*, Vol. **190**, pp. 103–120.
- O'KEEFE, J.D., and AHRENS, T.J., 1993. Planetary cratering mechanics. *Journal of Geophysical Research*, Vol. **98**, pp. 17011–17028.
- ÖPIK, E.J., 1961. The survival of comets and comet material. *Astron. J.*, Vol. **66**, pp. 381–382.
- ÖPIK, E.J., 1963. The stray bodies in the solar system. Part I. Survival of comet nuclei and the asteroids. *Advan. Astron. Astrophys.*, Vol. **2**, pp.219–262.
- OSTRO, S.J., and SHOEMAKER, E.M., 1990. The extraordinary radar echoes from Europa, Ganymede, and Callisto: A geological perspective. *Icarus*, Vol. **85**, pp. 335–345.
- PAGEL, M., WHEATLEY, K., and EY, F., 1985. The origin of the Carswell circular structure. *Geological Association of Canada, Special Paper*, Vol. **29**, pp. 213–224.
- PAIGE, D.A., SIEGLER, M.A., ZHANG, J.A., HAYNE, P.O., FOOTE, E.J., BENNETT, K.A., VASAVADA, A.R., GREENHAGEN, B.T., SCHOFIELD, J.T., McCLEESE, D.J., FOOTE, M.C., DeJONG, E., BILLS, B.G., HATFORD, W., MURRAY, B.C., ALLEN, C.C., SNOOL, K., SODERBLUM, L.A., CALCUTT, S., TAYLOR, F.W., BOWLES, N.E., BANDFIELD, J.L., ELPHIC, R., GHENT, R., GLOTCH, T.D., WYATT, M.B., and LUCEY, P.G., 2010. Diviner Lunar Radiometer Observations of Cold Traps in the Moon's South Polar Region. *Science*, Vol. **330**, pp. 479.
- PAPANASTASSIOU, D.A., and WASSERBURG, G.J., 1973. Rb–Sr Ages and initial strontium in basalts from Apollo 15. *Earth Planetary Science Letters*, Vol. **17**, pp.324–336.
- PERNA, D., DOTTO, E., LAZZARIN, M., MAGRIN, S., FULCHIGNONI, M., BARUCCI, M.A., FORNASIER, S., MARCHI, S., and BARBIERI, C., 2010. Inhomogeneities on the surface of 21 Lutetia, the asteroid target of the Rosetta mission — Ground-based results before the Rosetta fly-by. *Astronomy & Astrophysics*, Vol. **513**, pp. L4,1–3.
- PIERAZZO, E., VICKERY, A.M. and MELOSH, H.J., 1997. A Re-evaluation of Impact Melt Production. *Icarus*, Vol. **127**, pp. 408–423.
- PIERAZZO, E., and CHYBA, C.F., 1999. Amino acid survival in large cometary impacts. *Meteoritics & Planetary Science*, Vol. **34**, pp. 909–918.

- PIERAZZO, E., and COLLINS, G.S., 2004. A brief introduction to hydrocode modelling. In: H. Dypvik, M.J. Burchell, P. Claeys (eds), *Cratering in Marine Environments and on Ice*, Springer, Verlag, Berlin, pp. 323–340.
- PIERAZZO, E., and CHYBA, C.F., 2006. Impact Delivery of Prebiotic Organic Matter to Planetary Surfaces. In: P.J. Thomas, R.D. Hycks, C.F. Chyba, C.P. McKay (eds), *Comets and the Origin and Evolution of Life*, Adv. Astrobiol. Biogeophys., Springer, Berlin Heidelberg, pp. 323–340.
- PIERAZZO, E., ARTEMIEVA, N., ASPHAUG, E., BALDWIN, E.C., CAZAMIAS, J., COKER, R., COLLINS, G.S., CRAWFORD, D.A., DAVISON, T., ELBESHAUSEN, D., HOLSAPPLE, K.A., HOUSEN, K.R., KORYCANSKY, D.G., and WÜNNEMANN, K., 2008. Validation of numerical codes for impact and explosion cratering: Impacts on strengthless and metal targets. *Meteoritics & Planetary Science*, Vol. **43**, pp. 1917–1938.
- PIETERS, C.M., HEAD III, J.W., ISAACSON, P., PETRO, N., RUNYON, C., OHTAKE, M., FÖING, B., and GRANDE, M., 2008. Lunar international science coordination/calibration targets (L-ISCT). *Advances in Space Research*, Vol. **42**, pp. 248–258.
- PIETERS, C.M., GOSWAMI, J.N., CLARK, R.N., ANNADURAJ, M., BOARDMAN, J., BURATTI, B., COMBE, J.-P., DYAR, M.D., GREEN, R., HEAD, J.W., HIBBITTS, C., HICKS, M., ISAACSON, P., KLIMA, R., KRAMER, G., KUMAR, S., LIVO, E., LUNDEEN, S., MALARET, E., McCORD, T., MUSTARD, J., NETTLES, J., PETRO, N., RUNYON, C., STAUD, M., SUNSHINE, J., TAYLOR, L.A., TOMPKINS, S., and VARANASI, P., 2009. Character and Spatial Distribution of OH/H₂O on the Surface of the Moon Seen by M³ on Chandrayaan-1. *Science*, Vol. **326**, pp. 568–572.
- PIKE, R.J., 1977. Size-dependence in the shape of fresh impact craters on the moon. In: D. J. Roddy and R. B. Merrill (eds), *Impact and explosion cratering*, Pergamon Press, New York, pp. 489–509.
- PIKE, R.J., 1980. Formation of complex impact craters – Evidence from Mars and other planets. *Icarus*, Vol. **43**, pp. 1–19.
- POIRIER, J.P., 1994. Plastic rheology of crystals. In: T.J. Ahrens, D.C. Washington (eds), *Mineral physics and crystallography: A handbook of physical constants*, American Geophysical Union, pp. 237–247.
- POTTER, A., and MORGAN, T., 1985. Discovery of sodium in the atmosphere of Mercury. *Science*, Vol. **229**, pp. 651–653.
- POTTER, A., and MORGAN, T., 1986. Potassium in the atmosphere of Mercury. *Icarus*, Vol. **67**, pp. 336–340.
- POULET, F., BIBRING, J.-P., MUSTARD, J.F., GENDRIN, A., MANGOLD, N., LANGEVIN, Y., ARVIDSON, R.E., GONDET, B., GOMEZ, C., 2005. Phyllosilicates on Mars and implications for early Martian climate. *Nature*, Vol. **438**, pp. 623–627.
- PRATER, R.F., 1970. Hypervelocity impact. Material strength effects on crater formation and shock propagation in three aluminum alloys. Air Force Institute of Technology, Technical Report **AD0718461**.
- PREBLICH, B., McEWEN, A.S., and STUDER, D., 2005. Mapping rays and secondary craters from Zunil, Mars. *LPSC 36th*, abstract #2112.
- PROCKTER, L.M., WATTERS, T.R., CHAPMAN, C.R., DENEVI, B.W., HEAD III, J.W., SOLOMON, S.C., MURCHIE, S.L., BARNOUIN-JHA, O.S., ROBINSON, M.S., BLEWETT, D.T., and GILLIS-DAVIS, J., 2009. The Curious Case of Raditladi Basin. *LPSC 40th*, abstract #1758.
- PROCKTER, L.M., ERNST, C.M., DENEVI, B.W., CHAPMAN, C.R., HEAD III, J.W., FASSET, C.I., MERLINE, W.J., SOLOMON, S.C., WATTERS, T.R., BLEWETT, D.T., CREMONESE, G., MARCHI, S., MASSIRONI, M., and BARNOUIN-JHA, O.S., 2010. Evidence for young volcanism on Mercury from the third MESSENGER flyby. *Science*, Vol. **329**, pp. 668–671.

- QUAIDE, W.L., and OBERBECK, V.R., 1968. Thickness determinations of the lunar surface layer from lunar impact craters. *Journal of Geophysical Research*, Vol. **73**, pp. 5247–5270.
- QUANTIN, C., MANGOLD, N., HARTMANN, W.K., ALLEMAND, P., 2006. Density of small impact craters on Mars: dominated by secondaries or secondary and primary mixing? *Planetary Chronology Workshop 2006*, abstract #6025.
- QUANTIN, C., MANGOLD, N., HARTMANN, W.K., and ALLEMAND, P., 2007. Possible long-term decline in impact rates 1. Martian geological data. *Icarus*, Vol. **186**, pp. 1–10.
- RABINOWITZ, D., 1993. The size–distribution of the Earth approaching Asteroids. *Astrophysical Journal*, Vol. **407**, 412–427.
- RAJMON, D., 2006. Suspected Earth Impact sites. *LPSC 37th*, abstract #2372.
- REIMOLD, W.U., COOPER, G.R.J., ROMANO, R., COWAN, D.R., and KOEBERL, C., 2006. Investigation of Shuttle Radar Topography Mission data of the possible impact structure at Serra da Cangalha, Brazil. *Meteoritics & Planetary Science*, Vol. **41**, pp. 237–246.
- REINHARD, R., 1986. The Giotto encounter with comet Halley. *Nature*, Vol. **321**, pp. 313–318.
- REUFER, A., THOMAS, N., BENZ, W., BYRNE, S., BRAY, V., DUNDAS, C., and SEARLS, M., 2010. Models of high velocity impacts into dust-covered ice: Application to Martian northern lowlands. *Planetary & Space Science*, Vol. **58**, pp. 1160–1168.
- RICHARDSON, D.C., LEINHARDT, Z.M., MELOSH, H.J., BOTTKE Jr, W.F., and ASPHAUG, E., 2002. Gravitational Aggregates: Evidence and Evolution. In: W.K. Bottke Jr, P. Cellino, P. Paolicchi, R.P. Binzel (eds), *Asteroids III*, Univ. Arizona Press, Tucson, pp. 501–515.
- RICHARDSON Jr, J.E., MELOSH, H.J., ARTEMIEVA, N.A., and PIERAZZO, E., 2005a. Impact cratering theory and modeling for the Deep Impact mission: from mission planning to data analysis. *Space Science Reviews*, Vol. **117**, pp. 241–267.
- RICHARDSON Jr, J.E., MELOSH, H.J., GREENBERG, R.J., O'BRIEN, D.P., 2005b. The global effects of impact–induced seismic activity on fractured asteroid surface morphology. *Icarus*, Vol. **179**, pp. 325–349.
- RITZ, M., BROWN, W.L., MOREAU, C., OHNENSTETTER, D., 1996. An audiomagnetotelluric study of the Meugueur–Meugueur ring structure, Air, Niger: ring dyke or cone sheet? *Journal of Applied Geophysics*, Vol. **34**, pp. 229–236.
- RIVKIN, A.S., HOWELL, E.S., VILAS, F., and LEBOSKY, L.A., 2002. Hydrated Minerals on Asteroids: The Astronomical Record. In: W.K. Bottke Jr, P. Cellino, P. Paolicchi, R.P. Binzel (eds), *Asteroids III*, Univ. Arizona Press, Tucson, pp. 235–253.
- ROBINSON, M.S., MURCHIE, S.L., BLEWETT, D.T., DOMINIGUE, D.L., HAWKINS III, S.E., HEAD III, J.W., HOLDCKAW, G.M., McCLINTOCK, W.E., McCOY, T.J., McNUTT Jr., R.L., PROCKTER, L.M., SOLOMON, S.C., and WATTERS, T.R., 2008. Reflectance and Color Variations on Mercury: Regolith Processes and Compositional Heterogeneity. *Science*, Vol. **321**, pp. 66–69.
- RODDY, D.J., and DAVIS, L.K., 1977. Shatter cones formed in large-scale experimental explosion craters. In: D.J. Roddy, R.O. Pepin and R.B. Merrill (eds), *Impact and Explosion Cratering: Planetary and Terrestrial Implications*, Pergamon, New York, pp. 715–750.
- RUBIN, A.E., 2000. Petrographic, geochemical and experimental constraints on models of chondrule formation. *Earth Sci. Rev.*, Vol. **50**, pp. 3–27.

- RULE, W.K., 1997. A numerical scheme for extracting strength model coefficients from Taylor test data. *International Journal of Impact Engineering*, Vol. **5**, pp. 797–810.
- RYDER, G., 1990. Lunar samples, lunar accretion and the early bombardment of the Moon. *EOS Transactions American Geophysical Union*, Vol. **71**, pp. 313–323.
- SAAL, A.E., HAURI, E.H., LO CASCIO, M., VAN ORMAN, J.A., RUTHERFORD, M.C., and COOPER, R.F., 2008. Volatile content of lunar volcanic glasses and the presence of water in the Moon's interior. *Nature*, Vol. **454**, pp. 192–195.
- SAHAGIAN, D.L., 1993. Structural evolution of African basins: stratigraphic synthesis. *Basin Research*, Vol. **5**, pp. 41–54.
- SANDFORD, S.A., 1984. Infrared transmission spectra from 2.5 to 25 microns of various meteorite classes. *Icarus*, Vol. 115–126.
- SAWABE, Y., MATSUNAGA, T., and ROKUGAWA, S., 2006. Automated detection and classification of lunar craters using multiple approaches. *Advances in Space Research* **37**, pp. 21–27.
- SCHMALZL, J., 2003. Using standard image compression algorithm to store data from computational fluid dynamics. *Comput. Geosci.*, Vol. **29**, pp. 1021–1031.
- SCHMIDT, R.M., 1978. Centrifuge simulation of the JOHNNIE BOY 500 ton cratering event. *Proc. Lunar Planet. Sci. Conf.* **9th**, pp. 3877–3889.
- SCHMIDT, R.M., 1980. Meteor Crater: Energy of formation — implications of centrifuge scaling. *Proc. Lunar Planet. Sci. Conf.* **11th**, pp. 2099–2128.
- SCHMIDT, R.M., and HOLSAPPLE, K.A., 1979. Centrifuge Crater Scaling Experiment II: Material Strength Effects. Defense Nuclear Agency Report DNA **4999Z**. Washington D.C.
- SCHMIDT, R.M., and HOLSAPPLE, K.A., 1980. Theory and Experiments on Centrifuge Cratering. *Journal of Geophysical Research*, Vol. **85**, pp. 235–252.
- SCHMIDT, R.M., and HOUSEN, K.R., 1987. Some Recent Advances in the Scaling of Impact and Exploration Cratering. *International Journal of Impact Engineering*, Vol. **5**, pp. 543–560.
- SCHULTE, P., ALEGRET, L., ARENILLAS, I., ARZ, J.A., BARTON, P.G., BOWN, P.R., BRALOWER, T.J., CHRISTESON, G.L., CLAEYS, P., COCKELL, D.S., COLLINS, G.S., DEUTSCH, A., GOLDIN, T.J., GOTO, K., GRAJALES-NISHIMURA, J.M., GRIEVE, R.A.F., GULICK, S.P.S., JOHNSON, K.R., KIESSLING, W., KOEBERL, C., KRING, D.A., MacLEOD, K.G., MATSUI, T., MELOSH, H.J., MONTANARI, A., MORGAN, J.V., NEAL, C.R., NICHOLS, D.J., NORRIS, R.D., PIERAZZO, E., RAVIZZA, G., REBOLLEDO-VIEYRA, M., REIMOLD, W.U., ROBIN, E., SALGE, T., SPEIJER, R.P., SWEET, A.R., URRUTIA-FUCUGAUCHI, J., VAJDA, V., WHALEN, M.T., WILLUMSEN, P.S., 2010. The Chicxulub Asteroid Impact and Mass Extinction at the Cretaceous–Paleogene Boundary. *Science*, Vol. **327**, pp. 214–218.
- SCHULTZ, P.H., HERMALYN, B., COLAPRETE, A., ENNICO, K., SHIRLEY, M., and MARSHALL, W.S., 2010. The LCROSS Cratering Experiment. *Science*, Vol. **330**, pp. 468–472.
- SCHULZ, R., and BENKHOFF, J., 2006. BepiColombo: Payload and mission updates. *Advances in Space Research*, Vol. **38**, pp. 572–577.
- SCHWEHM, G., and SCHULZ, R., 1999. ROSETTA goes to comet Wirtanen. In: K. Altwegg, P. Ehrenfreund, J. Geiss, W. Huebner (eds), *Composition and origin of cometary materials*. Space Science Series of ISSI, Kluwer Academic Publication, *Space Science Reviews*, Vol. **90**, 313–319.

- SCOTT, R.G., PILKINGTON, M., and TANCZYK, E.I., 1997. Magnetic investigations of the West Hawk, Deep Bay and Clearwater impact structures, Canada. *Meteoritics & Planetary Science*, Vol. **32**, pp. 293–308.
- SEAGER, S., 2003. The search for extrasolar Earth-like planets. *Earth and Planetary Science Letters*, Vol. **208**, pp. 113–124.
- SEED, H.B., and GOODMAN, R.E., 1964. Earthquake stability of cohesionless soils. *Journal of the Soil Mechanics and Foundation Division*, Vol. **90** (SM6), ASCE, pp. 4128.
- SENF, L.E., and STEWART, S.T., 2008. Impact crater formation in icy layered terrains on mars. *Meteoritics & Planetary Science*, Vol. **43**, pp. 1993–2013.
- SHOEMAKER, E.M., 1962. Interpretation of lunar craters. In: Z. Kopal (eds), *Physics and Astronomy of the Moon*, New York, Academic, pp. 283–359.
- SHOEMAKER, E.M., 1963. Impact mechanics at Meteor Crater, Arizona. In: B.M. Middlehurst and G.P. Kuiper (eds), *The Moon, Meteorites and Comets*, University of Chicago Press, Chicago and London, pp. 301–336.
- SHOEMAKER, E.M., 1965. Preliminary Analysis of the Fine Structure of the Lunar Surface. In: Ranger VII Report, JPL Tech. Report, No. **32-700**, pp. 75–134.
- SHOEMAKER, E.M., SHOEMAKER, C.S., NISHIZUMI, K., KOHL, C.P., ARNOLD, J.R., KLEIN, J., FINK, D., MIDDLETON, R., KUBIK, P.W., and SHARMA, P., 1990. Ages of Australian meteorite craters-A preliminary report. *Meteoritics*, Vol. **25**, abstract #409.
- SIMIONI, E., 2011. Analisi delle prestazioni stereoscopiche e simulazioni con la stereo camera per la missione BepiColombo. PhD Thesis. Università degli Studi di Padova.
- SIMPSON, J.A., ERAKER, J.H., LAMPORT, J.E., and WALPOLE, P.H., 1974. Electrons and Protons Accelerated in Mercury's Magnetic Field. *Science*, Vol. **185**, pp. 160–166.
- SLADE, M.A., BUTLER, B.J., and MUHLEMAN, D.O., 1992. Mercury radar imaging — Evidence for polar ice. *Science*, Vol. **258**, pp. 635–640.
- SLAVIN, J.A., ACUÑA, M.H., ANDERSON, B.J., BAKER, D.N., BENNA, M., GLOECKLER, G., GOLD, R.E., HO, G.C., KILLEN, R.M., KORTH, H., KRIMIGIS, S.M., McNUTT Jr, R.L., NITTLER, L.R., RAINES, G.M., SCHRIVER, D., SOLOMON, S.C., STARR, R.D., TRÁVNÍČEK, P., ZURBUCHEN, T.H., 2008. Mercury's Magnetosphere After MESSENGER's First Flyby. *Science*, Vol. **321**, pp. 85–89.
- SLAVIN, J.A., ANDERSON, B.J., BAKER, D.N., BENNA, M., BOARDSEN, S.A., GLOECKLER, G., GOLD, R.E., HO, G.C., KORTH, H., KRIMIGIS, S.M., McNUTT Jr, R.L., NITTLER, L.R., RAINES, G.M., SARANTOS, M., SCHRIVER, D., SOLOMON, S.C., STARR, R.D., TRÁVNÍČEK, P., ZURBUCHEN, T.H., 2010. MESSENGER Observations of Extreme Loading and Unloading of Mercury's Magnetic Tail. *Science*, Vol. **329**, pp. 665–668.
- SMITH, P.H., TAMPPARI, L., ARVIDSON, R.E., BASS, D., BLANEY, D., BOYTON, W., CARSWELL, A., CATLING, D., CLARK, B., DUCK, T., DeJONG, E., FISHER, D., GOETZ, W., GUNNLAUGSSON, P., HECHT, M., HIPKIN, V., HOFFMAN, J., HVIID, S., KELLER, H., KOUNAVES, S., LANGE, C.F., LEMMON, M., MASDEN, M., MALIN, M., MARKIEWICZ, W., MARSHALL, J., McKAY, C., MELLON, M., MICHELANGELI, D., MING, D., MORRIS, R., RENNO, N., PIKE, W.T., STAUFER, U., STOKER, C., TAYLOR, P., WHITEWAY, J., YOUNG, S., and ZENT, A., 2008. Introduction to special section on the Phoenix mission: landing site characterization experiments, mission overviews, and expected science. *Journal of Geophysical Research*, Vol. **113**, pp. E00A18.
- SODERBLOM, L.A., CONDIT, C.D., WEST, R.A., HERMAN, B.M., and KREIDLER, T.J., 1974. Martian planet wide crater distributions: Implications for geologic history and surface processes. *Icarus*, Vol. **22**, pp. 239–263.

- SOLOMON, S.C., McNUTT Jr, R.L., GOLD, R.E., ACUÑA, M.H., BAKER, D.N., BOYNYON, W.V., CHAPMAN, C.R., CHENG, A.F., GLOECKLER, G., JEAD III, J.W., KRIMIGIS, S.M., McCLINTOCK, W.E., MURCHIE, S.L., PEALE, S.J., PHILLIPS, R.J., ROBINSON, M.S., SLAVIN, J.A., SMITH, D.E., STROM, R.G., TROMKA, J.I., and ZUBER, M.T., 2001. The MESSENGER mission to Mercury: scientific objectives and implementation. *Planetary and Space Science*, Vol. **49**, pp. 1445–1465.
- SOLOMON, S.C., 2003. Mercury: the enigmatic innermost planet. *Earth and Planetary Science Letters*, Vol. **216**, pp. 441–155.
- SOLOMON, S.C., McNUTT Jr., R.L., GOLD, R.E., and DOMINIGUE, D.L., 2007. MESSENGER Mission Overview. *Space Sci. Rev.*, Vol. 131, pp. 3–39.
- SOLOMON, S.C., McNUTT Jr, R.L., WATTERS, T.R., LAWRENCE, D.J., FELDMAN, W.C., HEAD, J.J., KRIMIGIS, S.M., MURCHIE, S.L., PHILLIPS, R.J., SLAVIN, J.A., and ZUBER, M.T., 2008. Return to Mercury: A Global Perspective on MESSENGER's First Mercury Flyby. *Science*, Vol. **321**, pp. 59–62.
- SPUDIS, P.D., and GUEST, J.E., 1988. Stratigraphy and Geologic History of Mercury. In: F. Vilas, C.R. Chapman, M.S. Matthews (eds), *Mercury*, The University of Arizona Press, Tucson, pp. 118–164.
- SPUDIS, P.D., BUSSEY, D.B.J., BALOGA, S.M., BUTLER, B.J., CARL, D., CARTER, L.M., CHAKRABORTY, M., ELPHIC, R.C., GILLIS-DAVIS, J.J., GOSWAMI, J.N., HEGGY, E., HILLYARD, M., JENSEN, R., KIRK, R.L., LaVALLEE, K.D., McKERRACHER, P., NEISH, C.D., NOZETTE, S., NYLUND, S., PALSETIA, M., PATTERSON, W., ROBINSON, M.S., RANEY, R.K., SCHULZE, R.C., SEQUEIRA, H., SKURA, J., THOMPSON, T.W., THOMSON, B.J., USTINOV, E.A., and WINTERS, H.L., 2010. Initial results for the north pole of the Moon from Mini-SAR Chandrayaan-1 mission. *Geophysical Research Letters*, Vol. **37**, pp. L06204,1–L06204,6.
- STEFFL, A.J., CUNNINGHAM, N.J., DURDA, D.D., and STERN, S.A., 2009. A Search for Vulcanoids Using STEREO Heliospheric Imager Data. *DPS 41st*, abstract #43.01.
- STESKY, R.M., BRACE, W.F., RILEY, D.K., and BOBIN, P.Y., 1974. Friction in faulted rock at high temperature and pressure. *Tectonophysics*, Vol. **23**, pp. 177–203.
- STÖFFLER, D., 1972. Deformation and transformation of rock-forming minerals by natural and experimental shock processes: I. Behavior of minerals under shock compression. *Fortschritte der Mineralogie*, Vol. **49**, pp. 50–113.
- STÖFFLER, D., and RYDER, G., 2001. Stratigraphy and isotope ages of lunar geologic units: Chronological standard for the inner solar system. In *Chronology and Evolution of Mars*, W.K. Hartmann, J. Geiss and R. Kallenbach (eds.), Kluwer Acad., Norwell, Mass., pp. 9–54.
- STUART, J.S., and BINZEL, R.P., 2004. Bias-corrected population, size distribution and impact hazard for the near-Earth objects. *Icarus*, Vol. **170**, pp. 295–311.
- STROM, R.G., CROFT, S., BARLOW, N., 1992. The Martian impact cratering record. In: H. Kieffer, B. Jakosky, C.W. Snyder, M.S. Matthews (eds), *Mars*, Univ. Arizona Press, Tucson, pp. 383–423.
- STROM, R.G., and SPRAGUE, A.L., 2003. *Exploring Mercury: the iron planet*. Springer-Praxis Publishing Ltd., Chichester, UK. 216 p.
- STROM, R.G., MALHOTRA, R., ITO, T., YOSHIDA, F., and KRING, D.A., 2005. The Origin of Planetary Impactors in the Inner Solar System. *Science*, Vol. **309**, pp. 1847–1850.
- STROM, R.G., CHAPMAN, C.R., MERLINE, W.J., SOLOMON, S.C., HEAD III, J.W., 2008. Mercury Cratering Record Viewed from MESSENGER's First Flyby. *Science*, Vol. **321**, pp. 79–81.

- SULLIVAN, R.J., THOMAS, P.C., MURCHIE, S.L., and ROBINSON, M.S., 2002. Asteroid Geology from Galileo and NEAR Shoemaker Data. In: W.K. Bottke Jr, P. Cellino, P. Paolicchi, R.P. Binzel (eds), *Asteroids III*, Univ. Arizona Press, Tucson, pp. 331–350.
- SUNSHINE, J.M., FARNHAM, T.L., FEAGA, L.M., GROUSSIN, O., MERLIN, F., MILLIKEN, R.E., and A'HEARN, M.F., 2009. Temporal and Spatial Variability of Lunar Hydration As Observed by the Deep Impact Spacecraft. *Science*, Vol. **326**, pp. 565–568.
- TANAKA, K.L., 1986. The stratigraphy of Mars. *Journal of Geophysical Research*, Vol. **91**, pp. E139–E158.
- THOMAS, N., KELLER, H.U., ARIJS, E., BARBIERI, C., GRANDE, M., LAMY, P., RICKMAN, H., RODRIGO, R., WENZEL, K.-P., A'HEARN, M.F., ANGRILLI, F., BAILEY, M., BARUCCI, M.A., BERTAUX, J.-L., BRIEB, K., BURNS, J.A., CREMONESE, G., CURDT, W., DECEUNINCK, H., EMERY, R., FESTOU, M., FULLE, M., IP, W.-H., JORDA, L., KORTH, A., KOSCHNY, D., KRAMM, J.-R., KÜHRT, E., LARA, L.M., LLEBARIA, A., LOPEZ-MORENO, J.J., MARZARI, F., MOREAU, D., MULLER, C., MURRAY, C., NALETTO, G., NEVEJANS, D., RAGAZZONI, R., SABAU, L., SANZ, A., SIVAN, J.-P., and TONDELLO, G., 1998. OSIRIS — The Optical, Spectroscopic and Infrared Remote Imaging System for the Rosetta Orbiter. *Adv. Space Res.*, Vol. **21**, pp. 1505–1515.
- THOMAS, N., BARUCCI, M.A., BESSE, S., DA DEPPO, V., DEBEI, S., FERRI, F., GROUSSIN, O., JORDA, L., KELLER, H.U., MARCHI, S., MASSIRONI, M., MOISSL, R., TUBIANA, C., VINCENT, J., and the OSIRIS Team, 2010. Rosetta/OSIRIS Observations of the Surface Geomorphology of 21 Lutetia. *EPSC 5th*, abstract #340.
- THOMPSON, S.L., 1970. Improvements in the CHART-D radiation hydrodynamic code I: Analytical equation of state. Sandia National Laboratories, Report **SC-RR-70-28**.
- THOMPSON, S.L., and LAUSON, H.S., 1972. Improvements in the CHART-D radiation-hydrodynamic code III: Revised analytical equation of state. Sandia National Laboratories, Report **SC-RR-710714**.
- TILLOTSON, J.H., 1962. Metallic equations of state for hypervelocity impact. General Atomic, Report **GA-3216**.
- TOKSÖZ, M.N., PRESS, F., ANDERSON, K., DAINITY, A., LATHAM, G., EWING, M., DORMAN, J., LAMMLEIN, D., SUTTON, G., DUENNEBIER, F., NAKAMURA, Y., 1972. Lunar Crust: Structure and Composition. *Science*, Vol. **176**, pp. 1012–1016.
- TOON, O.B., ZAHNLE, K., MORRISON, D., TURCO, R., COVEY, C., 1997. Environmental Perturbations Caused by the Impacts of Asteroids and Comets. Proceedings of the international conference held April 24–26, 1995 in New York, New York, USA, Vol. **822**, p. 401.
- TURNER, G., 1971. ^{40}Ar – ^{39}Ar Ages from the Lunar Maria. *Earth Planetary Science Letters*, Vol. **11**, pp. 77–78.
- VERDANT, M. and SCHWEHM, G., 1998. The International Rosetta Mission, *ESA Bulletin*, Vol. **93**.
- VERNAZZA, P., BRUNETTO, R., BINZEL, R.P., PERRON, C., FULVIO, D., STRAZZULLA, G., and FULCHIGNONI, M., 2009. Plausible parent bodies for enstatite chondrites and mesosiderites: Implications for Lutetia's fly-by. *Icarus*, Vol. **202**, pp. 477–486.
- WAGNER, R., HEAD III, J.W., WOLF, U., and NEUKUM, G., 2002. Stratigraphic sequence and ages of volcanic units in the Gruithuisen region of the Moon. *Journal of Geophysical Research*, Vol. **107**, No. **E11,5104**, pp. 14,1–15.
- WAGNER, R., HEAD III, J.W., WOLF, U., and NEUKUM, G., 2010. Lunar red spots: Stratigraphic sequence and ages of domes and plains in the Hasteen and Helmet regions on the lunar nearside. *Journal of Geophysical Research*, Vol. **115**, pp. E06015,1–26.

- WATSON, K., MURRAY, B.C., and BROWN, H., 1961. The Behavior of Volatiles on the Lunar Surface. *Journal of Geophysical Research*, Vol. **66**, pp. 3033–3045.
- WATTERS, T.R., SCHULZ, R.A., ROBINSON, M.S., and COOK, A.C., 2002. The mechanical and thermal structure of Mercury's early lithosphere. *Geophysical Research Letters*, Vol. **29**, pp. 1542,1–4.
- WEAVER, H.A., FELDMAN, P.D., MERLINE, W.J., MUTCHLER, M.J., A'HERN, M.F., BERTAUX, J.-L., FEAGA, L.M., PARKER, J.W., SLATER, D.C., STEFFL, A.J., DRUMMOND, J.D., and STERN, S.A., 2010. Ultraviolet and visible photometry of asteroid (21) Lutetia using the Hubble Space Telescope. *Astronomy & Astrophysics*, Vol. **518**, pp. A4,1–10.
- WEISS, R., and WÜNNEMANN, K., 2007. Large waves caused by oceanic impacts of meteorites. In: A. Kundu (eds), *Tsunami and Nonlinear Waves*, Springer, Verlag, Berlin Heidelberg, pp. 237–261.
- WEISSMAN, P.R., BOTTKE Jr., W.F., and LEVISON, H.F., 2002. Evolution of comets into asteroids. In: W. K. Bottke Jr, P. Cellino, P. Paolicchi, R.P. Binzel (eds), *Asteroids III*, Univ. Arizona Press, Tucson, pp. 669–686.
- WEITZ, C.M., MILLIKEN, R.E., GRANT, J.A., McEWEN, A.S., WILLIAMS, R.M.E., BISHOP, J.L., and THOMSON, B.J., 2010. Mars Reconnaissance Orbiter observations of light-toned layered deposits and associated fluvial landforms on the plateaus adjacent to Valles Marineris. *Icarus*, Vol. **205**, pp. 73–102.
- WELLS, K.S., CAMPBELL, D.B., CAMPBELL, B.A., and CARTER, L.M., 2010. Detection of small lunar secondary craters in circular polarization ratio radar images. *Journal of Geophysical Research*, Vol. **115**, pp. E06008,1–10.
- WERNER, S.C., HARRIS, A.W., NEUKUM, G., and IVANOV, B.A., 2002. NOTE. The Near-Earth Asteroid Size-Frequency Distribution: A Snapshot of the Lunar Impactor Size-Frequency Distribution. *Icarus*, Vol. **156**, pp. 287–290.
- WERNER, S.C., 2006. Major Aspects of the Chronostratigraphy and Geologic Evolutionary History of Mars. Doctoral Dissertation, Freie Universität, Berlin, Germany.
- WETHERILL, G.W., 1967. Collisions in the Asteroid Belt. *Journal of Geophysical Research*, Vol. **72**, pp. 2429–2444.
- WETHERILL, G.W., 1979. Steady-state populations of Apollo-Amor objects. *Icarus*, Vol. **37**, 96–112.
- WETHERILL, G.W., 1988. Where do the Apollo objects come from? *Icarus*, Vol. **76**, 1–18.
- WILHELMS, D.E., 1987. The geologic History of the Moon. U.S. Geol. Surv. Prof. Pap. 1348, 302 p.
- WILHELMS, D.E., OBERBECK, V.R., AGGARWAL, H.R., 1978. Size-frequency distributions of primary and secondary lunar impact craters. *Proc. Lunar Planet. Sci.* **9th**, pp. 3735–3762.
- WILLIAMS, J.G., 1969. PhD dissertation, University of California at Los Angeles.
- WISDOM, J., 1983. Chaotic behaviour and origin of the 3:1 Kirkwood gap. *Icarus*, Vol. **56**, pp. 51–74.
- WISDOM, J., 1985a. A perturbative treatment of motion near the 3:1 commensurability. *Icarus*, Vol. **63**, pp. 272–289.
- WISDOM, J., 1985b. Meteorites may follow a chaotic route to the Earth. *Nature*, Vol. **315**, pp. 731–733.
- WORONOW, A., 1977. Crater saturation and equilibrium: A Monte Carlo simulation. *Journal of Geophysical Research*, Vol. **82**, pp. 2447–2456.

- WORONOW, A., 1978. A general cratering history model and its implications for lunar highlands. *Icarus*, Vol. **34**, pp. 76–88.
- WORONOW, A., 1985. A Monte Carlo Study of Parameters Affecting Computer Simulations of Craters Saturation Density. *Proc. Lunar Sci. Conf.* **5th**, pp. C817–C824.
- WRAY, J.J., EHLMANN, B.L., SQUYRES, S.W., MUSTARD, J.F., KIRK, R.L., 2008. Compositional stratigraphy of clay-bearing layered deposits at Mawrth Vallis, Mars. *Geophysical Research Letters*, Vol. **35**, pp. 12202,1–6.
- WÜNNEMANN, K., and LANGE, M.A., 2002. Numerical modeling of impact-induced modifications of the deep-sea floor. *Deep Sea–Research Part II*, Vol. **49**, pp. 969–982.
- WÜNNEMANN, K., and IVANOV, B.A., 2003. Numerical modelling of the impact crater depth–diameter dependence in an acoustically fluidized target. *Solar System Research*, Vol. **51**, pp. 831–845.
- WÜNNEMANN, K., MORGAN, J.V., and JÖDICKE, H., 2005. Is ries crater typical for its size? An analysis based upon old and new geophysical data and numerical modeling. In: T. Kenkmann, F. Hörz, A. Deutsch (eds), *Large Meteorite Impacts III*, Geological Society of America Special Paper **384**, Boulder, Colorado, pp. 67–83.
- WÜNNEMANN, K., COLLINS, G.S., and MELOSH, H.J., 2006. A strain-based porosity model for use in hydrocode simulations of impacts and implications for transient crater growth in porous targets. *Icarus*, Vol. **180**, pp. 514–527.
- WÜNNEMANN, K., COLLINS, G.S., and OSINSKI, G.R., 2008. Numerical modelling of impact melt production in porous rock. *Earth and Planetary Science Letters*, Vol. **269**, pp. 530–539.
- ZEL'DOVICH, Y.B., and RAIZER, Y.P., 2002. *Physics of Shock Waves and High-Temperature Hydrodynamic Phenomena*. Dover Publication, Inc., Mineola, New York. 916 p.